Chem Soc Rev

REVIEW ARTICLE

View Article Online
View Journal | View Issue

Cite this: *Chem. Soc. Rev.*, 2018, 47, 3899

Emerging chemical strategies for imprinting magnetism in graphene and related 2D materials for spintronic and biomedical applications

Jiří Tuček,[a] Piotr Błoński,[a] Juri Ugolotti,[a] Akshaya Kumar Swain,[a] Toshiaki Enoki[b] and Radek Zbořil *[a]

Graphene, a single two-dimensional sheet of carbon atoms with an arrangement mimicking the honeycomb hexagonal architecture, has captured immense interest of the scientific community since its isolation in 2004. Besides its extraordinarily high electrical conductivity and surface area, graphene shows a long spin lifetime and limited hyperfine interactions, which favors its potential exploitation in spintronic and biomedical applications, provided it can be made magnetic. However, pristine graphene is diamagnetic in nature due to solely sp^2 hybridization. Thus, various attempts have been proposed to imprint magnetic features into graphene. The present review focuses on a systematic classification and physicochemical description of approaches leading to equip graphene with magnetic properties. These include introduction of point and line defects into graphene lattices, spatial confinement and edge engineering, doping of graphene lattice with foreign atoms, and sp^3 functionalization. Each magnetism-imprinting strategy is discussed in detail including identification of roles of various internal and external parameters in the induced magnetic regimes, with assessment of their robustness. Moreover, emergence of magnetism in graphene analogues and related 2D materials such as transition metal dichalcogenides, metal halides, metal dinitrides, MXenes, hexagonal boron nitride, and other organic compounds is also reviewed. Since the magnetic features of graphene can be readily masked by the presence of magnetic residues from synthesis itself or sample handling, the issue of magnetic impurities and correct data interpretations is also addressed. Finally, current problems and challenges in magnetism of graphene and related 2D materials and future potential applications are also highlighted.

Received 20th October 2017

DOI: 10.1039/c7cs00288b

rsc.li/chem-soc-rev

1. Introduction

Over the past one hundred years, most of the solid-state magnetic phenomena and features, occurring at both macroscopic and nanoworld levels, have been thoroughly described experimentally and theoretically for compounds with 3d- and 4f-block elements addressing the origin of magnetism, its quantum nature, essence of magnetic ordering, and various types of magnetically self-sustainable regimes (*i.e.*, ferromagnetism, antiferromagnetism, ferrimagnetism, *etc.*). To widely recognize the significance of magnetic phenomena and their numerous applications, the 1970 Nobel prize in Physics was awarded to Louis Néel for his pioneering studies on the magnetic properties of solids. However, in the late 1980s, it was speculated that compounds which are made up of non-metals only (*i.e.*, C, O, H, N, and P) could have shown magnetic ordering and, hence, self-sustainable magnetism. Such compounds must have an unpaired p electron and, hence, must show features of an organic radical; they represent a new class of magnetic substances termed organic magnets. In 1991, *p*-nitrophenyl nitronyl nitroxide (*p*-NPNN) was the first example of an organic magnet with ferromagnetic (FM) properties below 0.65 K.[1,2] Despite the diversity of organic chemistry, there exist only a few purely organic compounds with unpaired p electrons and magnetic moments that can magnetically order, but only at low temperature. Thus, with the discovery of fullerenes[3] and, especially, carbon nanotubes,[4] the attention of the scientific community searching for magnetically active organic materials was shifted to carbon (nano)allotropes.

Carbon is the building block of all the forms of life on Earth and is the fourth most abundant element in the solar system. The ground-state electronic configuration of carbon is given by $1s^2 2s^2 2p^2$; carbon can form single, double or triple bonds with

[a] *Regional Centre of Advanced Technologies and Materials, Department of Physical Chemistry, Faculty of Science, Palacký University in Olomouc, Šlechtitelů 27, 783 71 Olomouc, Czech Republic. E-mail: radek.zboril@upol.cz; Fax: +420 585634761; Tel: +420 585634337*

[b] *Tokyo Institute of Technology, 2 Chome-12-1 Ookayama, Meguro, Tokyo 152-8550, Japan*

another carbon atom. However, it is known that carbon, despite having two unpaired spins in the outer p-shell as an isolated atom, is diamagnetic due to the nature of bonds that are established between the carbon atoms. In particular, adopting the concept of molecular orbital theory (see Fig. 1), four electrons are paired in the carbon π-bonding orbital. In other words, carbon always forms four bonds, leaving no unpaired electrons. Thus, the magnetic moment of carbon shows only a diamagnetic term, resulting from the motion of electrons on the orbitals, with a zero paramagnetic contribution. As a result, all the carbon (nano)allotropes/nanostructures, known so far or predicted to exist, with an identical character of bonds between the carbon atoms are supposed to lack any magnetic features.

Carbon (nano)allotropes/nanostructures can be classified depending on various criteria.[5] Most frequently, dimensionality is selected as a standard for placing them into four groups, *i.e.*, (i) 0D (*e.g.*, fullerenes, quantum dots, nanodiamonds), (ii) 1D (*e.g.*, carbon nanotubes, nanohorns, and nanoribbons), (iii) 2D (*e.g.*, graphene), and (iv) 3D (*e.g.*, graphite, diamond) structures. With regard to morphology, carbon (nano)allotropes/nanostructures fall into two categories, *i.e.*, (i) open/flat (*e.g.*, graphene) and closed/hollow (*e.g.*, fullerenes, carbon nanotubes) structures. Another classification involves the type of bonds between carbon atoms. In general, carbon tends to readily hybridize its 2s and 2p orbitals upon bonding with other carbon atoms. Three different hybridized states in carbon are recognized, *i.e.*, (i) sp,

Jiří Tuček

Dr Jiří Tuček received his PhD in Applied Physics from the Palacký University in Olomouc, Czech Republic, in 2008. In 2013, he became an associate professor at the Faculty of Science of the Palacký University in Olomouc, Czech Republic. He is currently a Senior Researcher and the head of the "Magnetic Nanostructures" group at the Regional Centre of Advanced Technologies and Materials (RCPTM), Palacký University in Olomouc, Czech Republic. In 2015, he received The Zasshi-kai Lectureship Award from The Tokyo University, Japan, for young scientists for the contribution in the field of magnetism of nanostructured objects. His research interests include magnetism in the nanoworld, particularly the magnetic behavior and properties of carbon nanostructures (in particular, graphene) and iron-containing compounds such as iron and iron oxide nanosystems.

Piotr Błoński

Dr Piotr Błoński obtained his PhD degree in physics from the University of Wrocław, Poland (2006). After his PhD, he undertook several postdoctoral stays, at the University of Vienna, Austria, at the Institute of Chemical Research of Catalonia, Spain, and at the Institute of Nuclear Physics, Polish Academy of Sciences in Kraków. Currently, he is an assistant professor at the Department of Physical Chemistry and a junior researcher at the Regional Centre of Advanced Technologies and Materials (RCPTM), Palacký University in Olomouc, Czech Republic. His research focuses on modelling magnetic nanomaterials with an emphasis on carbon nanostructures.

Juri Ugolotti

Dr Juri Ugolotti is a researcher at the Regional Centre of Advanced Technologies and Materials (RCPTM) of the Palacký University in Olomouc, Czech Republic. He completed his undergraduate studies in Applied Chemistry in the UK and Italy, and he received his PhD in Chemistry from Imperial College London, UK. After post-doctoral spells at the University of Münster, Germany, and at the Academy of Science of the Czech Republic in Prague, he started working at RCPTM in 2014. His research interests span the synthesis, characterization and application of magnetic inorganic and organometallic materials and of carbon-based nanostructures.

Akshaya Kumar Swain

Dr Akshaya Kumar Swain obtained his PhD degree in materials science, which was jointly awarded by IIT Bombay-India and Monash University-Australia in 2015. He also obtained his MTech degree in solid state materials from IIT Delhi-India. He is currently working as an assistant professor of physics at the GITAM University-India and pursuing research on functional nanomaterials for application in spintronics and cancer therapy. His research interests include synthesis and magnetism of low-dimensional materials, particularly belonging to the carbon family.

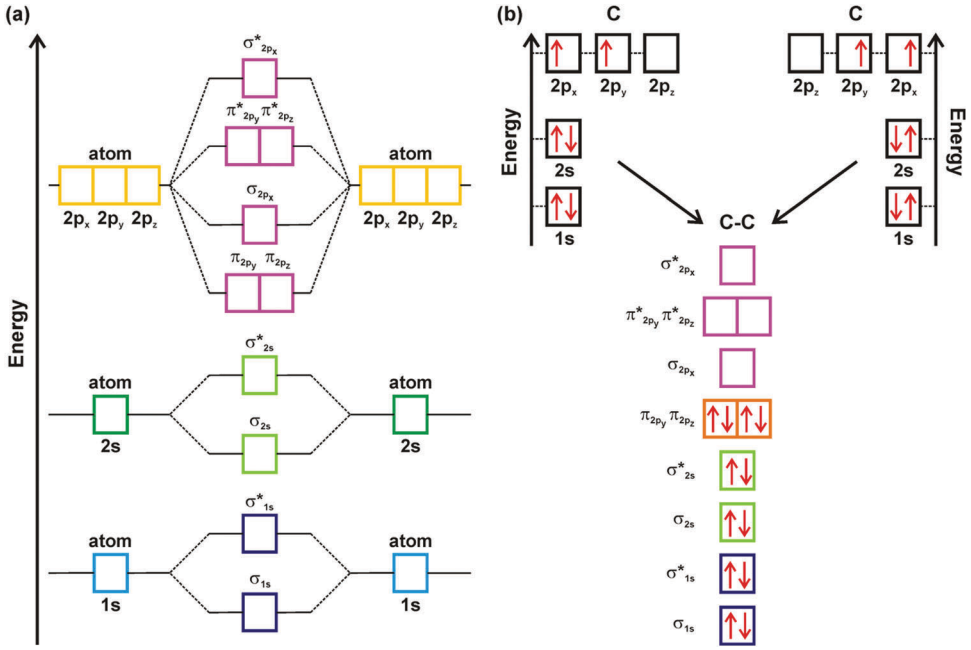

Fig. 1 (a) General molecular orbital energy-level diagram for the first two energy levels showing the formation of molecular bonding (σ, π) and antibonding (σ*, π*) orbitals. (b) Bonding scheme for two carbon atoms providing evidence for pairing of all the spins, confirming thus the diamagnetic nature of the C–C pair.

(ii) sp^2, and (iii) sp^3 (see Fig. 2a), depending on the number of σ-bonds established between the carbon atoms. In the case of sp^3 hybridization, carbon atoms present four single bonds with a tetrahedral arrangement while one double bond and two single bonds are characteristic of sp^2 hybridization with trigonal planar geometry (see Fig. 2a). The configuration showing one single and one triple bond conforms to sp hybridization with carbon atoms lying on a line (see Fig. 2a). Various hybridization states and their combinations generate a broad spectrum of already existing carbon (nano)allotropes/nanostructures as demonstrated in Fig. 2b.[5,6] Other structures with C atoms in various sp/sp^2/sp^3 ratios were predicted such as high-pressure phases or hypothetical forms found thermodynamically stable from theoretical calculations, all waiting to emerge from properly designed/optimized synthetic protocols.[5]

Toshiaki Enoki

Professor Toshiaki Enoki received his PhD in 1974 from Kyoto University. He was a research associate at the Institute for Molecular Science (1977–1987) and a visiting scientist at the Massachusetts Institute of Technology in 1984. In 1987, he moved to the Department of Chemistry at the Tokyo Institute of Technology as an associate professor, and then became a professor. Currently, he is a professor emeritus at the institute. He was a visiting professor at the University of Rennes I (2000, 2004, 2005), the Institute for Molecular Science (2003–2004), an honorary professor at Durham University (2010) and an honorary member of Ioffe Institute, Russian Academy of Sciences in 2013. His current research interests are focused on the electronic and magnetic structures of π-electron-based materials, such as nanographene, nanodiamond, and organic charge transfer complexes.

Radek Zbořil

Professor Radek Zbořil received his PhD degree from the Palacký University in Olomouc, Czech Republic. After his doctoral studies, he did several foreign stays at universities around the world in locations such as Tokyo, Delaware, and Johannesburg. Currently, he is a professor in the Department of Physical Chemistry and a General Director of the Regional Centre of Advanced Technologies and Materials at the Palacký University in Olomouc, Czech Republic. His research interests focus on nanomaterial research including iron- and iron oxide-based nanoparticles, silver nanoparticles, carbon nanostructures, and magnetic nanoparticles, their synthesis, physicochemical characterization, and applications in catalysis, water treatment, antimicrobial treatment, medicine, and biotechnology. He is an author and co-author of more than 450 scientific papers with more than 15 000 citations.

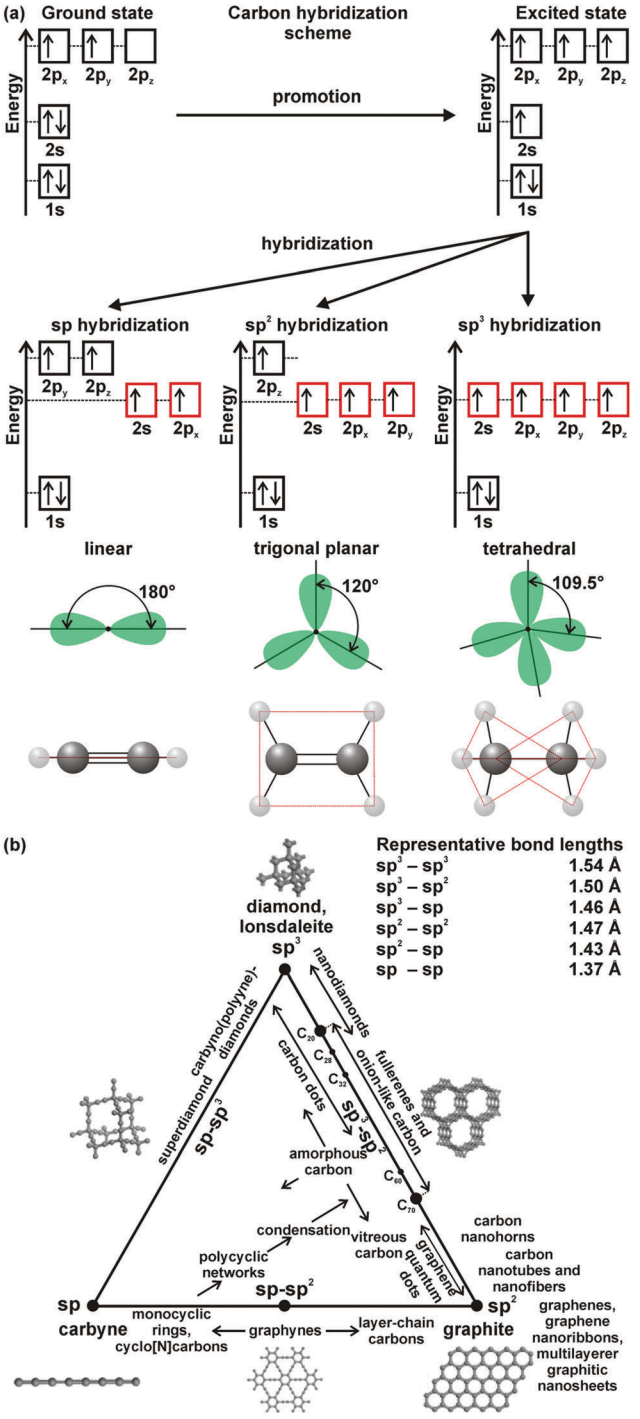

Fig. 2 (a) Schematic description of sp, sp^2, and sp^3 hybridization in carbon with an illustration of the bonding structure. (b) Ternary phase diagram of carbon (nano)allotropes/nanostructures depending on the hybridization state they show. The positions/intervals of the most common carbon (nano)allotropes/nanostructures are indicated. Carbon forms with a single hybridization state are found at the vertices of the triangle, carbon species with mixed hybridization states lie along the sides of the triangle, and carbon compounds with all the three hybridization states are placed inside the triangle. The representative bond lengths between carbon atoms with specific hybridizations are also listed. Panel (b) reprinted with permission from ref. 5. Copyright 2015 American Chemical Society.

Due to the participation of all the valence electrons in establishing strong sp^3, sp^2, and sp bonds, carbon is regarded as an element with the least probability to retain unpaired electrons, thus behaving largely in a diamagnetic manner. Indeed, besides superconductors, graphite is ranked as a material with the most negative magnetic susceptibility reported so far ($\sim -50 \times 10^{-6}$ emu g^{-1}).[7] The diamagnetic behavior of graphite is solely caused by delocalization of electrons which move along the graphitic rings in the plane; due to small contribution of motion of electrons in the direction perpendicular to the graphitic rings, the diamagnetic susceptibility of graphite is highly anisotropic. In diamond, three contributions to its magnetic susceptibility were identified, *i.e.*, two diamagnetic terms originating from s (core) and p (valence) electrons and a van Vleck (paramagnetic) term emerging from magnetic dipole transitions occurring between the valence and conduction bands with a strong dependence on the symmetry of the chemical bond.[7] As the van Vleck term is relatively small, diamond shows a dominant diamagnetic response (with a magnetic susceptibility of $\sim -0.5 \times 10^{-6}$ emu g^{-1}). Carbyne, an example of purely sp carbon (nano)allotrope, is also diamagnetic due to electron currents flowing along its structure.

Other carbon nanostructures such as carbon nanotubes and carbon nanohorns were found to be magnetically unattractive. In particular, single-walled and multi-walled carbon nanotubes, composed entirely of sp^2 bonds, are diamagnetic. If magnetic features for carbon nanotubes were reported, they were ascribed to the presence of catalyst particles (*e.g.*, Fe, Co). However, a few exceptions exist in the literature. The possibility of imprinting stable magnetization in carbon nanotubes was addressed by theoretical computations and experiments; it was found that a magnetic ground state may emerge for finite-sized zigzag-cut carbon nanotubes in the case of hydrogenation, truncation with edge termination, and capping by fullerene hemispheres.[8,9] FM behavior was then explained in terms of larger exchange splitting compared to energy loss due to breaking the bonding states in some carbon nanotubes; the FM response was found to strongly depend on the chirality and diameter of the nanotubes. Another hypothesis introduces the concept of emergence of free radicals communicating *via* the itinerant electrons of the carbon nanotube network.[10] The magnetic ground state can be alternatively stabilized by topological line defects involving pentagon and octagon rings with emergence of peculiar edge-localized states similar to those of graphite flakes.[11] The theory predicts that metallic carbon nanotubes may behave in an FM (antiferromagnetic (AFM)) manner if localized spins occupy the same (different) sublattice while semiconducting carbon nanotubes may show a dominant FM response with weak dependence on the distribution of the localized spins over respective sublattices; the communication pathways are believed to be maintained by an isotropic Heisenberg interaction and anisotropic Ruderman–Kittel–Kasuya–Yosida (RKKY) interaction of Ising and Dzyaloshinskii–Moriya nature, the latter emerging due to spin–orbit interactions breaking the SU(2) spin symmetry of the system.[12] In the case of carbon nanohorns (*i.e.*, short single-walled carbon nanotubes

closed on one side), diamagnetic features were reported; it is speculated that a large diamagnetic contribution originating from the sp^2 network is partly cancelled by a constant van Vleck paramagnetic term.[13] Similar to carbon nanotubes, carbon nanohorns are diamagnetic in nature; emergence of magnetic features in nanohorns was observed upon adsorption of oxygen.[14]

The hope that pure carbon structures may show unpaired spins and eventually magnetic ordering is redirected to such carbon (nano)allotropes with mixed hybridization states (*i.e.*, sp^2/sp^3 ratio) in which some of the valence electrons are not involved in a bonding process. In particular, fullerenes with "pseudo" sp^3 and sp^2 bonds, the ratio of which depends on the number of carbon atoms (see Fig. 2b), show both diamagnetic and paramagnetic behavior. The diamagnetic contribution originates from electrons moving around the hexagonal rings,[15] while motion of electrons around double bonds which are adjacent to the vertices of pentagons is identified to be responsible for the paramagnetic term.[16] It is then assumed that the diamagnetic contribution should gradually increase with the size of fullerenes (*i.e.*, with increasing number of hexagons), eventually reaching the value of the diamagnetic susceptibility of graphite.[17] However, it was observed that the diamagnetic susceptibility of fullerenes with a number of carbon atoms less than 100 varies in a random manner, most probably resulting from a dependence of the characteristics of bonds in pentagons and hexagons on the structure.[18] For larger fullerenes, diamagnetic susceptibility increases as expected. For C_{60}, the most studied fullerene, the paramagnetic and diamagnetic contributions are almost equal; hence, C_{60} is non-magnetic. In order to increase the paramagnetic term in C_{60}, several strategies have been proposed such as intercalation with oxygen or intrinsic defects (*e.g.*, C_{60}^- ions). FM/AFM features were observed for some fullerene derivatives such as C_{60} charge transfer complexes (*e.g.*, C_{60}–TDAE (tetrakis-dimethylamino-ethylene)–$C_2N_4(CH_3)_8$),[19] $C_{60}R_n$ compounds (where R is H, F, CF_3 or polymer fragments, and n is odd),[20–22] and fullerenes polymerized by irradiation or introduction of under pressure (orthorhombic, tetragonal, and rhombohedral fullerene polymers).[23–25] Among them, C_{60}–TDAE, a donor–acceptor type system, has been studied heavily; it undergoes a transition to the FM state at $\sim$16 K.[19] The emergence of the FM regime was explained in terms of formation of an ion-radical ($TDAE^{+\bullet}$–$C_{60}^{-\bullet}$) pair due to charge transfer from the π-orbitals of a donor molecule (TDAE) coupled by strong spin-exchange. If TDAE is replaced with other donating compounds, FM behavior is preserved;[26] however, with C_{70}, no long-range magnetic ordering was ever observed. $(ND_3)K_3C_{60}$ is another example of a fullerene-based compound behaving in AFM manner stabilized up to $\sim$37 K by spatial disorder and inhomogeneity effects.[27] Nanodiamonds – close dimensional relatives to fullerenes – with a core–shell structure composed of a diamond core (sp^3 carbon atoms), a middle layer (sp^{2+x} carbon atoms), and a graphitic outer shell (sp^2 carbon atoms) with dangling bonds terminated by functional groups[5] – were found to be largely diamagnetic with minor paramagnetic centers whose existence is further promoted by the introduction of nitrogen vacancies.[28] However, no magnetic ordering has been observed so far for nanodiamonds. Similar to non-functionalized fullerenes, onion-like carbon shows a large diamagnetic contribution and a small paramagnetic term.

In the beginning of the nineties of the 20th century, it was theoretically predicted that carbon may become magnetic once the structure adopts an arrangement with a mixture of planar 3-fold coordinated sp^2- and tetrahedral sp^3-hybridized carbon atoms.[29,30] In particular, for a hypothetical layered intermediate graphite-diamond structure with 50% of sp^2-bonded and 50% of sp^3-bonded carbon atoms, resulting in a high level of unpaired electrons (0.59 per carbon atom), the saturation magnetization was estimated to reach 230 emu g^{-1}, similar to that of α-Fe (220 emu g^{-1}). Carbon nanofoam, firstly synthesized in 1999, is an example of a carbon (nano)allotrope with a $sp^3/(sp^2 + sp^3)$ bonding ratio of 35% on average and a structure resembling hyperbolic schwarzite.[31] Carbon nanofoam is modelled as a tetrapod with 12 heptagons surrounded by hexagons with tetravalent carbon atoms (with heptagons showing trivalent carbon radicals with a lone electron). Magnetic carbon nanofoam shows a Curie temperature of $\sim$92 K and a saturation magnetization of $\sim$0.42 emu g^{-1} (at 1.8 K). The origin of magnetic moments in carbon nanofoam was explained considering several factors: (i) the presence of carbon rings other than 6-membered rings causing localization of the π-electron cloud encouraging localization of unpaired spins; (ii) sp^3-bond carbon atoms providing cross-linking between different schwarzite layers and preventing π-electron delocalization; (iii) potential presence of carbon vacancies; and (iv) presence of hydrogen and oxygen promoting spin formation and localization by disrupting the conjugated C–C bond system.[32] However, it seems that establishment of an interaction pathway is strongly dependent on the $sp^3/(sp^2 + sp^3)$ ratio with a non-trivial trend. Moreover, magnetic carbon nanofoam is highly unstable losing its magnetic features within several months after synthesis if not protected against a chemical attack by formation of strongly convoluted sheets and/or impermeable frameworks.

Similarly, if the structure contains both sp- and sp^2-bonded carbon atoms, magnetic moments are observed to evolve;[33,34] the examples of carbon nanoallotropes with mixed sp and sp^2 hybridization states include graphyne and graphdiyne.[5] In graphdiyne, the magnetic moments are believed to arise due to the unique construction of the carbon matrix and specific sp-hybridization. They can be enhanced if the structure of graphdiyne is doped with nitrogen with a pyridine configuration.[35] Graphdiyne then behaves in a paramagnetic manner (*i.e.*, spin-half paramagnet) without any magnetic ordering; an AFM ground state was observed for annealed graphdiyne when hydroxyl groups, adsorbed on the graphdiyne sheet and forming a chain-like motif, were identified as the major sources of magnetic moments.[34]

In 2004, when graphene was firstly isolated,[36] the realm of carbon witnessed a striking attention from the scientific community to synthesize graphene, study, understand, and tune its unique physicochemical properties[37–40] and, eventually, equip it with features it misses, including a magnetic response. Since then, dozens of theoretical and experimental papers have

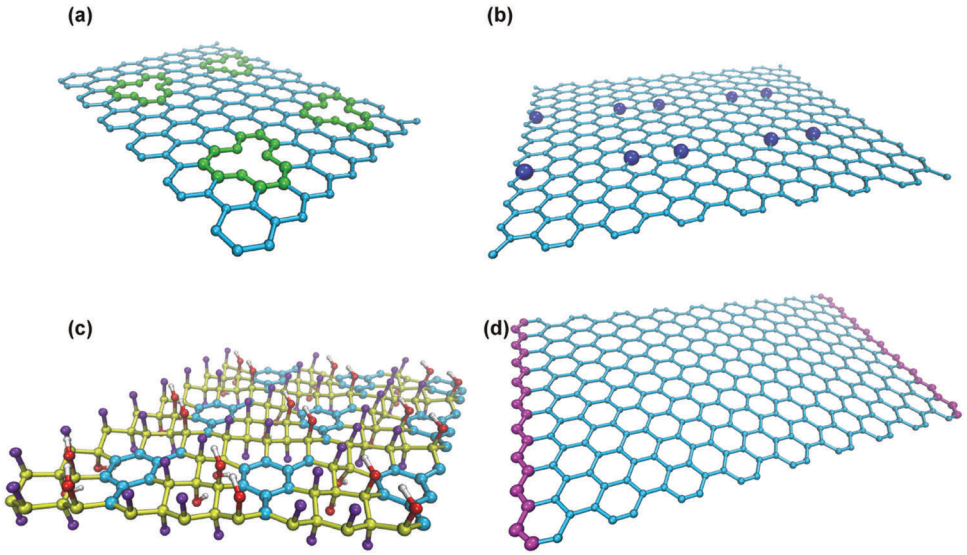

Fig. 3 Defects imprinting a magnetic behavior into graphene: (a) vacancies; (b) substitution with non-carbon atoms; (c) sp^3 functionalization; (d) edges.

appeared reporting attempts to synthesize "magnetically-active" graphene-based systems which would be competitive with traditional inorganic magnets thus opening the doors towards applications in electronics,[41] spintronics,[42] biomedicine,[43] and magnetic (bio)separations.[44]

Graphene, intrinsically of diamagnetic nature due to a delocalized π-bonding network, was found to show magnetic features only in cases when defects were introduced into its lattice as indicated by numerous theoretical works and confirmed by several experimental studies.[45] The defects include local topology perturbations,[46] vacancies,[47] Stone–Wales (SW) defects,[48] pentagonal–octagon pairs,[49] substitution with non-carbon atoms in the graphene lattice,[50,51] adatoms (*i.e.*, atoms attached to the surface of the graphene sheet),[52,53] mixed sp^2/sp^3 hybridization (*i.e.*, covalent sp^3 functionalization),[54,55] and zigzag-type edges (*i.e.*, confinement-related phenomena) (see Fig. 3).[56,57] In short, these defects are manifested as semi-localized π "midgap" states or flat bands in the electronic band structure of graphene with the peaks in the density of states at the Fermi level (E_F) showing spin polarization, giving rise to localized magnetic moments. Defect-induced FM behavior in graphene and its derivatives (*e.g.*, graphone, graphane) has been experimentally observed to evolve at low temperatures; however, its sustainability at room temperature is heavily questioned as the π-electron system of graphene is too weak to maintain magnetic interactions (*i.e.*, RKKY-like interactions) between induced localized moments at elevated temperatures. Recently, several reports have appeared demonstrating the possibility of preparing graphene-based systems with magnetic ordering stable up to room temperature. Currently, the imprinting of self-sustainable magnetism at room temperature to graphene and/or its derivatives is widely recognized as a key challenge for further development of 2D carbon-based materials with a tremendous potential, especially, in spintronics and biomedical fields.

Several review works have been published so far aimed at giving an overview about the recent advancements in magnetism of graphene and related 2D materials;[42,58–60] however, they have focused only on the theoretical aspects of imprinting self-sustainable magnetic features in graphene or have chosen only particular defects without any systematization and critical assessment or have concentrated solely on the application potential of magnetically active graphene systems and their 2D analogs. Moreover, in this respect, substitution and functionalization of graphene sheets as new emerging approaches toward magnetism in graphene have been ignored so far. The present review thus aspires to comprehensively and critically cover the issue of magnetism in graphene, its derivatives and 2D analogs with regard to a recent huge progress in the field from the theoretical, experimental, and application perspective. The aims include to systematically classify the methods used to equip graphene with magnetic properties, evaluate the effectiveness of various approaches in imprinting of magnetism in graphene and discuss their possible exploitation for challenging future applications. Particularly, in Section 2, graphene is introduced with an emphasis on its structure and electronic features, highlighting areas of its potential applications. Moreover, the models providing description and understanding of defect-induced magnetic behavior in graphene are briefly discussed. Section 3 is devoted to point and line defects in graphene, their nature, experimental creation and their role in the evolution of magnetic features in graphene. Section 4 reviews confined graphene-based systems including graphene nanoribbons, graphene nanoflakes, and graphene quantum dots. The attention is devoted to identifying the role and effect of the intrinsic parameters of the system (*e.g.*, edge geometry, size, lattice doping, and edge modification) and external stimuli (*e.g.*, electric field and strain) on the evolution and tuning of the magnetic response of confined graphene-based representatives. In Section 5, the issue of doping of the graphene lattice with non-carbon elements (*i.e.*, nitrogen, sulfur) is addressed; here, the type (n-type/p-type), chemical nature, and concentration of the dopant are discussed as crucial parameters affecting directly the

electronic structure of graphene and, hence, evolved magnetic properties. Section 6 introduces the concept of chemical covalent functionalization of the graphene surface with various adatoms (*e.g.* hydrogen, nitrogen, fluorine) and functional groups (*e.g.*, –OH, –COOH) as a promising strategy to develop graphene-based systems with a magnetic ordering sustainable up to room temperature. Section 7 briefly summarizes recent advancements in magnetically active graphene intercalated compounds. In Section 8, the emergence of magnetism in graphene analogues and other selected 2D materials is discussed; in particular, the attention is devoted to transition metal dichalcogenides, metal dihalides, metal dinitrides, MXenes, hexagonal boron nitride, and other relevant 2D compounds/molecules. Since the magnetic behavior of graphene imprinted with defects of whatever nature can be incorrectly interpreted as due to magnetic impurities (*i.e.*, d-block elements), Section 9 sheds light on the proper determination of magnetic admixtures in the sample (*i.e.*, magnetic residues from synthesis itself or sample handling) and discusses experimental approaches to quantify/exclude them, thus preventing misleading interpretations. Moreover, mathematical procedures used to correctly analyze the measured magnetization data and separate individual magnetic contributions are also briefly outlined. Finally, the review summarizes the current status in the field of graphene magnetism, highlights the potential future challenges, and envisages application fields where ''magnetic'' graphene could become a prominent material.

2. Graphene, its structure, properties and applications and theoretical models providing an understanding of defect-induced magnetic behavior in graphene

Carbon atoms in graphene are sp^2-hybridized leaving a free p_z orbital perpendicular to the plane (see Fig. 4). The in-plane sp^2-orbitals form the σ-bonds. The honeycomb lattice of graphene is formed by three sp^2-bonded carbon atoms.[37] However, the Bravais lattice of graphene is different from the honeycomb lattice and is superposition of two triangular Bravais lattices (termed as A- and B-sublattice, or alternatively denoted as α- and β-sublattice, respectively). Hence, the honeycomb lattice of graphene provides two free electrons per unit cell.[61]

Graphene follows a linear dispersion relation, reflecting the relativistic nature of the electrons and holes in graphene, which behave as massless Dirac fermions in a biparticle lattice.[37,61] The corresponding Hamiltonian can then be represented adopting the relativistic Weyl equation,[37] *i.e.*,

$$H = \sigma V_F p, \quad (1)$$

where p is the momentum, V_F is the Fermi velocity and σ is the pseudospin operator. Cone-shaped electronic bands (also called Dirac cones) for the π-valence and π*-conduction states can be obtained by solving the relativistic Weyl equation. These Dirac cones touch each other at a point called the Dirac point resulting in a zero-gap semiconducting behavior. In other words, the π- and π*-bands equip graphene with most of its remarkable electronic properties *via* the half-filled band that permits free-moving electrons.

The peculiar electronic structure of graphene is responsible for emergence of unusual physical phenomena including, for example, the half-integer quantum Hall effect,[62,63] ambipolar electric field effect,[36] non-linear Kerr effect,[64] Casimir effect,[65] photothermoelectric effect,[66] bipolar supercurrent,[67] and positive piezoconductive effect.[68] Due to its structural and electronic features, graphene is equipped with superior properties such as, for example, a high charge carrier mobility (up to 200 000 $cm^2 V^{-1} s^{-1}$ at room temperature at a carrier density of 10^{12} cm^{-2}), very low resistivity (10^{-6} Ω cm), large thermal conductivity (1500–2500 $W m^{-1} K^{-1}$), high optical transmittance (97.7% for red light), large surface area (2630 $m^2 g^{-1}$), and high tensile strength (130.5 GPa) and Young's modulus (~1 TPa). The physicochemical characteristics of graphene can be further easily/appropriately tuned by doping its lattice with non-carbon atoms, functionalizing its surface with various atoms, molecules, functional groups or deposition on various substrates,[39] significantly extending its portfolio of applications. So far, graphene has been suggested as a promising material in various fields such as, for example, electronics (ultralight flexible displays and touch panels,[69] field-effect, high speed and ballistic transistors,[70] spin transistors and spin logic devices,[42] light-emitting diodes,[71] components

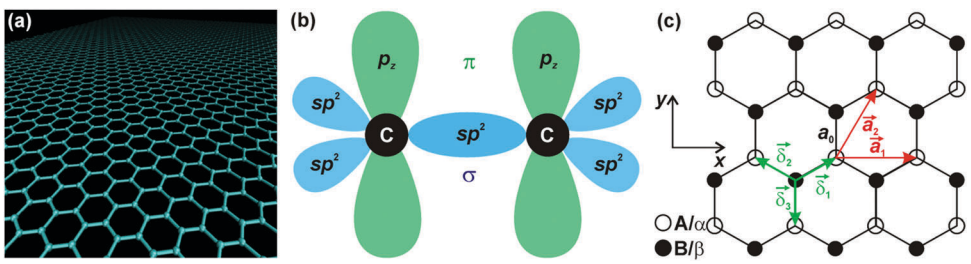

Fig. 4 (a) Pictorial representation of graphene sheet and (b) sp^2 hybridization in graphene. (c) The honeycomb lattice structure of graphene. The atoms in the sublattice are separated by a_0 = 0.142 nm. The basis vectors of the Bravais lattice are represented by a_1 and a_2 and are given as $a_1 = a_0\sqrt{3}(1; 0)$ and $a_2 = a_0\sqrt{3}(1/2; \sqrt{3}/2)$. The nearest vectors that connect the atoms from the A-(α-) to the B-(β-)sublattice are represented by δ_1, δ_2, and δ_3 and given as $\delta_1 = a_0/2(\sqrt{3}; 1)$, $\delta_2 = a_0/2(-\sqrt{3}; 1)$, and $\delta_3 = a_0/2(0; -1)$.

of radio frequency integrated circuits[72] and nanoelectromechanical systems[73]), energy storing and generating devices (electrodes in ultra-/super-capacitors,[74] Li-ion batteries,[75] and fuel cells[76]), optics (photoactive medium in solar cells,[77] photodetectors,[78] and broadband polarizers[79]), printing technologies (conductive inks,[80] inks for electromagnetic shielding[81]), medicine (DNA sequencing,[82] agents for cellular imaging and carriers of drugs/biomolecules[83]), environment- and water-treating technologies (sensors and sorbents of pollutants,[84] water desalination[85]), and additives improving mechanical properties of composites (car bumpers[86]). However, most of the proposed applications of graphene are still in the laboratory stage as problems are frequently faced with scaling-up the production of graphene-based systems, preserving, at the same time, their purity, chemical identity, and, hence, application-desired physicochemical properties.

Besides, graphene shows strong ballistic transport, long spin lifetime and spin relaxation length, limited hyperfine interactions, and weak spin–orbit coupling (a result of low nuclear charge and orthogonality of π- and σ-bands), *i.e.*, prerequisites, which are highly required in spintronics. Importantly, due to the spin–orbit coupling, the quantum spin Hall effect emerges in graphene, when the spin-up and spin-down carriers move in the opposite directions along the same edge.[87] However, as already mentioned above, it misses localized magnetic moments in its pristine state. Thus, defects of whatever nature are needed to free electrons from bonding resulting in evolution of unpaired spins. Magnetic susceptibility (χ_{mass}) of the defected graphene is then given by $\chi_{mass} = \chi_{mass,dia} + \chi_{mass,para} + \chi_{mass,ferro}$, where $\chi_{mass,dia}$ is the diamagnetic term involving orbital, Landau, and core diamagnetic contributions, $\chi_{mass,para}$ stands for a paramagnetic term including Curie-like response of non-interacting (isolated) defect-induced paramagnetic centers, paramagnetic Pauli contribution from conduction electrons, and paramagnetic van Vleck contribution, and $\chi_{mass,ferro}$ represents the ferromagnetic term reflecting the establishment of interaction pathways between the defect-induced paramagnetic centers.

A theoretical understanding of graphene magnetism can be well described by the tight-binding model, Hamiltonian model, Hubbard model, mean field approximation (Hartree–Fock, Monte Carlo, renormalization, *etc.*), density functional theory (DFT) approach, *etc.* From the theoretical viewpoint, the electron–electron interaction as the diagonal elements of the Hamiltonian matrix plays an important role. The problem can be solved with an appropriate guess that could tackle the matrix self-consistently breaking the spin–lattice symmetry.

The one-orbital mean-field Hubbard model is probably the simplest model to analyze the magnetic properties of sp^2 carbon nanostructures. The unhybridized p_z atomic orbitals of sp^2 carbon atoms in graphene give rise to low energy π-symmetry electronic states. The mean-field Hubbard model considers these π-symmetry electronic states. The Hamiltonian is given as

$$H = H_0 + H_I, \tag{2}$$

where H_0 and H_I are the kinetic and interaction parts of the Hamiltonian, respectively. H_0 represents the nearest-neighbor tight-binding Hamiltonian given as

$$H_0 = -t \sum_{\langle i,j\rangle\sigma} \left[c_{i\sigma}^{\dagger} c_{j\sigma} + \text{h.c.} \right], \tag{3}$$

where $c_{i\sigma}^{\dagger}$ and $c_{j\sigma}$ are the creation and annihilation operators, respectively, that create and annihilate an electron at site i with spin σ. The term "h.c." is the Hermitian conjugate part of the Hamiltonian. The consideration of nearest-neighbor atoms is denoted by the angular bracket ($\langle\rangle$). The hopping integral $t \approx 2.7$ eV. The elements of the Hamiltonian matrix are determined by the atomic structure. If the atoms i and j are covalently bonded, the off-diagonal matrix elements are set to $-t$. The eigenvalues of the Hamiltonian matrix have electron–hole symmetry. Thus, the bonding (occupied) and anti-bonding (unoccupied) states are always in pairs with an energy relation given as $\varepsilon = -\varepsilon^*$. The mid-gap states with energy $\varepsilon = 0$ are called the zero-energy states. Although the tight-binding model can predict the electronic structure of sp^2 carbon atoms, addition of the on-site Coulomb interaction helps in explaining the emergence of magnetism. Thus, the interaction part of the mean-field Hubbard model is given as

$$H_I = U \sum_i n_{i\uparrow} n_{i\downarrow}, \tag{4}$$

where U is the magnitude of the on-site Coulomb interaction. The spin-resolved electron density at the i-site is given by $n_{i\sigma} = c_{i\sigma}^{\dagger} c_{j\sigma}$. It should be noted that this model involves only the nearest neighbor interactions. Thus, only two electrons are considered that occupy the same p_z atomic orbital. This limitation can be overcome by using a mean-field approximation where an electron with spin-up/-down at the i-site interacts with the average electron density with spin-down/-up. Hence, the Hamiltonian in the mean-field approximation is given by

$$H_{mf} = U \sum_i \left\{ n_{i\uparrow} \langle n_{i\downarrow} \rangle + \langle n_{i\uparrow} \rangle n_{i\downarrow} - \langle n_{i\uparrow} \rangle \langle n_{i\downarrow} \rangle \right\}. \tag{5}$$

The diagonal terms in the Hamiltonian are only effected by such formulation. This can be solved self-consistently by arbitrarily choosing a value for $\langle n_{i\sigma} \rangle$. In the case when the chosen value breaks the spin spatial symmetry, AFM solutions can be obtained.[88,89] With a right guess for the starting value of $\langle n_{i\sigma} \rangle$, one can easily converge the solution with repeated iterations. Eventually, the spin density at each i-atom is obtained self-consistently and is given by

$$M_i = \frac{1}{2} \left(\langle n_{i\uparrow} \rangle - \langle n_{i\downarrow} \rangle \right) \tag{6}$$

The total spin (S) of the system is given by $S = \sum_i M_i$. The induced magnetic moment in the carbon nanostructure mainly depends on U/t. With a right guess for U/t, one can easily obtain similar solutions compared to those from the first-principles calculations.

Doubts can be raised on the suitability of the above-discussed model by demanding further clarifications. Does the graphene

system follow the mean-field approximation? How does it compare to the results obtained by a method that considers all the electrons? What could be the best guesses for U/t to get a converged solution? The validity of the mean-field approximation can be checked by comparing its results with that obtained using the exact diagonalization and quantum Monte Carlo simulations.[90] If the empirical value of the parameter U/t is chosen wisely, a close match between the mean-field Hubbard model and first-principles computations can be achieved.[91–93] It should be noted that the equivalence of all electrons or ignoring the localized atomic core states, which are performed in the first-principles methods, actually does not play any important role. However, it does if one computes the hyperfine interactions because the spin polarization of the 1s carbon atoms can effectively contribute.[88,94] Else, choosing a suitable value of $U/t \approx 1.3$, the results achieved by the DFT model, considering an exchange–correlation function belonging to a generalized-gradient-approximation (GGA) family, can be reproduced. Similarly, choosing $U/t \approx 0.9$, the local-spin-density approximation results can also be predicted.[93] A suitable range for $U \approx 3.0$–3.5 eV was reported from magnetic resonance studies of *trans*-polyacetylene which is very similar to a zigzag-edged graphene nanoribbon with a minimum width.[95,96] The DFT model using GAA employs the identical interval of U/t, *i.e.*, 1.1–1.3. A Mott–Hubbard transition of AFM ordering in graphene can be obtained in the case in which one chooses the value of U/t to be greater than 2.23.[97]

Alternatively, the benzenoid graph theory can be used to compute and analyze the tight-binding Hamiltonian spectrum of graphene. For a thorough description of the benzenoid graph theory, one is advised to read the work by Fajtowicz *et al.*[98] In short, the theory is based on counting principles. The number of zero-energy states in the tight-binding model can be predicted (counted) from the graph's nullity in the benzenoid theory and is given by

$$\eta = 2\alpha - N, \tag{7}$$

where N is the total number of sites and α is the possible maximum number of sites that are not nearest to each other. Further, the Stoner criterion decides the onset of magnetism. The Stoner criterion is based on the competition between the loss of kinetic energy and the gain in exchange energy due to spin polarization of a system. The exchange splitting of the electronic states in the spin polarization system can cause a gain in the exchange energy,[99] *i.e.*,

$$\Delta S = \varepsilon_{\uparrow} - \varepsilon_{\downarrow} = \frac{U}{2}\sum_i n_i^2, \tag{8}$$

where $\sum_i n_i^2$ measures the degree of localization of the corresponding state. The loss of kinetic energy is proportional to this state. Thus, irrespective of the degree of localization, for any $U > 0$, the spin polarization occurs by the zero-energy states. In other words, spin polarization is a medium to prevent the instability of low-energy states in the system. The benzenoid theory is limited as it does not give the alignment of the spins in these states. Lieb's theorem[100] can be used to extract such information and, hence, to compute the total spin of the system. This theorem does not require any periodicity of the lattice structure and is valid in all the dimensions. Interestingly, both of the counting principles described above are linked as $\eta \geq N_A - N_B$, where N_A and N_B are number of sites on the A- and B-sublattice of graphene, respectively.

As mentioned above, the Stoner criteria decide on the evolution of ferromagnetism considering a competition between the exchange and kinetic energy. Usually, the s- and p-block elements have higher kinetic energy than the exchange energy. Thus, they tend to be non-magnetic as the loss of kinetic energy dominates over the gain in exchange energy. The energy effects become considerably important when the dimension of the system is reduced. The energies are also modified by the presence of defects and other atoms in the interface or surface. As a result, intrinsically non-magnetic s- and p-block elements may become magnetic.

3. Defected graphene: morphology and magnetic properties

The presence of defects in the graphene structure modifies its chemical, mechanical and electronic properties and can lead to the formation of magnetic moments. While pristine, defect-free graphene is diamagnetic, a sizeable amount of theoretical and experimental research has shown how defects can impart magnetic ordering to graphene and how this magnetism can be predicted, generated and tuned. The seminal work at the start of the current century by Esquinazi *et al.*[101–103] on irradiated graphite has generated a vast array of publications, and comprehensive reviews on the topic have been published.[45,104–108] In order to fully understand the impact of defects on the magnetism of graphene, it is necessary to review at the same time the types of defects that can be present on a graphene sheet, with particular focus on the magnetism-generating defects.[37,109–111] These involve point defects (0D), line defects (1D) and grain boundaries (2D), whereas 3D defects, like voids, are present in graphite. The defects, moreover, can be due to single or multiple vacancies when one or more atoms are removed, can be of topological type only, thus not involving any loss or gain of atoms (for example, Thrower-Stone–Wales (TSW) defects[112,113]), or can be due to internal or external adatoms and impurities, and to adatom/vacancy interactions. By extending the study to multilayer graphene, interstitial atoms can also be included among the defects. Moreover, a unique property of extended sp^2 carbon-based materials is the ability to reconstruct defects by forming non-hexagonal units with limited or no dangling bonds, and defects can also migrate or interact with each other, as in the case of the adatom/vacancy interactions. Here, the effect on magnetism of vacancies and TSW/line defects is covered, while among the external impurities only hydrogen will be considered. The theoretical works reviewed in this section are in particular devoted to the understanding of the exact source of this magnetism and to the estimation of the formation energy and mechanism of the various defects. Experimentally, mainly electron and ion

(proton) irradiation, epitaxial growth and chemical treatment have been employed to create defects, with crucial support from surface techniques like scanning tunneling microscopy (STM) and transmission electron microscopy (TEM) to detect and also to generate them.

3.1. Defects of graphene: formation and morphology

Removal of one or more carbon atoms from a graphene sheet creates a vacancy that can be a single vacancy, divacancy or, in general, multivacancy depending on the number of atoms involved (see Fig. 5). The simple expulsion of a carbon atom generates a defect with D_{3h} symmetry in which three dangling σ bonds form around the missing atom. However, a reconstruction can take place, driven by an energy-lowering Jahn–Teller distortion in which two of the carbon atoms with dangling bonds create a "soft" σ C–C bond, resulting in a defect, called V_1(5-9), with one dangling bond left and C_{2v} symmetry.[114–117] The new bond formed has a calculated length of ∼2 Å. A further distortion can take place in which the C atom with the dangling bond is displaced out-of-plane (see Fig. 6).[115,118,119] The formation energy of the graphene monovacancy has been consistently calculated at values of 7.4–7.8 eV.[114,115,118,120,121] This relatively high value accounts for the presence of a carbon atom with an unsaturated bond. Moreover, the reconstructed defect imparts strain to the graphene lattice surrounding the defect.[122] The electronic environment of the V_1(5-9) vacancy also reflects the newly formed bond and the dangling one. In particular, a localized spin density is present at the unsaturated C center (see Fig. 7).[116]

Monovacancies have been experimentally detected. Aberration corrected high resolution transmission electron microscopy (AC-HRTEM) and high angle annular dark field scanning transmission electron microscopy (HAADF-STEM) techniques in particular have been used for creation of defects by irradiation at energies above 80 keV and for their visualization (see Fig. 8).[122–127] Interestingly, both symmetric and reconstructed defects, corresponding to Fig. 8a and d, have been detected.

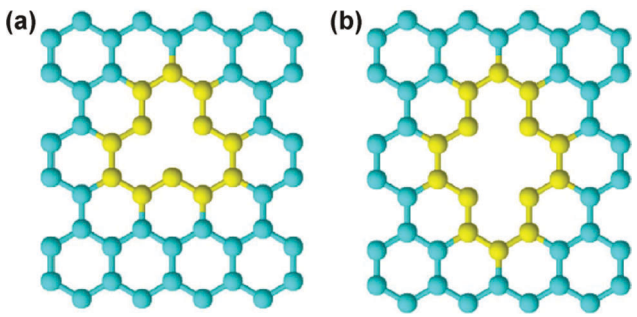

Fig. 5 Examples of (a) single vacancy and (b) double vacancy before reconstruction. Reprinted with permission from ref. 117. Copyright 2017 Elsevier B.V.

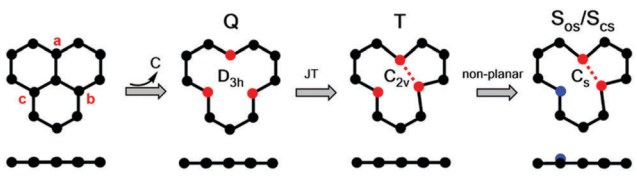

Fig. 6 Top and side views of a graphene single vacancy, with the respective point groups, type of distortion (JT: Jahn–Teller) and spin multiplicity (Q: quintet, T: triplet, S: singlet, OS: open shell, CS: closed shell). Reprinted with permission from ref. 119. Copyright 2017 American Chemical Society.

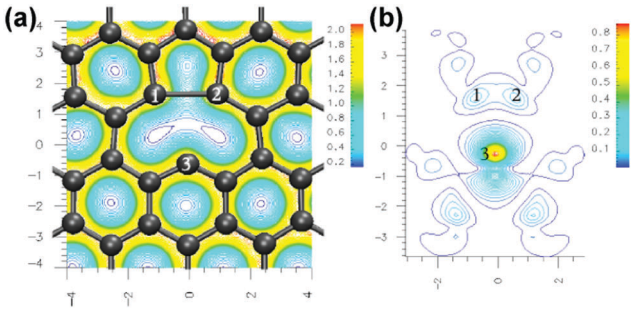

Fig. 7 C monovacancy: structure with (a) charge density (in e Å^{-3}) and (b) spin density (in e Å^{-3}). Reprinted with permission from ref. 116. Copyright 2004 American Physical Society.

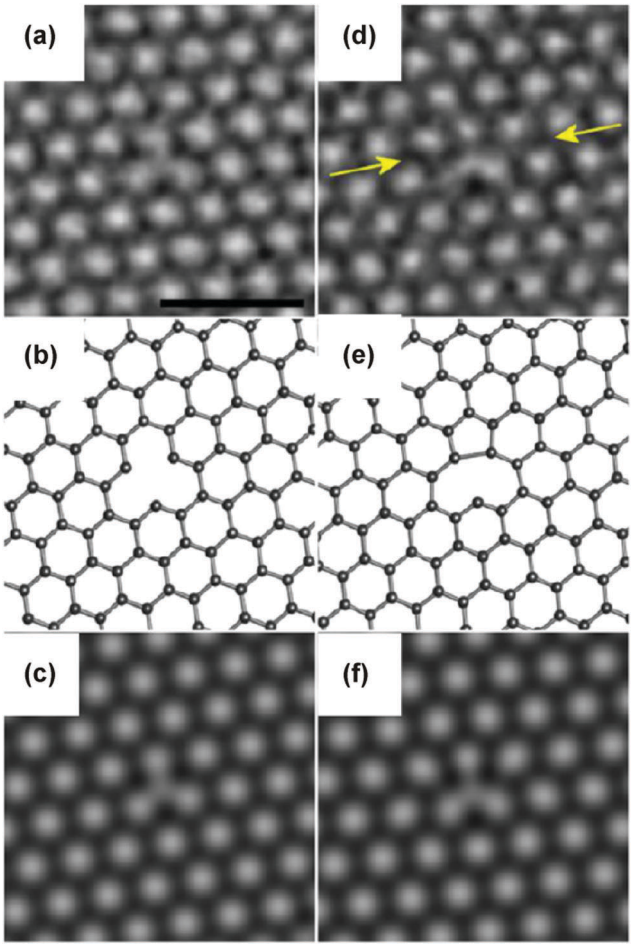

Fig. 8 AC-HRTEM images of (a) a symmetric C monovacancy and (d) after reconstruction. Panels (b and e) are the DFT calculated models and panels (c and f) the multislice TEM simulations of images in panels (a and d), respectively. Reprinted with permission from ref. 122. Copyright 2013 American Chemical Society.

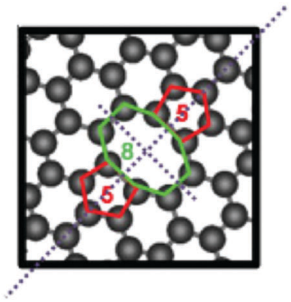

Fig. 9 Depiction of a V_2(5-8-5) divacancy defect. Reprinted with permission from ref. 132. Copyright 2012 American Physical Society.

Single vacancies can diffuse in the graphene lattice. The calculated barrier for this diffusion depends on the model used to simulate the migration, and is between 0.9 and 1.7 eV.[114,128] Experimentally, the diffusion of single vacancies does not take place at room temperature within the timescale of the measurements.[123] The migration and coalescence of vacancies can however be influenced by the presence of multiple vacancies, which induce bond strain extending into the lattice portion where the vacancies are present.[129]

When two connected carbon atoms are simultaneously displaced, or when two single vacancy defects coalesce, a divacancy forms. Also in this case, a reconstruction can take place. By formation of the long σ bonds analogous to that of the single vacancy, a corresponding V_2(5-8-5) structure appears (see Fig. 9).[130–132] However, this structure can convert into one with a lower energy, V_2(555-777). Other possible reconstructions are V_2(5555-6-7777), which lies at an intermediate energy between the other two, V_2(585) with dangling bonds and V_2(555-777) with a tilted carbon dimer. All these structures have been characterized by electron microscopy and confirmed by simulations (see Fig. 10).[133,134] The formation energy of divacancies is of the same order of magnitude as that of single vacancies (~8 eV), accounting for ~4 eV per atom.[114,121,135] The much lower energy per atom needed with respect to monovacancies is due to the absence of dangling bonds left after the structure reconstruction. On the other hand, the migration barrier is much higher than that of single vacancies, being estimated to be ~7 eV,[114] thus allowing the accessible visualization of the defect by electron microscopy.

Studies of the influence of strain on graphene with vacancies have provided an insight into the mechanical and electronic properties of the material. For vacancy content up to 0.2%, the elastic modulus of graphene sheets increases by nearly 100%, and then decreases with higher defect density, while the fracture strength instead decreases in the presence of defects (see Fig. 11 for a STM image of defected graphite used for investigation of the influence of strain).[136,137] Also, the energy required for vacancy formation in graphene can be reduced by ~37% by the application of biaxial tensile strain.[138] A tensile strain lower than ~50% is needed to open a band gap in defected graphene when compared to pristine graphene.[139]

The reactivity of graphene single vacancies is determined by the presence of the dangling bond, which can be saturated by

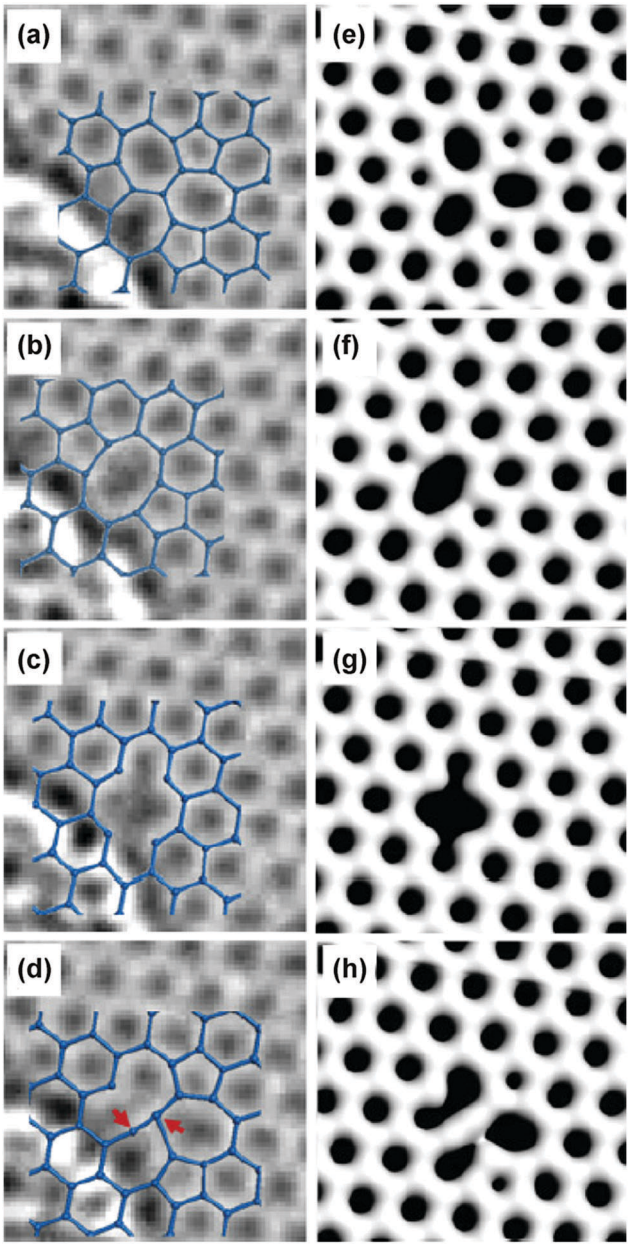

Fig. 10 (a–d) Structures of different double vacancy defect reconstructions ((a): V_2(555-777); (b): V_2(585); (c): V_2(585) with dangling bonds; (d): V_2(555-777) with a tilted carbon dimer, shown by the red arrows). (e–h) Corresponding charge density plots obtained from *ab initio* calculations. Reprinted with permission from ref. 134. Copyright 2011 American Physical Society.

adatoms, thus further changing the properties and structure of the defect.[140,141] In this section, only the influence of H as a chemisorbed adatom, isolated or connected to a vacancy, will be discussed, for cases in which single or limited H atoms are present on graphene structures thus constituting a defect rather than a functionalization. Chemisorption and physisorption of H atoms on graphene have both been studied, mainly from the theoretical point of view, but experimental works have also been published.[142–149] Various models have been proposed, including pyrene, coronene and a 4 × 4 supercell, and coronene has been

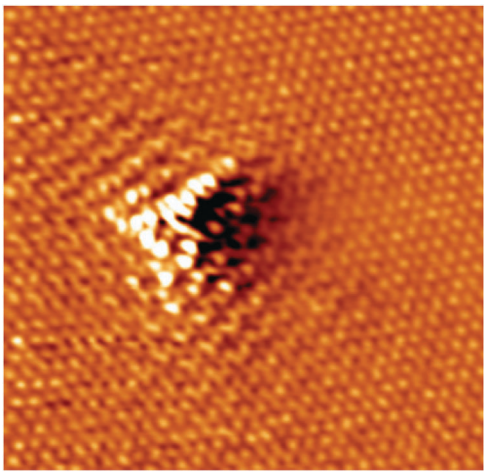

Fig. 11 STM image of a defect on graphite created by Ar^+ irradiation at 140 eV (image taken in air at room temperature). Reprinted with permission from ref. 136. Copyright 2014 Macmillan Publishers Limited.

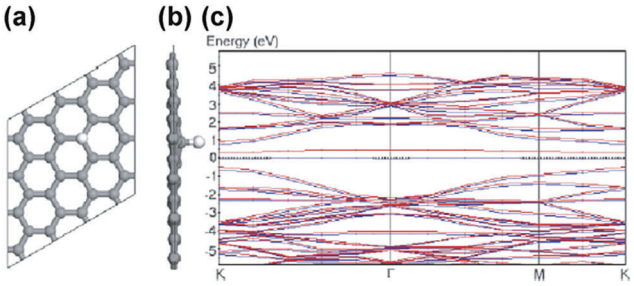

Fig. 13 (a) Top view, (b) side view, and (c) band structure for an H atom adsorbed on a graphene sheet (32-atom model). Reprinted with permission from ref. 142. Copyright 2004 American Physical Society.

suggested as the one with the minimum size suitable for calculations of H chemisorption on graphene (see Fig. 12).[146]

The C–H bond formed, in which the C atom hybridizes to sp^3 and its p_z orbital is removed from the general graphene π-system,[45] has been calculated as being of length 1.11–1.13 Å.[142,146] Studies performed at the PB3-D3/cc-pVZD level of theory indicate that the energy barrier for H chemisorption is mainly attributed to the structural work connected to the defect reconstruction. The presence of the bond creates a band gap of 1.25 eV, containing two non-dispersing states (see Fig. 13). This effect has been attributed to the influence of the H^+ ionic core.[142]

When a pair of hydrogen atoms is chemisorbed on graphene, four different outcomes are possible, depending on whether the two H atoms are on the same or opposite side of the graphene sheet and whether they are on C atoms which are part of the same or different sublattices. Calculations have suggested that the formation energy of the pairs in all four cases is dependent on the distance between the C atoms carrying the H atoms, resulting in lower energies for distances up to 5 Å and then increasing at larger distances.[144] The presence of chemisorbed H atoms can affect the mechanical properties of graphene, leading to deterioration of the material. Atomistic simulations have shown that the fracture strain and fracture stress of hydrogenated graphene decrease substantially in both armchair and zigzag directions when compared to pristine graphene.[148]

TSW defects in graphene are generated by the 90° rotation of a C–C bond. Upon this rotation, two C–C bonds are formally broken and two new bonds are formed, with the result that four hexagons turn into two pentagons and two heptagons, a so called SW(55-77) structure (see Fig. 14).[150] The opposite curvature of pentagons and heptagons results in the formal conservation of

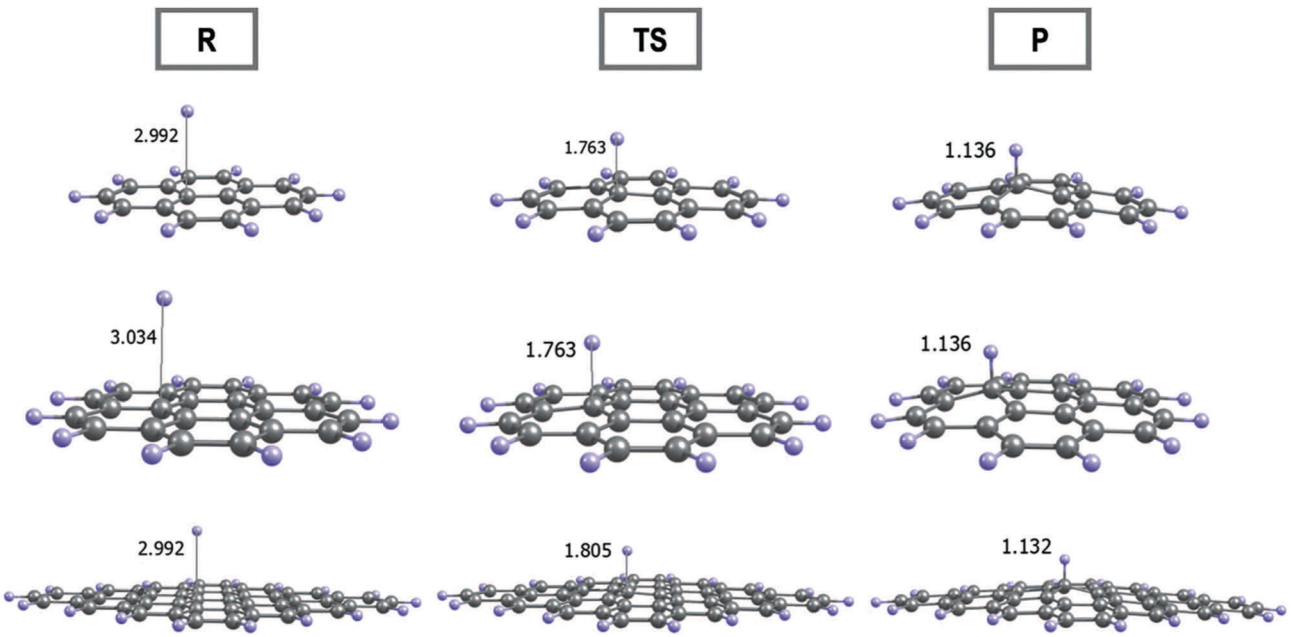

Fig. 12 C–H distances (in Å) in the physisorbed state (R), transition state (TS) and chemisorbed state (P) for the three different models, *i.e.*, pyrene (top), coronene (center) and 4 × 4 supercell (bottom). Reprinted with permission from ref. 146. Copyright 2014 AIP Publishing LLC.

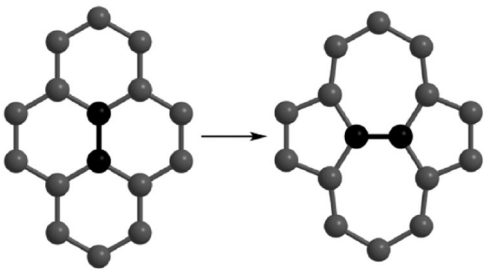

Fig. 14 TSW transformation by C–C bond rotation (in black) with the formation of a SW(55-77) defect. Reprinted with permission from ref. 150. Copyright 2015 Pleiades Publishing, Ltd.

the planar structure; it is worth reminding that the presence instead of 12 pentagons along with hexagons but without heptagons generates a spherical allotrope as in the case of fullerene.[151,152] Calculations have pointed out that the most stable geometry of a graphene single layer with a SW(55-77) defect has an out-of-plane sinusoidal shape, with the sine-like structure having the lowest energy (see Fig. 15).[153–155] As already mentioned, the TSW defect leaves the total number of atoms unchanged and also the hybridization of the components of the system is not mutated, each carbon atom being bonded to three neighboring atoms. However, the bond lengths in the SW(55-77) system diverge substantially from the periodic C–C bond of 1.46 Å of pristine graphene. Calculated values obtained from DFT methods indicate bond lengths down to 1.28 Å for the common heptagon–heptagon bond[140] within the defect area.[110]

The calculated formation energy associated with flat TSW defects reported in several works is of ~5 eV, with small variations depending on the type of codes used for the calculations,[140,153,155,156] whereas structures presenting sine-like distortions have in average slightly lower calculated formation energies.[135,150,156] The kinetic barrier to overcome for the simultaneous 90° rotation of the two C atoms producing the TSW defect is of 10 eV, whereas the opposite rearrangement with recreation of the hexagonal structure is 5 eV, making the TSW defect, once formed, rather stable.[140] AC-HRTEM at <100 keV with different electron fluxes has been employed to successfully visualize TSW defects and their rapid healing.[157,158]

TSW defects are reported to affect the mechanical,[159–161] chemical[142] and electronic[107,162–165] properties of graphene. TSW defects from defect reconstruction are deemed responsible for enhanced chemical reactivity due to the locally changed π-electron density,[167] whereas the bond rotation responsible for the TSW defect has the effect of creating a band with energy ~0.5 eV higher than E_F, due to the displaced p_z orbitals of the atoms of the defect site.[162]

The reconstruction of multiple defects in a graphene lattice can lead to the formation of line defects,[166–170] which can be seen as the 1D analogue of the 2D grain boundary defects in graphite.[171,172] However, it must be noted that "grain boundary" is often used as a synonym of "line defect" in graphene (see Fig. 16). Line defects can consist of the periodic repetition of pentagonal–heptagonal or pentagonal–optagonal motifs as well as disordered distributions of different polygons. The planar nature of the graphene sheet allows for rearrangements not present in their 3D counterparts, resulting in the formation of peaks in "3D landscapes" upon structural relaxation and consequent reduction of the defect energy. The height of the peaks has been calculated as being close to the distance between the defects (see Fig. 17).[173,174] Moreover, the relative stability of defects created by pairs of 5-7 defects against extended Haeckelite-like structures has also been assessed,[166] whereas simulations performed using GGA for DFT with spin polarization have shown the formation of pentagonal–octagonal-based line defects on graphene sheets upon inclusion of C and N adatoms.[175]

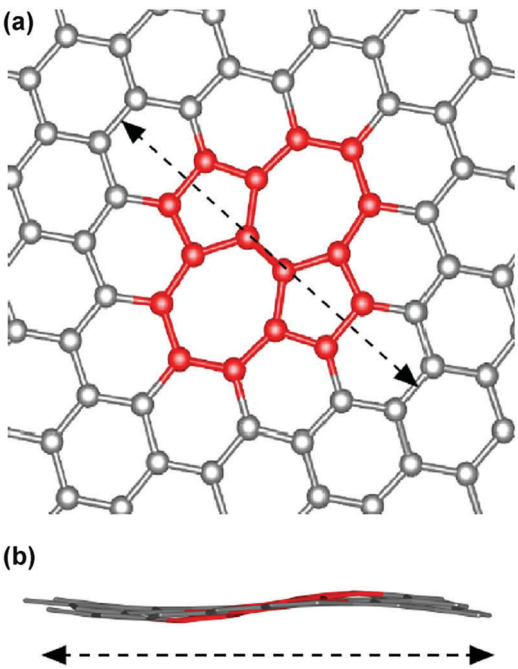

Fig. 15 (a) Top and (b) side views of a SW(55-77) defect, in which the sinusoidal distortion is shown. Reprinted with permission from ref. 154. Copyright 2014 American Physical Society.

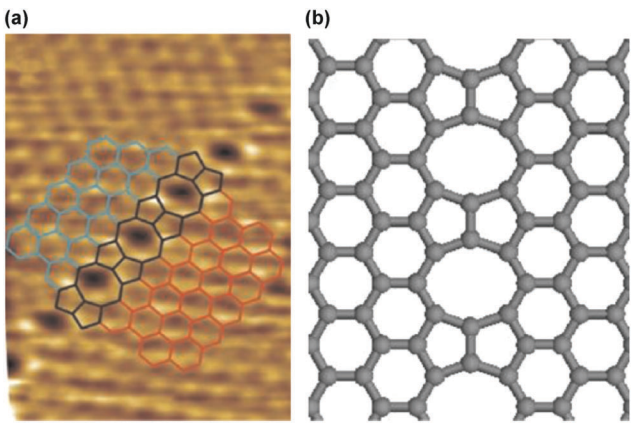

Fig. 16 (a) STM image of a line defect in graphene and (b) schematic representation of the defect. Reprinted with permission from ref. 170. Copyright 2014 Elsevier B.V.

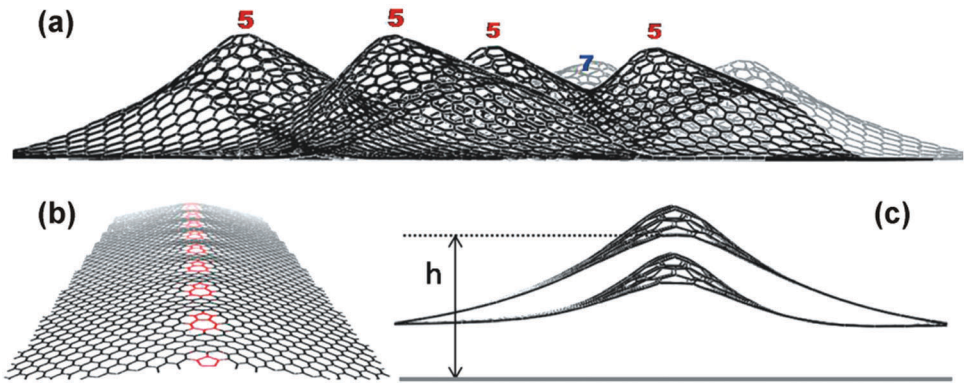

Fig. 17 (a) Calculated peak formation in the presence of scattered pentagonal (5) and heptagonal (7) defects (full relaxation mode). (b) Ridge-like deformation from regular pentagonal–heptagonal defect distribution. (c) Computed flattening effect generated by the van der Waals attraction to the substrate. Reprinted with permission from ref. 173. Copyright 2010 American Chemical Society.

STM has been successfully employed to characterize line defects and the design of graphene sheets with specific line defects has been reported.[167,176–178] In particular, deposition of graphene on a Ni(111) surface results in the formation of various line defects corresponding to the different orientations of graphene on the metallic surface, and the material produced in this way can be transferred to other substrates upon dissolution of the Ni layer.[167] Migration of grain boundary defects in graphene has also been observed atom-by-atom using AC-HRTEM.[179] The migration takes place when a significant curvature of the boundary is present.

The presence of line defects and grain boundaries influences the mechanical properties of the material. Graphene sheets can be strengthened or weakened by the presence of line defects, depending on their density and arrangement (see Fig. 18). According to molecular dynamics (MD) and DFT calculations, for both zigzag- and armchair-oriented graphene layers the strength of the sheet increases with the angle of the grain boundary, because the strain induced in the structure containing the line defect decreases with the increase of such an angle. However, if the distribution of the defects is not regular, the opposite behavior can be observed, in which the grain boundary induces weakening of the structure.[180,181]

Grain boundaries on graphene also affects the electronic properties of the material. Computational studies combined with STM and scanning tunneling spectroscopy (STS) on graphite have pointed out the main superlattice periodicities of the line defects and have identified grain-boundary structures of low formation energy.[165,182] Moreover, STS measurements of structures with specific superlattice periodicity have shown the presence of two localized states at positions of −0.3 and +0.4 V, respectively. These strong states, which were not detected on pristine graphite, extend to a distance up to 4 nm.[182]

3.2. Magnetism of defected graphene

Defect-induced magnetism in graphene is well documented, with the experimental roots around the turn of the millennium

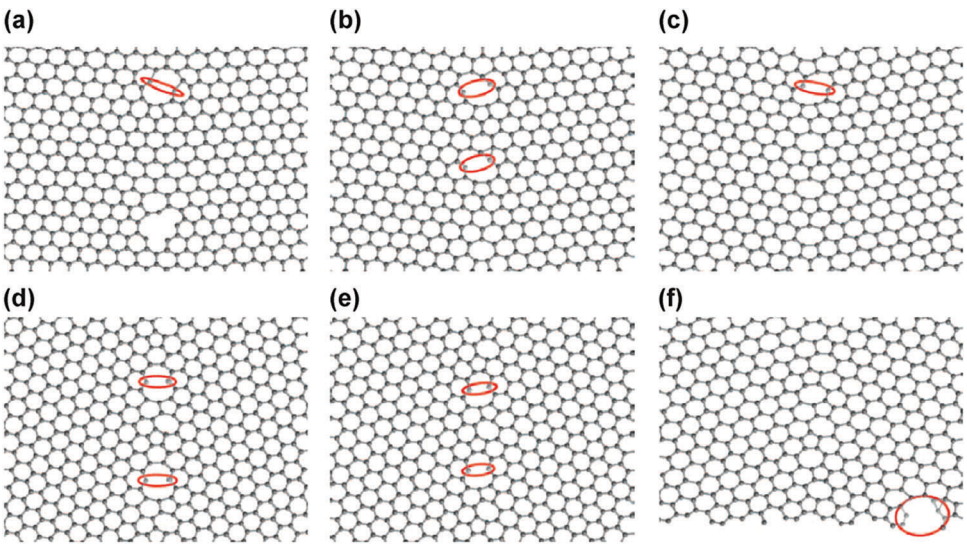

Fig. 18 Starting phase of structural failure in (a–c) zigzag-oriented and (d–f) armchair-oriented graphene upon strain applied perpendicularly to the grain boundary defect. Reprinted with permission from ref. 181. Copyright 2010 American Association for the Advancement of Science.

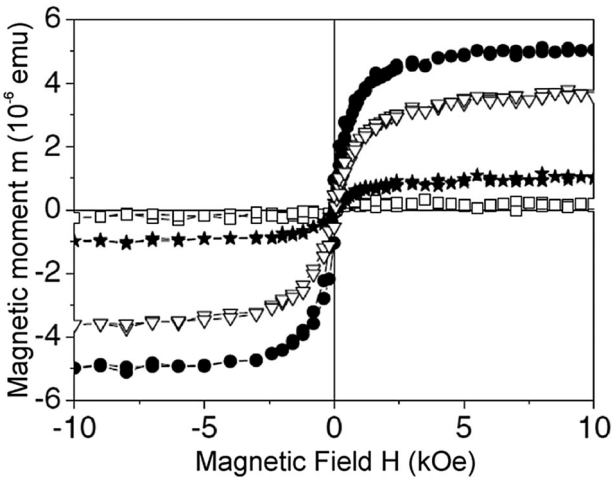

Fig. 19 Magnetic moment of graphite samples (sample holder subtracted) after different irradiation conditions (□ = first irradiation stage, ★ = second irradiation stage, ● = third irradiation stage, and ▽ = fourth irradiation stage). Reprinted with permission from ref. 103. Copyright 2003 American Physical Society.

when the studies on irradiated graphite by Esquinazi *et al.*[101–103] appeared alongside analogous works focused on other carbon allotropes.[25,183,184] The proton irradiation of pyrolytic graphite at high energy and different doses in these early studies showed triggering of magnetic ordering (*i.e.*, of FM and AFM nature). Moreover, this magnetic ordering appeared to be stable at room temperature.[103] Measurements of the magnetic moment with the applied field parallel to the graphene sheets produced different magnetic responses depending on the intensity and dose of the irradiation (see Fig. 19). A similar result was obtained with the magnetic field oriented perpendicularly to the graphene plane. Soft X-ray dichroism technique on irradiated graphitic material suggested that the observed ferromagnetism originated only from the π-electrons.[185] A substantial part of these early works was dedicated to the assessment of the influence on magnetism by possible metallic (Fe-based in particular) impurities. While this factor dictated in some case the retraction of the study,[186,187] it became soon clear that the observed magnetic ordering was in most instances an intrinsic property of the material and not due to external impurities, and consequently several works focusing on the explanation of this behavior were published.

Vacancies and H chemisorption have been in particular investigated as the source of magnetism in defected graphene. As pointed out in several theoretical studies, magnetic moments in the presence of vacancies are due to the formation of localized states at E_F because of the lattice distortions generated by the defect and consequent electron–electron interactions.[45,47,89,116,125,188,189] In the case of single vacancies, the single dangling bond formed upon reconstruction of the defect contributes to the creation of an intrinsic magnetic moment (see Fig. 20).[45,47] The quantification of this magnetic moment covers values between 1 and 2 μ_B depending on the type of calculations performed and the evaluation of the effect of surrounding defects.[47,119,138,190–194] In particular, different results between the calculations based

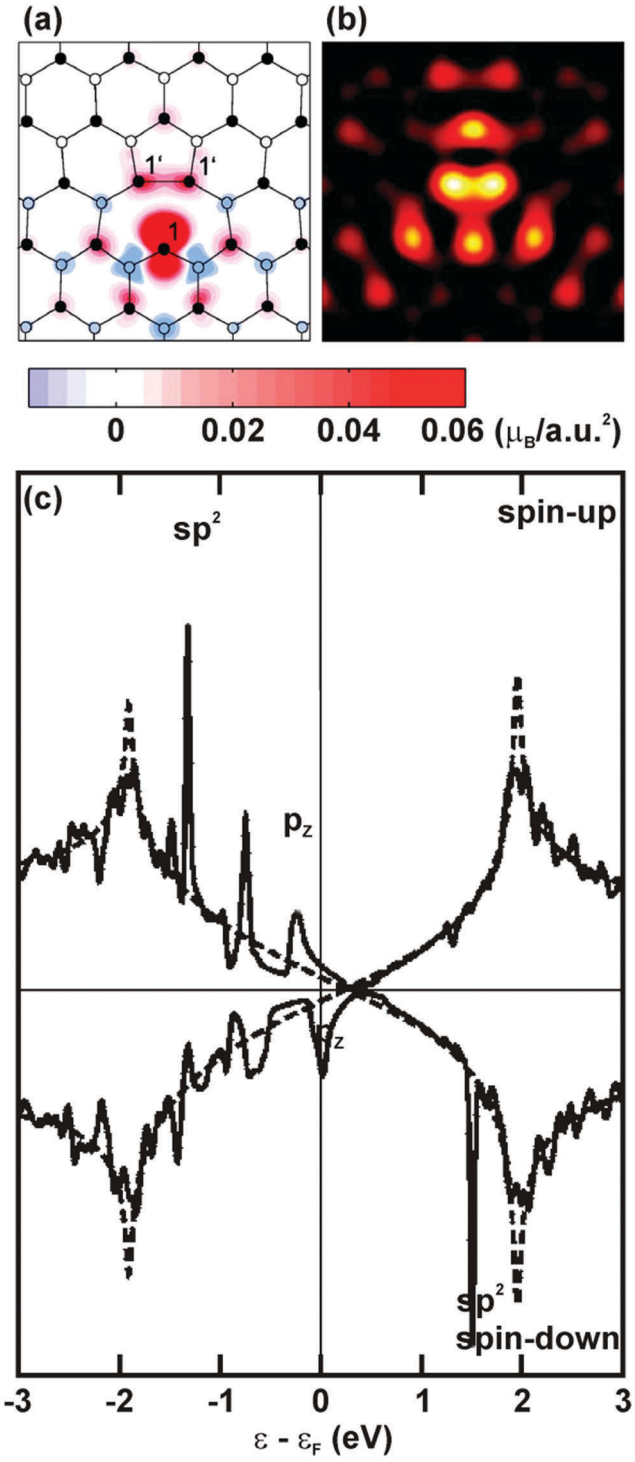

Fig. 20 Graphene single vacancy: (a) theoretical spin-density distribution (C atoms of the two different sublattices are represented by empty and filled circles, respectively); (b) corresponding simulated STM image; (c) density of states for n = 4. Reprinted with permission from ref. 47. Copyright 2007 American Physical Society.

on periodic LDA or GGA functionals and those in which hybrid functional methods like B3LYP-D* were used have been reported.[119] The average magnetic moment of 1.5 μ_B for a single vacancy is the result of the sum of the σ component related to

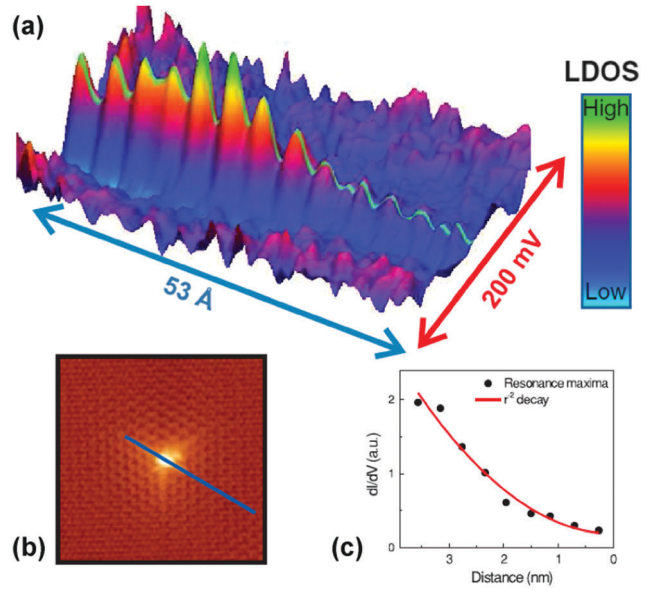

Fig. 21 (a) LDOS as a function of voltage and position (blue line in image (b)) of a graphite vacancy, (b) STM image of the defect, and (c) r^{-2} decay of the intensity of the resonance. Reprinted with permission from ref. 125. Copyright 2010 American Physical Society.

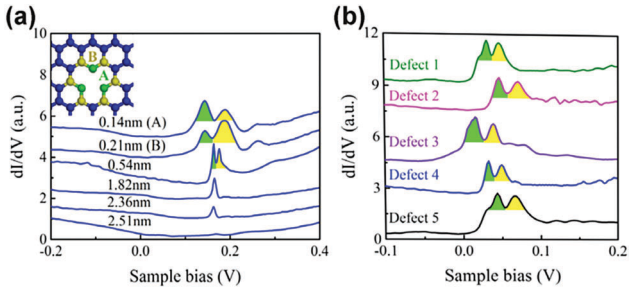

Fig. 22 STS spectra of graphene with monovacancy: (a) appearance of a spin-split resonance peak at decreasing distances from the vacancy. The two top spectra are measured in correspondence to the A and B atoms shown in the inset, respectively; (b) spin-split resonance peaks of five different vacancies. Reprinted with permission from ref. 196. Copyright 2016 American Physical Society.

the newly formed C–C bond upon reconstruction, of value 1 μ_B, and the π component ascribed to the dangling unsaturated bond. The formula $(1 + x)$ μ_B for the total magnetic moment of the defect has been proposed, where the x value is subjected to the variations ascribed to the chosen model. The evaluation of the competition between the symmetric planar configuration of the single vacancy and the nonplanar reconstruction is also responsible for the spread values reported, with metastable states corresponding to local energy minima also taken into consideration.[194,195]

STM measurements supported by calculations have proved to be a powerful instrument for the detection of magnetism in graphene with vacancies. Through this technique, it has been shown in correspondence to the Fermi energy at the vacancy sites a sharp electronic resonance, thus confirming the theoretical studies (see Fig. 21). Moreover, differential conductance measurements have indicated that the magnetic moment generated by defects in a surface graphitic layer is influenced by the presence of the layers underneath.[125]

Studies on graphene with monovacancies synthesized on metal foils, for instance on Rh or Pt, have supplied important information about the magnetism of the defected 2D material. In particular, the contribution of the π electrons to the local magnetic moment generated by a single carbon vacancy in graphene, connected to the presence of two spin-split density-of-states peaks located in the proximity of the Dirac point, has been assessed by STM and STS.[196] Spectra collected at decreasing distance from a monovacancy on graphene on Rh foil reveal the appearance of a resonance peak, that splits into two states for distances from the vacancy <0.6 nm, in agreement with theoretical studies (see Fig. 22).[47] Remarkably, the detected spin-split states are still present even at energies distant from E_F. According to first-principles calculations, n- and p-doped graphene should also present the spin-split states.

In order to find ways to tune the magnetism of defected graphene, the application of various types of strain to graphene with monovacancies has been investigated. In the case of shear distortion, a DFT study has shown that reversible electronic transition between two magnetic states is achieved when a deformation of a shear angle of 1 degree is applied. The magnetic moment undergoes a variation of 0.8–1.2 μ_B depending on the size of the calculated supercell and remains nearly constant at deformations >1 degree. This behavior is attributed to the breakage of the local symmetry of the monovacancy induced by the shear distortion, influencing both the σ and π bands of the states of the vacancy (see Fig. 23).[197] On the other hand, strain applied in the form of compression up to 2% to graphene with a single vacancy can result in the weakening and eventually disappearance of magnetism together with the formation of ripples, thus showing a correspondence between local curvature and magnetism. With the application of compressive strain of 3% and above, the rippling leads to a reconstruction of the defect, with formation of two pairs of deformed pentagons and hexagons and no magnetic behavior (see Fig. 24).[198]

The number and location of the vacancies also play a major role in the establishment of a magnetic moment. Due to the bipartite structure of the graphene lattice, the presence of vacancies solely on one sublattice leads to FM coupling, whereas a defect distribution on both sublattices results in AFM coupling (see Fig. 25).[47] Models have therefore been proposed in order to predict and tune the magnetic moment in systems with multi-vacancies through manipulation of the position of the defects and n- and p-doping.[199–201]

For experimental evidence such as the magnetism of irradiated graphite, the simple vacancies alone are not the main source for this property due to their likely annihilation taking place *via* the interaction with adatoms and interstitials.[47,116] A source of defect-related magnetism is the presence of H atoms chemisorbed on the graphene lattice. As mentioned before, the bonding with H by a graphene C atom without vacancy removes the p_z orbital of that atom from the π-system of the graphene lattice, thus creating the same effect of a C vacancy but without

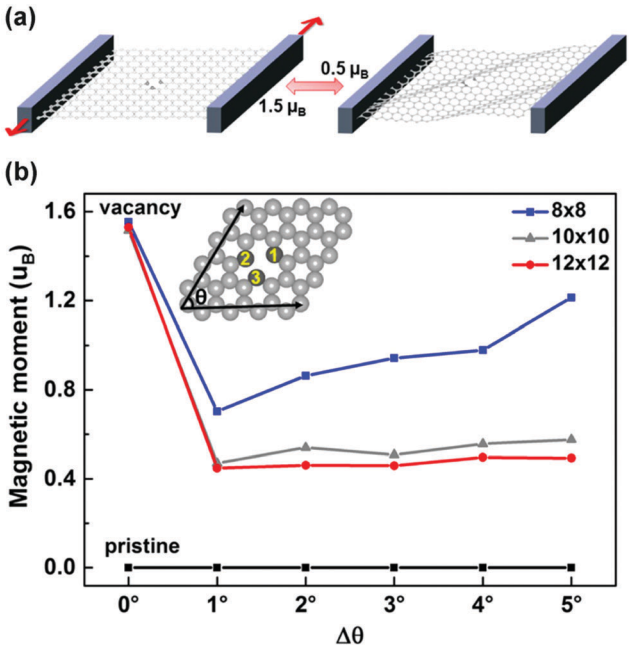

Fig. 23 (a) Representation of the reversible change of magnetism of a graphene sheet with single vacancy upon shear deformation. (b) Variation in magnetic moment of graphene supercells of different sizes under shear deformation of 0–5° compared to pristine graphene (initial angle = 60°, see inset). Reprinted with permission from ref. 197. Copyright 2017 Macmillan Publishers Limited.

the presence of unsaturated bonds. The H chemisorption brings the C atom bonded to H slightly out of plane and generates a small displacement of the surrounding portion of lattice.[47,143] STM experiments (see Fig. 26) have shown that the adsorption of a single H atom contributes to the formation of a magnetic moment, and that interaction due to direct exchange is possible. In agreement with the theory and with works dealing with monovacancies,[47,196] two spin-split states have been detected, but in the case of H chemisorption they are visible only in the vicinity of E_F and they do not survive n- or p-doping.[143]

Theoretical and experimental studies have pointed out that if two H atoms adsorb in the same sublattice then FM coupling takes place, whereas the absorption in two different sublattices leads to a non-magnetic interaction, with the non-magnetic configuration being the one of lower energy.[144] By manipulating

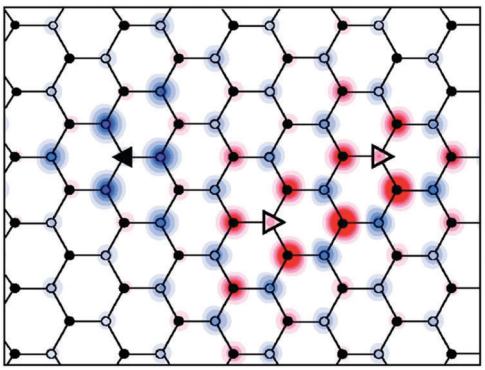

Fig. 25 Theoretical spin-density distribution in graphene with two defects on the A-sublattice (empty triangles) and one on the B-sublattice (filled triangle). Reprinted with permission from ref. 47. Copyright 2007 American Physical Society.

the number of H atoms chemisorbed in the two different sublattices, the corresponding variations in the net magnetic moment have been detected.[143] In the case of graphite, H adsorbed *via* irradiation at low fluence has been evaluated together with the H already present in the sample. It has been reported that the magnetic moments formed undergo FM coupling with Curie temperatures above 300 K.[202] The triggering of ferromagnetism in multilayer materials has been attributed to the stacking order of the layers upon irradiation. This can generate a mechanism by which the graphene sublattices become inequivalent depending on the position of chemisorbed H in the underlying layer.[45,89]

Chemisorbed hydrogen can be present as a single type of defect or associated with vacancies, in which case it is bonded to the carbon atom that carries the dangling bond upon reconstruction. The influence of adsorbed hydrogens in association with vacancy defects can impart half-metallic properties to graphene. This half-metallicity depends on the number of C atoms intercalated between two H atoms, appearing only when this number is odd. The magnetism in these systems is mainly regulated by the p_z orbitals of the C atoms surrounding the vacancy.[203]

Among other experimental techniques, muon spectroscopy has also been employed to study the origin of magnetism in graphene.[204] Muon spectroscopy is a very powerful spectroscopic technique as muons are very sensitive probes of local magnetic

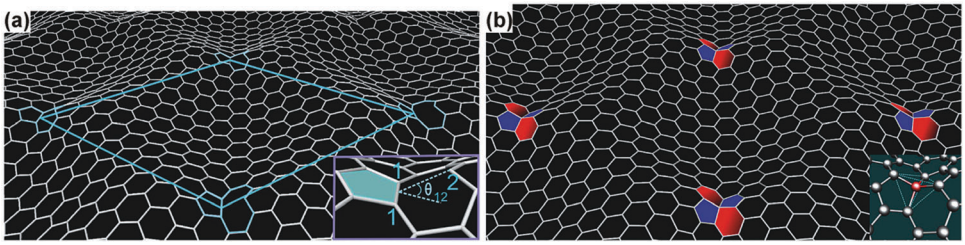

Fig. 24 (a) Rippling of a graphene sheet with vacancies (with highlighted 10 × 10 supercell) upon compression of 1.2%. The inset shows the resulting geometry of the vacancies. (b) Vacancy reconstruction upon an isotropic compression just below 3%. Reprinted with permission from ref. 198. Copyright 2012 American Chemical Society.

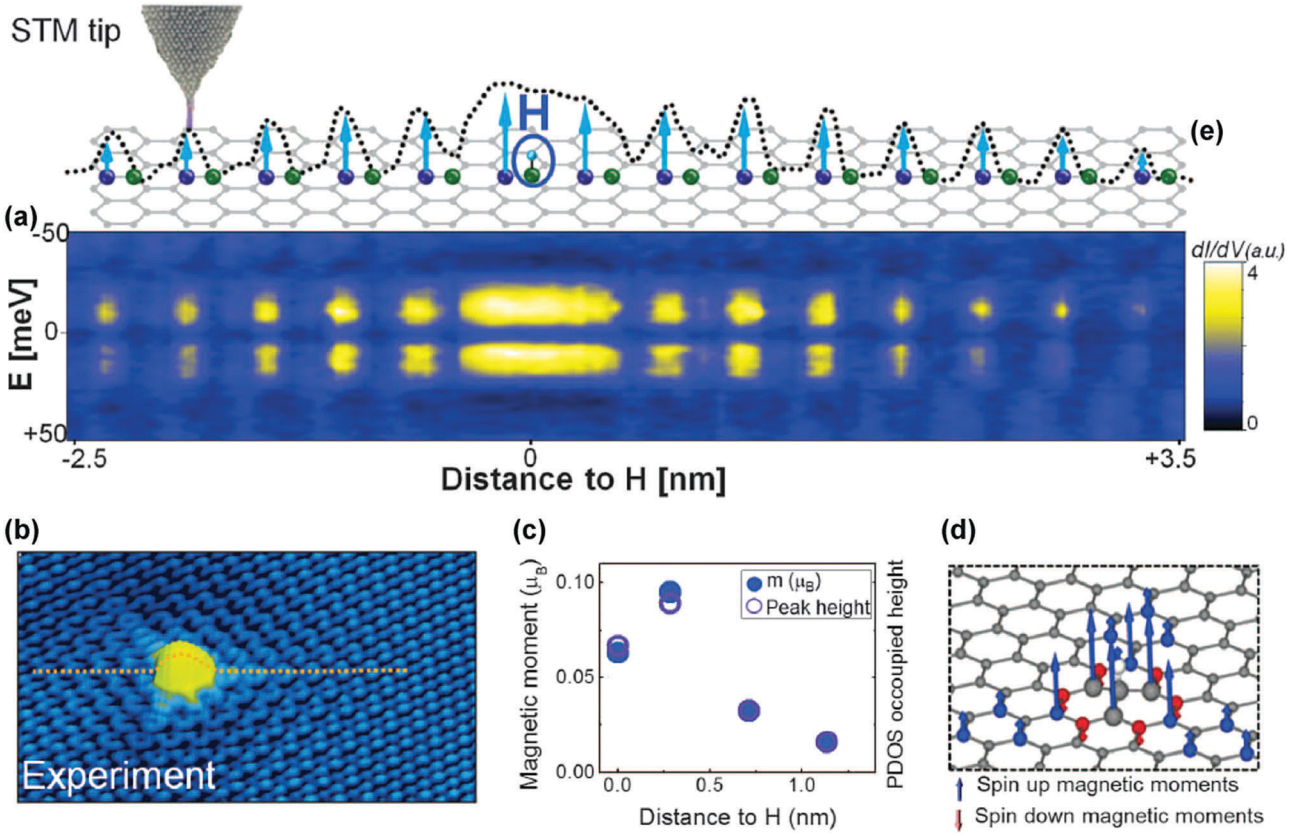

Fig. 26 Chemisorbed H on graphene: (a) conductance map obtained by the STM technique; (b) STM topography; (c) comparison between the values of the local magnetic moment computed by DFT calculations and the heights of the occupied projected density-of-states peak; (d) magnetic moments (calculated) generated by the chemisorbed hydrogen; (e) schematic representation of the structure of graphene along the dashed line shown in panel (b). The green (purple) balls denote the positions of carbon atoms that are part of the same (opposite) sublattice with regard to the site of H chemisorption. The dotted line then shows the profile of the height corresponding to the measured occupied peak; the arrows denote the relative contribution to the magnetic moment of each carbon atoms. The STM measurements were performed at a temperature of 5 K. Reprinted with permission from ref. 143. Copyright 2016 American Association for the Advancement of Science.

fields and can interact with hydrogen. In particular, the muons which are, after being thermalized, implanted into graphene can capture an electron to form the atom "muonium" (Mu). In defective graphene, the muon precession was found to originate from the nuclear dipolar interaction with a single proton, located at a distance of 1.7 Å from the muon. As the amplitude correlates with the density of defects in graphene, increasing drastically after hydrogenation of graphene samples, formation of a CH-Mu group is suggested to occur, which is stable up to 1200 K. However, these results exclude the presence of magnetic ordering evolving in the chemically derived defective graphene systems. Nevertheless, as strongly highlighted in a muon spectroscopic study, these conclusions do not automatically rule out the appearance of magnetism in other experimentally proven cases such as proton-irradiated graphite, synthesized small graphene fragments or graphene nanoribbons.[204]

From the point of view of the magnetic properties, the TSW defects do not create sublattice imbalance in the graphene structure since they do not involve loss of atoms, thus according to Lieb's theorem,[100] $S = 1/2(N_A - N_B) = 0$, and no magnetization is expected.[89] However, the TSW defects can perturb the magnetic state of the lattice *via* interaction with other defects such as adsorbed hydrogen atoms,[205] and they can be a source of magnetism in size-confined systems.[206]

The presence of grain boundaries has been proposed as a reason for the magnetism of defective highly oriented pyrolytic graphite (HOPG).[46] At the 2D array of point defects due to the grain boundary, localized electron states take place together with self-doping, with establishment of ferromagnetism. The magnetic moment associated with the defect has been evaluated to be 0.2–1.5 μ_B, for distances between defects ranging from 0.5 to 4 nm. Similar considerations have been drawn for single graphene sheets. In the presence of line defects generated by repeating V_2(5-8-5) defects, the presence of magnetic ordering and self-doping has been detected using first-principles calculations.[207] The evolution of the electronic structure as a function of the distance between the defects was studied, and the establishment of magnetic ordering and n-doping on the graphene sheets with reduction of the distance was found. The formation energies and spin distribution of systems with different number of zig-zag chains (N) between the two central carbon atoms of the pentagonal–octagonal periodic defects (C_2) have been evaluated, with detection of three stable magnetic configurations (see Fig. 27).

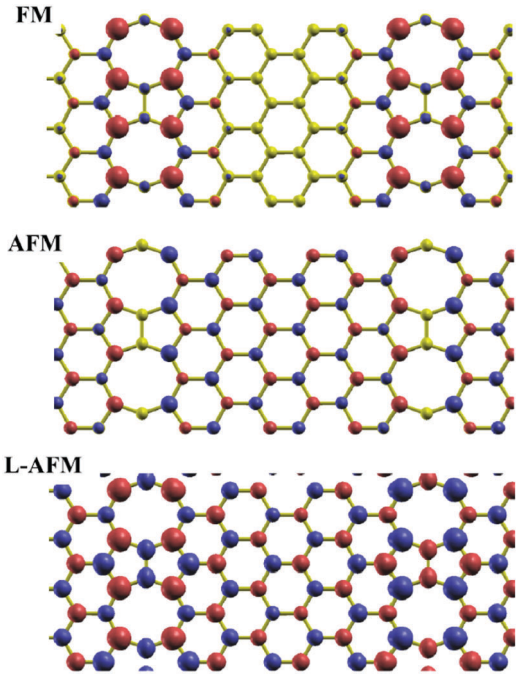

Fig. 27 Spin-density distribution for N = 6 showing FM, AFM and FM ordering at the line defect but AFM ordering in the surrounding line defect (L-AFM) arrangements (red color: isosurfaces of spin-up density; blue color: isosurfaces of spin-down density). Reprinted with permission from ref. 207. Copyright 2015 American Physical Society.

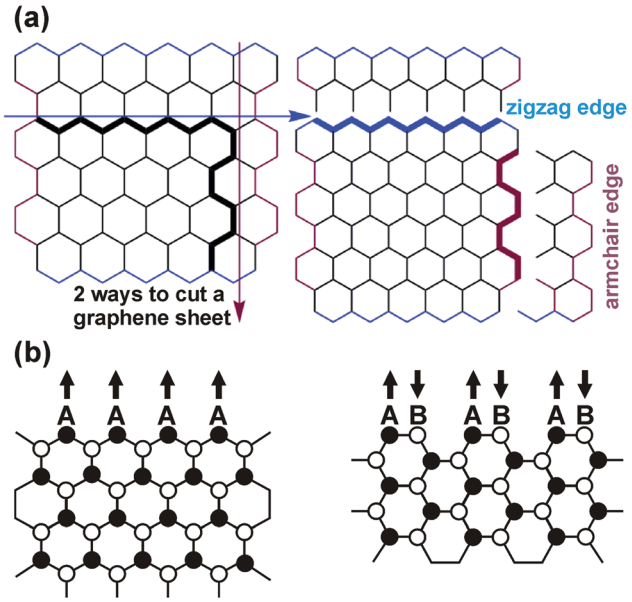

Fig. 28 (a) Two ways of cutting a graphene sheet with a formation of zigzag or armchair edged graphene. (b) Zigzag and armchair edges with the A- and B-sublattice indicated and an arrow denoting the pseudospins. Panel (b) reprinted with permission from ref. 212. Copyright 2013 Wiley-VCH Verlag GmbH & Co. KGaA.

Ab initio calculations based on CVD-grown graphene have shown how small C-rings, made of three or four units, can initially form at the boundary region of two graphene fragments.[208] The fusion of these small rings with larger ones leads to the formation of periodic defects in which high localization of electrons takes place, with establishment of net magnetization. The bipartite structure of the graphene lattice collapses at the line defect, thus the magnetization observed at the boundary cannot be attributed to lattice inequality as seen, in agreement with Lieb's theorem, in the case of other types of defects. Moreover, selected application of strain along extended line defects can tune the magnetism induced by the defects. In particular, calculations have shown that tensile strain applied along the zigzag direction of the defect can enhance the magnetism and its stability, up to a certain critical value that however does not correspond to structural breakage. On the other hand, tensile strain applied along the armchair direction induces an immediate reduction of magnetism, up to breakage of the structure.[209]

4. The role of confinement and edges on emergence of magnetism in graphene

Confining graphite spatially is widely considered as a pioneering strategy to imprint magnetic features into all-carbon materials. It is an approach proposed before the first isolation of graphene; the confined species of carbon were termed nanographenes or nanographites (*i.e.*, stacked nanographene sheets) and their magnetic properties were covered in the review papers by Enoki and Takai,[210] Enoki *et al.*,[211] and Enoki.[212] Currently, three spatially confined carbon forms derived from graphene are recognized: (i) graphene nanoribbons, (ii) graphene nanoflakes, and (iii) graphene quantum dots.

The theoretical calculations predict that the magnetism of finite size graphite/graphene strongly depends on its shape. If a sheet of graphene is cut into two pieces, two types of edges can be formed, *i.e.*, a zigzag or an armchair edge (see Fig. 28), thereby modifying its electronic band structure. Graphene with zigzag and armchair edges mimics the structure of *trans*- and *cis*-polyacetylenes, respectively. The resulting edges can be terminated by hydrogen or any foreign atom to create edges without σ-dangling bonds, *i.e.*, saturating the edge structure and promoting its stabilization. As graphene can be represented by the two sublattices in its unit cell, the zigzag edge involves sites only from one sublattice while both sublattices are paired along the armchair edge. Following the theoretical predictions, zigzag edges are manifested as non-bonding π-electron edge states with an energy level appearing at the contact point of the π- and π*-bands; the presence of such states was documented by several experimental studies.[56,211,213–217] These states are absent in the case of the armchair edges. The edge states along the zigzag edges emerge due to the broken symmetry of the pseudospins. The unpaired electrons (with S = 1/2) in the non-bonding π-orbital of the zigzag edge are localized, thereby forming a strongly spin-polarized region. As a result, the finite-sized graphene becomes magnetic.

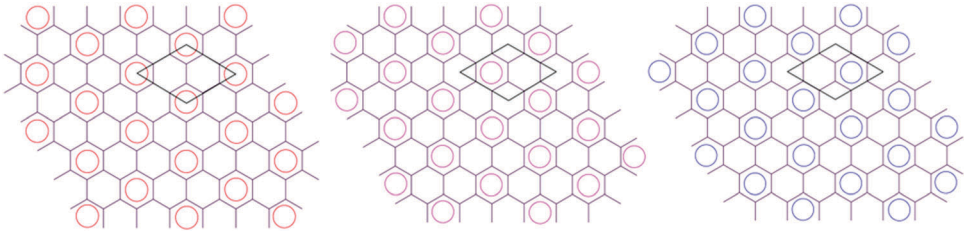

Fig. 29 Triply degenerate Clar's representations of graphene. The unit cell of the honeycomb lattice is manifested by a parallelogram that has two independent sublattice sites.

In this context, Clar's aromatic sextet rule[218] can be considered in order to describe the electronic stability of aromatic molecules. Its concept can be extended to graphene in the limit when the size of the graphene systems becomes infinite. The sextet rule states that a molecule that has the maximum number of sextets is more stable. Thus, every three hexagons in the honeycomb lattice of graphene would give rise to one sextet forming a triply degenerate superlattice as shown in Fig. 29. As the sextets are placed only on 1/3 of the hexagon rings, it implies that graphene is less stable, which leads to an electronic activity of the graphene sheet. The electronic properties of graphene sheets then get modified based on the type of edges they carry after being cut into pieces.[212] Graphene with the zigzag edges (represented as, *e.g.*, triangular and linear molecules with zigzag edges, see Fig. 30) is described by a fewer number of sextets while for graphene with armchair edges (represented as armchair molecules, see Fig. 30), the sextet rule gives a larger number of sextets. Hence, graphene with armchair edges is energetically favored in comparison to that having zigzag edges featuring unpaired electrons of π-origin. In the case of zigzag-edged graphene (see Fig. 30), the unpaired electrons exist in the non-bonding π-orbitals. Following Hund's rule, it can be readily shown that the triangular molecules that have 3, 6, and 10 hexagon rings behave in an FM manner due to the presence of 1, 2, and 3 unpaired electrons, respectively. In contrast, linear molecules (see Fig. 30) show an AFM state, as the interaction between the spins is of an AFM character. The final ground magnetic state of the system is then determined by the dominance of the nature of the interaction among these edge states (*i.e.*, non-bonding states).[212] The theoretical and experimental results on various nanographenes' sizes and shapes confirm that magnetism in graphene emerges largely due to the π-electrons forming strongly spin-polarized edge states. In addition to the edge states, the defects of the σ-electron nature in graphene can give rise to localized spins. For instance, non-bonding carbon atoms can be created by virtue of any chemical attack or ion bombardment on the π-electron conjugated network of the graphene sheet. This can also result in magnetic graphene due to the σ-dangling bond with a localized spin ($S = 1/2$). Thus, a variety of magnetic states can be expected due to the simultaneous presence of defects and edge states. In the past few years, there have been more efforts devoted to understanding the basic difference between the edge states and the σ-dangling bonds that have helped in comprehending the origin of magnetism in carbon nanostructures.[89,219–223]

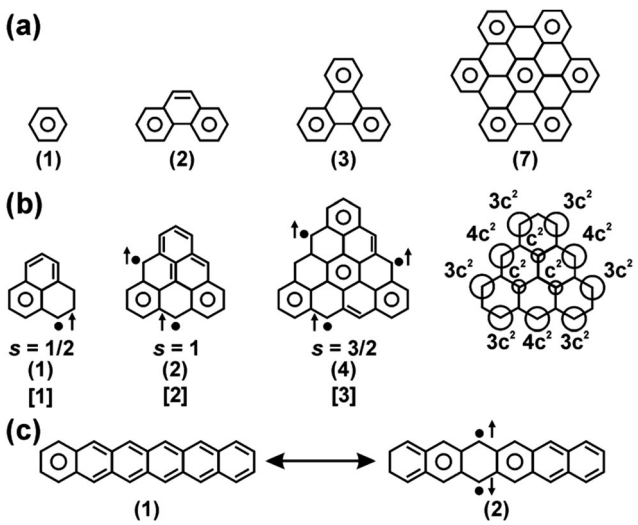

Fig. 30 Clar's representation for (a) armchair-edged molecules, (b) zigzag-edged triangular molecules, and (c) zigzag-edged linear molecules. The right structure of panel (b) displays the spatial distribution of the local density of states in a zigzag-edged triangular molecule with six hexagons. The numbers in () and [] represent the number of sextets and unpaired electrons, respectively. The spin state of the particular structure is given by *s*. Reprinted with permission from ref. 212. Copyright 2013 Wiley-VCH Verlag GmbH & Co. KGaA.

As already mentioned in Sections 2 and 3, Lieb's theorem[100] can be helpful in computing the spin state of graphene, *i.e.*, $S = 1/2(N_A - N_B)$, where N_A and N_B are the number of spins in the A- and B-sublattice. It can then be readily confirmed that the armchair-edged nanographene is non-magnetic while its zigzag-edged counterpart displays a magnetic ordering of either FM or AFM nature depending particularly on its geometry. The edge-state-driven magnetism is then described by the mean-field Hubbard Hamiltonian given as (see Section 2)[212]

$$H = -t\sum_{\langle i,j\rangle,\sigma}\left(c_{i\sigma}^{+}c_{j\sigma} + \text{h.c.}\right) + U\sum_{i}\left(n_{i\uparrow}\langle n_{i\downarrow}\rangle + n_{i\downarrow}\langle n_{i\uparrow}\rangle\right), \quad (9)$$

where the first term is the single-orbital Hamiltonian (with t indicating the transfer integral between neighboring i-th and j-th sites belonging to the A- and B-sublattice, respectively) and the second term stands for the on-site Coulomb interaction. As clearly seen, the appearance of the second term implies formation of magnetic moments. When solved, for example, for triangular-shaped nanographene with all the three edges of

zigzag character, a spin gap emerges around E_F, showing a spin polarization in the edge-state spins (*i.e.*, imbalance in spin channels ↑ and ↓). Spins sitting on the A-sublattice are oriented in an antiparallel manner to that on the B-sublattice; they are well localized near the zigzag edges and their strength rapidly decays from the edge to the interior of the triangular-shaped nanographene. At edges, atoms belonging to only the A-sublattice (or B-sublattice) are present, implying that the spins at the edges show parallel arrangement. Hence, the FM structure evolves with a non-zero spontaneous magnetization. For hexagonal-shaped nanographene with all the six edges of zigzag nature, spins with orientation ↑ sit along three edges while spins with orientation ↓ occupy the other three edges. As spins on the adjacent edges are oriented opposite to each other, the AFM structure is established over the hexagonal-shaped nanographene with no spontaneous magnetization. The expected magnetic behavior of both triangularly- and hexagonally-shaped nanographene sheets coincides exactly with the prediction from Lieb's theorem. Here, it should be highlighted that due to a weak spin–orbit interaction in carbon (~ 5 cm^{-1}), edge-state spins are weakly anisotropic. Then, the edge-state-driven magnetic structure is predicted by treating nanographene in the approximation of a weakly anisotropic Heisenberg spin system in a low-dimensional lattice.[212]

For an arbitrarily-shaped sheet of nanographene with a combination of armchair and zigzag edges (see Fig. 31), a ferrimagnetic (FIM) structure is supposed to be established. In particular, two interaction pathways between edge-state spins are recognized: (i) intra-edge interaction between spins lying along the same edge and (ii) inter-edge interaction between spins on opposite edges.[212] The intra-edge exchange interaction (expressed by the exchange integral J_0) is strong and is of FM character ($J_0 \approx 10^3$ K). The opposite FM edges can magnetically communicate by an inter-edge interaction (expressed by the exchange integral J_1) mediated by the conduction π-electrons. The inter-edge interaction is moderate ($J_1 \approx$ 10–100 K) and can be of either FM or AFM nature depending on the mutual geometrical relationship between the two zigzag edges. The competition between the strong intra-edge FM interaction and moderate inter-edge FM/AFM interaction, the strength of which is affected by the particular shape of the nanographene sheet, is then expected to stabilize the FIM structure with a nonzero spontaneous magnetization as antiferromagnetically coupled FM spin clusters are compensated.[211,212]

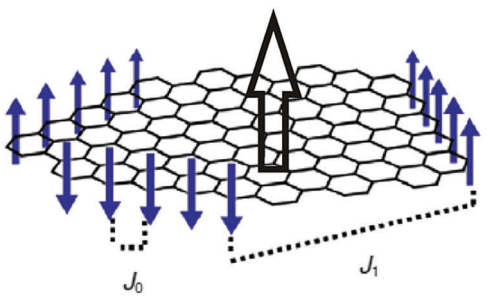

Fig. 31 Schematic representation of an arbitrarily-shaped sheet of nanographene showing the spatial distribution of edge-state spins (with blue filled arrows). J_0 and J_1 denote the intra-edge and inter-edge interactions, respectively. The white open arrow represents the net magnetic moment given as a vector sum of FM moments sitting on the zigzag edges. Reprinted with permission from ref. 212. Copyright 2013 Wiley-VCH Verlag GmbH & Co. KGaA.

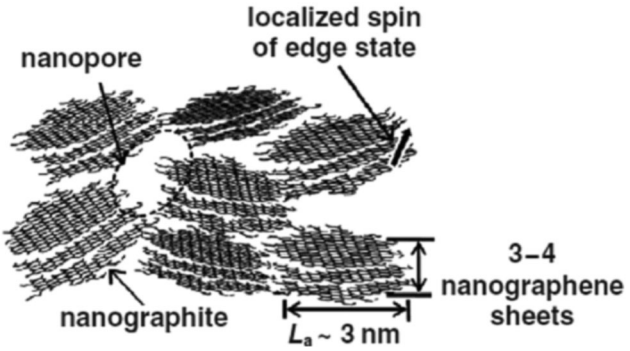

Fig. 32 Schematic representation of nanoporous activated carbon fiber with the localized edge-state spins sitting on the zigzag edges. The organization of nanographite domains in the activated carbon fiber favors the formation of a nanopore. Reprinted with permission from ref. 212. Copyright 2013 Wiley-VCH Verlag GmbH & Co. KGaA.

If the edges are fluorinated, spins located at zigzag edges are reduced. In contrast, if the zigzag edge on one side of the nanographene ribbon is dihydrogenated while the zigzag edge on the opposite side of the nanographene ribbon is monohydrogenated, a fully localized non-bonding state is supposed to appear around E_F; all the carbon atoms are spin-polarized even in the interior of the nanographene ribbon.[212] Another example involves oxidation of one side with the zigzag edge; in such a case, the side with the monohydrogenated zigzag edge is magnetic while the side with oxidized edge forms an electron conduction pathway. Thus, roles of edges can be tuned by their chemical modification (see below).[212]

If nanographites with the localized spins at the edges form a network (known as activated carbon fibers, see Fig. 32), a spin-glass behavior is observed maintained by the π-conduction electron-mediated interaction between the edge-state spins, similar to the s–d interaction in traditional metallic magnets.[211,212,224] It was found that the adsorption/desorption of water into the micropore space in the networked nanographite domains reduces/enhances the effective magnetic moments of the edge-state spins, which was explained in terms of encouraging the exchange interaction among the edge-state spins on the adjacent nanographene sheets by reduction of the inter-sheet distance caused by the internal pressure of water, eventually squeezing the nanographite domains. Such a phenomenon seems very promising in detection of guest molecules which, upon physisorption, switch on/off the magnetic response of the networked nanographite domains.[211,212]

4.1. Graphene nanoribbons

Graphene nanoribbons (GNRs) are strips of graphene sheets with a finite width not exceeding 50 nm (usually with a high aspect ratio).[5] They are classified as quasi-one-dimensional

carbon nanoallotropes and are often adopted as a theoretical model system to describe and understand the role of edge and finite-size effects on the physical properties of graphene.[215,225,226] Currently, they are viewed as a prototypical example to study both theoretically and experimentally the role of various defects in the evolution of self-sustainable magnetic ordering in graphene.

Currently, three main approaches are used to synthesize GNRs, *i.e.*, (i) cutting from graphene employing lithographical procedures or catalytic particles, (ii) bottom-up synthesis from polycyclic molecules, and (iii) unzipping the carbon nanotubes.[5,227–229] With lithographic techniques, GNRs can be prepared by etching the exfoliated graphene flakes, graphene grown on metallic surfaces by chemical vapor deposition or epitaxial graphene on SiC. However, smooth edges are difficult to achieve even if other techniques are used such as TEM, STM or atomic force microscopy. Moreover, the yield of lithographic techniques is low. Alternatively, graphene can be cut by catalytic particles such as Fe or Ni in the presence of a hydrogen atmosphere. The problem is faced with unpredictability of cutting directions, resulting thus in a wide variety of shapes of graphene nanostructures. Recently, plasma etching was suggested as a tool providing engineering of the edge termination. The chirality of the edge segments was found to strongly depend on the initial chirality of the GNR itself, local environments, and out-of-equilibrium nature of the hydrogen plasma etching. By plasma etching, the edges are flat without structural reconstructions and terminated with hydrogen atoms preventing any hybridization of the outermost carbon edge atoms.[230]

Bottom-up syntheses of GNRs are based on growing them from molecular precursors.[231] They involve several steps, starting from monomeric precursors which react at the surface of an appropriate catalytic metal. Upon sublimation at a modestly hot metallic surface (with a temperature of $\sim$200 °C), polymer chains are formed. Dehydrogenation/cyclization of polymer chains at higher temperatures ($\sim$400 °C) results in the formation of GNRs. They are very narrow with a narrow size distribution and show an atomically precise edge configuration. However, in bottom-up synthetic procedures, metallic substrates are always required, limiting thus a bulk production of GNRs. This approach has not been fully explored yet and is widely viewed as a synthetic technique with future advancements.

The third approach to prepare GNRs involves unrolling or unzipping multi-walled carbon nanotubes. Several strategies to unzip multi-walled carbon nanotubes have been reported so far (see Fig. 33);[5,227] most of them exploit solution-based processes. The edge structure and crystallinity of GNRs were found to depend on various parameters such as the degree of nanotube crystallinity and uniformity in the length, diameter, and number of layers of carbon nanotubes. GNRs from unzipped carbon nanotubes can be produced in high yields with significantly lower costs compared to the other two approaches. However, as GNRs are prone to stack due to van der Waals interactions, setting of suitable conditions for their large-scale production should be carefully considered in order to avoid agglomeration, entanglement, and wrinkling of graphene strips.

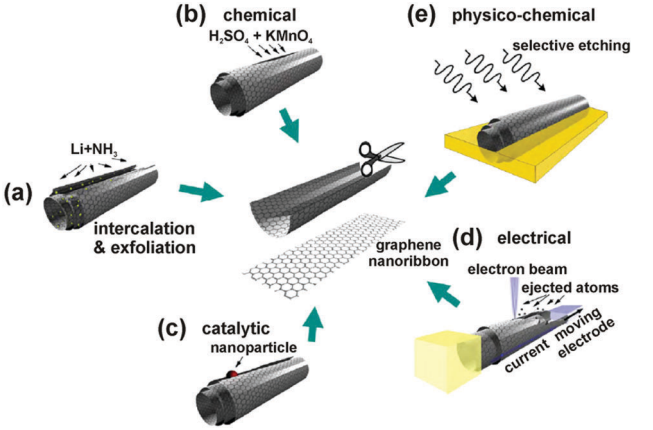

Fig. 33 Various strategies exploited for the preparation of GNRs involving unrolling or unzipping the carbon nanotubes: (a) intercalation/exfoliation of multi-walled carbon nanotubes by unzipping them by treatment in liquid NH_3 and Li, followed by exfoliating the graphene strips by HCl and heat treatment; (b) chemical procedures involving oxidizing agents (*e.g.*, $KMnO_4$, H_2SO_4) which break the C–C bonds; (c) catalytic cutting of multi-walled carbon nanotubes by exposing to metal nanoparticles (*e.g.*, Fe, Co, Ni) facilitating cutting of the carbon nanotubes along their length; (d) electrical cutting with an electrical current applied through the carbon nanotube; (e) physicochemical approach involving embedding of multi-walled carbon nanotubes in the polymer matrix, followed by etching the walls by an Ar plasma. Reprinted with permission from ref. 227. Copyright 2010 Elsevier Ltd.

Two canonical types of GNRs are recognized depending on the geometrical termination of their edges, *i.e.*, armchair and zigzag GNRs.[5] The edge pattern is defined considering the GNR's orientation with respect to the graphene lattice. From the geometrical aspect, armchair and zigzag edges are configurations with a high symmetry. In the case of zigzag GNRs, the edge consists of two sides of each hexagon resembling the periodic triangular appearance (see Fig. 34).[5] For armchair GNRs, the edge is formed by the hexagonal sides with adjacent hexagons contributing alternatively with one and three sides in a periodic manner (see Fig. 34).[5] The width of armchair GNR is defined by

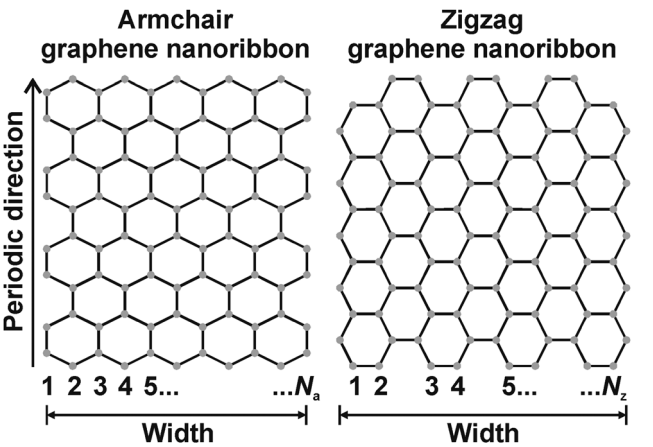

Fig. 34 Structures of the armchair and zigzag GNRs with their width given by the number of dimer lines (N_a) and zigzag chains (N_z), respectively.

the number of dimer lines (N_a) while for zigzag GNR, the width is given by the number of zigzag chains (N_z; see Fig. 34).[5] All other ordered orientations are of chiral nature. Here, it should be stressed that the carbon atoms sitting at the edge are not saturated. In the case of armchair GNRs, no edge reconstructions occur as the armchair edges are stable, hence preserving the planar patterns. However, zigzag edges are metastable undergoing spontaneous reconstructions even at room temperature. A pattern consisting of a pentagon and heptagon formed upon transformation of two hexagons was suggested as a potential reconstruction of the zigzag edge, resembling the appearance of an edge cut through a Haeckelite structure of a line of the SW defects. Thus, hydrogen atoms are often introduced to saturate the carbon atoms at the zigzag edge to preserve the planar structures of zigzag GNRs.[5] Moreover, a partial hydrogenation was theoretically identified to produce narrower GNRs from their wider counterparts.[232] The hydrogenation proceeds from the edges to the interior of GNRs, maximizing the number of carbon–carbon π–π bonds; the adsorption of hydrogen is of alternating nature skipping from one edge to another edge, terminated once all the hydrogen atoms available are adsorbed. The theoretical calculations imply that partially hydrogenated GNRs show similar electronic and magnetic features compared to those of narrow GNRs, which represent their graphene parts.[232]

It has been shown by tight-binding calculations that the band structure of GNRs depends heavily on the edge termination.[233] Armchair GNRs are predicted to behave as semiconductors with an extremely low carrier effective mass and a finite band gap which increases with a decrease in the width of the nanoribbon. Based on the size of the energy gap and its dependence on the nanoribbon's width, armchair GNRs can be classified into three families with $N_a = 3p$, $N_a = 3p + 1$, and $N_a = 3p + 2$, where p is an integer (see Fig. 35).[233] It is believed that the semiconducting behavior of armchair GNRs is driven by the quantum confinement effect together with a significant role of edge effects. As the carbon atoms sitting at the edge of armchair GNRs are passivated with hydrogen atoms, distinct bonding of carbon atoms at the edge is expected compared to that of carbon atoms in the interior. The carbon atoms at the edge show bond lengths shorter than those of carbon atoms in the interior of the armchair GNR, eventually opening its band gap. More importantly, the theory predicts that the electronic structure of all three classes of armchair GNRs is more or less similar, with the presence of four important subbands.[234] Their origin stems from π-bonds of carbon atoms; as they have different shapes, it is possible to alter them by external stimuli, further tuning the electronic structure and, hence, physical properties of armchair GNRs. However, unmodified armchair GNRs are not magnetic.[233] If the number of layers is increased, multilayered armchair GNRs fall into three classes, *i.e.*, two semiconducting and one metallic. For a given width, the band gap in multilayer armchair GNRs is expected to be smaller than that in their bilayered counterparts.[235]

Similar to armchair GNRs, zigzag counterparts show a direct energy gap, behaving in a metallic or semiconducting manner depending on the edge spin orientation. More importantly, their electronic structure is described by a set of doubly degenerate flat edge-state bands appearing at E_F, resulting in a large density of states at E_F.[233,236] At E_F, the peak of density of states is half-filled, implying emergence of the Stoner instability, a prerequisite for evolution of magnetic states. If spin degrees of freedom are introduced into the theoretical calculations, a magnetic insulating ground state was predicted for zigzag GNRs with FM ordering at the edge and antiparallel spin orientation between the two edges;[233,236] moreover, the intra-edge FM correlations were proposed to be significantly strengthened by the on-site Coulomb interaction.[237] The band gap is inversely proportional to the width of zigzag GNRs identically as in the case of their armchair analogues. The generated spin states are located mainly at the edges on carbon atoms (see Fig. 36);[233] the moments sitting on the edge atoms were predicted to be weakly dependent on the width of the nanoribbon, implying that the dependence of the band gap on the width of the nanoribbon results purely from the quantum confinement of orbitals.[238] The evolution of spin-polarized edge states is more energetically favored compared to non-spin-polarized solutions; upon an increase in the width of

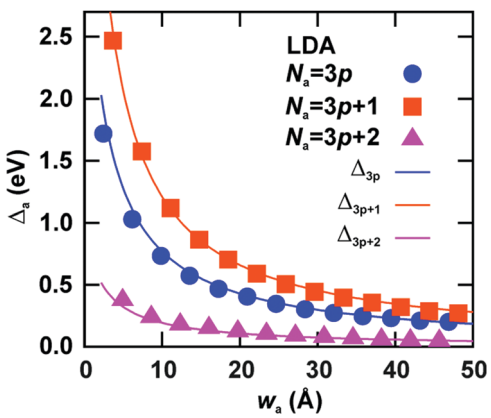

Fig. 35 Variations in band gaps for armchair GNRs as a function of their widths (w_a). Reprinted with permission from ref. 233. Copyright 2006 American Physical Society.

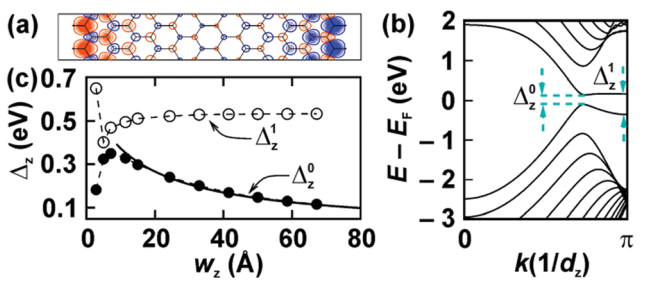

Fig. 36 (a) Spatial modulation of spin density for zigzag GNR with N_z = 12. (b) Band structure of zigzag GNR (with N_z = 12). The spin states in the A- and B-sublattice are degenerate in all the energy bands. Δ_z^0 and Δ_z^1 represent the direct band gap and the energy splitting at $kd_z = \pi$, respectively. (c) Profile of Δ_z^0 and Δ_z^1 with the width (w_z) of zigzag GNRs. Reprinted with permission from ref. 233. Copyright 2006 American Physical Society.

zigzag GNRs, the energy difference between the spin-polarized and non-spin-polarized edge states increases. The existence of spin-polarized edge state is further encouraged by FM coupling along the edge.[233] The temperature dependence of the electron paramagnetic resonance linewidth implies that the edge-state spins are strongly coupled with the conduction π carriers.[239] It is believed that the edge states can withstand potential fluctuations due to electron–electron interactions. However, if the potential disorder is strong enough, electron–hole puddles (*i.e.*, inhomogeneous charge distributions) evolve inducing a magnetic transition when the coupling between the opposite zigzag edges is switched from AFM to FM character. The electron–hole puddles are formed as a consequence of a local breaking of charge neutrality.[240] In general, the difference between FM and AFM inter-edge coupling decreases with an increase in the width of zigzag GNRs, becoming negligible once the width significantly exceeds the decay length of spin-polarized edge states. The energy gaps in zigzag GNRs are believed to emerge as a result of staggered sublattice potentials from magnetic ordering. In other words, it can be inferred that the band gap stems from the exchange difference on the two sublattices of the graphene lattice. Moreover, it turns out that the spins occupying the A- and B-sublattice are degenerate in all the bands and show identical band gap.[233] For bilayered GNRs (*i.e.*, two identical graphene strips in a layered structure), the magnetic ordering at the edge atoms is predicted to disappear due to coupling of edge states between the top and bottom layers for particular stacking configurations. For various stacking arrangements, different band gaps and edge magnetizations are expected to evolve due to energy competition between inlayer and interlayer interactions, encouraging stabilization of ground magnetic state of either non-magnetic or FM or AFM origin. Moreover, metal–semiconductor transitions and splitting of spin-up and spin-down states can also be observed depending on the stacking configurations, spin arrangements, and widths of GNRs.[241,242] For example, if the layers are shifted by 0.61 Å (perpendicular to the ribbon's axis), such stacking of the two layers is favored in terms of thermodynamics showing, however, a non-magnetic ground state. If the shifts are larger than 1.42 Å, AFM inlayer and interlayer states develop, which are found to be the most stable among others.[243] In order to prevent losing magnetic ordering in bilayered zigzag GNRs, the two layers must alternatively have different widths. While edges at one side are pinched due to interlayer coupling, resulting in no magnetic ordering, the edges at the other side are coupled antiferromagnetically between the layers analogously as in the case of opposite edges in the monolayered zigzag GNRs.[244] If placed in an external electric field, asymmetric energy-gap opening for spin-up and spin-down occurs, leading to a half-metallic behavior in bilayered zigzag GNRs with different widths of layers.[244] For multilayered zigzag GNRs, the value of the gap then depends on the type of edge alignment.[235]

However, the existence and stability of edge states were heavily questioned by several theoretical studies. It was proposed that edge states can be suppressed, weakened or even eliminated by three mechanisms, which include edge reconstruction, edge passivation, and edge closure.[245] Moreover, quantum fluctuations were identified to play an eminent role, eventually ruining the long-range spin correlations by forming rung singlets.[246] In particular, this happens in cases when decoherence, which is affected by the environment interactions, is slower than the quantum dynamics. Similarly, edge magnetic moments are supposed to get reduced upon increasing the strength of nonlocal Coulomb interactions when spin- and charge-density fluctuations compete with each other.[247] As a result, dispersion of the edge states is renormalized, eventually generating a single-particle gap. However, no phase transition is observed, indicating that FM coupling along the edges, encouraged by the on-site interaction, is not affected by the competing short-range charge correlations, which are favored due to the long-range Coulomb interactions.[247] Suppression of spin polarization and, hence, stability of spin states in GNRs were predicted to occur for edge defects (*e.g.*, vacancies) and impurities; upon increasing their concentration, edge states at E_F are reduced or removed.[248] In particular, GNRs become non-magnetic if the concentration of defects exceeds a critical value of $\sim$0.10 Å^{-1}. Moreover, the local edge spins can completely disappear once two defects are positioned within a distance smaller than 3 unit edge segments (see Fig. 37). In other words, a tiny randomness

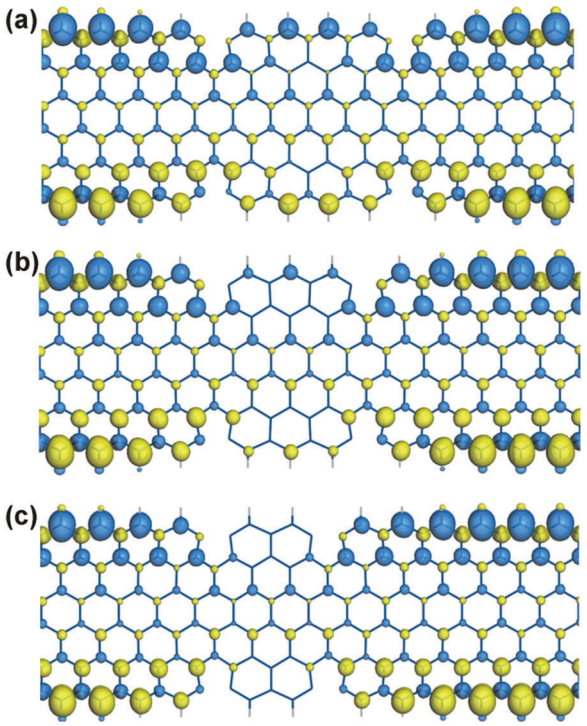

Fig. 37 Isosurfaces of the charge difference between the spin-up and spin-down states when vacancies are introduced at the edges of GNRs: (a) edge vacancies separated by 5 unit edge segments; (b) edge vacancies separated by 4 unit edge segments; (c) edge vacancies separated by 3 unit edge segments. The range of isovalues is set at (−0.004, 0.004) μ_B Å^{-1}. Reprinted with permission from ref. 248. Copyright 2008 American Physical Society.

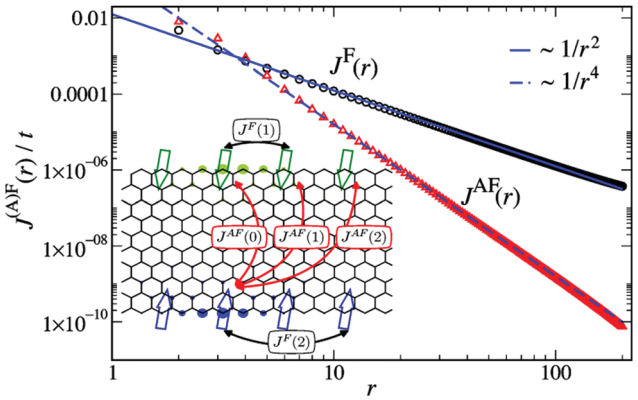

Fig. 38 Evolution of effective FM intra-edge [$J^{F}(r)$] and AFM inter-edge [$J^{AF}(r)$] interactions as a function of lateral distance (r) for a zigzag GNR with a width of 10. The inset schematically shows the structure of the zigzag GNR with some effective exchange interactions of the effective spin-ladder model indicated. The circles correspond to the amplitudes of the Wannier functions calculated for the two of these edge states on the nanoribbon's sites (one shown on the upper edge and one shown on the lower edge). Reprinted with permission from ref. 249. Copyright 2017 American Physical Society.

in the edge structure can even ruin edge magnetism and spin transport in GNRs.[248]

Very recently, the issue of edge magnetism in zigzag GNRs was theoretically addressed adopting the effective spin-ladder models constructed within the large-scale quantum Monte Carlo simulations; more specifically, zigzag GNRs are mathematically described as two antiferromagnetically coupled FM Haldane–Shastry spin-half-chains.[249] The results showed that FM intra-edge interactions decay relatively weakly with a lateral distance, r (proportional to $1/r^2$), while AFM inter-edge interactions fade away much faster with r following the $1/r^4$ power-law (see Fig. 38). In addition, the quantum disordered region appears if the strength of AFM inter-edge coupling exceeds a finite critical value, determining a quantum critical point; such a region was identified as a spin-gapped ground state of the effective quantum spin model for chiral GNRs.[246] In other words, upon increasing the strength of AFM inter-edge interactions, the system undergoes a quantum phase transition from the gapless state to the phase of quantum-disordered-region nature for which dominant singlets are observed to form along the inter-chain bonds.[249]

Experimentally, FM properties were observed for potassium-split GNRs and oxidatively unzipped and chemically converted GNRs;[250] in both cases, multi-walled carbon nanotubes were used as a starting material for GNRs. FM ordering was found to be self-sustainable up to room temperature for potassium-split GNRs; for oxidatively unzipped and chemically converted GNRs, vanishing of the FM response upon increasing the temperature was explained in terms of potential reconstruction, passivation, or closing by an oxidative unzipping process of majority of edges. The analysis of magnetization data confirmed clustering of spins with $S = 1/2$ in both types of GNRs. Moreover, a co-existence of AFM regions with the FM structure was observed, manifested by a non-zero exchange bias. The negative exchange bias was detected for potassium-split GNRs suggesting the existence of smooth edges. From electron spin resonance (ESR) spectra, carbon-related localized states were identified to be responsible for the emerged magnetism.[250]

Besides extensively studied armchair and zigzag edge terminations, the existence of other types of edge structures was reported. These include extended Klein's edges, cove edges, and reconstructed edges. The extended Klein's edge, predicted theoretically and observed experimentally, is defined as an array of single atom carbon atoms extending from a zigzag edge, *i.e.*, with an atomic site showing a π-orbital on the edge.[251–253] The Klein edges are favored to form among other edge terminations in the tearing process of graphene; hydrogenated Klein's and reconstructed Klein's edges were proposed to be energetically favored over hydrogen-terminated zigzag edges, with stabilities approaching those reported for the armchair edges.[254] It was shown that if the Klein's bearded bonds are partially attached to the GNR with both armchair and zigzag edges, partial flat bands appear at zero energy even for $|N_A - N_B| = 0$, which gives rise to a spin polarization near the edge.[255] The cove-shaped GNRs contain protruding phenyl rings along both edges and can thus be described as alternating armchair and zigzag segments;[256,257] however, the spin-polarized flat bands were found to emerge only once modified with the Klein's bearded bonds.[255] Reczag edges, already mentioned above and defined as the zigzag-57 edge with alternating 5- and 7-membered rings (*i.e.*, a structure with two under-saturated carbon atoms moved adjacent to each other), are energetically more stable than zigzag edges; in the electronic structure, they are manifested as flat bands extended around E_F, *i.e.*, a prerequisite for evolution of edge magnetic moments.[258] Other reported edge geometries involve ac(677) and ac(56) edges; the ac(677) edge structure is formed when the two separate "armrest" hexagons are merged into the adjacent heptagons by the Stone–Wales mechanism while the ac(56) edge motif is established upon diffusion of carbon atoms from the distant armrests to the seat positions.[258] These reconstructed armchair edges need more energy for stabilization than pure armchair edges and are not magnetic.[258]

The stability, edge states, and aromaticity of various types of edges can drastically vary depending on the level of hydrogenation (see Fig. 39 and Table 1).[259] The theoretical results imply that GNRs are magnetic only at an extremely low hydrogen concentration (see Table 1); however, they show metastability as they are very reactive. On the other hand, non-magnetic GNRs are considered as the most stable systems with a low reactivity at a standard/high level of hydrogenation (see Table 1).[259] Moreover, the Clar's rule can be applied to decide about the aromaticity of the structure; for pure graphene with an ideal aromaticity, a value of 1/3 is expected. It turns out (see Table 1) that some zigzag edges and mono- and di-hydrogenated armchair edges show 1/3 aromaticity of graphene and, hence, are not magnetic and non-metallic. If the edges have an aromaticity lower than graphene, a competition between the bulk and edge is expected to occur. As a result, some carbon atoms are forced to have less or more than four saturated bonds, eventually leading to the evolution of the edge states.[259]

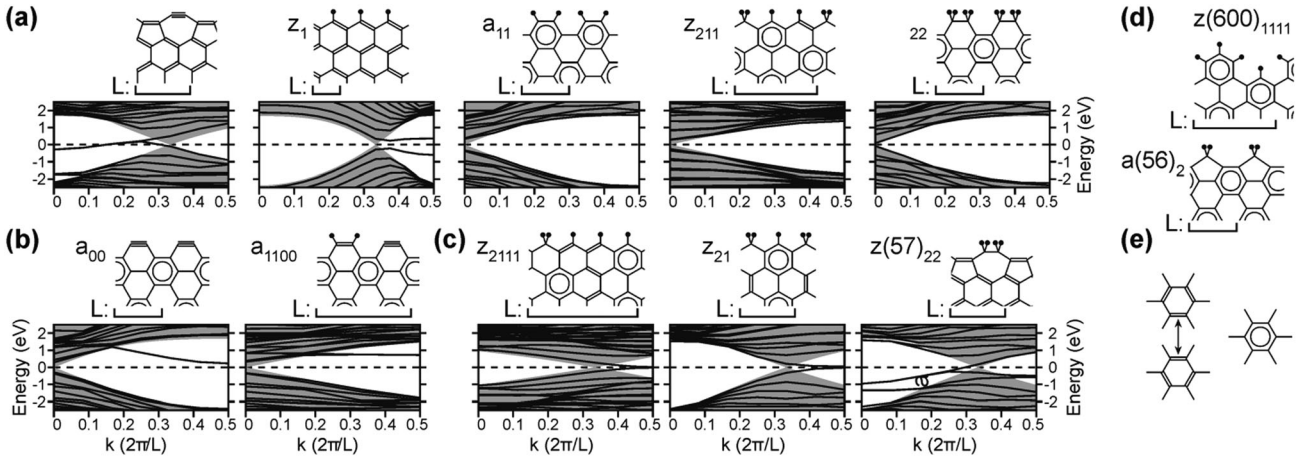

Fig. 39 (a) Schemes and electronic band structures of the five most stable hydrogen-passivated edges of GNRs. Hydrogen atoms are marked with filled circles. The systems considered show a periodicity along the ribbon's edge indicated by *L*. The grey area in the electronic structures corresponds to the electronic bands allowed in bulk graphene and the dashed line marks E_F. (b) Other stable armchair edge structures. (c) Other stable zigzag and reconstructed zigzag edge structures. (d) Structures of other reconstructed armchair and zigzag edges. (e) Standard representation of the benzenoid aromatic carbon ring used for computation of the aromaticity of various edge motifs considered. Reprinted with permission from ref. 259. Copyright 2008 American Physical Society.

Table 1 Formation energy (E_{H2}) and hydrogen density (ρ_H) for various edge structures. $z_{n_1n_2\ldots n_x}$ represents GNRs with zigzag edges, where n_i denotes the number of hydrogen atoms on a given site and *x* is the number of adjacent edge sites within the periodicity, *L* (see Fig. 39), $a_{m_1m_2m_3m_4}$ represents GNRs with armchair edges for the supercells with one (m_1m_2) and two ($m_1m_2m_3m_4$) hexagon columns, where m_i denotes the number of hydrogen atoms attached to the *i*-th carbon site, and $z(57)_{ij}$, $z(600)_{ijkl}$, and $a(56)_i$ represent GNRs with reconstructed zigzag and armchair edges, where the subscripts *i*, *j*, *k*, and *l* indicate the number of hydrogen atoms on a given site. Adopted with permission from ref. 259. Copyright 2008 American Physical Society

Edge type	ρ_H (Å^{-1})	E_{H_2} (eV Å^{-1})	Edge features
$z(57)_{00}$	0.000	0.9650	Non-magnetic and metallic edge, non-aromatic
z_0	0.000	1.1452	Magnetic and metallic edge, non-aromatic
z_{100}	0.136	0.7854	Magnetic and metallic edge, non-aromatic
z_{200}	0.271	0.7260	Magnetic and metallic edge, non-aromatic
z_{110}	0.271	0.4306	Magnetic and metallic edge, non-aromatic
$z(57)_{11}$	0.407	0.3337	Non-magnetic and metallic edge, non-aromatic
z_1	0.407	0.0809	Magnetic and metallic edge, non-aromatic
z_{211111}	0.474	0.0463	Magnetic and metallic edge, non-aromatic
z_{21111}	0.488	0.0397	Magnetic and metallic edge, non-aromatic
z_{2111}	0.508	0.0257	Magnetic and metallic edge, non-aromatic
z_{211}	0.542	0.0119	Non-magnetic and non-metallic edge, aromatic
$z(600)_{111}$	0.542	0.0459	Non-magnetic and non-metallic edge, aromatic
z_{21}	0.610	0.0382	Non-magnetic and metallic edge, non-aromatic
z_{221}	0.678	0.1007	Magnetic and metallic edge, non-aromatic
z_2	0.813	0.2224	Magnetic and metallic edge, non-aromatic
$z(57)_{22}$	0.813	0.2171	Non-magnetic and metallic edge, non-aromatic
$a(56)_0$	0.000	1.4723	Magnetic and metallic edge, non-aromatic
a_{00}	0.000	1.0078	Non-magnetic and non-metallic edge, aromatic
$a(56)_1$	0.235	0.7030	Non-magnetic and metallic edge, non-aromatic
a_{1100}	0.235	0.4946	Non-magnetic and non-metallic edge, aromatic
a_{10}	0.235	0.6273	Magnetic and metallic edge, non-aromatic
a_{11}	0.469	0.0321	Non-magnetic and non-metallic edge, aromatic
$a(56)_2$	0.469	0.4114	Non-magnetic and non-metallic edge, aromatic
a_{21}	0.704	0.2092	Magnetic and metallic edge, non-aromatic
a_{2211}	0.704	−0.0163	Non-magnetic and non-metallic edge, aromatic
a_{22}	0.939	−0.0710	Non-magnetic and non-metallic edge, aromatic

The presence of edges offers a potentiality to modify their chemical and electronic features with defects, doping with foreign atoms, hydrogenation, oxidation, functionalization with various functional groups and with adsorption of some gas molecules or when exposed to external stimuli such as strain and external electric and magnetic fields. In general, the type of edge modification determines whether the GNR is a conductor or a semiconductor; a conducting behavior is associated with the decorating atom and its covalent bond while a semiconducting feature is closely related to the edge-induced magnetic moments.

If GNRs are doped with nitrogen and boron creating holes and carriers, respectively, in their structure, the triplet state is

expected to be more stable compared to the singlet state, thus favoring an FM ground state.[260] For armchair GNRs, both the band gap and ionization potential gradually decrease as their widths increase. In zigzag GNRs, the dependence of band gap and ionization potential on their widths shows a distinct trend whether unpaired electrons are present or not.[260] Lately, from theoretical calculations seeking the most energetically favorable atomic configurations in doped GNRs, it was suggested that nitrogen atoms preferentially substitute carbon atoms at both armchair and zigzag edges. In the case of boron (as a p-type dopant), the preference for site substitution is different for armchair and zigzag GNRs. While carbon atoms are substituted by boron at zigzag edges, in armchair GNRs, boron replaces carbon atoms at positions (*i.e.*, three-coordinated sites) next to the edge. In zigzag GNRs, boron induces a spin-dependent donor-like state if it is located at the edge while acceptor states are formed as boron atoms move to the center of the nanoribbon. For nitrogen n-type doping, the opposite effect is expected, *i.e.*, acceptor-like states with nitrogen at the edge and donor-like states with nitrogen located in the GNR inner regions.[261,262] More specifically, if pyridine- and pyrrole-like N-doping defects are introduced into zigzag GNRs, they turn them into half-metals or spin-gapless semiconductors;[263] they tend to be localized near the edge of GNRs. A similar effect is expected for nitrogen atoms attached to only one zigzag edge.[264] As a result, the two edge states separate near E_F; the system adopts the FM ground state due to reduction of the magnetic moments at the doped side. Appropriate charge doping is thus expected to give rise to half-metallic and single-edge conducting zigzag GNRs.[264] In the case of co-doping zigzag GNRs simultaneously with nitrogen and boron, it was theoretically predicted that for an AFM ground state, the BN defect states destroy the doped-side spin-polarized edge currents promoting their flowing at the undoped side near the conduction band-edge region with almost a perfect one-spin-channel transmission.[265] On the other hand, fully spin-polarized currents flowing along the undoped side of zigzag GNR were identified to evolve near E_F. Such BN-induced spin-polarized states are robust with regard to the width of GNRs, doping concentration, and geometries of heterojuctions.[265] Half-metallic behavior can also be observed for hybrid C/BN zigzag GNRs (*i.e.*, with a BN row introduced into the nanoribbon's structure) for a specific nanoribbon's width and ratio between C and BN; the unexpected half-metallicity was proposed to originate from the competition between the charge and spin polarizations and π orbital hybridization between C with B and N, breaking the electronic symmetry of the two edge states.[266]

Despite showing a non-magnetic response, magnetic states can be induced in armchair GNRs if periodically repeating defects such as vacancies or divacancies are introduced into their lattice. They are found to promote metallic character and net magnetization due to the spin polarization of the local defect states. Besides the geometry of the defect, the band gap is significantly affected by the repeating periodicity of the defect and its position within the GNR structure relative to the edge.[267] Moreover, a magnetic state induced by vacancies in armchair GNRs can be tuned by applying a strain as evidenced for a two-vacancy system when singlet–triplet splitting was found to strongly depend on the product of strain and inter-vacancy distance.[268] Alternatively, a magnetic ground state may develop if armchair GNRs are doped with extra electrons. The spin polarization then stems from the localized edge state appearing around the Brillouin zone boundary. Moreover, if some electrons are injected, indirect-gap armchair GNRs show half-metallic properties while heavily doped direct-gap armchair GNRs become antiferromagnets.[269] More specifically, a dominant AFM behavior appears around half-filling with electrons while an FM ground state is favored with electron filling lower than 0.8 and can be manipulated by the gate voltage. Thus, FM interactions are believed to be strengthened substantially by the next-nearest-neighbor hopping energy.[270]

As shown theoretically, the magnetism in armchair GNRs can be induced and tuned if a line defect composed of two pentagons and one octagon (*i.e.*, 558-type line defect), is introduced as a grain boundary in the nanoribbon's lattice.[271] If the end configuration of the 558 grain boundary is varied, the structures were found to fall into three groups. For some particular configurations, a transition from the non-magnetic to FM state occurs in defective armchair GNRs. In FM systems, the evolved magnetic features stem from the zigzag chains of the 558 grain boundary which are closely correlated with the spin splitting of the energy bands.[271]

If passivated with oxygen, planar armchair GNRs may adopt a degenerate magnetic ground state due to emptying the O lone-pair electrons.[272] The degenerate magnetic ground state established over planar armchair GNRs involves metallic FM ordering and AFM ordering with three families distinguished upon the band gap, *i.e.*, one metallic and two semiconducting classes. Due to steric interactions between oxygen atoms and more beneficent hybridization of atomic orbitals, non-planar geometries are energetically favored over planar appearance of oxygen-functionalized GNRs, becoming eventually non-magnetic and classified into three semiconducting families depending on the behavior of the band gap.[272] On the other hand, for GNRs with armchair edges saturated with H_2, the theoretical calculations lead to shifted labeling of the three nanoribbon's classes with $N = 3p$, $3p - 1$ and $3p + 1$ ($p = 1, 2, 3, \ldots$).[273] The shift in classes, and, hence, in width values, was explained by modification of sp^2-hybridization to sp^3-like hybridization by interaction of π orbitals of graphene on the outermost edge and hydrogen orbitals.[273]

Besides boron and nitrogen, armchair GNRs were doped or edge-modified by other elements such as Mg, Mn, Fe, and Au.[274–277] In particular, Fe atoms are preferentially doped at the center of GNRs and their magnetic moments vary from 1.95 to 2.93 μ_B depending on the doping site. Fe atoms are supposed to break the degeneracy of the opposite spin states. Spin polarization can reach 60% and can be tuned upon varying the position of Fe atoms in the nanoribbon's lattice. Due to a number of conduction channels that cross E_F, the system shows a high metallicity, which does not depend on the nanoribbon's width or position of the Fe atom.[275] In contrast, Au atoms were identified to preferentially substitute carbon atoms near the edge of armchair GNRs. The Au-doped armchair GNRs behave as semiconductors with an FM configuration showing a lower

energy compared to an AFM case. The spin-up and spin-down states are completely degenerate as no spin dependence in the band structure is observed. Moreover, the edge substitution modifies the band gap, encouraging the occurrence of the semiconductor–metal transitions in Au-substituted armchair GNRs.[276]

Recently, it was shown that if armchair GNRs are exposed to a strain along the armchair direction, edge states can evolve even for a very small intrinsic spin–orbit coupling.[278] Moreover, the edge-state conductivity was found to be quantized. A deeper theoretical analysis identified the helical nature of edge states, confirming the presence of the spin Hall effect. A transition from the quantum spin Hall state to a trivial insulator regime was then observed upon reaching a critical value of strain. Compared to zigzag GNRs, the emerged spin texture in armchair GNRs was found to be invariant to the Fermi energy with spin directions of the edge states opposite to each other on the same boundary.[278]

As a weak spin–orbit interaction exists in carbon resulting in small magnetic anisotropy energy, it is heavily questioned, whether magnetic ordering in GNRs can sustain thermal fluctuations and magnetic impetus. It was theoretically proposed that if suitably ligated GNRs are further functionalized with 3d transition metals, the system becomes equipped with large magnetic moments and large magnetic anisotropy energy.[279] The suggested concept was verified for GNRs edge-functionalized with –F and –CN groups and then decorated with Co and Mn atoms. If GNRs are terminated with –CN groups and Co atoms, high magnetic anisotropy energy is expected; the direction of their magnetization can be then changed by applying an external electric field. For –CN-terminated GNRs with Mn atoms attached, a half-metallic behavior with giant magnetic moments was observed, which seems to be more stable than that reported for half-metallic zigzag GNRs.[279]

In the case of zigzag GNRs, it has been shown that the nature of coupling between opposite edges can be altered by their width.[57] Upon increasing the nanoribbon's width, a transition from the AFM state to the FM regime is witnessed; in the AFM state, zigzag GNRs behave as direct-band gap semiconductors while metallic features are observed for FM zigzag GNRs.[57] In addition, opposite edges of zigzag GNRs can interact in an FM manner if (i) extra carriers (*i.e.*, electron/holes) are injected into the lattice of GNRs by doping (*e.g.*, N or B),[280] (ii) GNRs interact with an internal magnetic field on a suitable substrate during graphene deposition,[281] and (iii) one edge is saturated by two hydrogen atoms and the other edge by only one hydrogen atom.[282] More specifically, upon increasing the level of doping with electrons/holes, the angle (θ) between the directions of spins at the opposite edges continuously decreases from 180° (AFM state) to 0° (FM state). The canted, non-collinear spin structures appear for $0^\circ < \theta < 180^\circ$ (see Fig. 40).[283] Furthermore, if boron atoms are attached to both edges, the FM ground state is promoted showing a half-metallic behavior irrespective of the width of zigzag GNRs. However, if nitrogen atoms are introduced at both zigzag edges, the system preserves an AFM ground state with the metallic behavior.[284] Recent theoretical works confirmed that half-metallicity can be imprinted in zigzag GNRs once functionalized on either edge with species of donor and acceptor nature. As a result, an effective potential gradient emerges. Other strategy involves hybrid modification at one edge manifested by evolution of spin-polarized impurity state at E_F. For example, if zigzag edges are decorated with CH_3–NO_2 pair, the spin-down channel is metallic while semiconducting behavior is expected for the spin-up channel; the spin density is distributed largely over the carbon atoms at the edges.[285] Half-metallic state can be alternatively induced by introducing a BN defect in the structure of zigzag GNRs.[286] As the zigzag C–C chains located in the middle part of the ribbon are gradually replaced with BN segments, the system eventually transforms to the zigzag BN nanoribbons with electronic features dependent on the level of substitution. If the doping concentration exceeds a threshold value, when carbon atoms, resembling the arrangement of terminated polyacene C chains, are located only at the edges and all the interior carbon atoms are replaced with BN chains, the hybrid system becomes a half-metallic antiferromagnet for all the widths. The evolution of half-metallicity was explained in terms of charge transfer from the adjacent carbon atoms to boron atoms promoted by the Lewis acid nature of boron, leading eventually to the generation of the interface potential gradient similar to the case of applying an external electric field.[286] On the other hand, if holes are pumped in zigzag GNRs, they become conductive, accompanied by the reduction of their spin gaps. Above the threshold value of hole doping, the spin gap is closed and the system shows a magnetic ground state with a net magnetic moment over the structure.[287] If the structure of zigzag GNRs shows periodically repeating protruded edge step segments (with a length of less than 9.776 Å), the system undergoes a transition from the non-magnetic semiconducting state through the metallic regime and eventually to a magnetic semiconducting state as the step-to-step distance gradually increases.[288]

Recently, it was shown that square-shaped carbon tetragons, connecting asymmetrically the two segments of zigzag GNRs, can serve as spin switches changing the orientation of magnetic moments at the two edges (see Fig. 41);[289] the switching process was predicted to occur for a large variety of acene dimer configurations, representing the narrowest zigzag GNRs. Moreover, such spin switches can lift the spin degeneracy, eventually providing to tune the magnetic ground state of the system by charge doping, stabilizing a half-metallic and FM behavior.[289]

Vacancies and divacancies are considered as point defects modifying the ground magnetic state of zigzag GNRs. It is believed that if a vacancy is introduced into zigzag GNRs, it reconstructs and then interacts with the edge states. The structural local reconstruction of the lattice and, hence, emerging spin polarization of the orbitals at the close proximity of the defect are responsible for evolution of net magnetic moments. As a result, the AFM ground state is altered with establishment of the FIM state.[267] The effect of the vacancy defect on the electronic and magnetic properties of zigzag GNRs can be fine-tuned by its symmetry, size, and position within the lattice with respect to the edges.[290]

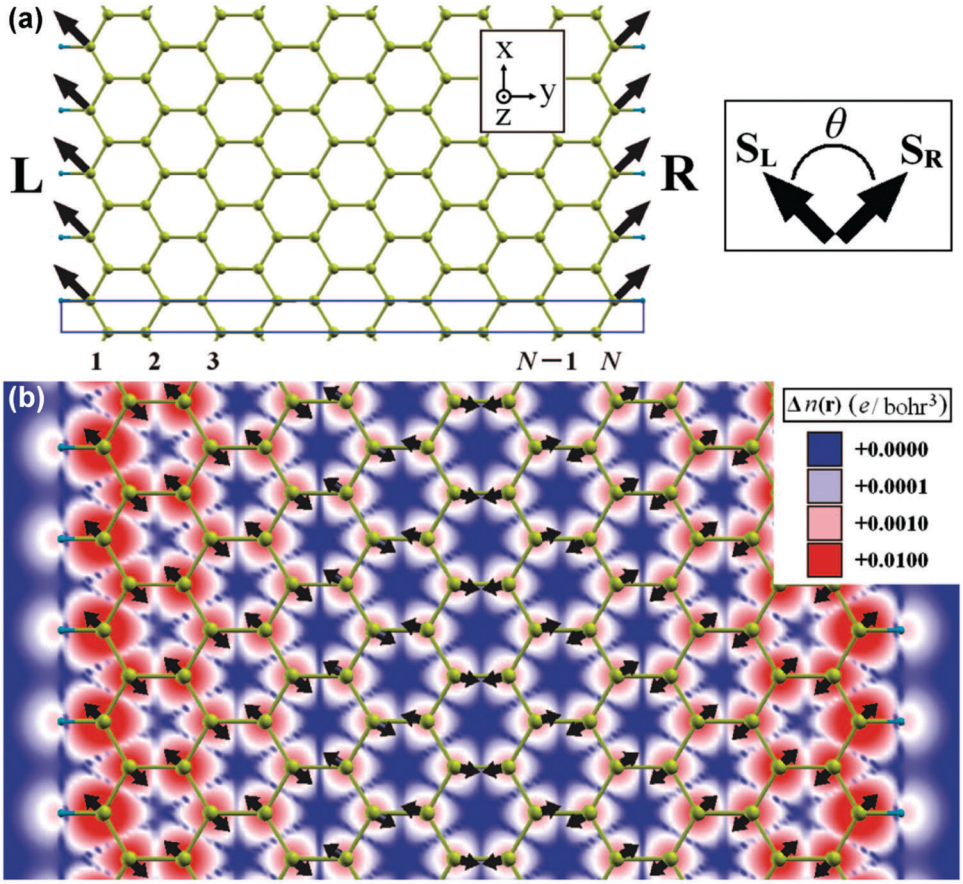

Fig. 40 (a) Schematic representation of a GNR with yellow and light blue balls corresponding to C and H atoms, respectively. The blue rectangle stands for the unit cell and N is the ribbon's width. The black arrows represent the orientation of the magnetic moments at the left (S_L) and right (S_R) edge and θ denotes the relative angle between S_L and S_R. (b) Spatial distribution of the spin density in the canted magnetic state for $\theta = 90^\circ$ and doping concentration $x = 0.16$ e nm^{-1}. The black arrows denote the calculated directions of the magnetic moments of the respective carbon atoms. Reprinted with permission from ref. 283. Copyright 2009 American Chemical Society.

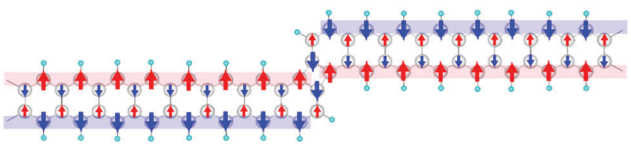

Fig. 41 Scheme of the spin configuration for different zigzag GNRs connected with a carbon tetragon as a spin switch. Reprinted with permission from ref. 289. Copyright 2016 American Physical Society.

A transition from the AFM to the FM ground state was observed if the line defects of 558-type (*i.e.*, two pentagons and one octagon) were introduced into zigzag GNRs (see Fig. 42) and exposed to strain or doped with nitrogen and boron.[291] In the case when no strain is applied or zigzag GNRs with the array of 558-type defects are not doped, opposite sides are coupled antiferromagnetically (see Fig. 42) as there is no moment at the C_I and C_{II} positions and the spins linked with them are in an antiparallel arrangement. FM coupling appears in the case of application of uniaxial tension or doping of nitrogen, boron, aluminum, or phosphorous (with a number of valence electrons different from carbon by one); the C_I and C_{II} positions become magnetically active and mediate FM interactions across the GNR.[291] Lately, it was proposed that without strain, 558-type line defects form near the zigzag edges.[292] If the defects move from the interior of the GNR to its edge, the system gradually undergoes a transition from the AFM conducting through AFM half-metallic to FM metallic state. Upon an increase in strain, the band gaps of AFM semiconducting GNRs are reduced gradually becoming AFM half-metals. A further increase in strain forces GNRs to adopt FM metallic behavior. The threshold values of strain for these transitions decrease upon movement of the 558-type line defect to the edge. Moreover, the occurrence of magnetic transitions is found to heavily depend on the nanoribbon's width.[292] More importantly, if the 558-type line defect sits at one edge, the defective zigzag GNRs are supposed to show a long-range magnetic ordering at edges with a high Curie temperature of up to 276 K.[293] Doping with nitrogen and boron at the particular sites of the 558-type defect can tune the magnetic response of defective zigzag GNRs.[294] If A and B sites are doped (see Fig. 43),[294] AFM spin alignment is preferred while non-magnetic states emerge for other doped sites. The exception involves doping the D site with boron favoring the FM state across the GNR. More importantly, if carbon atoms are replaced by nitrogen and boron at the A site,

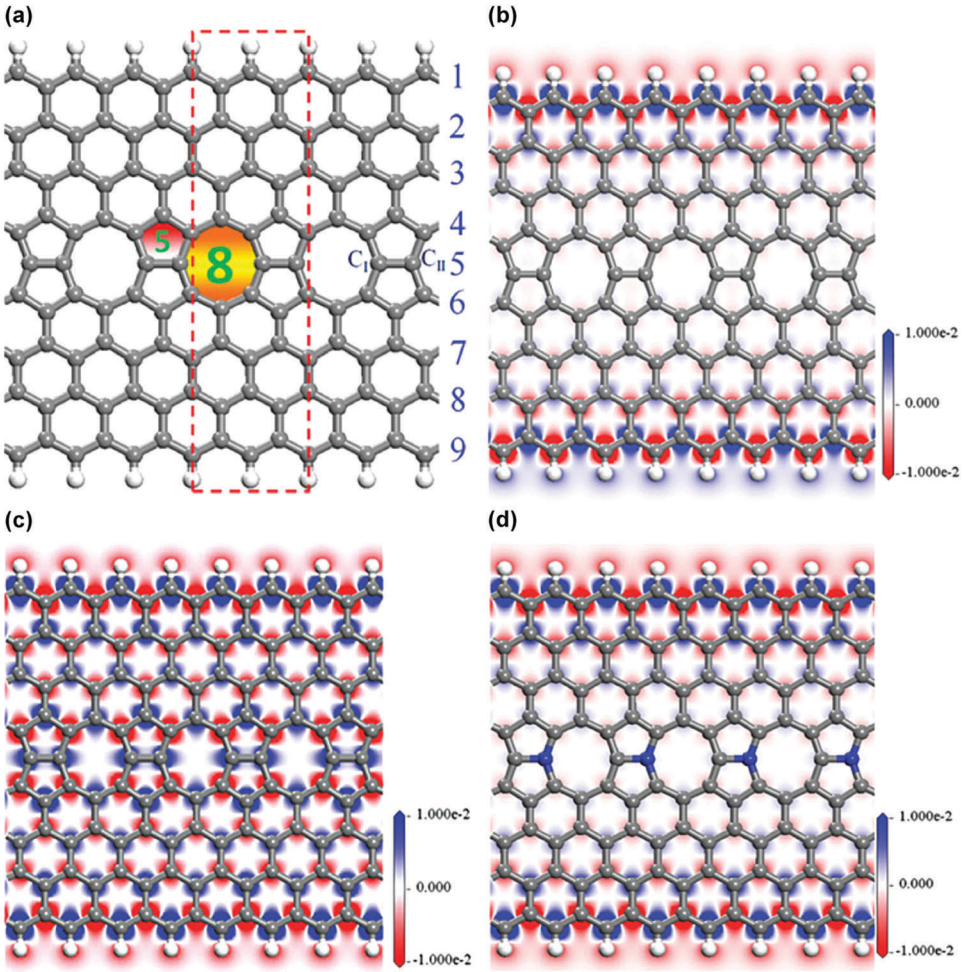

Fig. 42 (a) Scheme of the structure of a zigzag GNR with the 558-defect in its lattice with the C_I and C_{II} positions indicated. (b) Spin-density plot of the zigzag GNR with the 558-defect. (c) Spin-density plot of the zigzag GNR with the 558-defect when exposed to a uniaxial tension. (d) Spin-density plot of the zigzag GNR with the 558-defect doped with nitrogen at the C_{II} position. Reprinted with permission from ref. 291. Copyright 2012 American Physical Society.

half-metallicity appears. For boron doping the B and D sites of defective GNRs, the system becomes a spin-gapless semiconductor upon applying a transverse electric field. The eminent spin filtering capacity of suitably doped defective zigzag GNRs was then explained in terms of breaking the symmetry of the transmission channel.[294]

A pair made of a pentagon and a heptagon ring, periodically repeating along the nanoribbon's length, was recently considered as another line defect in zigzag GNRs.[295] The 5-7 line defect separates the GNR into two non-defective regions (*i.e.*, upper and lower parts) terminated with the zigzag edges. If the 5-7 line defect is positioned close to one edge of the GNR, the system behaves as a ferromagnet with a metallic character and non-degenerate spin state. The electronic features can be changed by varying the nanoribbon's width or the position of the 5-7 line defect within the lattice of the zigzag GNR. Once the symmetry about the 5-7 line defect is removed, the degeneracy in the spin-up and spin-down states vanishes. A transition from an AFM semi-metal to an AFM semi-metal semiconducting state occurs upon changing the position of the 5-7 line defect within the nanoribbon's structure towards its edge. The degeneracy of spin-up and spin-down states of zigzag GNRs with the 5-7 line defect can be lifted by doping with boron and nitrogen atoms, tuning thus the magnetic polarization.[295]

Interesting electric and magnetic features useful for applications were predicted for zigzag GNRs with SW defects.[296] Due to the asymmetry of the SW defects, they are believed to induce finite magnetic moments in the lattice of defective zigzag GNRs. If the defect moved from the position near the edge of the GNR to its interior, the net magnetic moment of defective zigzag GNRs was found to decrease to zero; reduction in the net magnetic moment was accompanied by a transition from the metallic to semi-half-metallic and even to semiconducting state. If an extra defect was placed close to the opposite side of the defective zigzag GNR symmetrically with the firstly introduced defect, the net magnetic moment vanished and the electronic features were found to depend on the distance between the defect and the closer side of the GNR.[296] If the zigzag edges are reconstructed with the SW defects, a new type of edge state is theoretically expected to appear; they show a dispersive character with non-zero amplitudes in both graphene sublattices.[297]

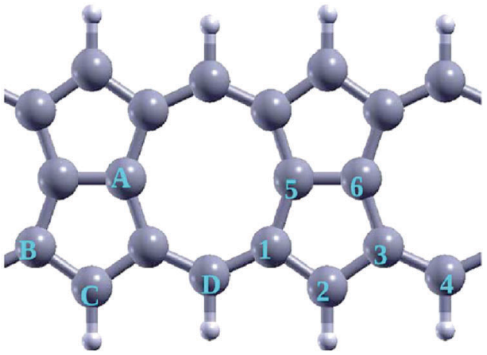

Fig. 43 Structure of defective zigzag GNR with various doping sites denoted as A–D and 1–6. The grey and white balls represent the carbon and hydrogen atoms, respectively. Reprinted with permission from ref. 294. Copyright 2014 The Royal Society of Chemistry.

Moreover, two components were identified in the wave functions amplitudes; they have different decay lengths with the distance from the edge. The decay length for one amplitude component is finite even at the Dirac point while for the other amplitude component, it diverges.[297] In the case of the SW line defect, it was theoretically shown that it sits most favorably near the edge; such defective zigzag GNRs behave as AFM semiconductors with an indirect band gap.[298] If they are exposed to an axis tensile strain, the band gap of AFM semiconducting systems progressively enlarges. Transitions from semiconducting, half-metallic, and metallic states accompanied by an AFM-to-FM passage are expected to occur with shifting of the SW line defect from the center of the nanoribbon to its edge by increasing the tensile strain.[298]

If zigzag GNRs are curved by an angle θ (see Fig. 44), alteration in the ground magnetic state was suggested to happen. For curvatures of $89^\circ \leq \theta < 180^\circ$, the AFM ground state persists.[299] However, if $\theta \leq 88^\circ$, the system is expected to undergo a magnetic transition from the AFM to a non-magnetic state upon increasing the curvature. Upon further bending, the AFM state is finally restored (see Fig. 44). Such a behavior was explained in terms of the overlap of the wave functions localized on the carbon atoms at the curving sites and inter-layered coupling evoked by a large bending of the structure.[299] However, if a divacancy is introduced into the lattice of zigzag GNRs, a distinct transition sequence occurs upon increasing the curvature. In particular, the system is predicted to show AFM, FM, and non-magnetic states if $164^\circ \leq \theta \leq 180^\circ$, $142^\circ \leq \theta \leq 163^\circ$, and $65^\circ \leq \theta \leq 141^\circ$, respectively.[300] In contrast, no change in the magnetic ground state was observed upon twisting zigzag GNRs despite a decrease in the atomic bonding energies and, hence, variation of gaps between the lowest unoccupied and the highest occupied molecular orbitals; AFM coupling between the opposite edges still persists with an appearance of spin flip at some sites at zigzag edges.[301]

Adsorption of hydrogen atoms on the surface of zigzag GNRs was identified to equip them with additional magnetic features.[302] As hydrogen atom is adsorbed, the spin density evolves on the surrounding orbitals; its symmetry and extent of

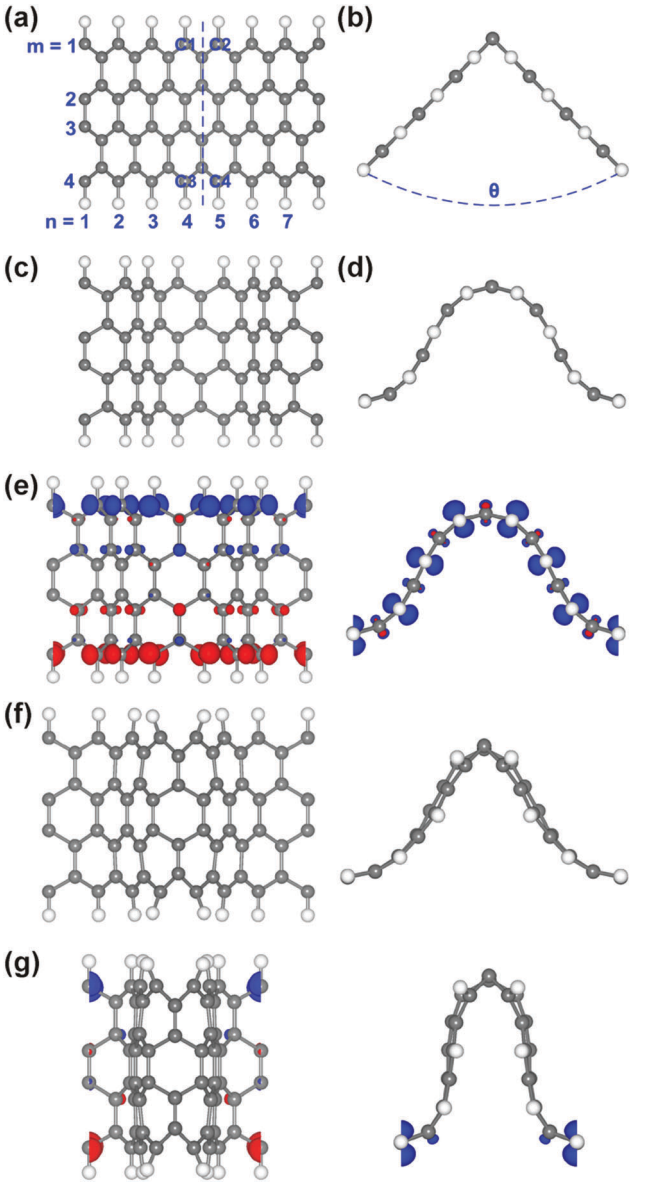

Fig. 44 (a) Top and (b) side views of a bent zigzag GNR. C_1, C_2, C_3, and C_4 denote edge carbon atoms close to the curving site and θ represents the bending angle. (c) Top and (d) side views of the zigzag GNR relaxed after bending by $\theta = 89^\circ$. The top (left) and side (right) views of the spatial spin distribution for the zigzag GNR relaxed after bending by an angle of (e) 89°, (f) 88°, and (g) 52°. Reprinted with permission from ref. 299. Copyright 2012 American Institute of Physics.

localization were predicted to depend on the distance between the site with the adsorbed hydrogen atom and the edge. The interaction among such induced magnetic moments can be of either FM or AFM nature, dictated by the number of adsorbed hydrogen atoms at each graphene sublattice. Moreover, the magnitude of these interactions was found to strongly vary if the position of the adsorbed hydrogen atoms, relative to the edge, was changed.[302]

Hydrogenation, *i.e.*, edge modification with hydrogen atoms, was suggested as another approach to alter the ground magnetic state of zigzag GNRs.[303] If one zigzag edge is saturated with one

hydrogen atom and the opposite edge with two hydrogen atoms, zigzag GNRs become FM semiconductors. In such cases, the difference between the energy of the AFM and FM states varies inversely with the nanoribbon's width.[303] With introduction of a line defect (of 558-type) into the asymmetrically hydrogen-edge terminated zigzag GNRs, they can become spin-polarized metals, metals with a Dirac point, or half-metals depending on the position of the line defect in the nanoribbon's lattice. In particular, half-metallicity is observed when the line defect is positioned far away from the edge. If the line defect then moves to the edge, a behavior resembling that of spin-polarized metals or metals with a Dirac point is observed, regardless of the nanoribbon's width.[304] Alternatively, if doped with p-type or n-type entities, a perfect spin filtering effect may further emerge.[305] Interestingly, with the zigzag edges passivated with H_2, a magnetic-to-non-magnetic transition is observed for a critical value of the nanoribbon's width, which changes with the number of nanoribbon's layers.[273]

Similarly to the case of hydrogenation, equipping the zigzag edges with hydroxyl groups may facilitate transition from AFM to FM coupling between the opposite nanoribbon's sides.[306] If the edges are passivated asymmetrically with hydroxyl groups, different potentials emerge at the two edges, eventually resulting in spin splitting in the bands. If the concentration of –OH groups is higher than 70%, the energy difference between the ground AFM and excited FM states becomes small, providing tuning between AFM semiconducting and FM half-metallic phases upon applying a small external magnetic field. The small energy difference between FM and AFM states for –OH concentrations higher than 70% allows for tuning between AFM semiconducting and FM half-metallic regimes by applying a small magnetic field.[306] Similarly, for asymmetrical adsorption of CO_2 molecules at the two zigzag edges, the FIM state is developed with a lower stabilization energy compared to that of the AFM state and new edge states appearing in the gap of CO_2-edge passivated zigzag GNRs.[307]

The zigzag edges of GNRs can be oxidized by terminating them with various oxygen-containing groups such as hydroxyl, lactone, ketone, and ether.[308] It was theoretically predicted that the oxidized GNRs are more stable compared to hydrogen-terminated GNRs except for ether groups. The stable oxidized GNRs show a spin-polarized ground state with an AFM ordering of opposite edges, similar to fully hydrogenated analogues (see Fig. 45).[308] More strikingly, apart from the edge modification by ketone groups, edge oxidation causes lowering of the critical electric field needed for entering the half-metallicity state. If the external magnetic field is further increased, a drastic decrease in the magnetization is witnessed, eventually vanishing at a certain intensity of the electric field when all the oxidized GNRs become non-magnetic.[308]

Interestingly, the electronic features and nature of the magnetic ground state can be observed in systems composed of joint structures with decorated polydiacetylene (PDA) derivatives deposited on zigzag GNRs with perfect, 57-reconstructed, and partially hydrogen-terminated edge patterns.[309] Zigzag GNRs with hydrogen-terminated edges adopt a half-metallic or

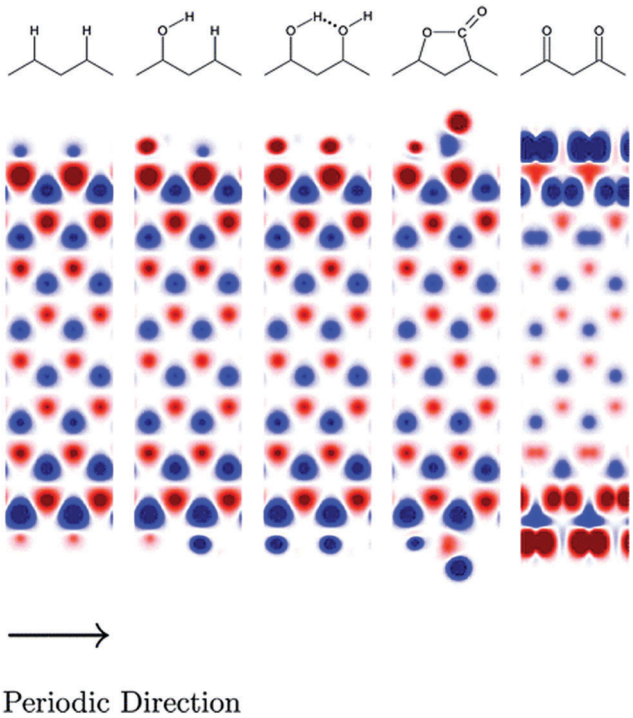

Fig. 45 Ground-state spin densities of the zigzag GNR oxidized by hydroxyl, lactone, ketone, and ether groups including the fully hydrogenated system for comparison. The red color denotes the spin density at the A-sublattice and the blue color stands for the spin density at the B-sublattice of the zigzag GNR. Reprinted with permission from ref. 308. Copyright 2007 American Chemical Society.

metallic behavior once decorated with PDA derivatives with several pairs of acceptor/donor groups (*i.e.*, NO_2/NH_2, F/H, Cl/H, or CN/CH_3) attached. Such systems may undergo transitions between spin-gapless semiconducting, half-metallic, and metallic regimes accompanied by an AFM-to-FM passage upon changing the nanoribbon's width or increasing the number of –C≡C– bonds present in the linking bridge of the NO_2/NH_2 groups bound to the PDA derivatives (see Fig. 46).[309] Similar transitions (*i.e.*, between AFM spin-gapless semiconducting, FM half-metallic, AFM metallic, and non-magnetic metallic states), triggered by the width and number of –C≡C– bonds, were reported for joint systems of the PDA derivatives decorating zigzag GNRs with 57-reconstructed edge patterns. Partial hydrogenation was found to eliminate the effect of edge reconstruction and electronic and magnetic features of the relevant joint structures with zigzag GNRs with perfect edges. The diverse spectra of electronic and magnetic properties of these joint structures are believed to evolve due to a floating dipole–dipole field, induced by the donor/acceptor groups bridging the ladder-structure PDA derivatives with a remarkably delocalized π-conjugated backbone and transferred by π–π interactions.[309]

It is worth mentioning that the type of the intra-edge interaction can be modified if the nanoribbon's zigzag edges are decorated with fluoranthene groups.[310] If a single fluoranthene group (FAG) was attached to a zigzag edge, the two FAG-separated segments were predicted to be correlated in an

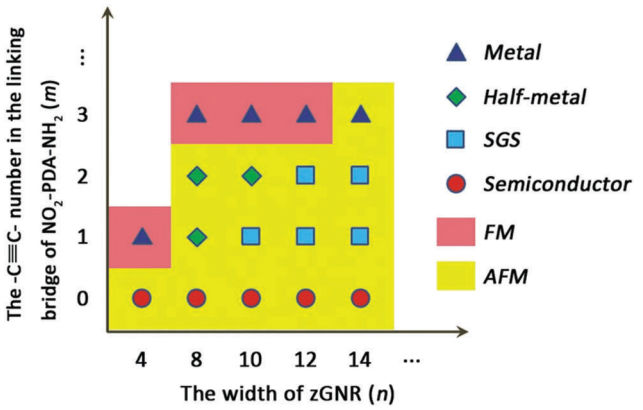

Fig. 46 Influence of the width of zigzag GNRs and the number of $-C\equiv C-$ bonds in the linking bridge on the electronic and magnetic behavior of the n-NO_2–(m)PDA–NH_2 joint systems where n = 4, 8, 10, 12, and 14 and m = 1, 2, and 3. Reprinted with permission from ref. 309. Copyright 2013 WILEY-VCH Verlag GmbH & Co. KGaA.

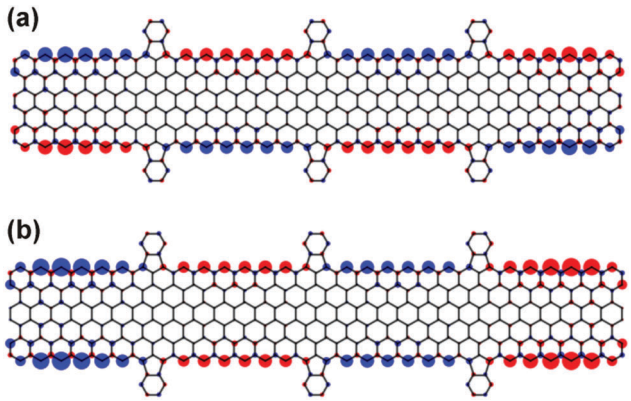

Fig. 47 Calculated profile of magnetization for GNRs with zigzag edges functionalized with several FAGs for (a) ground-state configuration and (b) excited state. Red and blue colors denote the sign of the magnetic moment and the size of the colored ball represents its magnitude. Reprinted with permission from ref. 310. Copyright 2016 American Physical Society.

AFM fashion (see Fig. 47) contrary to the edge-unmodified GNRs in which spins are always ferromagnetically coupled along the zigzag edge. As the introduction of a pentagonal defect breaks down the bipartite nature of the graphene lattice, the relation between the sign of the interaction between the edge spins and the sublattice degree of freedom is no longer valid. In addition, the presence of FAGs can revert AFM inter-edge interactions for sufficiently narrow GNRs. In other words, pentagon defects attached to the zigzag edges of GNRs can be viewed as an agent providing engineering of the spin exchange interactions.[310] Moreover, if only one edge is perturbed with topological defects such as discontinuous patches of pentagons and heptagons, emerging competing magnetic orderings result in spin frustration accompanied by a maximum suppression of magnetic order in the vicinity of these defects at the edge.[311] Thus, the FIM ground state is stabilized due to nonequivalence of the edges. Moreover, depending on the type of localization and spin polarization of the defect-induced edge states, non-uniform energy shifts are predicted to be observed promoted by exchange interactions due to the occupied states of the zigzag GNR localized close to the defect sites. Thus, spatial separation occurs between the states that are localized on the unmodified edge and those sitting at the defect-altered edge.[311] As a result, a complex pattern of occupied and unoccupied frontier bands evolves dictating the magnetic properties of the system. More importantly, the topological defects at the edges can open an energy window for transport of electrons with the minority spin at the edge of the conduction band above a narrow band gap, eventually leading to a half-metallicity feature without the need for involving any non-carbon element.[311]

As radicals and various coupling agents possess unpaired electron(s) and, hence, inherent magnetic moments, functionalizing the zigzag edges with them was suggested as a promising idea to modify the magnetic features of GNRs. The relevance of the proposed concept was theoretically tested for zigzag GNRs with edges terminated with trimethylenemethane (TMM) and 6-oxoverdazyl (OVER) radicals in *syn–syn*, *anti–anti*, and *syn–anti* configurations (see Fig. 48);[312] TMM is an example of a *syn* radical while OVER is classified as an *anti* radical (see Fig. 49). For *syn–syn* and *anti–anti* configurations, the AFM (low-spin) ground state is expected to evolve while for zigzag GNRs terminated with the *syn* radical at one side and the *anti* radical at the opposite side, the FM (high-spin) state is favored with a strong magnetic coupling across the nanoribbon. Furthermore, the spin alternation rule and classification scheme for radicals and couplers were thoroughly described providing identification of such terminating configurations stabilizing the FM ground state.[312]

As edges of GNRs are highly reactive, they can be easily chemically modified under experimental conditions and sample handling. However, such a functionalization of edges may cause suppression or disappearance of their magnetic features. Among several organic compounds considered, C_2H_4 was identified as an ideal terminating group for zigzag GNRs to preserve the edge magnetism.[313] Zigzag GNRs with C_2H_4-terminated edges can be produced under mild experimental conditions with electronic and magnetic properties reproducing those of zigzag GNRs with edges terminated by hydrogen. The enhanced stability of the sp^2 coordinated edges in the C_2H_4-terminated zigzag GNRs was explained in terms of multiple hyper-conjugation interactions. In this context, it was stressed that even a pure sp^2 termination does not need to be a sufficient guarantee for the edge magnetism as, for example, in the case of zigzag edges terminated with C_2H_2, the magnetism is destroyed due to coupling of C_2H_2 terminating groups with the π-electron system of zigzag GNRs.[313] Besides C_2H_4, the pure sp^2 coordinated edge states can be preserved and stabilized by iodine termination.[314] The sp^3 coordination is usually suppressed due to the strong steric effect of iodine atoms.

Similarly to their armchair counterparts, zigzag GNRs can be doped with elements other than boron and nitrogen. The examples include Ni, Ti, and Au atoms.[315–317] In particular, it was proposed that Ni atoms are preferentially located along the zigzag edges; however, their presence quenches the local

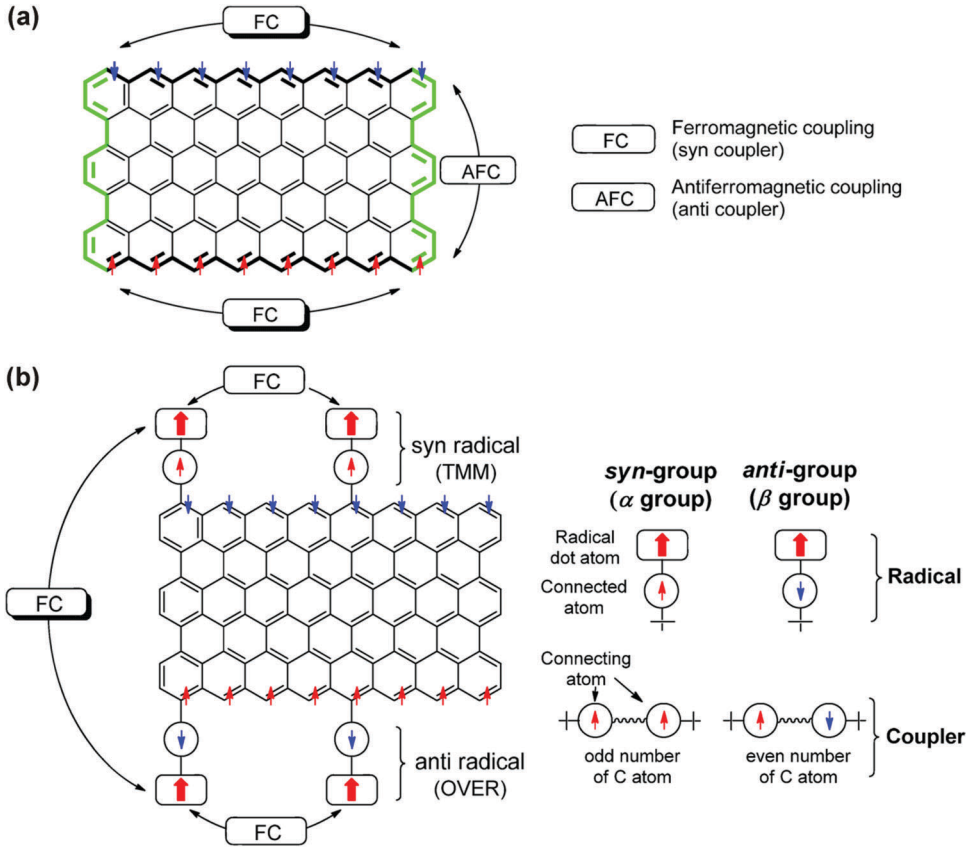

Fig. 48 (a) Scheme showing distribution of spins on each edge of a zigzag GNR (N_z = 8). (b) Scheme showing a ferromagnetically coupled zigzag GNR terminated by a radical and classification of radical couplers into *syn* and *anti* groups. Reprinted with permission from ref. 312. Copyright 2015 American Chemical Society.

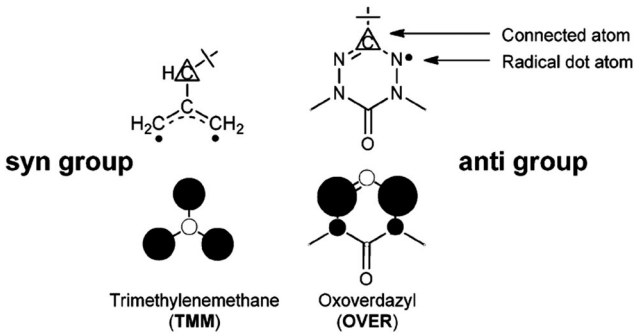

Fig. 49 Structure and spin-density plot of TMM and carbon-connected OVER belonging to the *syn* and *anti* groups, respectively. The hollow and filled circles represent spin-up and spin-down density, respectively. Reprinted with permission from ref. 312. Copyright 2015 American Chemical Society.

magnetic moments of C atoms bound to Ni atoms by a factor of nearly five. The quenching decays fast with distance and is negligible at sites farther than 9 Å from the position of the Ni atom. If Ni atoms are present only at one zigzag edge, AFM coupling between the opposite sides of zigzag GNRs is still preserved. Nevertheless, the adsorbed Ni atoms give rise to d-related states appearing above and below E_F, responsible for spin-dependent transport.[315] A similar effect is observed for Ti atoms which suppress the edge magnetic moments if positioned near the zigzag edge. They are supposed to introduce extra sub-bands showing spin polarization, which neutralizes the magnetic moments of edge carbon atoms.[316] In the case of Au atoms, an FM or AFM ground state was observed depending on the positions of Au atoms in the lattice of zigzag GNRs. The system was found to behave as a spin-gapless semiconductor once Au atoms were placed in the center and edge sites of zigzag GNRs. More importantly, for such a configuration, spin-gapless semiconducting feature is still present irrespective of the nanoribbon's width. Moreover, besides site dependence, the spin-gapless semiconducting behavior was identified to be fine-tuned by impurity atom concentration.[317] Interestingly, the FM ground state can be stabilized by doping zigzag GNRs with planar tetrahedrally coordinated carbon; such defective zigzag GNRs are not only magnetic but are also equipped with metallic features.[318]

Another strategy to alter the magnetic features of zigzag GNRs is to place them on various substrates. Different hybridization between the 2p orbitals of graphene and those of substrates and eventual charge transfer between the surface and zigzag GNR are theoretically predicted to suppress or destroy the edge magnetism. Alternatively, it was suggested that the net magnetization of zigzag GNRs deposited on a substrate is reduced due to inversion of occupied/unoccupied bands (*i.e.*, reordering of edge bands).[319] In this context, it was

found that the edge magnetic states are not affected only in the case of zigzag GNRs with hydrogen-terminated edges deposited on an Au(111) substrate.[320] Another example involves depositing zigzag GNRs on a zigzag hybrid fluorographene–graphane substrate. The spin-up and spin-down band gaps can then be tuned in the opposite direction by varying the fluorographene-to-graphane ratio in the hybrid substrate. If the interlayer spacing is lowered, a transition from half-semiconducting to half-metallic behavior occurs in zigzag GNRs.[321] For electrically polarized substrates like PTO, the AFM ground state is preserved; the ferroelectric substrate polarization causes only a decrease in the local magnetic moments of all the carbon atoms due to substrate-induced charge transfer.[322]

An electric field is often employed as an external stimulus to alter the magnetic features of zigzag GNRs. For zigzag GNRs with antiferromagnetically coupled opposite sides, it was predicted that in-plane homogeneous electric fields applied across the zigzag edges induce half-metallic behavior.[323] Its origin was explained in terms of the effect of the external electric field on energy levels of the edge states shifting them either up or down depending on the orientation of spins at the particular edge. Due to the antiparallel arrangement of spins at the opposite zigzag edges, the external electric field is supposed to move the occupied and unoccupied β-spin states closer together in energy while further separating the occupied and unoccupied α-spin states (see Fig. 48).[323] As the magnitude of the external magnetic field increases, the electrostatic potential is increased on the right side while it is reduced on the left side of the nanoribbon. As a result, right-sided localized edge states show an upward shift in energy while energies for edge states localized at the left side of the nanoribbon are shifted downwards, leaving eventually states with only one spin direction at E_F (see Fig. 50).[323] In other words, the system becomes conductive for one spin direction while remains insulating for another spin orientation.[323] Such a behavior occurs only if a critical electric field is reached; its value is found to decrease as the nanoribbon's width increases since the electrostatic potential difference between the opposite sides is proportional to the size of the system. Moreover, the critical electric field needed to establish a half-metallic or a non-magnetic state can be reduced if edges are functionalized with suitable functional groups in a configuration with an electron donating group at one edge and an electron withdrawing group at the opposite edge (*e.g.*, O–H/C–N, N–O_2/N–H_2, and O–H/N–O_2).[324] As a result, such functionalized zigzag GNRs are equipped with a perfect spin filtering feature if placed in an external electric field.

Moreover, it was suggested that if the electric field is increased, AFM coupling between the opposite edges is reduced as a result of decreased magnetic moments at the edges. This is reflected in the profile of the spin wave dispersion, indicating potentiality to manipulate the spin wave lifetime by the electric field, without inducing magnetic instability in the system.[325]

Despite their similar electronic band structure and magnetic properties, symmetric and asymmetric zigzag GNRs were found to show different transport behavior under an applied bias voltage; the symmetry/asymmetry of zigzag GNRs is inferred

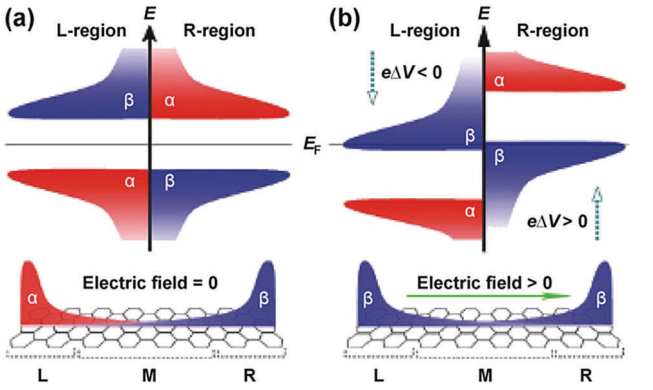

Fig. 50 (a) Diagram of electronic states for zigzag GNRs without application of an external electric field. On the left (L) side, α- and β-spin states represent the occupied and unoccupied localized edge states, respectively, while on the right (R) side, α- and β-spin states represent the unoccupied and occupied localized edge states, respectively. Note that the energy gap is identical at both sides. The bottom plot shows the spatial distribution of spin corresponding to the highest occupied valence band states without application of an external electric field. (b) Diagram of electronic states for GNRs with application of a transverse electric field. With the electric field, the electrostatic potential on the left side of the zigzag GNR is lowered (by $e\Delta V < 0$) while it is increased on the right side of the zigzag GNR (*i.e.*, by $e\Delta V > 0$). The bottom plot shows that only the β-spin states lie at E_F. Reprinted with permission from ref. 323. Copyright 2006 Nature Publishing Group.

from the existence/absence of the mirror plane.[326] While asymmetric zigzag GNRs strictly follow the characteristics of conventional conductors with one conductance quantum under bias voltages, symmetric counterparts show unexpectedly small currents and conductance gap around E_F. The difference in transport properties of asymmetric and symmetric zigzag GNRs was explained in terms of distinct coupling between π and π* sub-bands due to the different nanoribbon's symmetry. Furthermore, the current can be increased for symmetric zigzag GNRs once the symmetry of their electronic structure is broken, *e.g.*, by introducing the asymmetric edge terminations.[326]

Strain is another external parameter providing control over the magnetic response of zigzag GNRs. Recently, it was theoretically shown that if the strain is applied along the zigzag edge, FM behavior can be stabilized and preserved at very high temperatures (~400 K).[327] Enhancement in edge magnetism was explained in terms of reduction of critical Coulomb interaction with increasing strain.[327]

In chiral GNRs, a potential evolution of magnetic behavior was predicted to be dictated by the percentage of carbon atoms at the zigzag edges.[328] If the percentage of carbon atoms with zigzag arrangement equals 50%, chiral GNRs show an AFM semiconducting ground state. In other cases, they behave as spin degenerate semiconductors. The critical chiral angle that guarantees the appearance of spin polarization was theoretically estimated to be 13.9°. The FM state was identified as metastable, the occurrence of which strongly depends on the width of chiral GNRs. Its metastability results from a weaker character of inter-edge FM coupling compared to that of inter-edge AFM interactions.[328] Furthermore, other theoretical data

confirmed that FM interactions among the zigzag segments along nanoribbon's edges become dominant beyond the armchair limit.[329] If the nanoribbon's width increases, AFM inter-edge interactions strongly weaken, leading to correlation lengths comparable with a long-range FM edge response. This is consistent with the appearance of a typical low-energy peak along the nanoribbon's edge, implying formation of enhanced electronic correlations. More specifically, its position in the energy spectrum linearly depends on the interaction strength and chirality angle.[329] In addition, it seems that local magnetization in sufficiently wide chiral GNRs is dominantly governed by chirality with negligible dependence on the nanoribbon's width.[330]

Besides armchair, zigzag, and chiral types, structurally complex GNRs with various heterojunctions were experimentally observed or theoretically predicted. They are commonly classified as hybrid GNRs and are composed of armchair and zigzag segments *via* rotating the cutting direction. They show irregular edge morphologies with a mixture of armchair and zigzag heterojunctions; the most prominent examples include wedge-like zigzag/zigzag (zigzag/armchair),[331] chevron-like armchair/armchair,[332] L-shaped,[333] Y-shaped,[334] Z-shaped,[335] sawtooth-shaped,[336] and cross-shaped[337] junctions. These heterojunctions are believed to affect the carrier scattering and, hence, imprint the electronic and magnetic features onto hybrid GNRs distinct to those of GNRs with ideal armchair or zigzag edges. Their presence in real samples is expected to be unavoidable due to current limitations of traditional production methods including lithographic etching and chemical synthesis.

In general, hybrid GNRs undergo a transition from the non-magnetic to the magnetic semiconducting state by increasing the length of zigzag segments (see Fig. 51).[338] It was theoretically confirmed that introducing the armchair segments as "impurities" will not alter the electronic and magnetic features shown by zigzag GNRs. Although the opposite zigzag edges are coupled in an AFM manner, the magnetization on two edges is not equal. The electronic and magnetic properties of hybrid GNRs were found to be tuned not only by the length of the zigzag segments but also by the nanoribbon's width. More importantly, if placed in an external transverse electric field, a half-metallic behavior was expected to appear for magnetic hybrid GNRs.[338]

For sawtooth zigzag-edged GNRs with edges passivated with hydrogen, an FM ground state was proposed irrespective of their size.[339] They behave as magnetic semiconductors whose spin splitting energy is modulated periodically with the nanoribbon's width. Moreover, such structures may show a dual spin-filtering effect with a 100% spin polarization and high-performance dual spin diode effect. More importantly, if sawtooth zigzag-edged GNRs are placed inside the transverse electric field (see Fig. 52), they become spin conductors with spin carriers that are both spin-polarized in energy space and spatially separated at the two opposite edges of GNRs.[340] In other words, electrons of one spin direction conduct the current at one edge while the holes of the other spin orientation conduct the current at the opposite edge with a different energy. In addition,

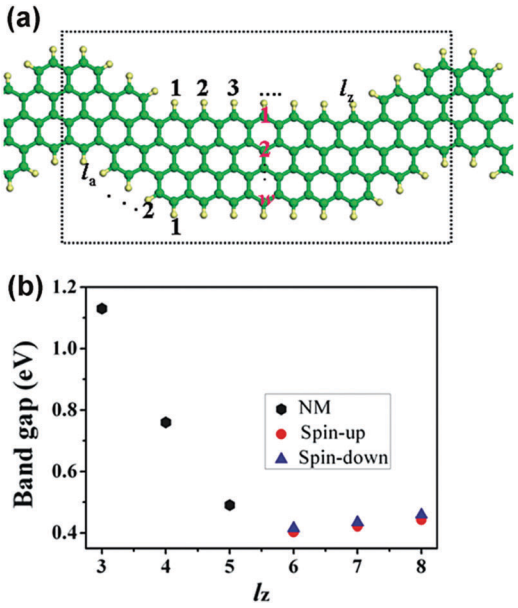

Fig. 51 (a) Structure of hybrid GNRs with a different width (w) and length of armchair (l_a) and zigzag (l_z) segments. Carbon and hydrogen atoms are represented by green and light yellow balls, respectively. One unit supercell in the direction of the nanoribbon's axis is marked with a rectangle. (b) Variation of the band gap on the length of the zigzag segment (l_z). The black dots stand for the band gaps of non-magnetic hybrid GNRs while red dots and blue triangles represent the band gaps of magnetic hybrid GNRs with spin-up and spin-down configurations, respectively. Reprinted with permission from ref. 338. Copyright 2012 American Chemical Society.

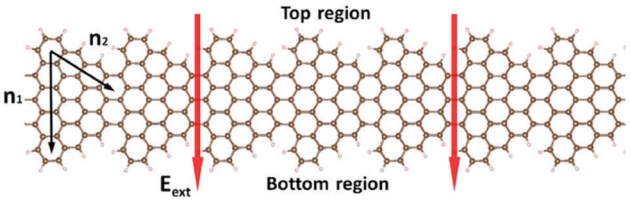

Fig. 52 Structure of a sawtooth zigzag-edged GNR with (n_1, n_2) denoting its size and E_{xt} representing the electric field applied across the sawtooth zigzag-edged GNR. Reprinted with permission from ref. 340. Copyright 2013 American Physical Society.

these states were found to be robust against the edge disorder. Thus, the suggested concept offers another degree of freedom for the manipulation and control of spins in spintronic devices.[340]

Triwing zigzag GNRs consist of three ribbon wings which can be joined together with either sp^2 or sp^3 junctions. The structures with sp^2 hybridized junctions behave as FM metals whose magnetic moments increase with the width of the wing (see Fig. 53a and b).[341] On the other hand, the systems with sp^3 hybridized junctions show features of FIM conductors with a universal magnetic moment equal to 1 μ_B (see Fig. 53c and d). The electric field does not seem to change the metallic behavior of triwing zigzag GNRs with sp^2 hybridized junctions while its application in parallel and perpendicular directions tunes the bands from the *l*-wing or *m*-/*n*-wings, respectively, for the counterparts with sp^3 hybridized junctions. Thus, half-metallicity may

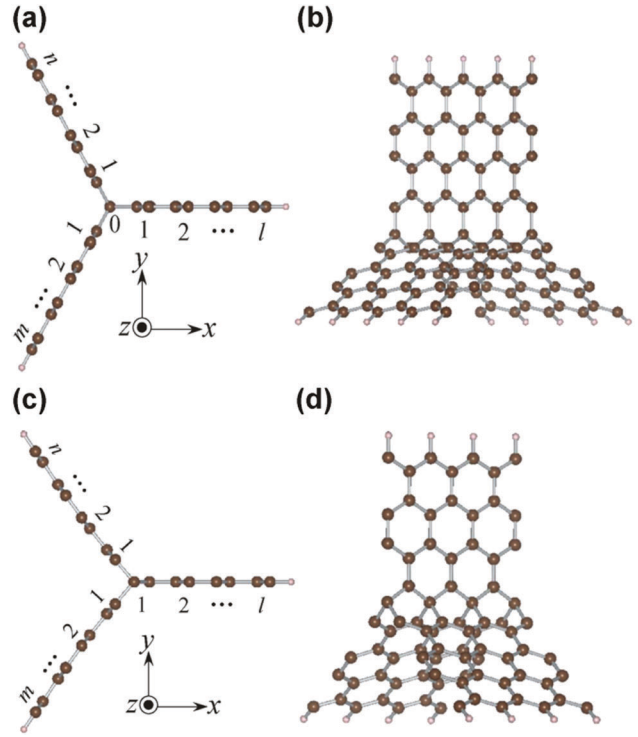

Fig. 53 (a) Top and (b) side views of the geometric structure of a triwing zigzag GNR consisting of three wings joined together *via* a linear carbon array with sp^2 hybridization. (c) Top and (b) side views of the geometric structure of the triwing zigzag GNR composed of three wings joined together *via* their inner edge carbon atoms. Reprinted with permission from ref. 341. Copyright 2012 The Royal Society of Chemistry.

appear for the sp^3-hybridized-junctioned structures.[341] Alternatively, asymmetrical BN doping can induce the half-metallic behavior and suppress the spin polarization of the doped wings.[342]

4.2. Graphene nanoflakes

Graphene nanoflakes (GNFs) are arbitrarily shaped graphene fragments, which are finite in both dimensions; they are sometimes classified as quasi zero-dimensional carbon nanostructures of sp^2 character. They are alternatively termed as graphene nanodisks, graphene nanoplatelets or graphene nanoislands. They are from $\sim$1 to $\sim$50 nm in size and show various regular or irregular shapes. The regularly shaped GNFs resemble the appearance of regular convex polygons such as triangles, squares, rectangles, parallelograms, pentagons, and hexagons. The sides of GNFs consist of purely armchair or zigzag edges or their combinations. Various types of GNFs are schematically shown in Fig. 54.[343] To synthesize them, methods used for the preparation of GNRs are very frequently adopted; most of the synthetic protocols rely on bottom-up approaches starting from molecular carbon-based precursors. However, cutting them to a specific shape is very problematic and needs sophisticated optimization in future procedures. Thus, the magnetic features of GNFs are largely predicted by theoretical studies with very rare confirmations from experimental observations. Theoretically, GNFs are frequently represented by all-benzenoid polycyclic aromatic hydrocarbon molecules.

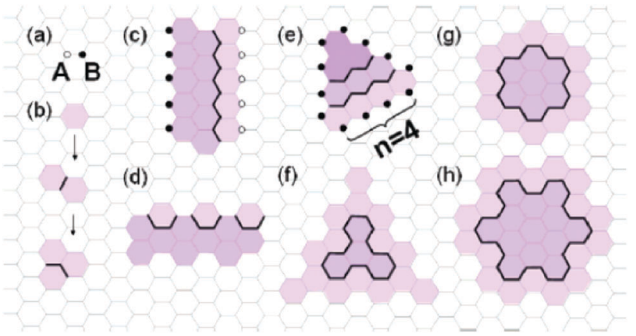

Fig. 54 Various types of GNFs that can be constructed by stitching up (with black lines) from smaller sub-flakes (darker shade): (a) A- and B-sublattice of graphene; (b) GNF formed by stitching up the A–B balanced hexagons; (c) GNF corresponding to zigzag GNR; (d) GNF corresponding to armchair GNR; (e) zigzag-edged triangularly-shaped GNF; (f) armchair-edged triangularly-shaped GNF; (g) zigzag-edged hexagonally-shaped GNF; (h) armchair-edged hexagonally-shaped GNF. Reprinted with permission from ref. 343. Copyright 2008 American Chemical Society.

In this context, a hexagonal fragment can be well described with the model of a coronene molecule whereas a triangular fragment closely resembles the shape of a hypothetical triangulane molecule.

Graphene nanodisks are spatially confined structures with closed edges; they are formed by connecting the benzene rings the number of which defines their size and edge patterns. Typical examples of graphene nanodisks are shown in Fig. 55.[344]

Alike to GNRs, GNFs with zigzag edges show a magnetic ground state as demonstrated by experiments employing the ESR technique.[49] The theory predicts that non-zero net spin exists for triangular GNFs with all the three edges of zigzag nature; the net spin is believed to emerge due to a topological frustration of π-bonds.[243] From a computational viewpoint, GNFs can be constructed by stitching up the sub-flakes as shown in Fig. 54. The stitch is then defined as a single path of bonds merging the two sub-flakes together; an even stitch contains an even number of atoms and *vice versa*. This implies that for an even stitch, the number of A- and B-sites is equal while one extra A- or B-site is present in an odd stitch. Thus, the odd stitch is supposed to create or annihilate one non-bonding state while the number of non-bonding states is not changed for the even stitch. Adopting the proposed counting rule then

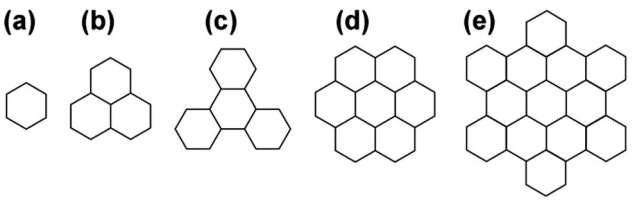

Fig. 55 Various types of graphene nanodisks: (a) benzene; (b) trigonally-shaped zigzag-edged nanodisk (phenalene); (c) trigonally-shaped armchair-edged nanodisk (triphenylene); (d) hexagonally-shaped zigzag-edged nanodisk (coronene); (e) hexagonally-shaped armchair-edged nanodisk (hexabenzocoronene). Reprinted with permission from ref. 344. Copyright 2007 American Physical Society.

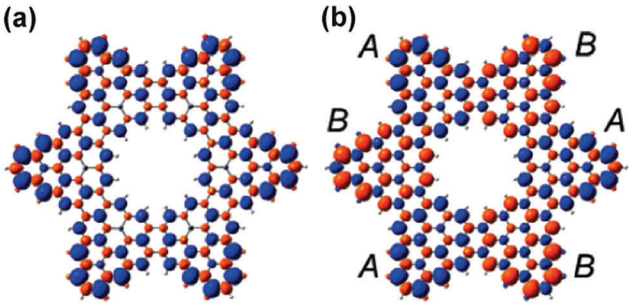

Fig. 56 Two spin configurations of the structure known as the "Star of David" with (a) $S = 3$ and (b) $S = 0$ for an antisymmetric broken-symmetry ground state. Positive and negative spin densities are shown with blue and red, respectively. Regions with dominating A- and B-sublattice are marked with letters A and B. Reprinted with permission from ref. 345. Copyright 2008 American Chemical Society.

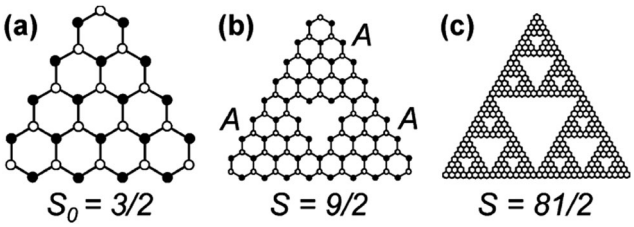

Fig. 57 Suggested Sierpinski sieve fractal structures of GNFs: (a) elementary triangularly-shaped building block; (b) fractal structure with a fractal level of 2; (c) fractal structure with a fractal level of 4. The A- and B-sublattices are denoted with filled and open circles, respectively; the A-sublattice globally dominates. S_0 and S represent the total spin of the fractal structures ($S_q = S_0 3^q$, where q is the fractal level). Reprinted with permission from ref. 345. Copyright 2008 American Chemical Society.

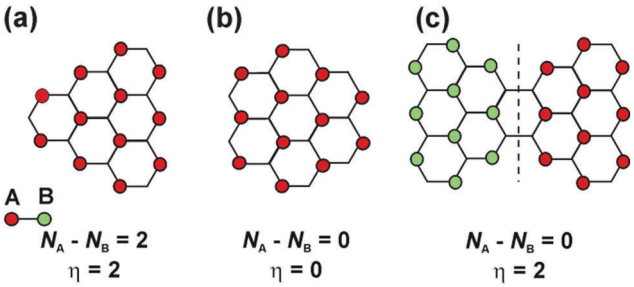

Fig. 58 (a and b) Structures of GNFs belonging to Class I with $\eta = |N_A - N_B|$. (c) Structure of the bowtie-shaped GNF falling into Class II with a zero sublattice imbalance but $\eta = 2$ (*i.e.*, $N_A = N_B = 19$ and $\alpha = 20$). The colored sites conform to a maximum set of non-adjacent sites. Reprinted with permission from ref. 346. Copyright 2009 American Physical Society.

provides constructing GNFs with geometries showing non-zero spin by stitching together hexagonal units with intrinsic zero spin. Moreover, non-bonding states in GNFs and flat edge states in GNRs differ in evolution; non-bonding states originate from singularities of the hopping matrix while flat edge states approach E_F asymptotically due to size effects. As a result, GNRs must have zero spin while GNFs can host a large spin. Non-bonding states are expected to emerge due to topology constraints; they have a half-filled character with a behavior resembling that of the outer shell of an FM atom. In zigzag-edged triangular GNFs, FIM ordering is established between the spins occupying A- and B-sites due to asymmetry in spatial distribution. A "Star of David" structure (see Fig. 56) is another example to accommodate a large spin.[343] It is a fractal that is constructed by repeatedly overlapping two triangles in the opposite direction with the overlap portion removed. The total spin of the "Star of David" structure is found to increase exponentially with the fractal level. The increase in the total spin is related to an increase in the boundary length, which enhances the probability of topological frustrations of π-bonds.[343] However, later calculations for the "Star of David" structure confirmed the existence of broken-symmetry configurations, eventually leading to AFM correlations of locally spin-polarized regions and zero net spin. Thus, other fractal structures – with a spin-polarized triangular fragment as a building unit – were proposed to host the large spin (see Fig. 57); they can be drafted adopting the Sierpinski sieve construction.[345]

Based on their magnetic behavior, GNFs are classified into two main categories, *i.e.*, finite structures with a large net spin and systems with AFM coupling between groups with an electron spin (see Fig. 58).[346] To classify them, a criterion of topological frustration is followed. The topological frustration emerges once all the p_z orbitals cannot be simultaneously paired in a given structure. GNFs with one sublattice showing topological frustration are grouped into Class I. For such structures, $\beta = \min\{N_A, N_B\}$, where β is the maximum number of non-adjacent edges and N_A and N_B are the number of carbon atoms on the A- and B-sublattice, respectively.[346] The number of zero-energy eigenstates, termed as nullity (*i.e.*, $\eta = \alpha - \beta$, where α is the maximum number of non-adjacent vertices), is given as $\eta = |N_A - N_B|$. In other words, if the sublattices are balanced, *i.e.*, $N_A = N_B$, η is zero. All highly symmetric forms of GNFs fall into Class I. Class II includes GNFs with both sublattices topologically frustrated. For such structures, $\beta \leq \min\{N_A, N_B\}$, implying that $\eta > |N_A - N_B|$.[346] The nullity is finite even for GNFs showing balanced sublattices. Further considering the Lieb's theorem, the total spin of the magnetic ground state of GNFs in Class I and II is given as $S = \eta/2$ and $S < \eta/2$, respectively. In other words, all spins in singly occupied orbitals are aligned in a parallel manner for structures belonging to Class I while AFM ordering is expected for structures of Class II.[346] Here, it should be stressed that except for the topological frustration, AFM coupling can arise from polarization of the low-energy states which approach E_F upon increasing the size of the system. Such an effect cannot cause evolution of the net spin; the energy of the non-interacting eigenstates is not E_F (with an exception for infinite systems) and the magnetic ordering develops only in the case where the interaction energy exceeds a positive threshold value, *i.e.*, when a critical size of a system is reached as valid for GNRs or hexagonal GNFs.[346]

For triangularly-shaped GNFs with zigzag edges (see Fig. 59a),[91] the total spin is always non-zero for all sizes; such systems are described as metallic ferromagnets. The states with zero energy are localized on one sublattice (*i.e.*, A-sublattice) and the magnetic ground state has a finite spin given as

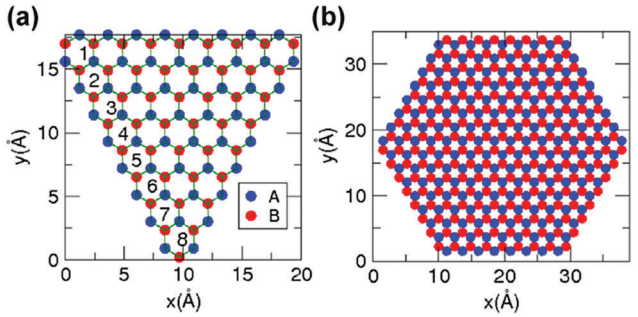

Fig. 59 Structure of (a) triangularly-shaped and (b) hexagonally-shaped GNFs. Reprinted with permission from ref. 91. Copyright 2007 American Physical Society.

$S = (N_A - N_B)/2$ for interactions included. In other words, zigzag triangular GNFs have an excess of unpaired electrons on one sublattice the number of which increases as the nanoflake's size increases. Thus, an FM ground state is expected as all the three zigzag edges are coupled in an FM manner.[347] Note that all the carbon atoms are spin-polarized. On the other hand, GNFs with a hexagonal shape and zigzag edges (see Fig. 59b) show $S = 0$, implying a potential AFM ground state.[91] For smaller hexagonally-shaped GNFs, hybridization is strong, thus avoiding evolution of magnetic ordering. However, if a critical size of hexagonal GNF is exceeded, exchange interactions become strong enough to magnetize the edges. Thus, local magnetic moments emerge above the critical size which was predicted to be equal to 1.5 nm. In other words, below a size of 1.5 nm, hexagonal GNFs behave as paramagnets while they become ferrimagnets if their size is larger than 1.5 nm.[91]

GNFs with zigzag edges can be classified whether they show lattice imbalance (*i.e.*, $N_A \neq N_B$) or not (*i.e.*, $N_A = N_B$).[348] In particular, triangularly- and pentagonally-shaped GNFs belong to the $N_A \neq N_B$ group, while rhombohedrally- and hexagonally-shaped GNFs fall into the $N_A = N_B$ class (see Fig. 60).[348] GNFs with sublattice imbalance can be non-magnetic or exhibit a fully compensated magnetic ordering satisfying $S = 0$. Such GNFs may undergo a quantum transition upon a change in their size. Actually, if the size of the sublattice-balanced GNFs exceeds a threshold value, a transition to a magnetic state occurs; the new structure shows attributes of FIM nature. The critical size, at which the sublattice-balanced GNFs adopt a new magnetic ordering, is dictated by the armchair defect concentration. In order words, uncompensated spins suddenly develop beyond the critical size of GNF.[348] In contrast, sublattice-imbalanced GNFs are always magnetic regardless of their size. In particular, for triangular GNFs, the inter-edge coupling is of FM nature. In pentagonal GNFs, viewed as an integration of triangularly- and hexagonally-shaped finite systems, the commensurate magnetic structure is predicted when identical and different sublattices are coupled in an FM and AFM manner, respectively.[348] Upon doping with charge carriers, a transition from the AFM to FM regime is expected for sublattice-balanced GNFs while for sublattice-imbalanced GNFs, the magnetic response is suppressed, eventually vanishing for high charge carrier concentration.[348]

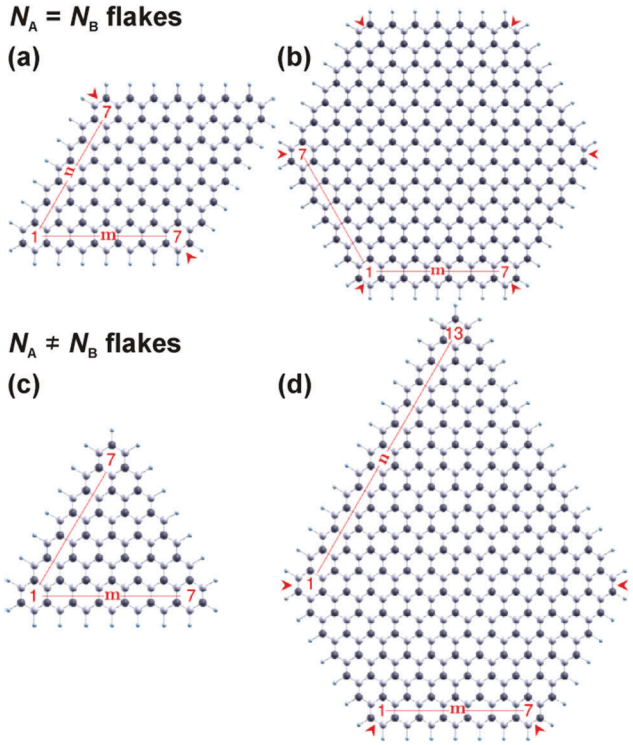

Fig. 60 Structure of (a) rhombohedrally-shaped, (b) hexagonally-shaped, (c) triangularly-shaped, and (d) pentagonally-shaped GNFs. Carbon atoms which belong to the two sublattices are marked with black and white. The nanoflake's size is determined by the number of hexagonal rings along the edge. Armchair defects are highlighted by red arrows and their number is equal to 2, 6, 4, and 0 for rhombohedrally-shaped, hexagonally-shaped, pentagonally-shaped, and triangularly-shaped GNFs, respectively. Reprinted with permission from ref. 348. Copyright 2017 American Physical Society.

Besides changes in magnetic features of both sublattice-balanced and sublattice-imbalanced GNFs, their electronic structure is altered if charge carriers are introduced into their lattice. In particular, initially semiconducting sublattice-balanced GNFs become metallic while in sublattice-imbalanced GNFs, a transition from semiconducting to half-metallic behavior and from semiconducting through half-metallic to metallic regime is predicted to occur for triangular and pentagonal members, respectively. More interestingly, a fully polarized spin transport is expected in the half-metallic state.[348] Similarly, spin-polarized currents were predicted for pure-hydrogenated rectangular GNFs if the electrodes are connected to the nanoflake partially along the zigzag-edge directions or if transition metal adatoms (*e.g.*, vanadium) are introduced over the nanoflake's surface, altering the symmetry in the spin-dependent scattering rates of the transmitted electrons.[349]

Other theoretical works have proposed that due to a different spin polarization at the A- and B-sublattice, zigzag triangular GNFs show a FIM structure as a ground magnetic state.[350] If foreign atoms (such as B, N, O, and F) are introduced into the lattice of zigzag triangular GNFs, they preferentially occupy the sublattice forming the edge. If GNFs are doped with boron and nitrogen, the net magnetic moment is reduced irrespective of

the doping site.[350] In the case of oxygen and fluorine, both an increase and a decrease in the net magnetic moment were observed depending on the doping position.[350] The enhancement/reduction in the magnetic response was explained in terms of different behaviors of the dopants and the interactions between the dopants and the neighboring carbon atoms (especially those sitting on the edge-forming sublattice). A perfect spin filtering effect was proposed for the undoped and boron-doped zigzag triangular GNFs, for which majority states are conducting.[350] In contrast, minority states are conducting for nitrogen-, oxygen-, and fluorine-doped systems, implying that the type of the spin conduction channel can be selected by appropriate doping.[350]

For hexagonal GNFs with zigzag edges, the theoretical calculations identified an AFM structure as a ground magnetic state (see Fig. 61a).[351] If doped with charge carriers (*i.e.*, holes and electrons), the FM state (see Fig. 61b) or mixed phase states are expected to evolve due to the competition between carrier doping (favoring FM coupling) and on-site Coulomb interactions (favoring AFM coupling).[351] In other words, at half-filling, a fully compensated AFM state is expected considering the potential energy gain characteristic of the weak-coupling mechanism. Upon injection of the charge carriers into the hexagonal GNFs, a magnetic state with an uncompensated net magnetic moment is stabilized as a result of effective FM exchange coupling among the ordered spins which is mediated by the introduced charge carriers localized in the proximity of the edges.[352] Alternatively, the encouragement of FM coupling over the AFM ground state can be understood in terms of contribution from indirect charge carrier mediated RKKY interactions once an odd number of charge carriers is doped/removed into/from the nanoflake. Such an alteration in the magnetic coupling involving impurities and their neighbors is, however, predicted to happen only for some geometries of hexagonal GNFs.[353] The magnetic phase diagram then becomes richer once the edges of zigzag hexagonal GNFs are functionalized with hydrogen; AFM, FM, mixed, and non-magnetic phases can appear depending on the level of doping and strength of the on-site Coulomb interaction (see Fig. 62). More importantly, if the temperature is increased, FM solution is more favored for both pure and carrier-doped zigzag hexagonal GNFs,[351] confirming its temperature stability as observed experimentally up to room temperature.[354]

As clearly seen above, hydrogen is viewed as a powerful agent to tune electronic and magnetic features of GNFs.[355] For both hexagonal and triangular GNFs with zigzag edges, increasing content of hydrogen activates a sequential transition from a behavior of a small-gap semiconductor through half-metal to a wide-gap semiconductor. Besides, raising the level of hydrogenation causes the occurrence of a magnetic transition from the FM to the non-magnetic state for triangular GNFs and from the AFM through FM to the non-magnetic state for hexagonal GNFs (see Fig. 63). The non-magnetic behavior for fully hydrogenated GNFs is expected as all the carbon π-bonds become saturated, leaving no unpaired electron.[355] If GNFs of both shapes are half hydrogenated, strong spin polarization arises

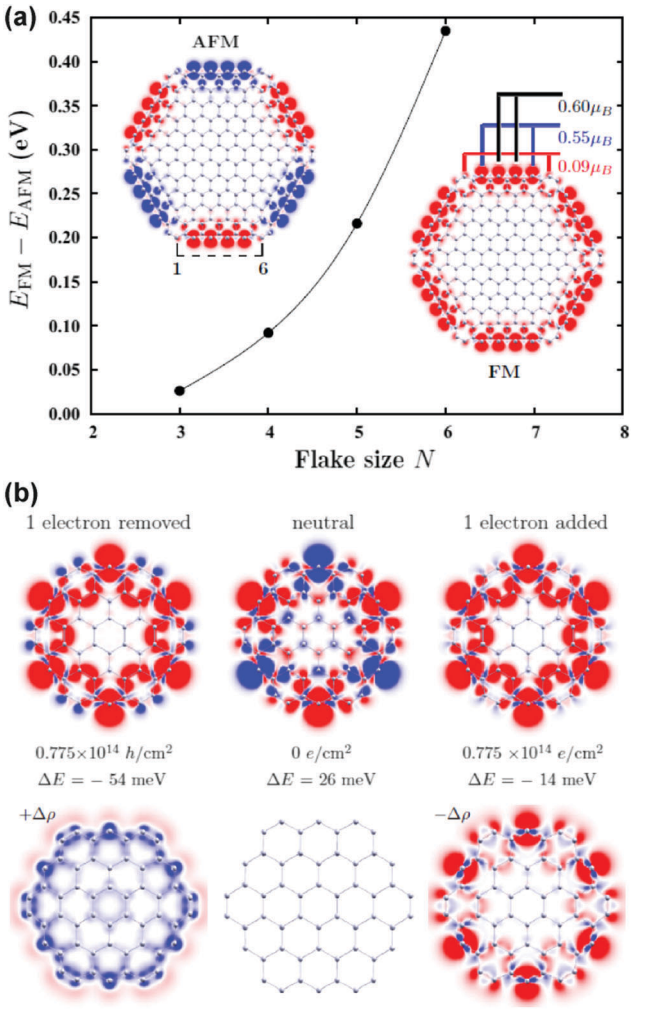

Fig. 61 (a) Evolution of the energy difference between the AFM ground state and the excited FM state upon increasing the size of the hexagonally-shaped zigzag-edged GNF without any charge doping. Red and blue color correspond to the spin-up and spin-down density, respectively. (b) Spin-density plots for the hexagonally-shaped zigzag-edged GNF for cases when one electron is removed (*i.e.*, a hole is introduced; upper left), system is neutral (upper middle), and one electron is doped (upper right). Again, red and blue color indicate spin-up and spin-down density, respectively. The bottom panel displays the difference in charge density between the neutral and charge-doped GNFs. It is worth mentioning that the doped carrier (hole or electron) is distributed only along the edges of the hexagonally-shaped zigzag-edged GNF. Reprinted with permission from ref. 351. Copyright 2014 American Physical Society.

around E_F, manifested by a large net magnetic moment which scales with a power of two with the nanoflake's size. The induced spin magnetizations are found to align parallel, showing a collective character promoted by a long-range magnetic coupling; such GNFs can act as spin filters.[356]

Within the family of nanodisks, trigonal zigzag members were found to show half-filled degenerate zero-energy states, behaving as metallic ferromagnets.[344] The degeneracy can be tuned arbitrarily by changing the nanodisk's size. Moreover, the relaxation time of these systems is quite long at low temperatures, depending on their size.[344]

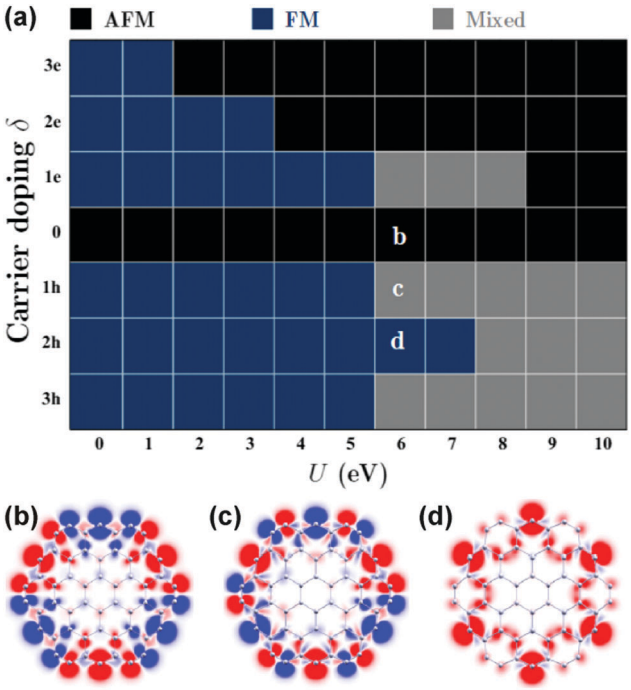

Fig. 62 Magnetic phase diagram as a function of varied on-site Coulomb interaction (U) and charge doping (δ) for a hexagonally-shaped zigzag-edged GNF (with N = 3). Representative spin-density plots for (b) AFM, (c) mixed, and (d) FM configurations (for U = 6 eV). Reprinted with permission from ref. 351. Copyright 2014 American Physical Society.

Bowtie-shaped GNFs (see Fig. 64) are peculiar systems with an immense potential as a molecular switch.[357] Their structure consists of two triangular GNFs with zigzag edges oppositely oriented and connected with a hexagon. Zero-energy states are supposed to evolve; they are spin-polarized due to the Coulomb repulsion between electrons. Bowtie-shaped GNFs show an AFM ground state with S = 0 (*i.e.*, zero net spin) when the direction of the spin of a carbon atom is opposite to that of its nearest neighbors. In the AFM ground state, spin-up and spin-down components are symmetric; the occupied spin-up energy levels are localized in the left triangle while the occupied spin-down energy levels lie in the right triangle of the bowtie-shaped GNF (see Fig. 65).[357] Identically, unoccupied spin-up and spin-down energy levels are found in the left and right triangles of the bowtie-shaped GNF, respectively. In contrast, in the FM state, the spin-up and spin-down energy levels are delocalized and distributed over the whole bowtie-shaped GNF (see Fig. 65). As a result, FM bowtie-shaped GNFs show a perfect spin filtering effect with a much higher conductance contrary to their AFM counterparts.[357] Moreover, if exposed to an external magnetic field, bowtie-shaped GNFs undergo an AFM-to-FM transition, acting as a switch from an OFF to ON state.[357,358] If bowtie-shaped GNF is doped with a single charge carrier, the FIM ground state is favored; in such a case, a sequential transition from the FIM to metamagnetic and, eventually, to the FM state is expected to occur upon an increase in the external magnetic field. The value of the critical transition-inducing field depends on the nanoflake's size; it decreases upon an increase in the size of the system. Moreover, the critical fields are believed to be affected more significantly by an off-diagonal disorder in contrast to a diagonal disorder, resulting in a substantial widening of the critical-field-distribution.[358] Conversely, if the bowtie-shaped GNFs are placed in an external electric field, the AFM ground state is destroyed; the non-magnetic behavior is

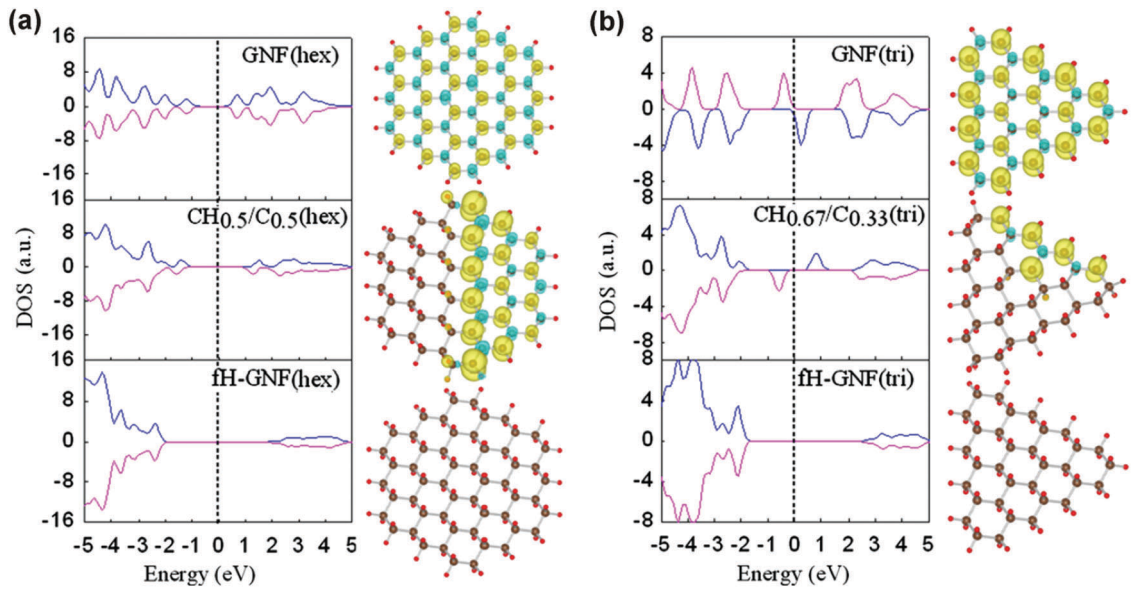

Fig. 63 Spin-polarized density of states and the isosurface of spin-polarized charge density for (a) differently hydrogenated hexagonally-shaped GNFs (*i.e.*, non-hydrogenated, half-hydrogenated ($CH_{0.5}/C_{0.5}$), and fully hydrogenated GNFs) and (b) differently hydrogenated triangularly-shaped zigzag-edged GNFs (*i.e.*, non-hydrogenated, extendedly ($CH_{0.67}/C_{0.33}$), and fully hydrogenated GNFs). H and C atoms are represented by red and brown balls, respectively. Yellow and blue isosurfaces correspond to the values of +0.006 e Å^{-3} and −0.006 e Å^{-3}, respectively. Reprinted with permission from ref. 355. Copyright 2013 Elsevier B.V.

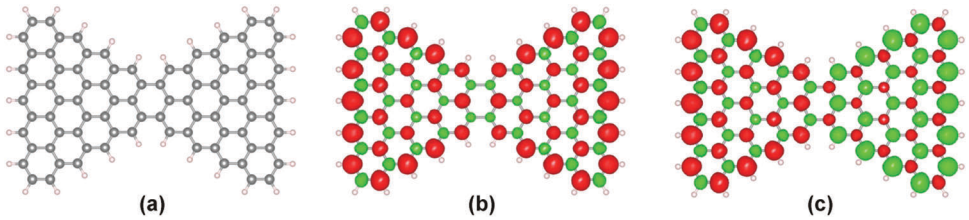

Fig. 64 (a) Structure of a bowtie-shaped GNF. Spin density for (b) FM and (c) AFM bowtie-shaped GNF. Red and green color indicate spin-up and spin-down orientation, respectively. Reprinted with permission from ref. 357. Copyright 2012 American Institute of Physics.

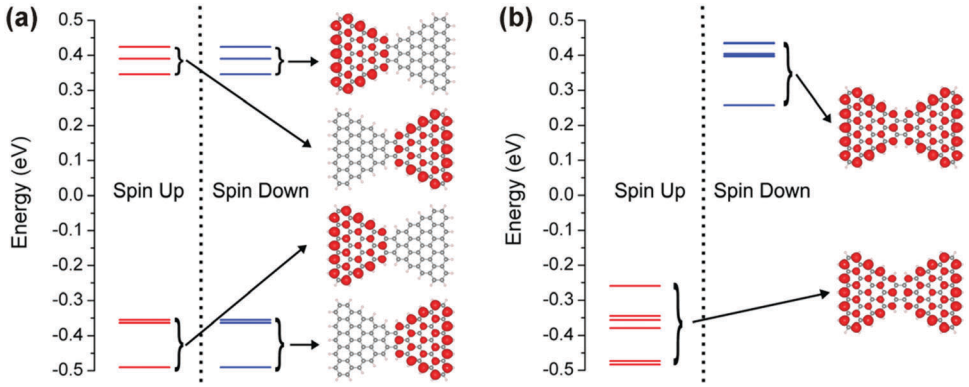

Fig. 65 Energy level spectra for (a) AFM and (b) FM bowtie-shaped GNFs. Reprinted with permission from ref. 357. Copyright 2012 American Institute of Physics.

favored after reaching a critical value of the applied electric field. Surprisingly, upon an increase in the electric field, the FM ground state was not observed at all as for GNRs. The occurrence of the AFM-to-non-magnetic transition was explained in terms of breaking the sublattice symmetry, eventually bringing enough energy to split the originally degenerate zero-energy states.[359] Moreover, the number of zero-energy states can be well controlled by asymmetric connection of the two zigzag-edged triangular GNFs in the bowtie-shaped arrangement; the level of topological frustration, varying the nullity, was found to modulate the strength of AFM coupling between the two zigzag-edged triangular GNFs.[360]

Alternatively, the two zigzag triangular GNFs can be connected together with chains of carbon atoms (see Fig. 66).[361] The two GNFs then interact in an FM manner if the chains are composed of an odd number of carbon atoms. In the case of an even number of carbon atoms, no coupling is established between the two GNFs. Such a behavior can be understood considering the singlet–triplet rule for a chain of carbon atoms, the anti-pattern rule for a magnetic bipartite graphene structure, and the Lieb-Mattis criterion determining the total magnetic moment.[361] Note that the singlet–triplet rule elucidates the ground state of a single hydrogen-terminated chain of carbon atoms; for odd or even number of carbon atoms, the chain shows a triplet or singlet ground state, respectively. Zigzag triangular GNFs can be assembled to form two-dimensional structures when individual GNFs in the network are linked by 1,3,5-benzenetriyl units.[362] Such a two-dimensional system behaves as a ferromagnet; the magnetic moments of the zigzag

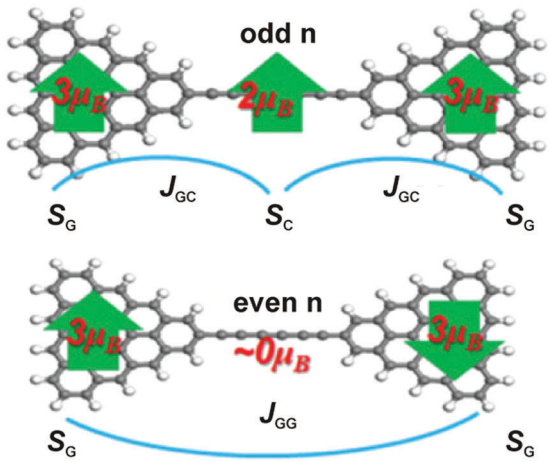

Fig. 66 Schematic representation of the two triangularly-shaped zigzag-edged GNFs connected with an odd and even number (n) of carbon atoms in a linear chain. J_{GC} denotes the exchange integrals characterizing the magnetic interaction between the carbon atom chain and GNFs on opposite sides, J_{GG} is the exchange integral characterizing the magnetic interaction only between the two GNFs on the opposite side of the carbon atom chain, and S_G and S_C are the total magnetic moments of GNFs and the carbon atom chain, respectively. The green arrows indicate the orientation and total magnetic moment carried by each triangularly-shaped zigzag-edged GNF. Reprinted with permission from ref. 361. Copyright 2011 American Physical Society.

triangular GNFs increase with their size. More importantly, if the carbon atoms at the zigzag edges of triangular GNFs are doubly hydrogenated, the strength of the magnetic interaction

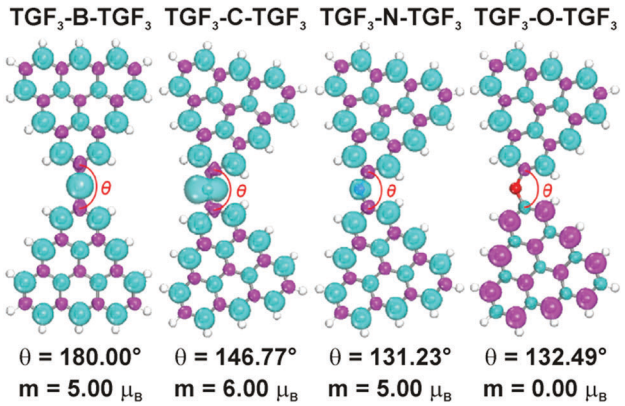

Fig. 67 Spin-density isosurfaces of two zigzag-edged triangular GNFs (with a length N = 3; TGF_3) connected together with B, C, N, and O atoms. θ denotes the angle between the linking atom and its nearest two carbon atoms and m represents the magnetic moment of the structure. The different colors indicate the opposite spin orientations; the magnetic moment was identified to originate mainly from 2p orbitals of the C atoms. Reprinted with permission from ref. 363. Copyright 2012 IOP Publishing Ltd and Deutsche Physikalische Gesellschaft.

among GNFs is enhanced stabilizing the FM state over the whole structure.[362]

Triangular GNFs with zigzag edges were theoretically used as building units to construct two-dimensional superstructures known as magnetic kagome lattices.[363] In particular, C, O, B, and N atoms served as bridging atoms (see Fig. 67). The ground magnetic state of designed kagome lattice was found to strongly depend on the chemical nature of the linking atom and lattice's size. If linked with C, B, and N atoms, zigzag-edged triangular GNFs interacted in an FM manner while an AFM coupling was favored for O as a linking atom. In other words, C, B, and N atoms were identified as mediators of FM coupling, the strength of which can be varied by changing the size of the zigzag-edged triangular GNFs and the bridging atom. Such two-dimensional kagome lattices, semiconducting in nature, were predicted to show a Curie transition temperature above 300 K and could be thus well suited for spintronic applications.[363]

Besides a perfect spin filtering effect and giant magnetoresistance,[364] a magnetoelectric effect is another application-promising phenomenon that was predicted to emerge in GNFs if deposited on a suitable substrate. In particular, it involves induction of magnetization by an electric field and induction of polarization by a magnetic field. To study the magnetoelectric effect, $C_{13}H_9$ as the smallest magnetic GNF was suggested as a model system.[365] The magnetoelectric effect was found to strongly depend on the chemical activity of the substrate affecting the distribution of the electronic states around E_F of GNF by interlayer interactions. In particular, a non-linear magnetoelectric effect observed in GNFs evolved from the interaction with the graphene substrate (see Fig. 68).[365] If an h-BH sheet was inserted between the GNF and graphene support, the magnetoelectric effect showed a linear nature accompanied by an enhancement of its coefficients (see Fig. 69).[365]

Experimentally, the issue of origin of magnetism in GNFs was addressed by the ESR technique; the surface areas of

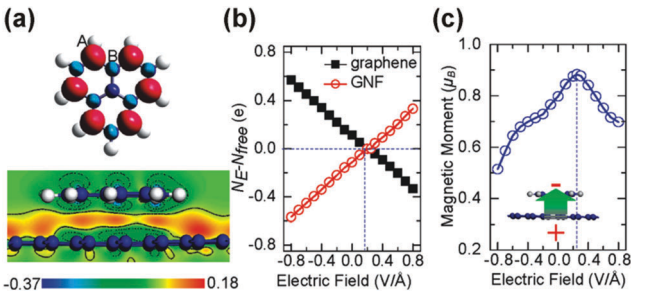

Fig. 68 (a) Spin density of GNF (*i.e.*, $C_{13}H_9$; magenta color for spin-up and light blue color for spin-down orientation) and charge redistribution induced by adsorbing GNF onto graphene (with red and blue colors indicating charge accumulation and depletion regions, respectively). (b) Amount of transferred electrons in the GNF and graphene in dependence on the strength of the electric field. (c) Dependence of the net magnetic moment of the GNF on the strength of the electric field. The inset in panel (c) shows the structure of the GNF lying on the graphene substrate with the bias electric field (green and gray balls marking carbon and hydrogen atoms, respectively). Reprinted with permission from ref. 365. Copyright 2012 American Chemical Society.

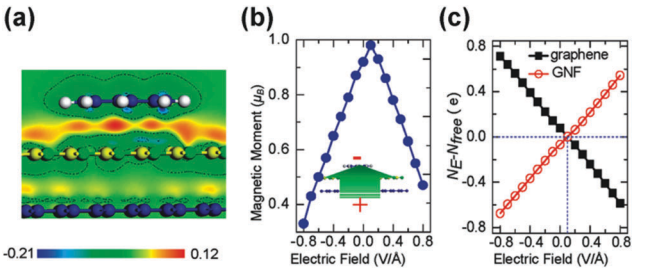

Fig. 69 (a) Charge redistribution induced by adsorbing the GNF (*i.e.*, $C_{13}H_9$) on h-BN-sheet/graphene with red and blue colors indicating charge accumulation and depletion regions, respectively (blue, green, yellow, and gray balls used for representation of carbon, nitrogen, boron, and hydrogen atoms, respectively). (b) Dependence of the net magnetic moment of the GNF on the strength of the electric field with the inset showing the structure of the GNF on the h-BN-sheet/graphene substrate with the bias electric field. (c) Variation in amounts of transferred electrons in the GNF and graphene as a function of the strength of the electric field. Reprinted with permission from ref. 365. Copyright 2012 American Chemical Society.

synthesized GNFs were $\leq 1\ \mu m^2$. The analysis of ESR spectra identified a broad component showing a transition to the FM state at 25 K as demonstrated by changes in the intensity and linewidth of the signal and g-factor. Assisted with DFT calculations considering various extended defects (*e.g.*, sheet edges, zigzag chains of chemisorbed H atoms, pentagon–octagon rows), the magnetic moments were proposed to evolve at C atoms in their vicinities. At low temperatures, FM coupling then develops among the magnetic moments emerging due to the H-saturated C atoms.[49]

4.3. Graphene quantum dots

Graphene quantum dots (GQDs) are finite carbon nanostructures with sizes ranging from 2 to 20 nm; they are classified as 0D carbon nanoallotropes.[5] They are composed largely of sp^2 hybridized carbon atoms, are crystalline and monolayered.

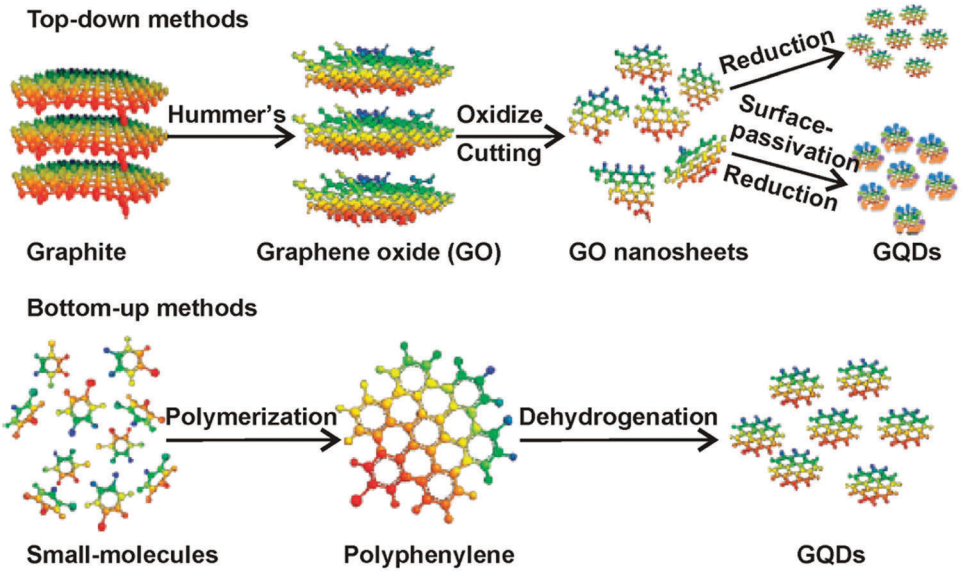

Fig. 70 Top-down and bottom-up procedures for the synthesis of GQDs. Reprinted with permission from ref. 366. Copyright 2012 The Royal Society of Chemistry.

However, in practice, they often consist of a few stacked graphene monolayers due to graphitic nanosheet nature of the precursors. Their physical properties are driven by quantum confinement and edge effects; the most prominent feature includes size- and functionalization-tunable photoluminescence.[5]

Several synthetic methods were developed for preparing GQDs. In general, they fall into two groups, *i.e.*, top-down and bottom-up approaches (see Fig. 70).[366] A general feature of all the top-down methods is to cut graphene sheets into GQDs; they include chemical ablation, electrochemical oxidation, and oxygen plasma treatment. As a starting material to cut, carbon black, coal, graphite, graphite fibers, single-walled and multi-walled carbon nanotubes, graphene or graphene oxide are used. In bottom-up methods, GQDs are assembled from small aromatic molecules.[5]

In many aspects, the magnetic properties of GQDs are identical to those of GNFs. In particular, the ground magnetic state depends strongly on the size, geometry, and symmetry of GQDs.[367] It was theoretically predicted that the magnetic response in GQDs emerges due to electron edge states with energy location within the finite-size quantization pseudo-gap.[368] Two types of edge states, *i.e.*, the zero-energy states and dispersed edge states, then determine the magnetic ground state of GQDs. While zero-energy states are related to the existence of a spin, the presence of dispersed edge states with almost zero energy establishes a diamagnetic behavior. Thus, GQDs (hexagonal, circular, and arbitrarily shaped) which contain mainly dispersed edge states are found to be diamagnetic. The susceptibility of variously shaped GQDs (with sizes from 2 to 7 nm) is shown in Fig. 71.[368] The shaded regions in the plots correspond to the pseudo-gap. The results presented in Fig. 71 match the analytical calculations of previously reported studies for a graphene sheet with a band gap of 2Δ.[226,369] The zero-energy states located at the zero-energy Dirac point are responsible for the Curie paramagnetism and are found in the triangular GQDs. The small triangular GQDs show spin paramagnetism at low temperatures, while orbital magnetism dominates at high temperatures for bigger triangular systems.

Among GQDs with various shapes, those with triangular appearance and zigzag edges have caught significant attention with regard to their magnetic behavior. Zigzag triangular GQDs show an FM ground state; however, its robustness against thermal fluctuations is heavily questioned as it can be destroyed even at low temperatures. Moreover, the FM ground state in triangular GQDs is predicted to be destabilized upon introduction of sufficiently strong disorder. The loss in magnetization is ascribed both to the bulk and edge disorder; while the bulk disorder alters the density of states around the van Hove singularities, the edge disorder affects the energy states in the vicinity of E_F where the edge states appear.[370] Similarly, the FM ground state in zigzag triangular GQDs can be ruined by edge reconstruction.[371] The theory predicts that triangular GQDs with pentagon–heptagon edges (see Fig. 72) are more stable than those with perfect zigzag edges in the absence of hydrogen passivation. If the zigzag edges are passivated with hydrogen, the stability of triangular GQDs significantly increases; they become more energetically favorable than those with reconstructed edges. If the edge reconstruction occurs, the band with zero-energy states still exists; however, the distinction between the two sublattices is smeared out. Moreover, due to a reduction in the symmetry of GQD upon edge reconstruction, the band with zero-energy states shows an increased dispersion. The mixing of the two sublattices then lowers the splitting between the spin-up and spin-down bands. These two effects appearing simultaneously are believed to be responsible for the loss of the net magnetization.[371] In contrast, for triangular GQDs with ideal zigzag edges, the splitting between the spin-up and spin-down energy states is always larger even though the dispersion of the zero-energy band increases with an increase in GQD size.

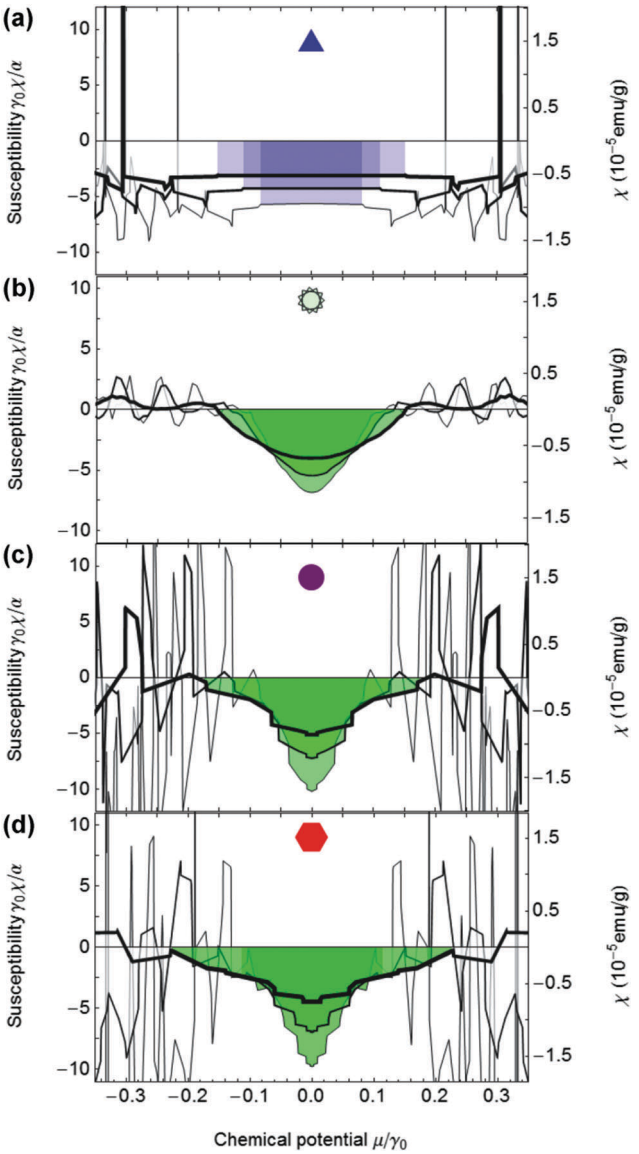

Fig. 71 Susceptibility of 2–7 nm sized GQDs with (a) triangular, (b) random, (c) circular, and (d) hexagonal shape. The pseudo-gap is indicated by the shaded regions. Reprinted with permission from ref. 368. Copyright 2013 American Physical Society.

This implies that magnetism in triangular GQDs with perfect zigzag edges should survive even for infinitely large dot-based systems.[371] Indeed, the magnetism originating from the zigzag edges in GQDs was found to be robust against imperfections such as the presence of other types of edges (regular or irregular) and random terminations. In particular, it was shown that the shape irregularities do not destroy the edge-state magnetism if the zigzag edges in GQDs are longer than three to four repeating units.[372]

On the other hand, if exposed to strain, FM correlations in GQDs with zigzag edges are significantly enhanced.[367,373] The strengthening of FM interactions is predicted to result from altering the nearest-neighbor hopping integrals upon increase in the strain. At the same time, the local magnetic moments in

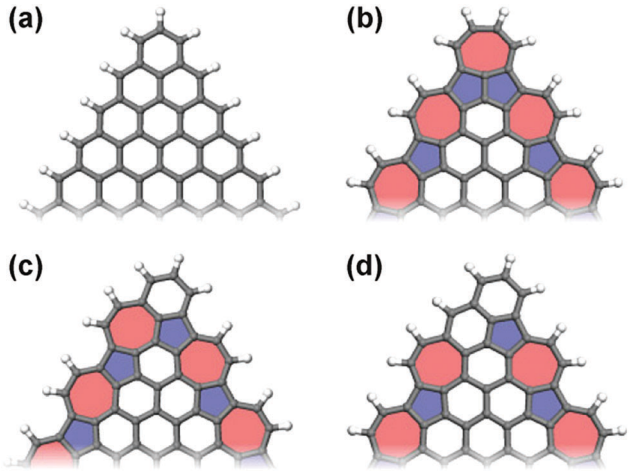

Fig. 72 Triangular GQDs with (a) ideal zigzag edges, (b) reconstructed edges with a pentagon–heptagon–pentagon corner, (c) reconstructed edges with a heptagon–hexagon–pentagon corner, and (d) reconstructed edges with a hexagon–hexagon–pentagon corner. Reprinted with permission from ref. 371. Copyright 2011 American Physical Society.

the ground state are modified and can drift from the zigzag to the armchair edges in the rectangularly-shaped GQDs.[368]

It was theoretically demonstrated that magnetic moments emerging at the zigzag edges of GQDs can be significantly affected by the intrinsic spin–orbit interaction.[374,375] Magnetic anisotropy, driven by spin–orbit coupling, was then found to determine the arrangement of magnetic moments at the edges energetically favoring their in-plane configuration with edge states gapped over the out-of-plane alignment.[374,375]

Similar to GNRs and GNFs, an external electric field can significantly modify the electronic and magnetic structure of GQDs. In particular, zigzag triangular GQDs in a bilayered arrangement are coupled in an FM state in the absence of the external electric field (see Fig. 73).[376] However, if the electric field is applied vertically (see Fig. 73), the FM behavior can be turned off or the total spin of the system can be reduced to a single electron/hole spin. The single electron/hole spin is found to be isolated in a charge neutral structure in an applied electric field, regardless of GQD size and without decoherence due to contacts.[376]

Following the theoretical predictions, the bisanthrene isomer of $C_{28}H_{14}$ molecule was identified as the smallest graphene derivative to show a spin-polarized state.[221] The shape of such a molecule resembles that of rectangular GQDs with spins aligned in an AFM manner at the two zigzag edges. The zigzag edges were found to be spin-polarized for a length of three consecutive units in minimum if the width of the system was 1 nm or wider. If the zigzag edges are 1 nm and longer, AFM ordering persists up to room temperature; for longer systems, spin wave structures were proposed to appear in some high-spin multiplicity states.[221] Upon increasing the length of the zigzag edges, oscillations were observed in the energy gap, however, with a smaller amplitude compared to that found in GNRs with infinitely long edges. More importantly, in an external in-plane electric field, the predicted half-metallic behavior seemed to survive even for finite systems with extremely short edges.[221]

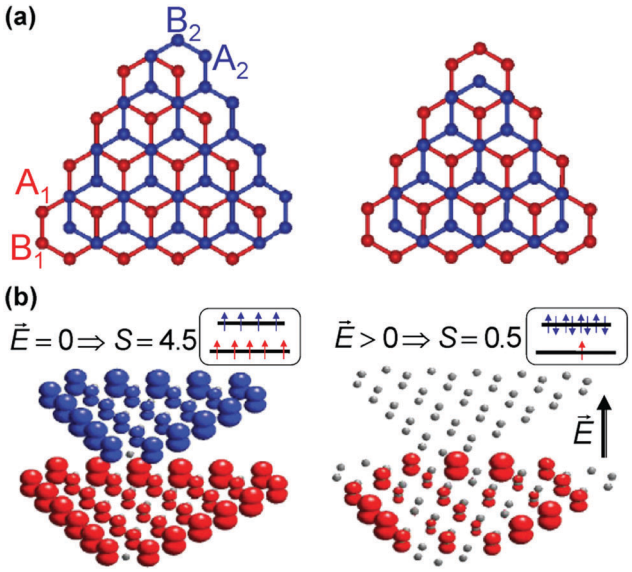

Fig. 73 (a) Structure of bilayered GQDs with zigzag edges and with equal (left) and different (right) sizes. (b) Isosurface plot of the difference in the spin-up and spin-down densities for cases with and without an external magnetic field (E). S denotes the total spin of the system. Reprinted with permission from ref. 376. Copyright 2011 American Physical Society.

Distinct magnetic features were experimentally reported for GQDs or graphene oxide quantum dots depending on their size and surface modification. In particular, GQDs with an average size and height of 4.2 and 6.6 nm, prepared by oxidative cutting of size reduced graphene oxide sheets by UV radiation, were found to show FM behavior even at room temperature (see Fig. 74a).[377] The reduced graphene oxide used for the synthesis of GQDs was diamagnetic at all temperatures down to 10 K, as reported by several other studies.[378,379] The FM response of GQDs was further verified by plotting hysteresis loops as displayed in Fig. 74b. The FM behavior evolving in these GQDs was explained in terms of the presence of defects similar to the case of GNRs, nanographites, and other systems exhibiting defect based magnetism.[250,380,381]

In contrast, graphene oxide quantum dots, synthesized by oxidative cutting, were mostly diamagnetic.[382] Particularly, in three systems with an average dot size of 1.6, 3.3, and 4.1 nm, the ratio of paramagnetic quantum dots increased from 1/70 to 1/15 and to 1/14, respectively, upon an increase in size. Hydroxyl groups were identified as a main source of magnetism in these graphene oxide quantum dots.[382] The suppression of edge state magnetism was explained in terms of a high-degree irregularity of the edge structure or spin cancellation between various magnetic fragments of the boundary. Besides, if the magnetic correlation length is smaller compared to the CQD size, CQD then behaves like a system with a single spin. Alternatively, the edge of such a GQD breaks into smaller fundamental magnetic order units which act more or less independently.[382] Here, it should be stressed that the magnetic correlation length was estimated to be 1 nm at room temperature and more than 100 nm at 2 K.

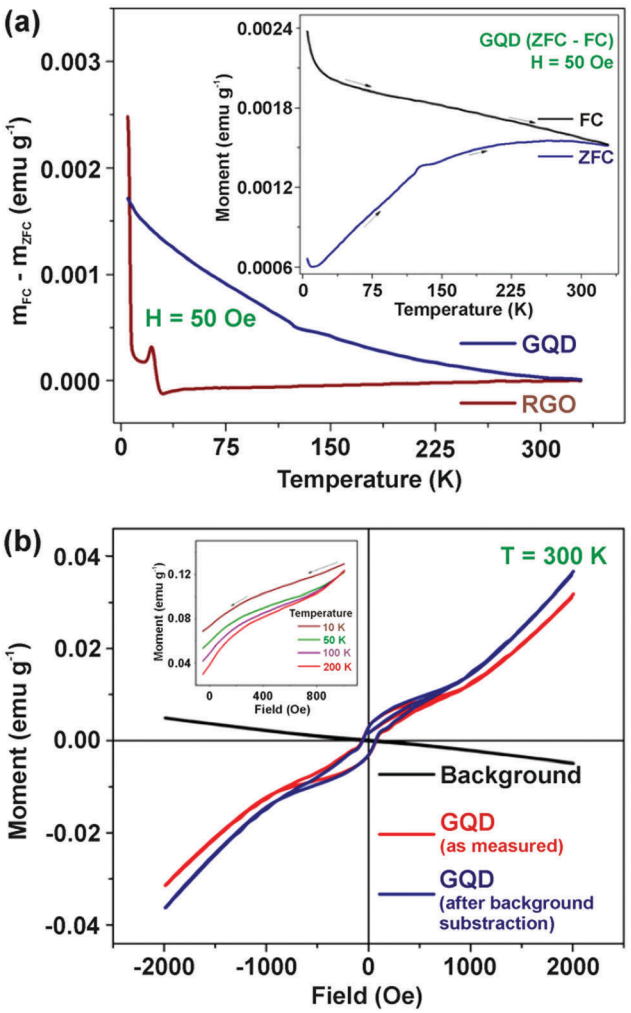

Fig. 74 (a) Comparison of zero-field-cooled (ZFC)/field-cooled (FC) measurements (*i.e.*, $m_{FC} - m_{ZFC}$) of GQDs and reduced graphene (RGO) quantum dots at H = 50 Oe. The inset in panel (a) shows the magnetic moment at various temperatures. (b) Moment *vs.* field measurement of the background and GQDs (with and without background subtraction). The inset shows the profile of the moment *vs.* temperature curve (only the first quadrant) at various temperatures. Reprinted with permission from ref. 377. Copyright 2013 Elsevier Ltd.

FM ordering self-sustainable up to room temperature was observed for very small GQDs (with an average diameter of 2.21 nm) and a composite containing mat-like polyaniline nanofibers and 0.315 wt% of GQDs (see Fig. 75).[383] The increase in the saturation magnetization of the composite (see Fig. 76) was ascribed to the electron transfer from the nitrogen atoms of mat-like polyaniline nanofibers to the encapsulated GQDs.[383]

5. Magnetism in graphene induced by doping with foreign atoms

Creating defects in a lattice is equivalent to disturbing its chemical surrounding. This can be achieved either by changing the nature of bonding or by disturbing the bonds. The most popular approach to generating defects in graphene involves

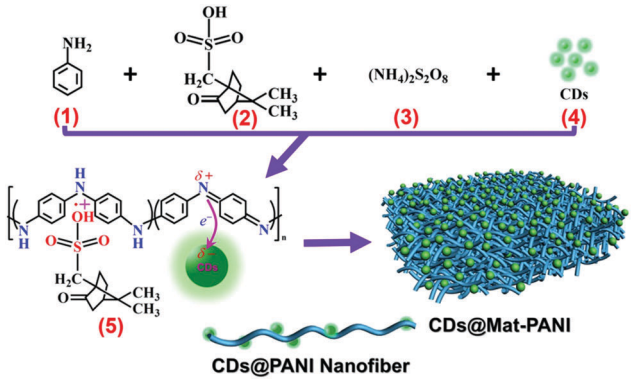

Fig. 75 Synthetic route towards a composite containing graphene quantum dots (CDs) and mat-like polyaniline nanofibers (Mat-PANI). Reprinted with permission from ref. 383. Copyright 2017 Macmillan Publishers Limited.

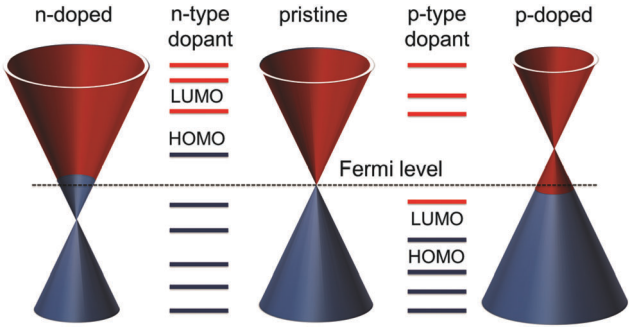

Fig. 77 Schematic showing n- and p-type dopants' Fermi level with respect to that of pristine graphene. Reprinted with permission from ref. 388. Copyright 2015 The Royal Society of Chemistry.

adopting a sequential oxidation and reduction path to produce graphene from graphite. The adsorption of oxygen in the basal plane of graphite during the oxidation of graphite can alter the chemical properties of the graphitic surface. Thus, defects can be easily formed due to the interaction of the carbon atoms with any foreign molecule. This can also be achieved by sintering the material in a suitable atmosphere. Another widely used technique to reduce the van der Waals forces between the layers of graphite involves intercalating a foreign species that could result in the formation of defects.

The carriers in graphene can be selected to be either electrons or holes by controlling the metals or molecules on the surface of graphene. n-Type doping in graphene can be achieved by using n-type dopants such as K, Ti, Fe, Cr atoms or NH_3 molecules.[384–386] Similarly, p-type doping can be realized by dopants such as NO_2 molecules.[387] In either of the cases, the electronic configuration of the system modifies by changing the position of E_F. The position of the highest occupied molecular orbital (HOMO) and the lowest unoccupied molecular orbital (LUMO) of the dopant with respect to the Dirac point in graphene is important in determining the direction of the charge transfer (see Fig. 77).[388] In the process of doping, exchange of electrons occurs between the dopant and graphene. Besides, the electrons may get confined in the orbital if it has a higher energy than E_F of graphene. In addition, redox reactions at the surface of graphene can also cause doping effects in graphene.[389] Doping with suitable dopants can be achieved by irradiating graphene.

Doping of graphene lattice with heteroatoms, such as nitrogen and boron, has been theoretically shown to stimulate n-type and p-type behavior in the case of N- and B-doped graphene, respectively.[390] The Dirac point of graphene was downshifted in N-doped graphene and upshifted in B-doped graphene with respect to E_F (see Fig. 78),[390] inducing a semi-metal-to-metal transition in doped graphene. Importantly, if π-electrons occupy narrow bands at E_F of graphene, Stoner magnetism can emerge.[391]

Indeed, it has been theoretically proposed and experimentally confirmed that depending on the concentration and packing geometry of doping sulfur[50] and nitrogen[51] atoms, it is possible to induce FM order in graphene. Both systems yielded similar transition temperatures to the FM state, 62 and 69 K, respectively, for S- and N-doped graphene (see Fig. 79), with graphitic dopants playing the principal magnetic role, albeit significant amount of pyridinic and chemisorbed nitrogen was identified in N-doped graphene samples. Pyrrolic nitrogen was not detected in N-doped graphene, which has previously been shown to cause

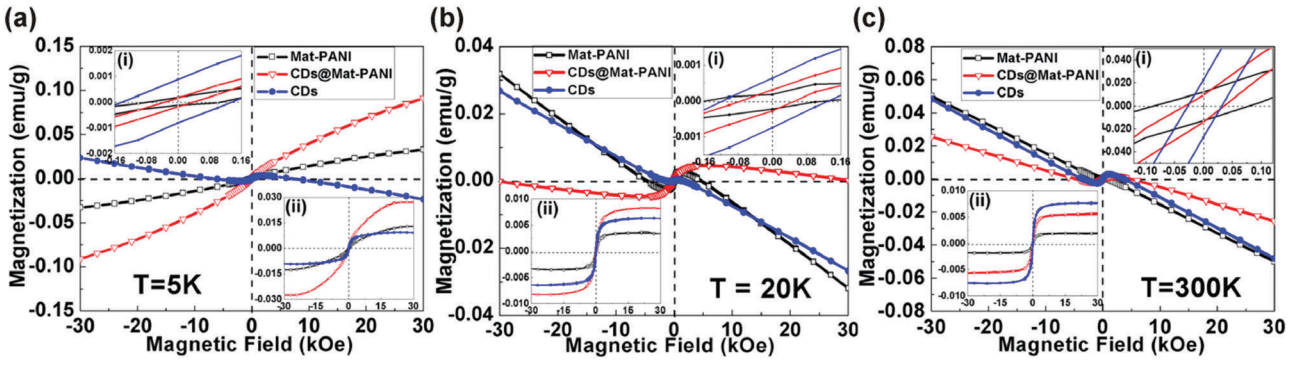

Fig. 76 Hysteresis loops of mat-like polyaniline nanofibers (Mat-PANI), graphene quantum dots (CDs), and a composite consisting of mat-like polyaniline nanofibers and graphene quantum dots recorded at a temperature of (a) 5 K, (b) 20 K, and (c) 300 K. The upper inset in panel (a–c) shows the behavior of the hysteresis loops at low applied magnetic fields. The lower inset in panel (a–c) shows the hysteresis loops after a subtraction of the diamagnetic component. Reprinted with permission from ref. 383. Copyright 2017 Macmillan Publishers Limited.

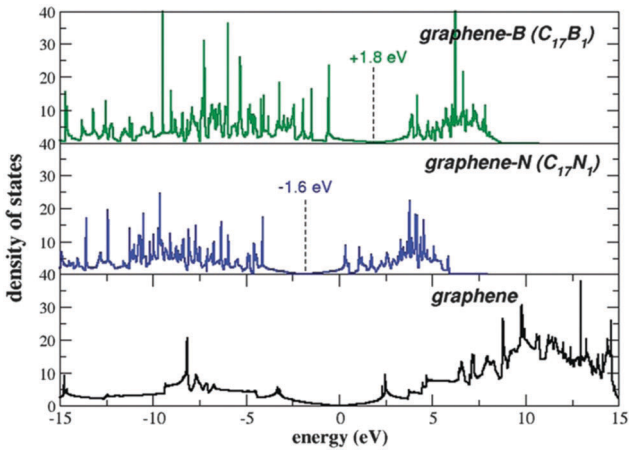

Fig. 78 Theoretical density of states of B- and N-doped graphene. B atoms serve as p-type dopants and N atoms as n-type dopants. Reprinted with permission from ref. 390. Copyright 2014 The Royal Society of Chemistry.

a decrease in magnetization values.[392] However, N-doped graphene with a solely pyrrolic nitrogen configuration at a very high concentration (~11.17 at% of N) was found to stabilize FM ordering up to ~678 K; the Curie temperature of pyrrolic N-doped graphenes was observed to decrease with increasing defect concentration.[393] Similarly, pyrrolic nitrogen at a concentration of 6.02 at% enhanced ferromagnetism in graphene oxide.[394] One shall note that a high oxygen content is regarded as a dominant source of magnetism, overwhelming the effects of nitrogen doping itself, and, moreover, oxygen-containing functional groups drastically reduce the electric conductivity of graphene – the main prerequisite for spintronics. Below 5 at% of nitrogen and ~4 at% of sulfur, graphene behaved dominantly as a diamagnet; although paramagnetic centers were imprinted upon doping, they did not lead to magnetically active configurations. Upon an increase in the doping concentration above these threshold doping values, FM states evolved when the

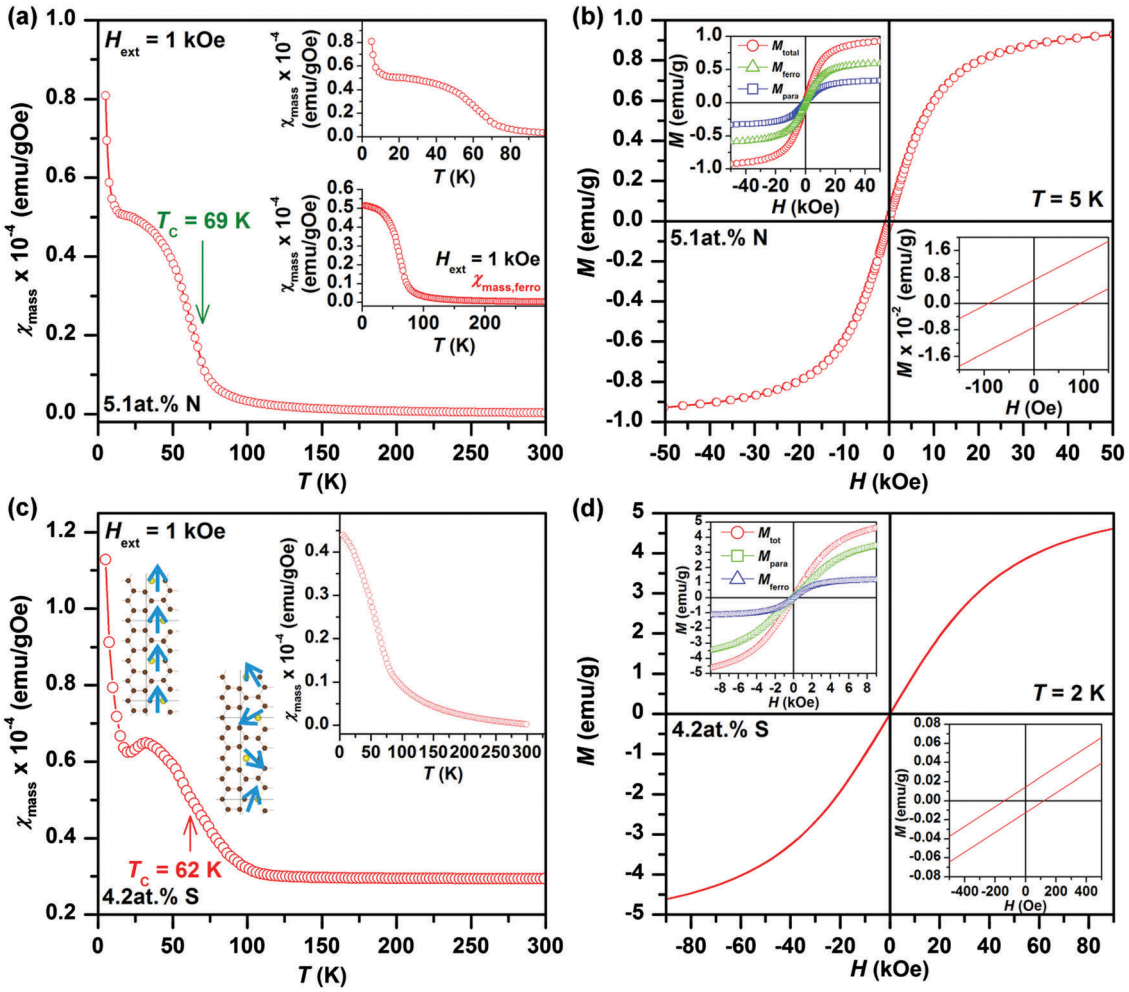

Fig. 79 Temperature evolution of the mass magnetic susceptibility (χ_{mass}) for (a) N- and (c) S-doped graphene at 5.1 at% (N) and 4.2 at% (S) recorded under an external magnetic field of 1 kOe with the Curie temperature (T_C), indicated. The ferromagnetic contributions derived from fitting of the χ_{mass} *vs.* *T* curve are shown in the insets. For N-doped graphene, the trend of χ_{mass} at low temperatures is also shown in the inset. Hysteresis loops of (b) N- and (d) S-doped graphene. The insets show the behavior of the hysteresis loop around the origin with nonzero coercivity and field-dependent profiles of magnetization for the ferromagnetic (M_{ferro}) and paramagnetic (M_{para}) components. Panel (a and b) reprinted with permission from ref. 51. Copyright 2017 American Chemical Society. Panel (c and d) reprinted with permission from ref. 50. Copyright 2016 WILEY-VCH Verlag GmbH & Co. KGaA.

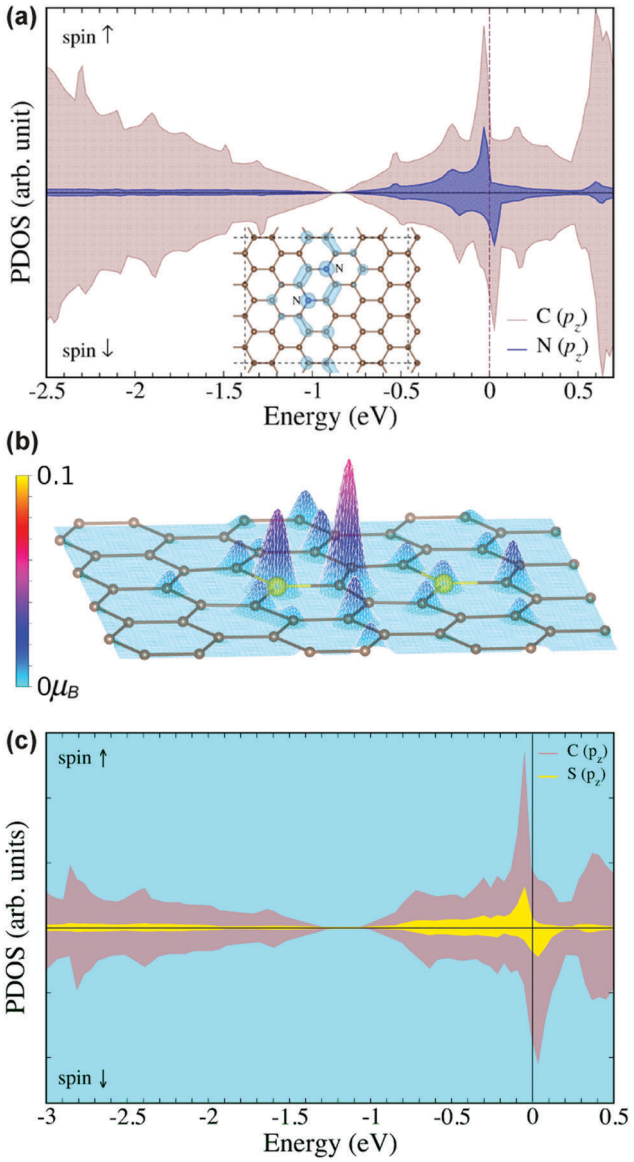

Fig. 80 (a) Theoretical partial densities of states (PDOS) calculated for N-doped graphene at 5.1 at% of N, where nitrogen occupies para positions in graphene. The supercell and an isosurface of spin density are shown in the inset. (b) Magnetic configuration of S-doped graphene at 4.2 at% of S superimposed on a 3D plot of the magnetic moment distribution within the supercell. (c) The corresponding calculated PDOS plot. Panel (a) reprinted with permission from ref. 51. Copyright 2017 American Chemical Society. Panel (b and c) reprinted with permission from ref. 50. Copyright 2016 WILEY-VCH Verlag GmbH & Co. KGaA.

doping-induced paramagnetic centers coupled *via* a π-electron system (see Fig. 80).[50,51] At low temperatures, the observed saturation magnetization reached ~1 emu g^{-1} (N-doped graphene) and ~5.5 emu g^{-1} (S-doped graphene), which is among the highest values ever reported for a graphene-based system in which the magnetism is imprinted either by doping or functionalization or edge modification. It must be noted that both S- and N-doping offer viable magnetic conductive materials with a huge potential in spintronic and other magnetic applications. In contrast, upon doping sulfur into the graphene lattice, a decrease in the saturation magnetization was witnessed accompanied by a change in the nature of magnetic ordering. These observations were explained in terms of saturation of dangling bonds at vacant and edge sites by sulfur atoms and, hence, quenching of local magnetic moments induced by vacancies and edges existing already in undoped graphenes.[395]

Recently, an ultralow energy ion implantation was exploited to incorporate different ion species (B, C, and N) into the graphene lattice. E_F gets reduced or increased due to doping by B or N, respectively,[396] and defects are formed when graphene is bombarded with carbon ions. STM images of graphene with different dopant atom species are shown in Fig. 81.[396] The electronic and magnetic properties can be tuned by selecting the type of dopant and its location in the structure. For example, N or B edge substitutions in armchair GNRs do not show any change in band gap[397] while a semiconductor–metal transition can occur due to N, B, and pyridine-like substitutions.

Besides boron, nitrogen, and sulfur, graphene can be doped with transitions metals. However, as their atomic radii are larger than that of a carbon atom, most of the transition metals are displaced outwards from the plane of graphene. They tend to form transition metal-vacancy complexes (*i.e.*, Au, Cu, V, Cr, Co, and Mn), which are predicted to show an interesting magnetic behavior.[398] For example, if an iron atom is substituted in the place of a single vacancy, it becomes non-magnetic; however, if doped in the site of a double vacancy, it shows a high magnetic moment. Similarly, a non-magnetic behavior is observed for a nickel atom substituting at a single vacancy. In such a case, a magnetic moment can emerge when exposed to a uniaxial strain.[399,400] On the other hand, cobalt atoms behave in a different manner as they give spin polarization, when doped at a single vacancy in graphene (see Fig. 82a). The cobalt atom was found to stabilize a symmetric structure of the carbon vacancy; in the electronic structure of the Co-substituted defect, a single level appears at E_F with a strong contribution stemming from the p_z orbitals of the neighboring carbon atoms, resembling a single vacancy (see Fig. 82b–d). Then, each Co-substituted defect possesses a magnetic moment of 1 μ_B. The total spin value of the system obeys Lieb's theorem. If the Co-substituted defects occupy only one sublattice of graphene, FM coupling is predicted while an AFM interaction is favored once the Co-substituted defects are on the opposite sublattices.[398]

6. Effect of functionalization on magnetic properties of graphene

In general, functionalization of graphene has been countlessly approved as an effective strategy to alter its physicochemical features tuning them appropriately for a given application. It involves modification of the graphene surface in both non-covalent and covalent manner by various adatoms, molecules, functional groups, and adsorbates. Particularly, functionalization leads to tuning of the band gap and hydrophobicity/hydrophilicity of graphene, eliminating its drawbacks in the pristine state. Moreover, it prevents stacking and aggregation of

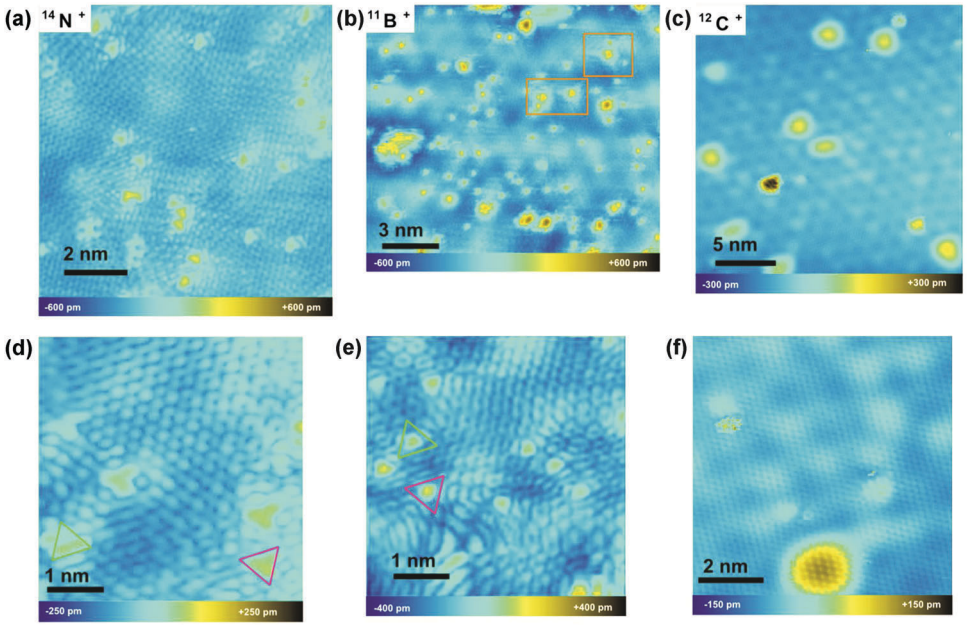

Fig. 81 STM images of graphene with different dopant atom species incorporated by ultralow energy ion implantation: (a) nitrogen-implanted; (b) boron-implanted; (c) carbon-implanted. Defects are seen on a larger scale; zoom of single atoms of (d) nitrogen and (e) boron. Both sublattice orientations were found (red and green triangles); (f) carbon-implanted sample. Reprinted with permission from ref. 396. Copyright 2015 American Chemical Society.

graphene sheets, facilitating its further processing with solvent-assisted techniques. Here, it should be stressed that functionalization with intrinsically magnetic species (*i.e.*, oxides of transition metals) is not discussed as the magnetic properties of such surface-modified graphene systems are solely driven by covalently or non-covalently attached magnetic compounds significantly overshadowing potential magnetic moments induced in graphene by functionalization; the topic of graphene functionalization with iron oxide nanoparticles was, for example, thoroughly covered in the review by Tuček *et al.*[401]

Graphene defects can be due to the presence of carbon adatoms, a consequence, for example, of a knock-on process that removed the atom from its position in the graphene lattice but with the atom still connected in some form to the sheet itself. Carbon adatoms can occupy various positions on the graphene sheets, for example, bridge (above a C–C bond), top (directly above a C atom), hollow (above the center of a hexagonal ring) and others (see Fig. 83). GGA calculations have shown that the "bridge" position has the lowest formation energy (position A in Fig. 83).[140] The calculated perpendicular distance of the adatom from the underlying graphene sheet is 1.87 Å. The two C atoms bonded to the adatom present a sp^2–sp^3 hybridization, while the adatom itself is sp^2 hybridized (see Fig. 84). The energy required to adsorb a C atom is 1.40 eV, nearly 1 eV lower than that necessary to adsorb directly above a lattice C. The diffusion of C adatoms through two bridge positions has a barrier of 0.47 eV, whereas migration across the graphene sheets requires energy 4 times higher.[141]

An atomistic simulation using the three-center tight-binding potential for carbon was performed to obtain low-energy defect structures.[402] Fig. 85 shows the low-energy structures for adsorption of 1–4 carbon atoms on graphene including their formation energies. A linear chain of the carbon adatoms is preferred. The lowest formation energy was found for adsorption of two atoms. Moreover, the formation energy of carbon adatom insertion into graphene is much higher than that of carbon adatom adsorption on graphene.

Carbon adatoms formed upon displacement are responsible for magnetism. As discussed above, adatoms can diffuse on the graphene sheet surface. Calculations have shown that the diffusing atoms migrate as non-magnetic units, but they become magnetic when they reach the equilibrium (bridge) position. Carbon adatoms contribute to magnetism with a magnetic moment of 0.5 μ_B. The paramagnetic/FM oscillations at various calculated cell size indicate that among the adatoms, RKKY interactions take place. Annihilation of magnetism can take place at high temperatures, unless clusters are formed, thus "pinning" the magnetism.[141]

Interestingly, it was found that the magnetism evoked by adatoms (and vacancies) can be effectively controlled by doping resulting in switching 'ON' and 'OFF' of the magnetic moments; nitric acid (HNO_3) or NO_2 gas were chosen as hole dopants whereas aniline as an electron dopant.[403] Such an observation unambiguously proved the itinerant nature of magnetic moments in graphene, *i.e.*, the existence of π magnetism. More specifically, if a graphene sheet with vacancies is sufficiently doped with charge carriers (*i.e.*, when $|E_F| \geq U_C$, where U_C is the Coulomb repulsion), the contribution to the magnetic moment originating from a singly occupied π state completely vanishes while the other contribution from an unsaturated σ bond remains unaffected. In other words, only half of the magnetism generated by a vacancy can be switched off by charge doping,

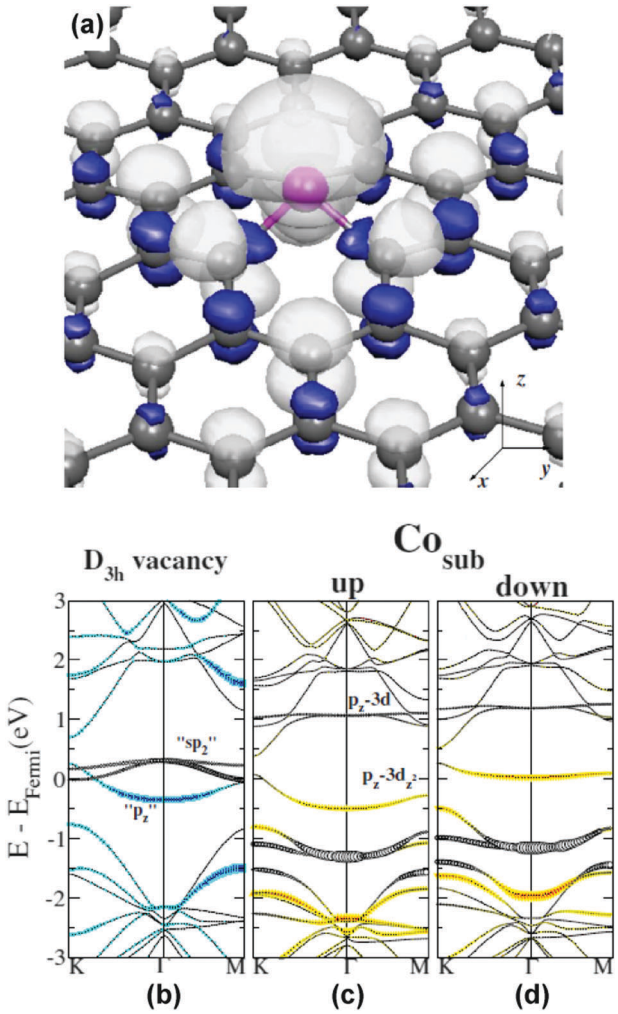

Fig. 82 (a) Isosurface of the spin density induced by the Co-substituted defect. Spin-up and spin-down densities are represented by light and dark colors, respectively, with isovalues of ± 0.008 e$^-$ Bohr^{-3}. (b) Spin-unpolarized band structure of a vacancy. (c) Majority spin-band structure of the Co-substituted defect; (d) minority spin-band structure of the Co-substituted defect. Reprinted with permission from ref. 398. Copyright 2010 American Physical Society.

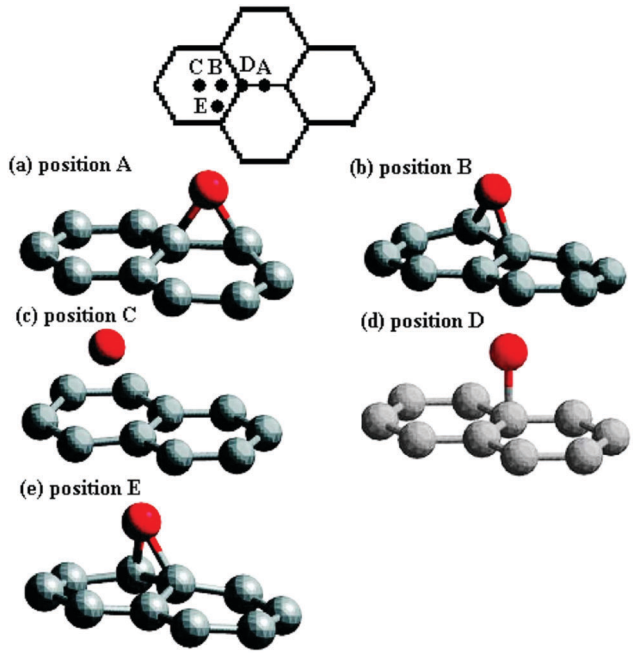

Fig. 83 Various adatom configurations on a graphene lattice. Reprinted with permission from ref. 140. Copyright 2005 American Physical Society.

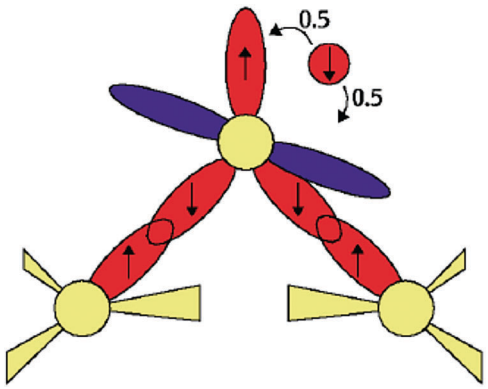

Fig. 84 Schematic of the bond orbital configuration in the case of an adatom at the bridge (equilibrium) position. Reprinted with permission from ref. 141. Copyright 2003 American Physical Society.

providing the potential to control the spin transport and, hence, spin diffusion in graphene.[403]

Importantly enough, density-functional calculations indicated that virtually any molecule attached to a carbon layer through a weakly polar single bond leads to an effect like that of hydrogen adsorption.[404] The graphene–adsorbate complexes exhibited a spin moment of 1 μ_B. The adsorption-induced spin polarization texture was shown to be remarkably similar for various adsorbed groups (see Fig. 86). The magnetic moments align ferromagnetically on the same sublattice, with an exchange coupling that falls off very slowly with the distance (r) between adsorbates ($\sim r^{-(1+\varepsilon)}$, $\varepsilon \approx 0.20$). In contrast, sp^3-functionalized opposite sublattices tend to couple antiferromagnetically. The band structure for graphene functionalized with adenine and methyl groups (see Fig. 86) showed that the magnetization comes from a very narrow defect state pinned at E_F. Similarly, one spin-polarized peak appeared close to E_F for various adsorbates chemisorbed on graphene through a single C–C bond (see Fig. 86).[404]

Various chemical routes such as hydrogen passivation, molecular grafting, or functionalization with various functional groups can be adopted to produce defects in graphene.[405–409] It was proved that atomic hydrogen can change the hybridization type in the parent graphene lattice from sp^2 to sp^3 bonding.[408] Fig. 87 shows the density of states for one-sided functionalization of bilayer graphene with several functional groups such as CN, NH_2, CH_3, COOH, and a combination of dopants and hydrogen.[406] The chemical nature of the dopant is independent of the band gap (0.6–0.7 eV) generated due to one-sided doping. However, functionalization by halogens or their combination

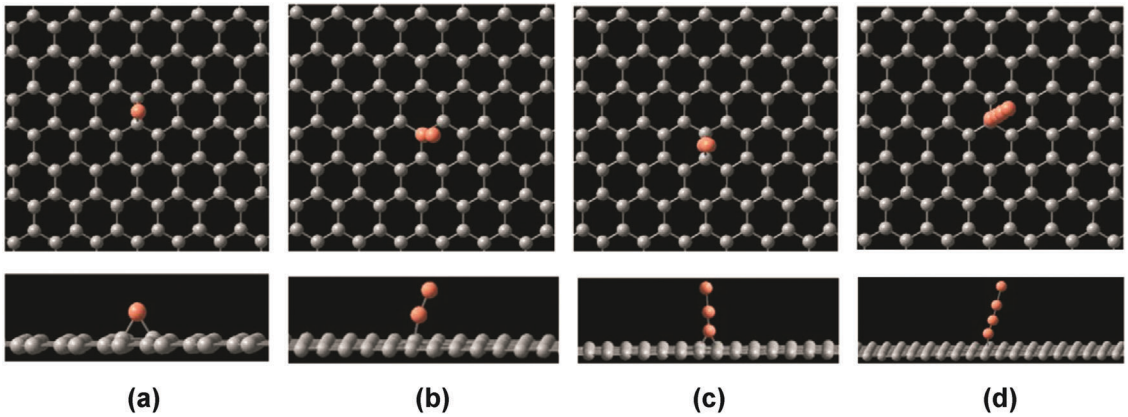

Fig. 85 Top and perspective views of the low-energy structures and formation energies (in eV) of adsorption of one, two, three, and four carbon atoms on graphene calculated by tight-binding approximation: (a) 5.52 eV; (b) 4.42 eV; (c) 7.58 eV; (d) 6.7 eV. Reprinted with permission from ref. 402. Copyright 2016 IOP Publishing Ltd.

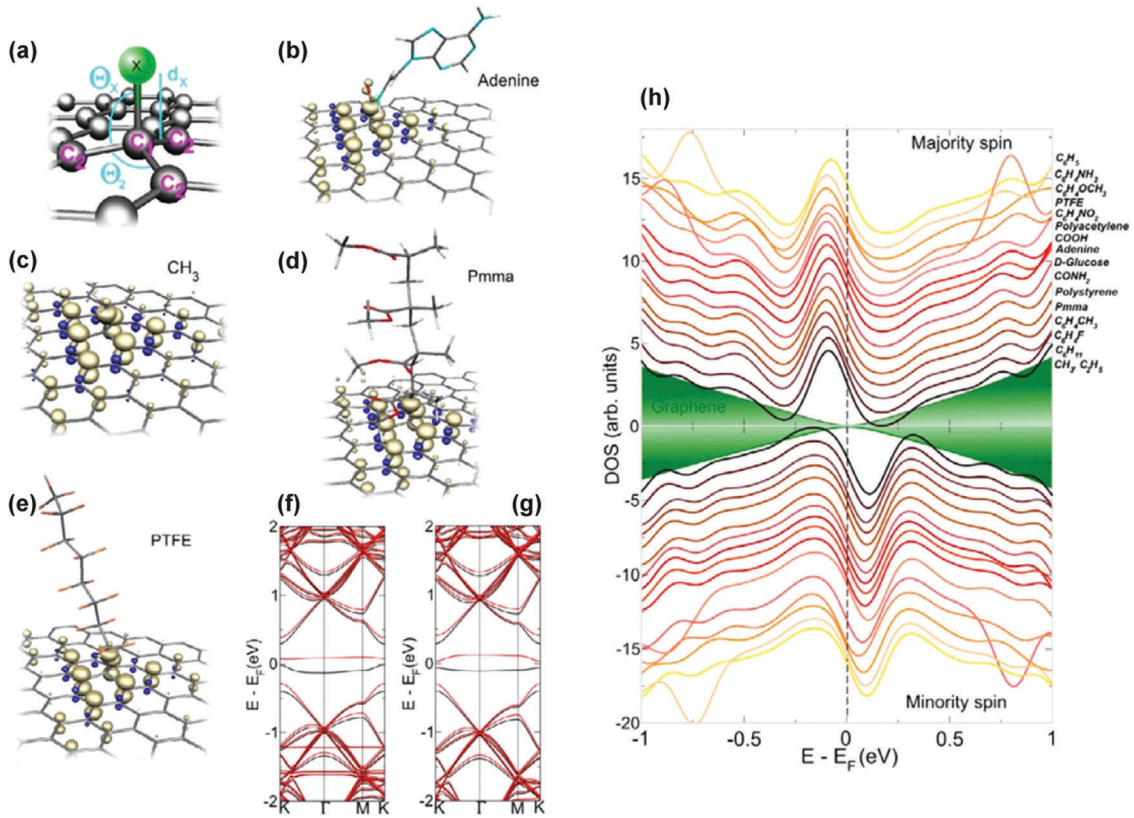

Fig. 86 (a) Adsorption geometry. (b–e) Isosurfaces of the magnetization density induced on graphene by functionalization using the adenine derivatives. Spin-polarized band structures for graphene with (f) a single adenine derivative and (g) a CH_3 molecule chemisorbed on top of one carbon atom. (h) Spin-polarized density of states (DOS) for a single molecule chemisorbed on a graphene supercell. The shaded regions indicate the density of states of pristine graphene. Reprinted with permission from ref. 404. Copyright 2012 IOP Publishing Ltd and Deutsche Physikalische Gesellschaft.

with hydrogen atoms was found to equip graphene with a wider band gap (1–3 eV).

Graphane, the fully hydrogenated graphene derivative, is a non-magnetic wide-gap semiconductor ($\sim$3.5 eV). Hydrogen can form a strong covalent bond with the carbon atom in graphene, thereby, consuming the π-electron to form sp^3 hybridization. This results in a strong resonance near E_F and increases the spin–orbit coupling. More specifically, the change from sp^2 to sp^3 states confines the p_z electrons into the chemical bonds, which is manifested by the disappearance of π-bands; the σ-bands are observed to move to the top of the valence band, which is accompanied by a large opening of the band gap. Although the hexagonal lattice of graphene is preserved in graphane, the periodicity decreases. Multilayered graphane, also

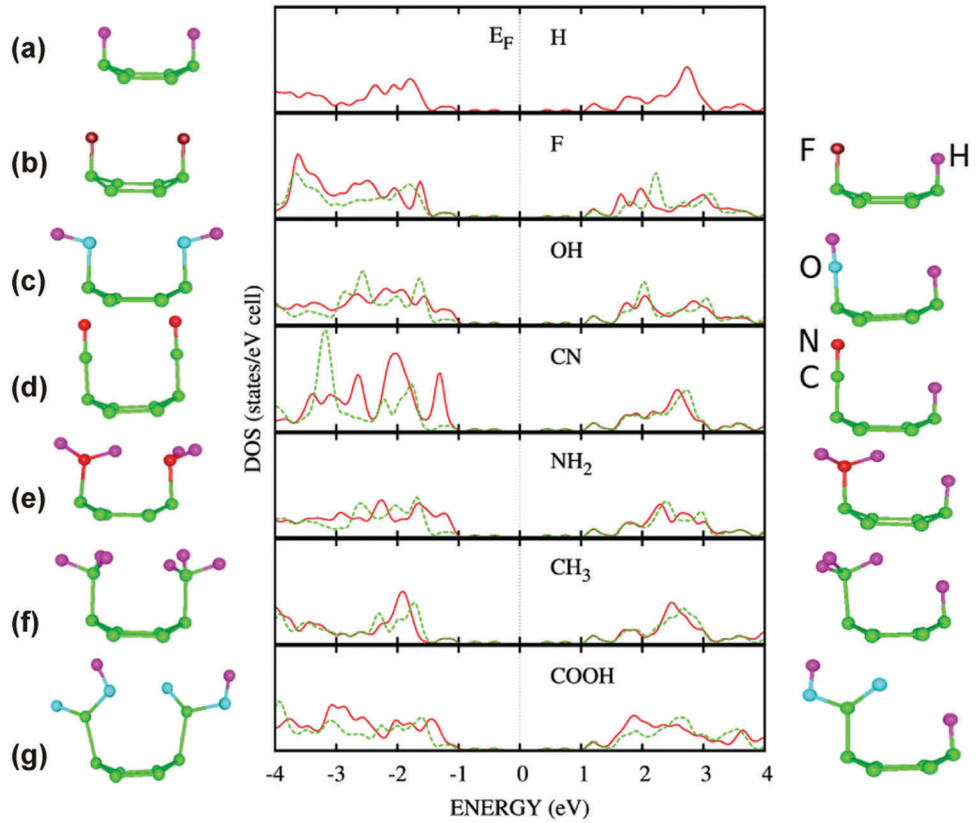

Fig. 87 Optimized configurations and total densities of states for one-sided functionalization of bilayer graphene. Left panel and red solid lines correspond to the case of two identical dopants, *e.g.*, F···F, per hexagon; right panel and dashed green lines correspond to the case when one dopant group per hexagon is replaced by hydrogen atoms, *e.g.*, F···H. Reprinted with permission from ref. 406. Copyright 2008 American Physical Society.

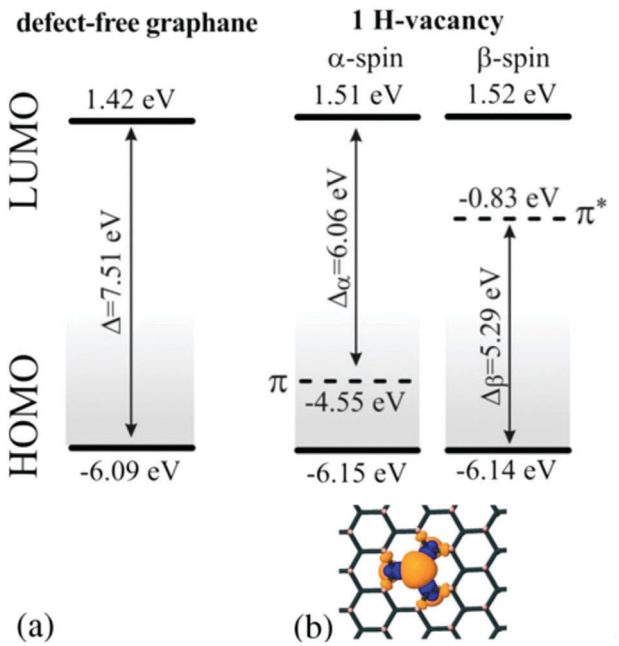

Fig. 88 Energetics of the bands in graphane with the defect levels (π and π*) induced by H-vacancy (dashed lines): (a) defect-free graphane; (b) graphane containing a single H-vacancy. The α- and β-spin states correspond to spin-up and spin-down states. Inset displays isosurfaces of spin-densities. Reprinted with permission from ref. 412. Copyright 2010 IOP Publishing Ltd.

called hydrographite, is a stable compound with a hexagonal crystal structure.[410] Hydrogenation of graphene was found to be reversible,[408] providing the flexibility to manipulate the coverage and to tailor its properties. Hydrogenation of graphene can be achieved by several techniques such as exposing graphene to hydrogen plasma, e-beam irradiation, or Birch reduction of graphite oxide. Graphane was found to show FM behavior that can resist against thermal fluctuations up to room temperature; the stability of the FM state was explained in terms of large extent of hydrogenation as proved theoretically. Besides, it was reported that AFM contribution can be detected arising as a result of multiple defects in agreement with computational predictions.[411]

Furthermore, a H-vacancy defect in the graphane lattice leads to the formation of a localized state with an unpaired spin and, accordingly, the formation of a defect level in the energy gap (see Fig. 88).[412] The armchair graphane is non-magnetic but AFM ordering can be seen on the same edge of zigzag edged graphane nanoribbons. Like GNRs, where spin states can be confined in zigzag GNRs by periodically repeating edge profiles, graphane nanoribbons can also produce similar effects.[413,414] Fig. 89 shows the energy-band diagram and band-projected charge density isosurfaces of various states of such a superlattice that mimics the edge roughness. The superlattice in Fig. 89 is a periodically repeating heterostructure of narrow (N_z = 6) and

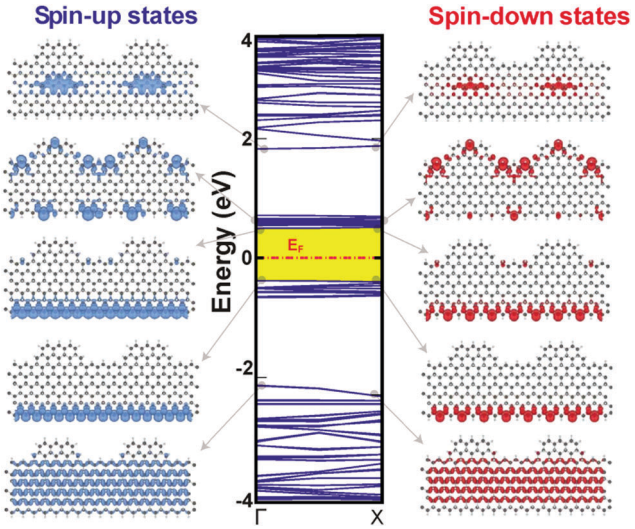

Fig. 89 The atomic and electronic band structure of a graphane nanoribbon including edge roughness. The yellow/gray shaded region is the band gap between the edge states. E_F is considered as the zero band energy. Reprinted with permission from ref. 414. Copyright 2010 American Physical Society.

wide (N_z = 8) segments of graphane nanoribbons, where N_z is the number of zigzag carbon chains along the nanoribbon's axis. It can be seen that at specific regions of periodic edge roughness, electronic states can be confined. On the other hand, it was proposed that edge states should theoretically disappear as a result of the absence of delocalized π-electrons due to completely sp^3 hybridized carbon atoms. Thus, only inner carbon atoms and hydrogen atoms determine predominantly the electronic structure of graphane nanoribbons, implying that they can be additionally modified in order to observe an emergence of magnetism.[415] Thus, spin polarization can be formed by creating domains of H-vacancies and CH-divacancies.[413] First-principles calculations using the Vienna ab initio simulation package (VASP) show that transition-metal-atom-embedded graphanes have larger magnetic moments in comparison to that of their corresponding graphene structure embedded with transition metal atoms or pristine graphane. The magnetic moment in graphane can be tailored by selecting a suitable dopant.[416] In particular, a maximum magnetic moment of 3.5 μ_B was found when Mn atoms were embedded in graphane.[417] More importantly, if a heterojunction structure with different transition metals (*i.e.*, nickel and vanadium), substituted in graphane, is theoretically considered, the spin-down current is observed to be totally suppressed and the spin-up current increases upon the application of the negative bias voltage.

Semi-hydrogenated graphene, known as graphone, shows a band gap of ~2.45 eV.[418,419] DFT calculations reveal that rectangular graphone is the most stable structure. Triangular graphone can undergo transitions to attain its stable structure by moving its two hydrogen atoms to the nearest carbon atoms at the starting point of the trigonal geometry. Fig. 90 shows the electron densities of triangular and rectangular graphone. The electrons in triangular graphone are localized around the hydrogen atom, while the electrons in rectangular graphone are not localized around the hydrogen atom. Thus, there exists a strong (weak) interaction between the two nearest hydrogen atoms in rectangular (triangular) graphone. This enhances the stability of rectangular graphone. Such kind of mutual interaction that exists between the two nearest neighbor hydrogen atoms in the rectangular graphone encourages AFM behavior. The unstable triangular graphone exhibits FM behavior with an indirect band gap of ~0.67 eV. Further, for single-side hydrogenated graphene with H-vacancies distributed on the neighboring carbon atoms belonging to the same graphane sublattice (graphone), the theory predicted[52] FM ordering with the estimated Curie temperature between 278 and 417 K. Fig. 91 shows that the induced magnetic moments are localized on the unhydrogenated atoms, while the hydrogenated C atoms and H atoms carry very small magnetic moments, which is due to the formation of strong σ-bonds between carbon and hydrogen atoms that break the π-bonding network and leave the electrons in the unhydrogenated C atoms localized and unpaired. The long-range magnetic coupling in graphone can be attributed to the large spatial extension of the valence electrons in the p-states.

The stability of graphone can be increased by fluorination. In fact, graphane (hydrogenated graphone) is less stable than a 100% fluorinated graphene.[420] DFT calculations show a dramatic change of electronic and magnetic properties upon fluorinating graphone. The insulating AFM graphone can be changed to an FM half-metallic fluorinated graphone. As the magnetism in graphone arises due to the localized and unpaired electrons originating from the unhydrogenated carbon atoms, any subsequent bond formation at these carbon atoms can quench the magnetic ordering. Further DFT study showed a two- and four-fold decrease in total magnetization upon adhesion of graphone on quartz and copper substrates, respectively.[421] However, in reality, no quenching of magnetization can be observed if polycrystalline copper or

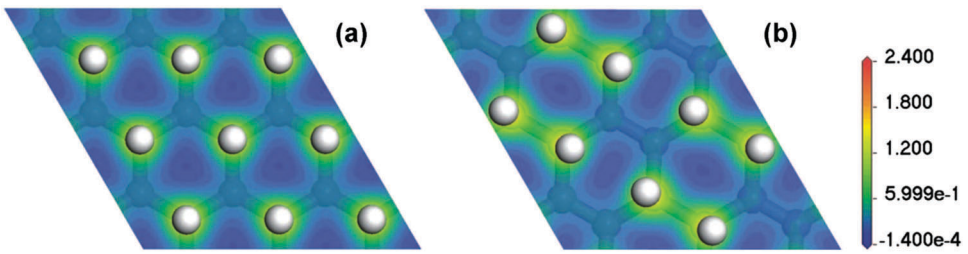

Fig. 90 Electron densities of (a) triangular (b) rectangular graphone. Reprinted with permission from ref. 419. Copyright 2012 AIP Publishing LLC.

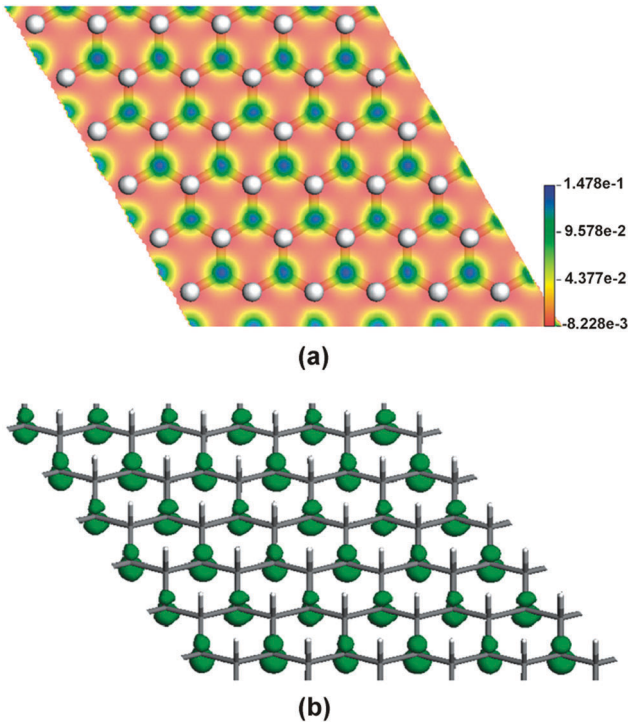

Fig. 91 (a) 2D plot of calculated spin-density difference (between spin-up and spin-down density) of graphone and (b) isosurface computed at a value of 0.26 e Å^{-3}. Reprinted with permission from ref. 52. Copyright 2009 American Chemical Society.

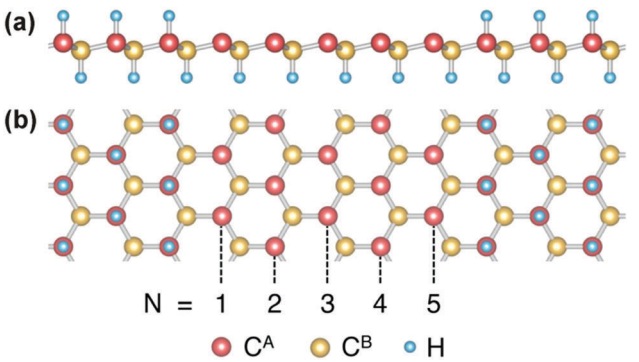

Fig. 92 (a) Side and (b) top views of the zigzag-edged semi-hydrogenated graphene nanorod in the fully-hydrogenated graphene layer where *N* denotes the width of the nanorod. Reprinted with permission from ref. 422. Copyright 2017 American Chemical Society.

amorphous silica substrates are used. This is due to the lack of effective bonding between the substrate and the corresponding C atoms.

Recently, an architecture comprising a semi-hydrogenated graphene nanorod incorporated into a fully-hydrogenated graphene sheet was theoretically proposed to show a robust ferromagnetism and bipolar semiconducting behavior (see Fig. 92).[422] Due to the areal magnetization promoted by half-hydrogenation, the FM response is not affected by the variation in the width and orientation of the nanorod in contrast to the magnetic behavior of related systems, relying solely on the edge states, and hence potentially ruined by chemical contamination and structural defects.[422]

Halogenation of the graphene system generates several interesting features by constructing a change in electron/hole density due to chemical adsorption. Fluorine doping can result in extra charge formation. For example, recent DFT calculations addressed the effect of doping on the magnetic properties of hydrogenated and fluorinated graphene.[423] A carbon atom can gain one unpaired electron when its neighboring carbon atom is attached to a functional group. Eventually, this process can occur in a series to gain unpaired electrons which would facilitate magnetism. The magnetic nature of the doped system is decided based on the presence of the unpaired electrons in the sublattices. Fluorinated and hydrogenated graphene possesses about 0.72 and 2.0 μ_B, respectively, without doping. The spin-up and spin-down density was found to vary depending upon the doping of extra charges (electrons/holes). The C–F bond length can be extended by adding more electrons by fluorination. Fig. 93 shows the band structures of the fluorinated graphene with various charge contents.[423] It is well known that E_F shifts due to doping of extra charges (see Section 5). E_F can shift down or up due to doping of holes or electrons, respectively. Hence, the spin polarization states of both spin-up and spin-down vary upon charge doping. However, fluorine doping has different effect on the graphene systems. In addition to the shift in E_F, spin-up and spin-down band distances also move disparately. In this respect, it was shown that the relative distance between E_F and the spin-up band lines hardly changes if the system is doped with positive charges that are smaller than 0.6 *e*. Fig. 94a and b display the geometrical structures of the hydrogenated and fluorinated carbon, respectively.[423] Hydrogen, carbon, and fluorine atoms are represented as white, cyan, and grey solid spheres, respectively. The unseen connections between the carbon atoms are shown by green triangles. The torsions of the two geometrical structures are also displayed. As is clear from Fig. 94c–f, the hydrogenated graphene has a maximum spin moment when it is not doped, while the spin moment decreases linearly upon doping (electrons/holes).[423] The fluorinated graphene has its maximum spin moment when doped with a positive charge of 0.6 *e*. It could undergo a change in the magnetic phase to become non-magnetic if it is doped with negative charges (−0.6 *e*). This can happen due to a change in the bond length as a result of the presence of extra charges.

Evolution of potential magnetic response in fluorinated graphite was studied with regard to various F/C ratios.[424] By employing the ESR technique, it was found that fluorinated graphites showed paramagnetic behavior with a *g*-value of ∼2, typical for paramagnetic defects and free radicals. A generation of local magnetic moments was proposed originating from dangling bonds that are formed due to the conversion of sp^2-bonds to sp^3-bonds as a result of carbon–fluorine reactions. Interestingly, strong exchange interactions were observed between the localized moments of F atoms in a partially fluorinated sample while the localized spins in highly fluorinated samples behaved like isolated spins.

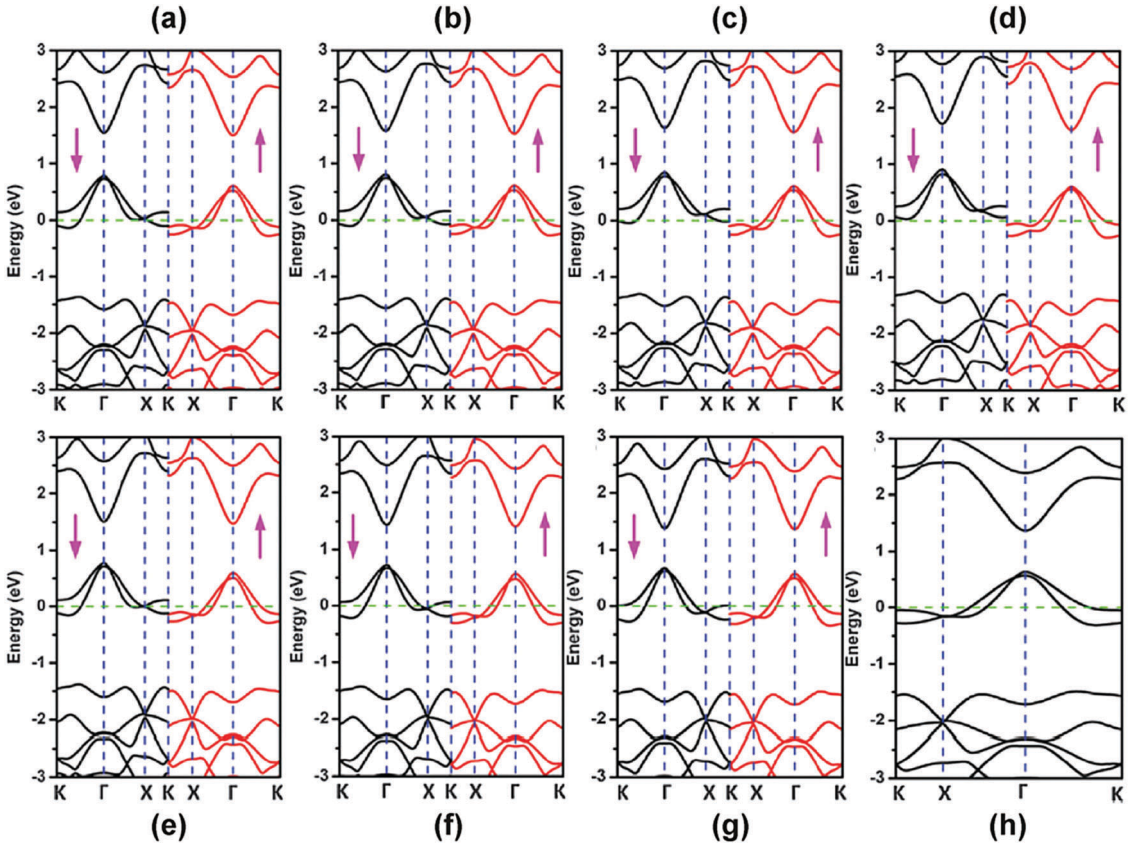

Fig. 93 Fluorinated graphene's band structures with charge (a) 0 *e*, (b) 0.1 *e*, (c) 0.3 *e*, (d) 0.6 *e*, (e) −0.1 *e*, (f) −0.3 *e*, (g) −0.5 *e*, and (h) −0.6 *e*. *e* is the unit of charge. The spin-up and spin-down bands are shown with red and black lines, respectively. E_F is marked with a green dashed line and set to zero. Reprinted with permission from ref. 423. Copyright 2013 The Royal Society of Chemistry.

Fluorographene, a two-dimensional stoichiometric graphene derivative, is one of the thinnest insulators with a wide electronic band gap (from 3.0–4.2 eV).[425–427] In fluorographene, the sp^3-hybridized C–C and C–F bond lengths are 1.58 and 1.37 Å, respectively. Density-functional calculations predicted that localized spin density can emerge in fluorographene and can be modulated by the degree of F coverage.[428] Fluorination was experimentally confirmed to be an effective route to generate noticeable spin-half paramagnetic centers in graphene (see Fig. 95).[53] However, possibly due to the adatom clustering, the measured number of paramagnetic centers was three orders of magnitude less than the measured number of F adatoms in the samples (see Fig. 95) and no long-range magnetic ordering was detected at that time. Thus, the cluster edges were proposed as the only source of magnetic moments that would determine the nature of magnetic response. Moreover, the number of spins (N) was found to increase monotonically with an increase in the degree of fluorination (*i.e.*, C_1F_x, $0 \leq x \leq 1$) up to $x \approx 0.9$. However, a complete fluorination showed a decrease in the value of N.[53]

More recently, in a combined experimental–theoretical work, Makarova *et al.*[429] proved that monoatomic chains of fluorine atoms on graphene led to strong magnetism in these purely organic graphene-based systems (see Fig. 96). The lattice sites that were occupied by F atoms became unavailable to the π-electron system, *i.e.*, the fluorine chains acted as high-energy barriers (a "nanoridge") for the graphene π-electron cloud. Thus, two edges separated by a nearly impenetrable CF-nanoridge were created, where one may expect a set of localized spin states in the A-sublattice on one side of the nanoridge and the B-sublattice on the other side. Magnetic susceptibility data yielded behavior typical of a quantum spin-ladder system with FM legs and AFM rungs (see Fig. 97), in analogy to the exchange couplings between the zigzag edge-inherited states in GNRs. The exchange coupling constant along the rungs was measured to be 450 K, which is strong enough to consider graphene with fluorine nanoridges as a candidate for a room temperature spintronic material.[429]

Like graphone, single-side semifluorinated graphene (C_2F) – a graphene derivative that was recently prepared experimentally[430] – should be FM according to Lieb's theorem since the fluorine atoms adsorb on the same sublattice of graphene. Very recently, the theoretical description of the magnetic moments by using the Wannier functions highlighted the direct exchange interaction in maintaining FM order in functionalized graphene, C_2F and C_2H.[431] Unlike graphone, C_2F was predicted to be at the edge of the AFM–FM instability, which in combination with the Dzyaloshinskii–Moriya interaction can lead to a skyrmion state at finite temperatures and magnetic fields (see Fig. 98).[431]

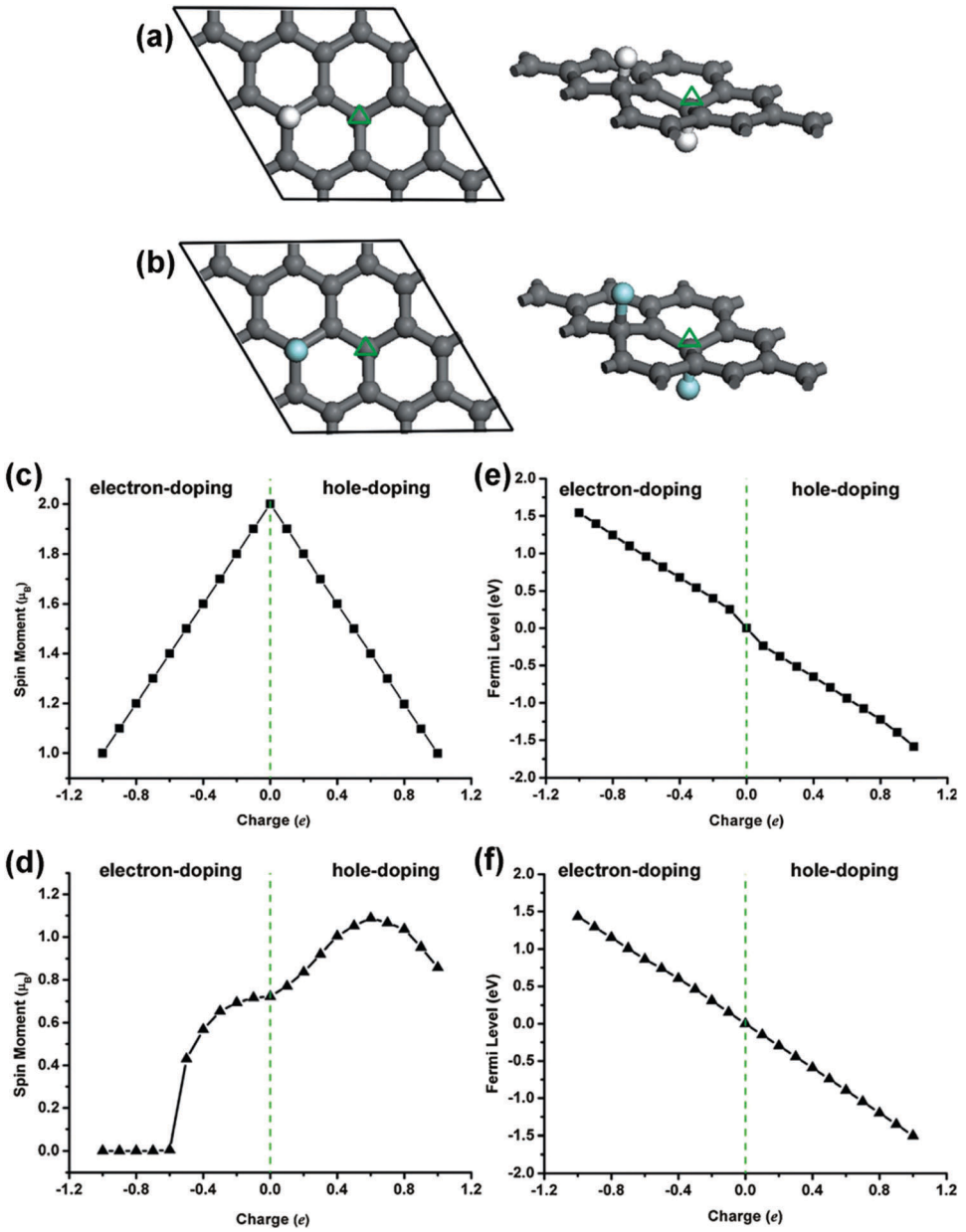

Fig. 94 Geometrical structures and relations between spin moment and charge of (a and c) hydrogenated and (b and d) fluorinated graphene. The relation between E_F and charge for (e) hydrogenated and (f) fluorinated graphene. E_F corresponding to the zero charge is set to zero. Reprinted with permission from ref. 423. Copyright 2013 The Royal Society of Chemistry.

Intriguing magnetic behavior was observed for graphene sheets functionalized with fluorine atoms with an arrangement closely resembling that of a so-called tabby pattern.[432] In particular, the attached fluorine atoms form monoatomic stripes which run along crystallographic directions, and are separated by non-fluorinated sp^2 carbon ribbons. As a result of bonds developed between the sp^3-hybridized carbon atoms and zigzag fluorine chains, sp^2–sp^3 interfaces were observed to evolve with spin-polarized edge states localized on both sides of chains. More importantly, fluorine patterns induced reduction of the effective dimensionality to 1D. For C_2F_x with $x < 1$, a behavior typical for low-dimensional quantum spin ladder systems was observed, with FM ordering along the zigzag edges and AFM coupling between the opposite zigzag edges. In addition, a thermally activated spin gap was detected at about 450 K. Ferromagnetism stable at room temperature was also found for C_2F_x with $x < 1$ and interpreted as a consequence of a dimensional crossover due to the onset of interlayer interactions after ageing or annealing. In contrast, the C_2F_x system with $x \approx 1$ exhibited a behavior characteristic of the two-dimensional magnetism without any signs of magnetic ordering at high temperatures; instead, a transition to a superparamagnetic regime at 40 K was observed. Thus, the results demonstrated that a magnetic dimensional crossover in

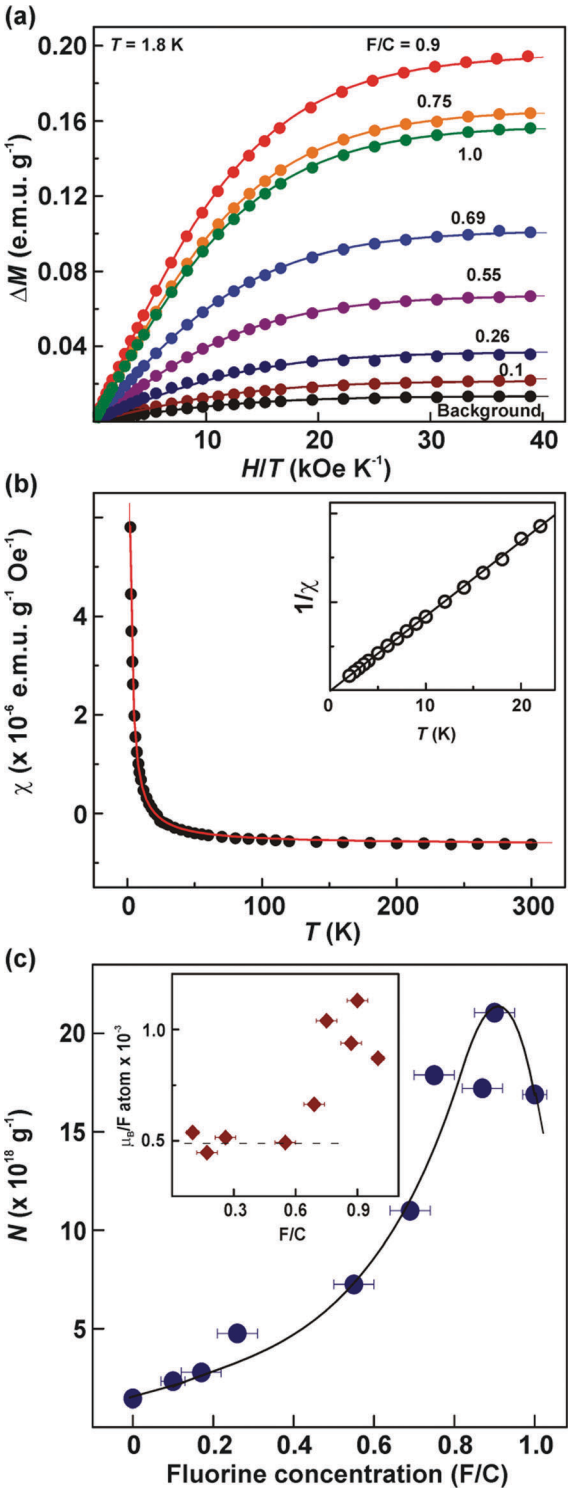

Fig. 95 (a) Magnetic moment as a function of parallel field for different F/C ratios. Symbols represent the measurements and solid curves are fits to the Brillouin function with $S = 1/2$ and assuming $g = 2$. (b) Example of the temperature dependence of magnetic susceptibility ($\chi = M/H$) in a parallel external magnetic field (H) of 3 kOe for F/C = 0.9. The inset shows the inverse magnetic susceptibility *vs.* temperature plot demonstrating the linear, purely paramagnetic behavior with no sign of magnetic ordering. (c) Number of spins (N) extracted from the Brillouin fits as a function of the F/C ratio. The inset shows the same N normalized to the concentration of adatoms in each sample. Reprinted with permission from ref. 53. Copyright 2012 Macmillan Publishers Limited.

graphene-based systems can be induced upon changes in the fluorine content and interlayer distance.[432]

The chemistry of fluorographene has been recently used to develop room-temperature magnetically ordered 2D systems.[54] While partially fluorinated graphene samples (*i.e.*, C_1F_x), prepared by thermal defluorination of exfoliated C_1F_1, were either diamagnetic but contained some paramagnetic centers or exhibited even an FM ground state with the Curie temperature of 22 K, hydroxyl-substituted fluorographene (termed hydroxofluorographene) prepared *via* simultaneous reductive defluorination and nucleophilic substitution with –OH groups showed room-temperature AFM ordering with a high saturation magnetization of $\sim$1 emu g^{-1}, and underwent a transition to an FM state at 62 K (see Fig. 99), as predicted by theoretical models and confirmed experimentally (see Fig. 100).[54] The different transition temperatures and failure/ability to establish magnetic order up to room temperature highlighted the different origin of magnetism in fluorographene and hydroxofluorographene. Magnetism of fluorographene with low levels of sp^3 functionalization stems from localized defect-induced magnetic moments. The magnetism in hydroxofluorographenes with an appropriate stoichiometry stemmed from the presence of aromatic islands forming diradicals that coupled through OH-enabled superexchange interactions (see Fig. 101). These new developments in sp^2-based room-temperature magnetism in 2D systems pave the way to the future organic spintronic applications.[51]

Adding atoms or molecules in a material through covalent bonding can influence several properties including the magnetic behavior.[433] The effects of addition of monovalent and divalent adsorbates with different electronegativity onto graphene were studied using first-principles calculations based on spin-polarized DFT. The energy difference between the magnetic and non-magnetic states (ΔE) was used to understand the stability of magnetic orderings in graphene systems. The atom/functional group X representing F, H, OH, CN, CH_3, and NH_2 was considered for monovalent adsorption while C, N, O, CH_2, and NH were selected as a divalent adsorbate. The monovalent adsorbate X would make a single covalent bond between carbon and the X atom. As a result, the bond length and bond angle, corresponding to sp^3 hybridization, change. The magnetic moment of the supercell then decreases with an increase in the size of the supercell.[433] A very high adsorption concentration of fluorine is required to establish a magnetic ground state due to its high electronegativity. Thus, the magnetism in the graphene system with monovalent addition becomes a charge-transfer-dependent process. However, H adsorption was found to induce the highest moment with a narrow energy gap. This is because the charge transfer is dependent on the electronegativity. The exchange interaction between sp^3 carbon and localized states is weakened by the electron transfer process. The spin split of density of states of graphene with various supercells for H and N adsorption is shown in Fig. 102.[433] The red and black arrows in the density-of-state plot for N addition can be attributed to the spin-polarized p_z orbital (see Fig. 102e–h).[433] Similar results were obtained by adopting LSDA+U calculations except that the positions of

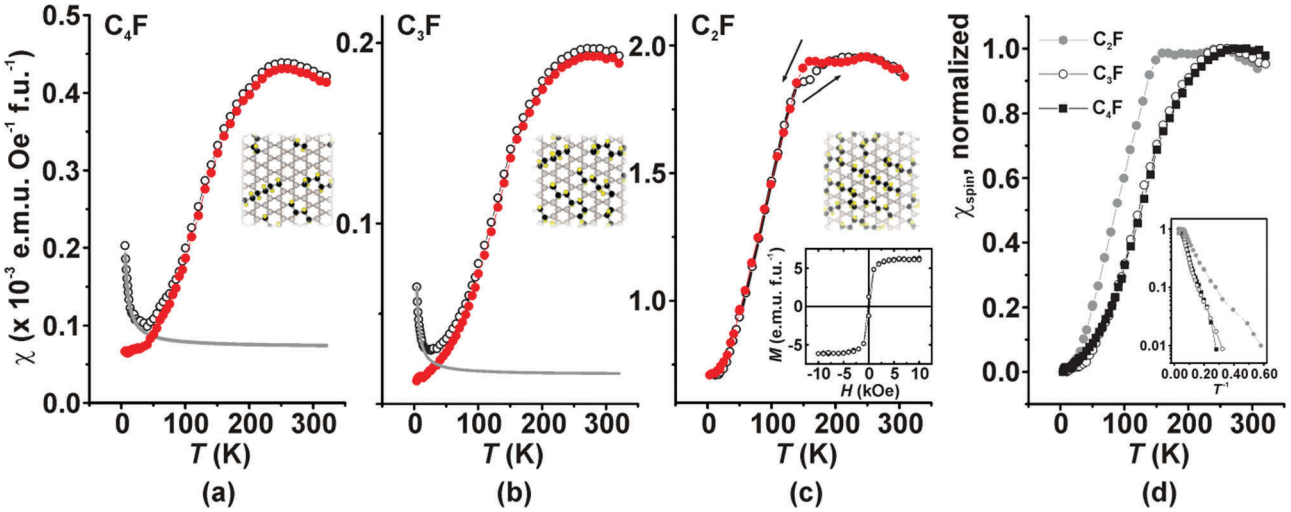

Fig. 96 (a–c) Raw data of magnetic susceptibility (χ) of the C_nF samples (n = 2, 3, and 4). C_4F and C_3F samples were measured at an applied magnetic field of 100 Oe upon heating after zero-field cooling (open circles); the same curves with the Curie contribution (grey) subtracted are represented by filled red circles. A C_2F sample was measured upon heating (filled circles) and upon cooling (open circles). The inset in panel (c) shows the room-temperature hysteresis loop of the C_2F sample. (d) Normalized spin susceptibilities for C_4F, C_3F and C_2F samples with the inset showing dependence of the spin susceptibility on reciprocal temperature for these samples. Reprinted with permission from ref. 429. Copyright 2015 Macmillan Publishers Limited.

localized states (on N atoms) for the spin-up branch were deeper in the valence band for U_{eff} = 4.6 eV.

In contrast, the induced magnetic moment in the case of divalent adsorption was found to be more stable and less dependent on the concentration of the adsorbates.[433] The π-bond breaks after the divalent adsorption and sp^3-like hybridization is seen at the carbon sites. However, the magnetic contribution from this π-bond breakage is very small because the hybridized carbon atoms belong to different sublattices of graphene. The adsorption of O, CH_2, and NH did not yield any magnetic ordering in the ground states due to the absence of any unpaired p_z electron. N adsorption induces a larger moment compared to C atom adsorption. ΔE for the divalent adsorption does not follow any regular fashion. Like the monovalent adsorption, the exchange interactions for the divalent adsorption on graphene were found to be distance-dependent.[433]

Covalent adsorption of an aromatic radical onto a graphene sheet can also imprint magnetic behavior and band gap opening. For example, attaching a phenyl group onto graphene was theoretically found to generate a band gap by modifying the band structure, thereby creating two spin-dependent states around E_F.[434] A nonzero magnetic moment can be induced due to an imbalance between the two sublattices in graphene caused by an aromatic adsorption on one of the carbon atoms in the sublattice. As a result, the corresponding p_z orbital is removed leaving the other sublattice unpaired. However, graphene is found to be less sensitive to adsorption of an aromatic molecule.

The magnetic ground state can vary depending on whether the adsorbate is physically or chemically adsorbed. Employing DFT calculations, it was predicted that the magnetic response for such adsorption emerges at a femtosecond time-scale due to core level excitations.[435] The dominant interaction between the physisorbed molecule and graphene is primarily governed by the van der Waals forces. In such cases, the ground state of the system is non-magnetic. The magnetic ground state is altered by the degree of electron transfer that happens at the femtosecond time-scale. This non-magnetic ground state can be magnetic only after a core electron gets excited and retains its magnetic state until the core electron is de-excited. In contrast, for covalently bonded molecules, the ground state is of magnetic nature and the magnetic state is suppressed by the excitation of a core electron.

Alternatively, ferromagnetism was observed in hydrogenated epitaxial graphene grown on SiC substrates.[436] The effect of substrate on the evolution of magnetic behavior in graphene was studied by growing a quasi-freestanding monolayer graphene which was prepared by intercalating hydrogen between the SiC substrate and the buffer layer. Due to the exchange coupling interaction between the localized states in the hydrogenated graphene layer and the localized states of the buffer layer, the hydrogenated epitaxial graphene was found to show FM ordering.[436] Moreover, a paramagnetic response for the buffer layer was observed, signifying the presence of localized magnetic moments at the defect sites. Upon hydrogenation, sp^3 defect states were created by virtue of C–H bonds. These newly generated states were believed to undergo a spin split in the vicinity of E_F due to the Coulombic interaction of the Si dangling bonds. Thus, the FM state was stabilized with the Curie temperature of 300 K or higher.[436] Even in the absence of the substrate, hydrogenated graphene was reported to exhibit an intrinsic ferromagnetism with the lower Curie temperature. The emergence of FM behavior was further confirmed by measuring the remanent magnetization by magnetic force microscopy (MFM, see Fig. 103).[436] A difference in the MFM signal is seen in between the single (1L) and bilayer (2L) areas implying a change in the degree of magnetization correspondingly; it was explained by the difference in hydrogen coverage by both layers. Fig. 103c then clearly shows a switching

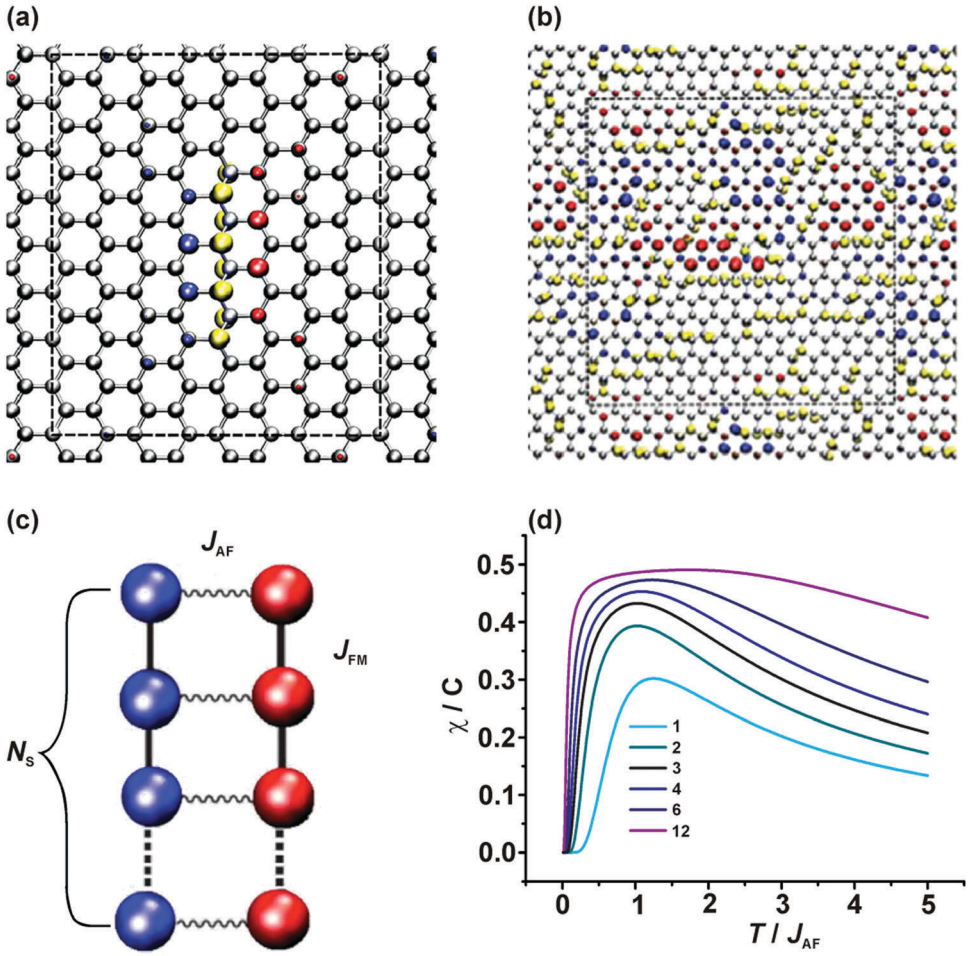

Fig. 97 (a) A zigzag chain of fluorine on graphene. Opposite spin orientations are shown in red and blue. F atoms are represented by yellow spheres. (b) The calculated spin density for a random distribution of fluorine chains. (c) A model of a spin ladder with an infinitely strong FM intra-leg interaction (J_{FM}) and an AFM inter-leg coupling (J_{AF}). (d) A plot of the magnetic susceptibility (χ) for the finite size spin ladder as a function of the reduced temperature. The numbers near the curves correspond to length of the spin ladder (N_S). Reprinted with permission from ref. 429. Copyright 2015 Macmillan Publishers Limited.

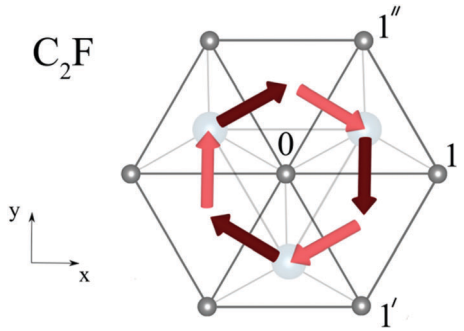

Fig. 98 Schematic representation of the Dzyaloshinskii–Moriya vectors in C_2F. Light and dark red arrows denote the Dzyaloshinskii–Moriya vectors with positive and negative z components, respectively. Reprinted with permission from ref. 431. Copyright 2016 American Physical Society.

mechanism in the presence of different layers.[436] The MFM signal changes its direction upon reversing the external magnetic field (visible through color inversion of the MFM images in Fig. 103a and b).[436] These MFM measurements clearly support the present FM behavior of hydrogenated graphene, thereby ruling out any previous doubts on the evolution of magnetism in graphene by magnetic contaminations.[436]

If a graphene sheet is functionalized with –OH groups, magnetic moments with high magnitudes can be induced on its basal plane; depending on the concentration of –OH groups (from 3 to 10 at% of OH coverage) after annealing of graphene oxide at different temperatures (removing epoxy groups), the saturation magnetization was found to vary from 0.91 to 2.41 emu g^{-1}.[437] More importantly, an inducing efficiency as a high as 217 μ_B per 1000 OH groups was observed. In addition, –OH groups showed high stability sustaining even at 900 °C. Thus, –OH groups were suggested as ideal sp^3-type candidates to equip graphene with robust magnetic moments.[437]

Unlike graphene which is hydrophobic in nature, graphene oxide forms stable dispersions in many solvents due to its oxygen-rich functional groups (*e.g.*, –OH, –O–, –COOH, C=O). In particular, epoxy and hydroxyl groups sit on the basal plane of the graphene oxide sheet (*i.e.*, in the interior region) while carbonyl and carboxyl groups are attached at its edge sites.[438]

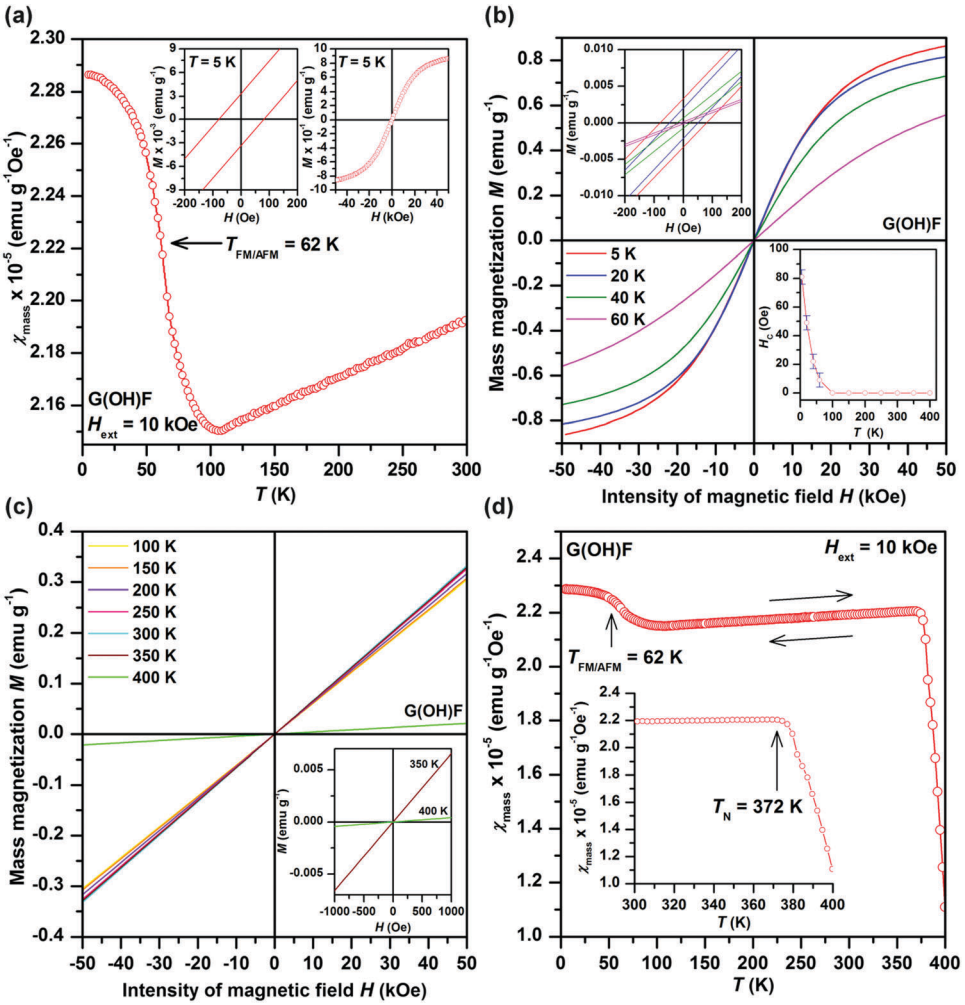

Fig. 99 (a) Temperature evolution of the mass magnetic susceptibility (χ_{mass}) of hydroxofluorographene (G(OH)F), measured under an external magnetic field of 10 kOe, with TFM/AFM indicating a transition from the FM to AFM state upon warming. The insets show the hysteresis loops of G(OH)F at 5 K, which indicate a non-zero coercivity and a saturation magnetization of $\sim$1 emu g^{-1}. (b) Isothermal magnetization curves of G(OH)F at temperatures of 5–60 K. The insets show the profile of the hysteresis loops around the origin and the temperature dependence of coercivity (H_C). (c) Isothermal magnetization curves of G(OH)F, recorded from 100 to 400 K. The inset shows the profile of the isothermal magnetization curves at 350 and 400 K, demonstrating a transition from an AFM state to a paramagnetic regime above 350 K. (d) Temperature evolution of χ_{mass} of G(OH)F, measured under an external magnetic field of 10 kOe. The arrows show the reversibility of the χ_{mass} profile on warming the sample from 5 to 400 K and then cooling from 400 to 5 K. The inset shows a sudden drop of χ_{mass} above 370 K, which is indicative of a transition from an AFM state to a paramagnetic regime with a Néel transition temperature (T_N) of about 372 K. Note: the paramagnetic signal from the non-interacting paramagnetic centers was subtracted from the χ_{mass} data. Reprinted with permission from ref. 54. Copyright 2017 Macmillan Publishers Limited.

Thus, graphene oxide contains a mixture of both sp^2 and sp^3 bonds and is regarded as an insulator with a band gap depending on the relative fraction of individual oxygen-containing groups (between $\sim$0.2 and $\sim$4.2 eV). Upon reduction, graphene oxide may undergo a transition from the insulating through semiconducting to the semi-metal state. A single epoxy group is found to be non-magnetic as it induces equal defects in the A- and B-sublattice of the graphene lattice. On the other hand, a single hydroxyl group can effectively generate a localized spin ($\sim$1 μ_B) sitting on the basal plane of the graphene sheet.

It was found that high-content hydroxyl groups can be formed on the basal plane of graphene oxide upon ring opening of the epoxy group. An increase in the level of hydroxyl groups caused a significant increase in the local spin density reaching a value of 5.17 μ_B per 1000 carbon atoms. In other words, converting epoxy groups to hydroxyl groups, combined with the Ar annealing method, increased the magnetization of graphene oxide from 0.136 to 3.11 emu g^{-1}.[439] Similarly, higher magnetization values were experimentally observed for graphene oxide after thermal annealing in Ar for 2 h. It was suggested that the elevated temperatures promote migration of epoxy groups over the surface of the graphene oxide sheets, eventually self-assembling into several long chains with a zigzag motif. The increase in the number of zigzag edges was then responsible for a higher value of the magnetic moment. Moreover, the density of epoxy groups was identified as crucial for cutting the graphene oxide sheets to small structures with a higher number of zigzag edges.[440]

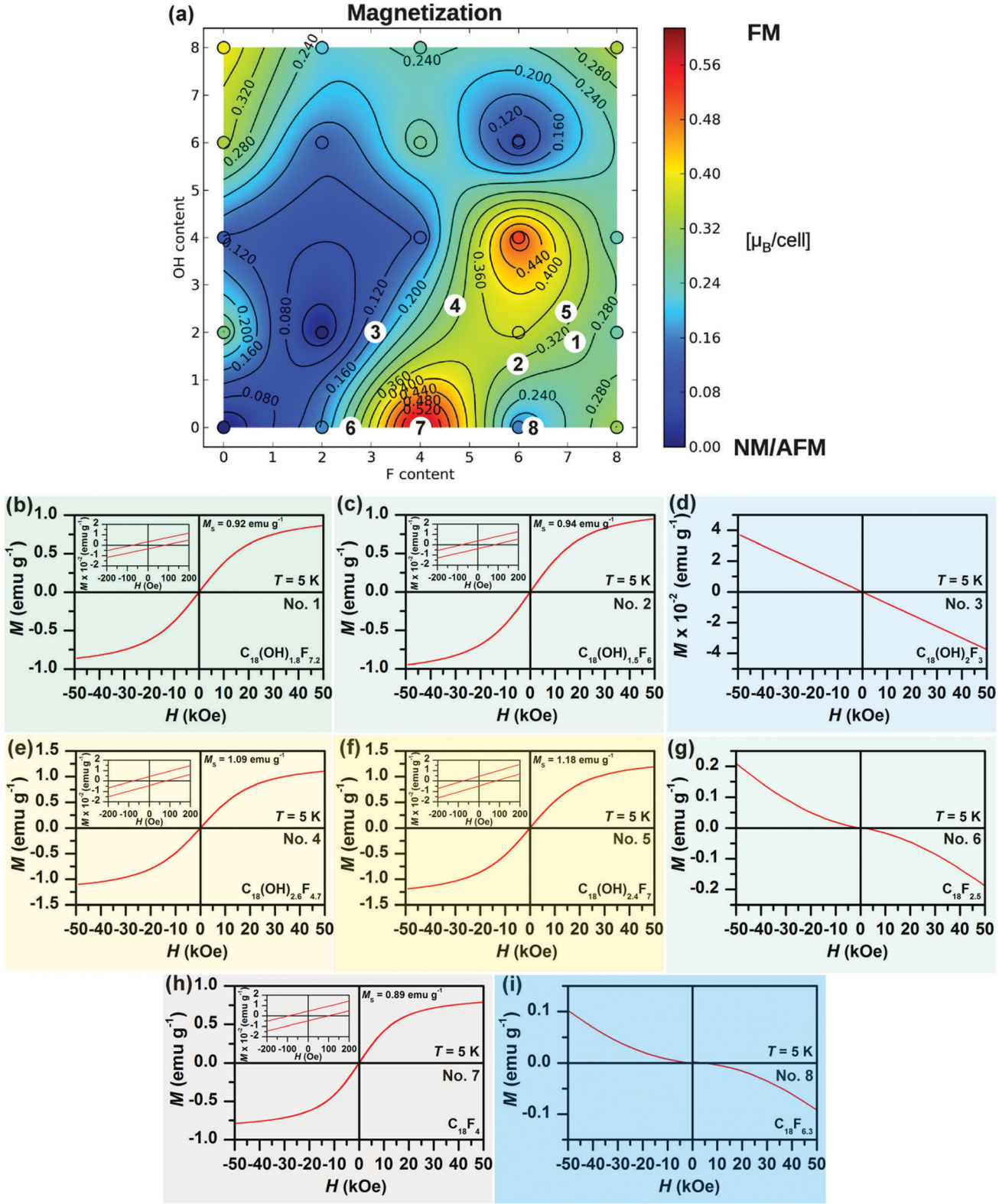

Fig. 100 (a) The theoretical mean magnetization map indicates which $C_{18}(OH)_yF_x$ stoichiometries are likely to exist in ferromagnetic (FM) and non-magnetic (NM) ground states. The white circles indicate experimentally studied samples (b–i) for which the isothermal magnetization (M) curves as a function of an external magnetic field (H), recorded at a temperature of 5 K are shown. The insets in panels (b, c, e, f and h) show the behavior of the respective hysteresis loops around the origin with the saturation magnetization (M_S) indicated. Reprinted with permission from ref. 54. Copyright 2017 Macmillan Publishers Limited.

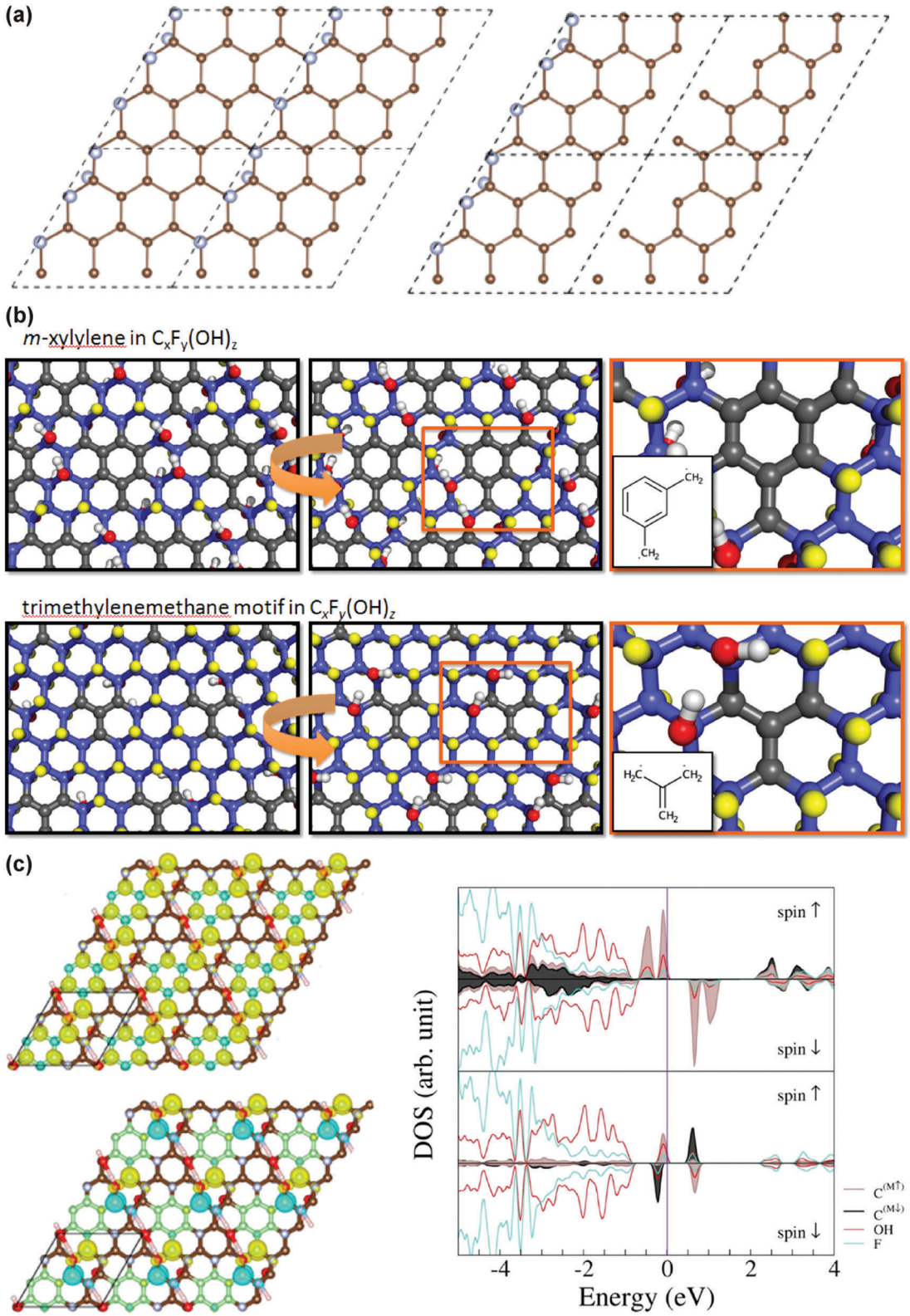

Fig. 101 (a) Structure of $C_{18}F_4$ which can be considered as an sp^3 structural defect in the sp^2 graphene lattice; the sp^3 carbon atoms due to F adsorption (shown in cyan) cut the graphene plane along the zig-zag line and virtually generate a graphene ribbon with a zig-zag edge. (b) Models of diradical motifs in the hydroxofluorographene system (shown in grey) leading to its room-temperature AFM properties. (c) Spin densities in the *m*-xylylene motif embedded in an sp^3 lattice of hydroxofluorographene with the corresponding FM and AFM phases, with spin-up and spin-down densities shown in yellow/blue. Right panels display corresponding densities of states which indicate the important role of –OH group in the superexchange interactions. Reprinted with permission from ref. 54. Copyright 2017 Macmillan Publishers Limited.

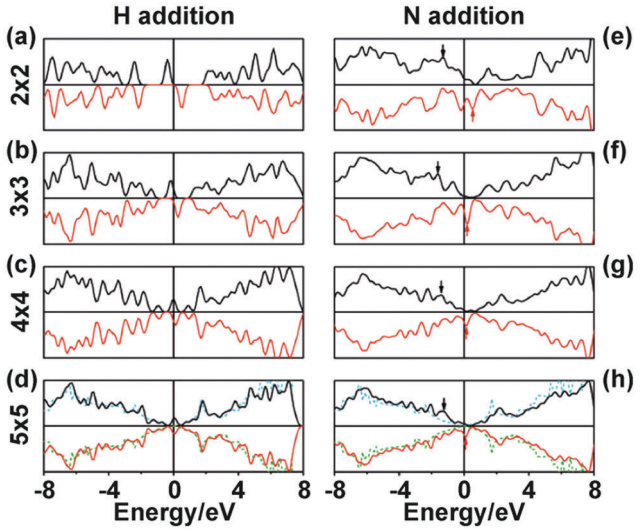

Fig. 102 Spin-split density of states of graphene with various supercell sizes for (a–d) H and (e–h) N additions. The black line represents spin-up and the red line represents spin-down. For comparison in the 5 × 5 supercell, the density of states of graphene is also shown in cyan (spin-up) and green (spin-down) dashed lines. Reprinted with permission from ref. 433. Copyright 2009 The Royal Society of Chemistry.

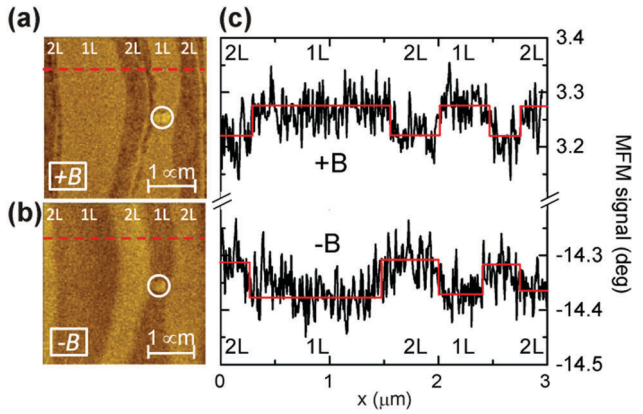

Fig. 103 MFM measurements of hydrogenated epitaxial graphene (1L and 2L) post applying a magnetic field (positive and negative) and the cross section of its magnetization. Reprinted with permission from ref. 436. Copyright 2013 American Physical Society.

Furthermore, theoretical studies have shown that the magnetic behavior in graphene oxide originating from hydroxyl groups is more stable than that observed in graphene surface-functionalized with hydrogen.[441] In particular, the energy barrier for migration was found to be three times higher for hydroxyl groups than for hydrogen, encouraging the magnetic stability in graphenes modified with hydroxyls. Moreover, the migration energy can be further increased upon increasing the number of water molecules linked to hydroxyl groups.[441] Magnetic configurations were predicted to form upon migration of hydroxyl groups from the solvent, facilitated by the ripples on graphene, during the production of graphene laminate. A magnetic configuration containing seven –OH groups was proposed as stable reflecting the symmetry of the graphene lattice. The as-formed clusters carry a large magnetic moment between 4 and 5 μ_B; the clusters were found to be structurally stabilized if the distance between them was larger than 3 nm, behaving thus as paramagnetic centers with negligible exchange interactions.[55]

Following several experimental and theoretical studies published so far, it is not currently clear which oxygen-containing group dominantly governs the magnetic properties in graphene oxide. It was recently reported that if the epoxy groups are destroyed by heat and/or chemical (by NaOH) treatment, the magnetic response of graphene oxide is significantly reduced.[442] This suggests that epoxy groups are responsible for the evolution of unpaired spins on carbon radicals, acting thus as sources of magnetism in graphene oxide.[442] Moreover, if organized as an epoxy-chain pair at various positions on zigzag GNRs, the FM ground state was theoretically predicted.[443] On the other hand, hydroxyl groups were identified to significantly enhance the magnetic response in graphene oxide as they are believed to induce paramagnetic centers with a spin of 5/2.[444] However, the emergence of magnetic moments from hydroxyl groups was found to strongly depend on the their configuration on the graphene oxide sheets; the generation of unpaired spins was predicted only for a case when two non-neighboring hydroxyl-bonded carbon atoms were connected with one carbon atom sitting in between them in the ring.[445]

The concentration of paramagnetic centers in graphene oxide can be increased by increasing the sp^3 content. The effect of degree of oxidation on the magnetic behavior of graphene oxide was recently studied in the work by Liaros *et al.*[446] Fig. 104 shows the temperature evolution of the mass susceptibility for graphene oxide with increasing oxidation (GO_3 > GO_2 > GO_1). The Curie temperature was found to increase by increasing the degree of oxidation in graphene oxide. The paramagnetic centers can magnetically communicate to exhibit FM behavior provided they are separated by a small distance. Else, the paramagnetic behavior will be preserved. The magnetic interaction between the localized magnetic moments at sp^3 states is realized by delocalized π-electrons.[446] Although the amount of paramagnetic centers can be increased by increasing the degree of oxidation, the number of delocalized π-electrons is believed to be reduced. Thus, it seems to be necessary to optimize the degree of oxidation to achieve a desired magnetic ordering sustainable at sufficiently high temperatures. Alternatively, the Curie temperature of FM graphene oxide can be increased by doping with nitrogen; if the content of nitrogen reached 8.80 at% (calculated as 100 N/C at%), N-doped graphene oxide showed FM behavior with a saturation magnetization of 1.66 emu g^{-1} (at 2 K) self-sustainable up to 100 K.[447]

Upon chemical, electrochemical, thermal, photocatalytic, or electric-current reduction, the amount of oxygen-containing groups is decreased and graphene oxide is transformed into a reduced form.[438] In general, the reduction of graphene oxide increases the sp^2/sp^3 ratio, resulting in a decrease in the band gap and an increase in the conductivity. However, the conversion of graphene oxide to reduced graphene oxide does

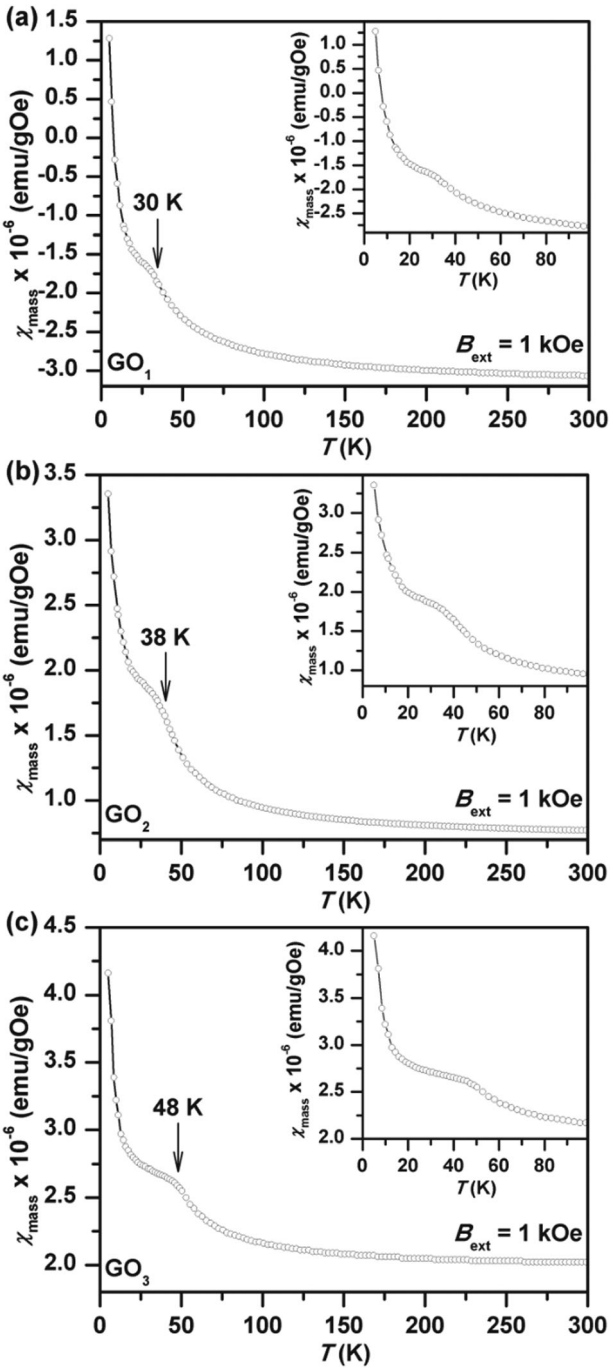

Fig. 104 (a–c) The temperature dependence of mass susceptibility (χ_{mass}) for graphene oxide with different degrees of oxidation ($GO_3 > GO_2 > GO_1$). The insets show the behavior of χ_{mass} at low temperatures. Reprinted with permission from ref. 446. Copyright 2016 The Royal Society of Chemistry.

not restore the features of pristine graphene since the conductivity of the reduced form is 10–100 times lower than that observed for ideal graphene. Moreover, besides residual oxygen-containing groups, reduced graphene oxide possesses structural defects including topological vacancies and pentagon–heptagon defects. A complete reduction to graphene was theoretically suggested to be hardly achieved due to a difficult removal of highly stable carbonyl and ether groups. Several studies reported FM behavior in reduced graphene oxide sustainable even at room temperature.[440,448,449] Fig. 105a shows an example of a sample composed of reduced graphene oxide sheets with saturation magnetization of $\sim$2.73 and $\sim$0.79 emu g^{-1} at 2 K and room temperature, respectively.[450] The origin of the FM response was explained in terms of defect states in the sheets of reduced graphene oxide. The defect states were found to be healed through several processes. Fig. 105b then displays the magnetization *vs.* field curves of reduced graphene oxide sheets annealed at various temperatures (in the interval from 200–800 °C). A sharp decrease in the value of the saturation magnetization ($\sim$0.08 emu g^{-1}) was noticed when reduced graphene oxide was annealed at 600 °C. At 600 °C, it was proposed that the defect states mend themselves by a self-repair mechanism that removes various vacancies and the C–C bond is reconstructed. The saturation magnetization then showed an increase with a further increase in the annealing temperature (700 and 800 °C). The increase in the saturation magnetization was understood as a result of the cleavage of the C–C bonds, which produces defects contributing towards an evolution of magnetism in reduced graphene oxide.[450] The paramagnetic centers in graphene oxide and reduced graphene oxide can be easily studied employing the ESR technique. A recent ESR study confirmed the formation of defect states in graphene oxide and its reduced form during the synthesis.[451] The shape of the ESR spectrum and the *g*-value then provide valuable information on the paramagnetic electrons and their interactions with the surrounding states.

A strong room-temperature FM ordering was observed for reduced graphene oxide prepared by high-temperature annealing of weakly oxidized graphene oxide in an Ar atmosphere.[452] The intrinsic nature of the witnessed ferromagnetism was confirmed by hysteresis in magnetoresistance. Graphene can exhibit both positive[453] and negative[454,455] magnetoresistance. The chiral nature of electrons in graphene is then believed to be responsible for a weak antilocalization manifested by a positive magnetoresistance.[456] The random resistor network caused by the inhomogeneous distribution of charged impurities was also suggested to produce a positive magnetoresistance.[364] In contrast, the formation of cyclotron orbits and delocalization effect under the influence of a magnetic field are then responsible for a negative magnetoresistance in graphene.[457–462] Fig. 106 and its inset display the temperature dependence of magnetoresistance and resistance, respectively, in weakly oxidized graphene oxide. Non-magnetic graphene does not show any hysteresis loop in either positive or negative magnetoresistance. The spin-dependent scattering of FM defects then causes the hysteresis of negative magnetoresistance.

Diamantopoulou *et al.*[463] studied the emergence of magnetism in graphene oxide and its alteration upon chemical reduction by sodium borohydride. Contrary to other experimental works, paramagnetic behavior with a saturation magnetization of $\sim$1.2 emu g^{-1} and weak AFM interactions were observed for pristine graphene oxide sheets. By employing the ESR technique, the presence of spatially isolated magnetic clusters carrying high spin moments (up to $S = 2$) was detected besides expected spin-half paramagnetic defect centers. If reduced, the saturation

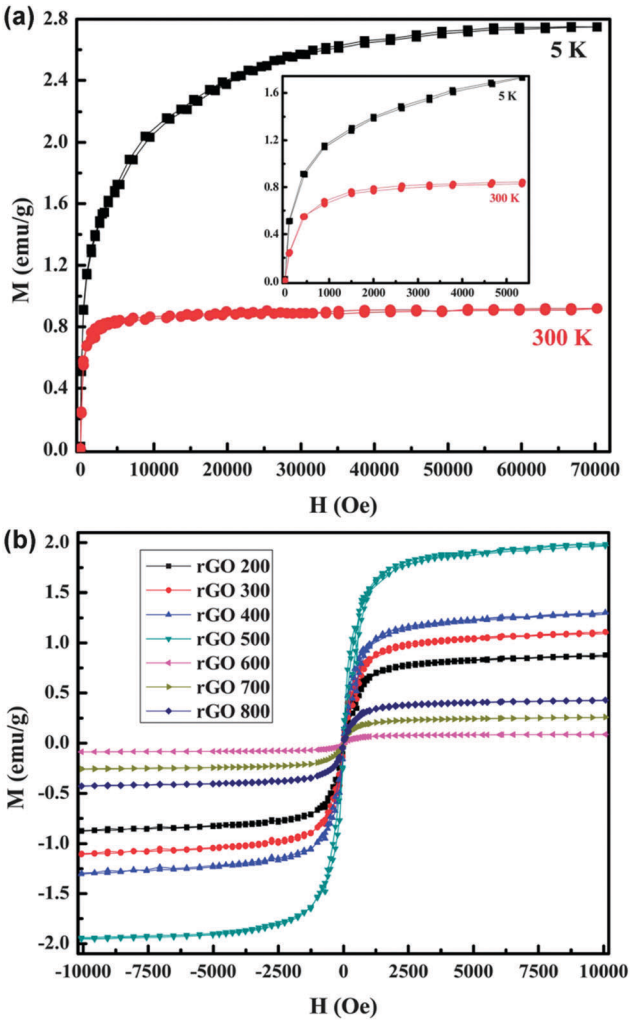

Fig. 105 Magnetization *vs.* field measurements for (a) reduced graphene oxide at 5 and 300 K and (b) reduced graphene oxide annealed at various temperatures (200–800 °C). Reprinted with permission from ref. 450. Copyright 2013 The Royal Society of Chemistry.

magnetization of the system dropped to ~0.17 emu g^{-1} with enhancement of a diamagnetic contribution, implying a dramatic elimination of paramagnetic centers and growth of sp^2 domains. From analysis of the ESR spectrum, two distinct spin systems were identified in chemically reduced graphene oxide, *i.e.*, localized π-defect states coupled strongly with the itinerant spins occurring within the formed sp^2 cluster and edge/vacancy defect spins, attributed to the persistent structural inhomogeneity in reduced graphene oxide after chemical reduction.[463]

Recently, room-temperature ferromagnetism was detected in reduced graphene oxide doped with nitrogen; such a system was prepared by direct reduction of graphene oxide in N_2 plasma at room temperature. The induced FM behavior was attributed to pyrrolic nitrogen bonding configurations; at low temperatures, pyrrolic nitrogen is predicted to be more stable than pyridinic and graphitic nitrogen.[464] Increased magnetization was found for reduced graphene oxide with increased doping with nitrogen; here, the N-doped reduced graphene samples were synthesized by annealing reduced graphene oxide,

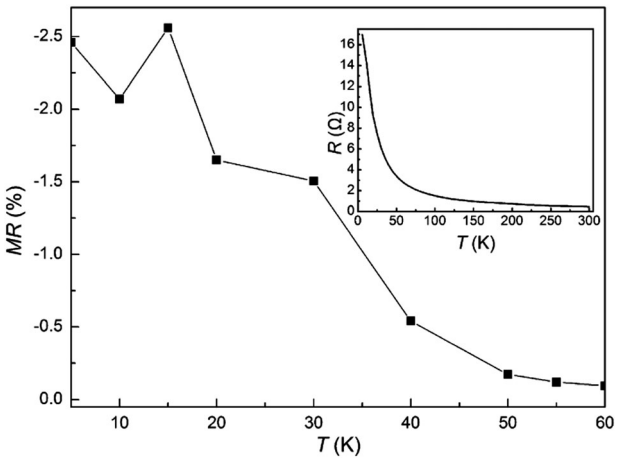

Fig. 106 Temperature dependence of magnetoresistance (MR) for weakly oxidized graphene oxide. The inset shows the temperature dependence of resistance (*R*) of weakly oxidized graphene oxide. Reprinted with permission from ref. 452. Copyright 2014 Elsevier Ltd.

pre-prepared by annealing graphene oxide in an Ar atmosphere at 700 °C for 1 h, in NH_3 at various temperatures (in the interval from 400 to 900 °C) for 1 h.[465] However, no clear scenario explaining an increase in the magnetization with increasing nitrogen content was suggested due to a complex interplay between pyridinic, pyrrolic, and graphitic nitrogen.[465]

The possibility of imprinting magnetism into graphene by covalent derivatization leading to graphene acid was recently suggested by DFT calculations (see Fig. 107).[466,467] The theoretical study of the thermodynamic stabilities of surface carboxylated graphenes, $C_x(COOH)_y$, with x/y ratios of up to the experimental value of 6.6 indicated, however, that most of the local COOH arrangements will be thermodynamically accessible with a small energy difference between them.[466] This implied that the topology of the carboxyl groups on the graphene surface will be given by a statistical distribution. One shall, however, notice that a statistical (random) distribution of the functional groups across the surface would prevent the formation of FM order. Therefore, experimental verification of the emergence of magnetic order in graphene acid is highly vital.

7. Magnetic ordering in graphene-based materials due to intercalation

Graphite intercalation compounds (GICs) have been extensively studied for more than a century; the earliest publication dates to 1840.[468–470] The advent of 2D materials has renewed interest in this field; reports on the intercalation of various species such as $FeCl_3$,[471–474] Ca,[475] Ce,[476] and Li[477] in few-layer graphene (FLG) have offered a new route to synthesizing graphene-based materials both for novel flexible displays and photovoltaics, as the associated electronics require materials that are flexible, optically transparent and electrically conductive, and for energy storage, magnetic/spintronic and superconductive applications. For the timely and comprehensive review of the recent progress

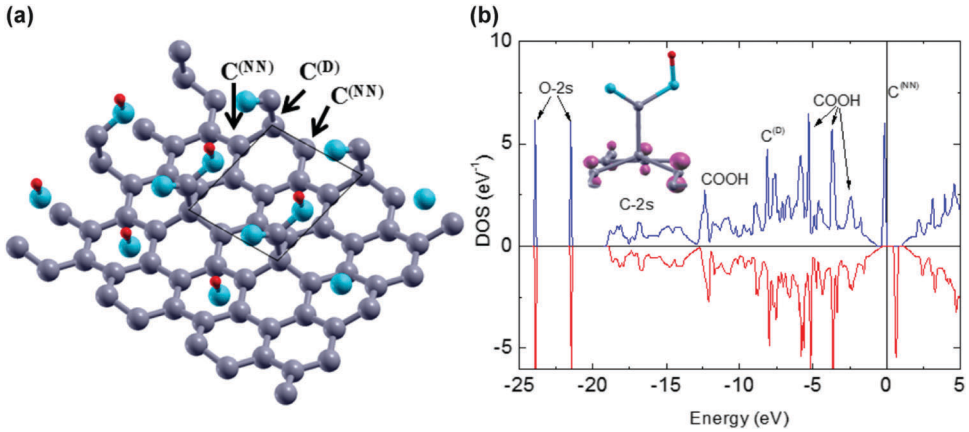

Fig. 107 (a) Model of carboxylated graphene sheet. (b) Theoretical density of states (DOS) of C_8COOH showing spin-polarized midgap states. The electron density associated with the spin-up channel of midgap states is shown in the inset. Reprinted with permission from ref. 467. Copyright 2017 American Chemical Society.

on intercalation methods, as well as tailored properties and potential applications offered by intercalation, the reader is referred to the work by Wan *et al.*[478]

The magnetic properties of $FeCl_3$ GICs have received significant attention in the last five decades mainly because they provide a model system for studying the magnetic phase transition of a 2D spin system.[479] *Ab initio* numerical simulations employing the Hubbard parameter (U), which reflects the strength of the on-site Coulomb interaction, and the J-parameter, which adjusts the strength of the exchange interaction, led to a theoretical understanding of the structural, electronic, and magnetic properties in $FeCl_3$-FLG.[480] It was reported that stage-1 $FeCl_3$-FLG has an AFM ground state and stage-2 $FeCl_3$-FLG exhibits FM ordering at the ground state (see Fig. 108). At the same time, the magnetic moments of $FeCl_3$ are expected to align ferromagnetically in the same intercalant layer.

More recently, Bointon *et al.*[481] *via* successful uniform intercalation of large area (1 cm^2) epitaxial FLG grown on 4H-SiC with $FeCl_3$ (see Fig. 109a and b) provided the evidence for magnetic ordering in the 2D limit of graphene. Fig. 109c shows the measured weak localization contribution to the magneto-conductance at various temperatures, which allowed extraction of the corresponding phase coherence length (L_φ; see Fig. 109d). Large values of L_φ for $T < 30$ K, a temperature matching the 2D magnetic correlations in the plane of $FeCl_3$, and a saturation of L_φ for T lower than $\sim$4 K, a temperature corresponding to three-dimensional (3D) AFM coupling between planes of $FeCl_3$, showed

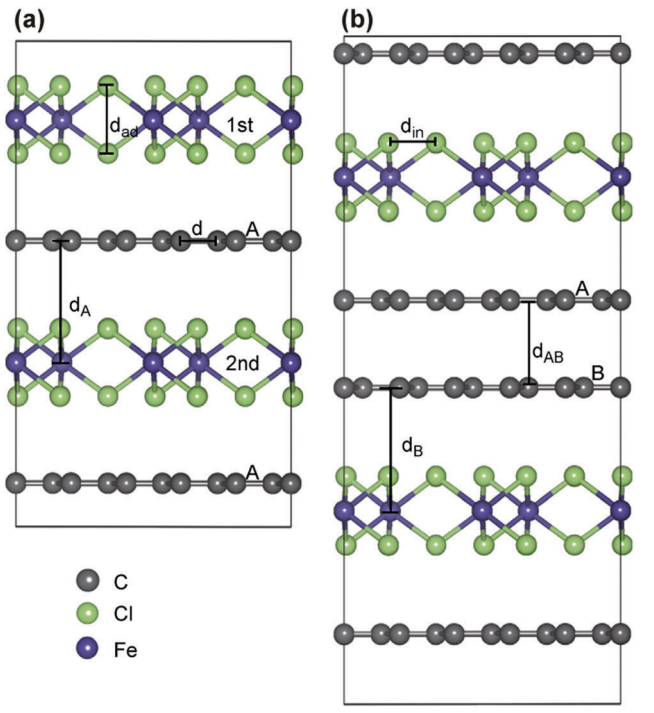

Fig. 108 GICs classified by the number of graphene layers between adjacent intercalant layers: (a) stage-1 $FeCl_3$-based GICs; (b) stage-2 $FeCl_3$-based GICs. Reprinted with permission from ref. 480. Copyright 2013 Elsevier B.V.

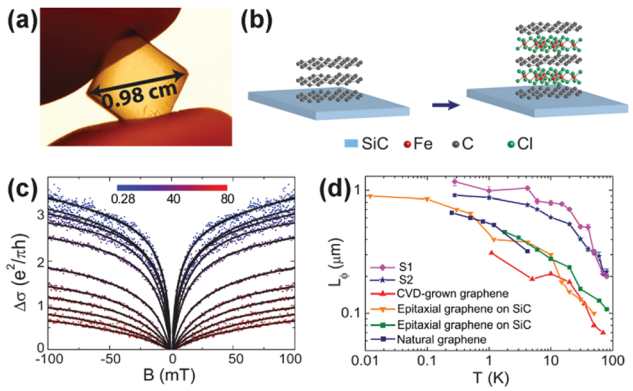

Fig. 109 (a) Intercalated FLG on 4H–SiC and (b) schematic crystal structure of trilayered stage-1 $FeCl_3$-FLG. (c) The measured weak localization contribution to the magneto-conductance (scatter points) and theoretical fits (solid line). (d) Temperature dependence of L_φ for pristine graphene prepared by different methods. The values are compared to the estimated values of $FeCl_3$/FLG. Reprinted with permission from ref. 481. Copyright 2014 American Chemical Society.

indeed that $FeCl_3$-FLG is a good platform for studying magnetic ordering in the extreme 2D limit of graphene.[481]

Graphene-based FM heterostructures have been considered as ideal candidates for a new class of tunnel magnetoresistance (TMR) or giant magnetoresistance (GMR) devices. Cutting-edge spin-polarized scanning tunneling microscopy (SP-STM) experiments combined with state-of-the-art first-principles calculations revealed an extremely high magnetic anisotropy energy for a cobalt-intercalated graphene/Ir(111) heterostructure (see Fig. 110a) with an out-of-plane easy axis (see Fig. 110b).[482] A series of spin-polarized dI/dV measurements of large surface areas, containing 33 intercalation regions of different sizes and various shapes acquired with a different out-of-plane magnetic field in the order of 0 T → −6.5 T → +6.5 T → −6.5 T and plotted as the percentage of area among all intercalation regions which were aligned in the +z direction *vs.* the applied field, showed a hysteresis loop (see Fig. 110c).[482] This indicated that even an upper field limit was not able to align 100% of the intercalation regions and, thus, the actual coercive field was higher than the value of ~4.5 T inferred from the loop. Further, the graphene layer presented a magnetic Moiré pattern with a high corrugation on the underlying cobalt monolayer. First-principles calculations showed that its origin lies in the variation of a site-dependent magnetization of the graphene: at top sites, the graphene was coupled ferromagnetically to the cobalt underneath, while it was antiferromagnetically coupled at fcc and hcp sites (see Fig. 111).[482]

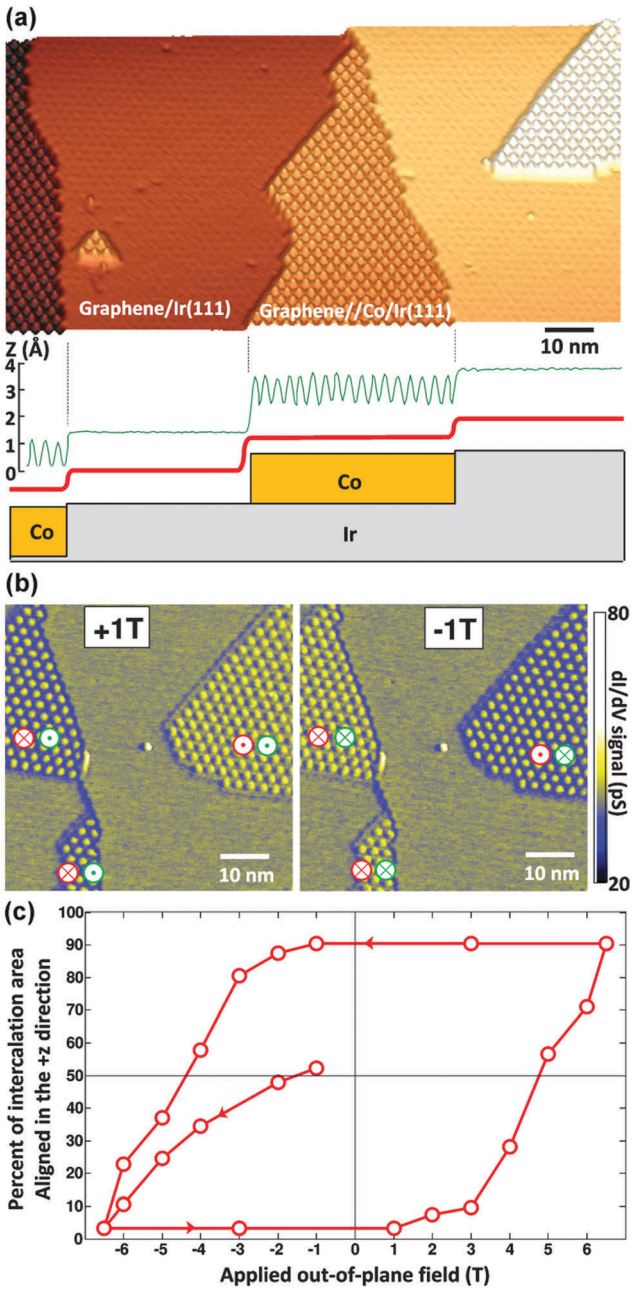

Fig. 110 (a) Topography of the graphene/Ir(111) surface. The line profile illustrates the difference between graphene/Ir(111) and graphene/Co/Ir(111) Moiré corrugations. (b) Maps of the spin-resolved differential tunneling conductance (dI/dV map) of the same area with an out-of-plane applied magnetic field of +1 T and −1 T, respectively. Green symbols represent magnetic orientation of the SP-STM tip and red symbols correspond to magnetic orientation of the intercalation regions. (c) Hysteresis loop obtained from large-scale spin-resolved dI/dV maps presenting 33 intercalation regions. Reprinted with permission from ref. 482. Copyright 2013 American Physical Society.

More recent spin-polarized low-energy electron microscopy (SPLEEM) experiments confirmed out-of-plane magnetization in thin-enough films of cobalt intercalated at the graphene/Ir(111) interface, while it is in-plane for thicker films.[483] Magnetization was purely out-of-plane for Co films thinner than 13 monolayers, while it was purely in-plane for Co films thicker than 24 monolayers. In the intermediate thickness range, magnetization exhibited a canted state. Vectorial imaging of magnetic domains revealed an unusually gradual thickness-dependent spin reorientation transition, in which magnetization rotated from out-of-the-film plane to the in-plane direction by less than 10° per cobalt monolayer. During this transition, cobalt films exhibit a meandering spin texture, characterized by a complex 3D, wavy magnetization pattern with a short wavelength, in which magnetic domains with a uniform magnetization separated by domain walls cannot be defined as the pattern resembles a flux closure configuration in three dimensions (see Fig. 112).[483]

Clearly, graphene-based magnetic heterostructures thus have the potential to open new prospects in nanomagnetism and surface magnetism.

8. Magnetism in selected graphene analogues and 2D materials

The recent progress in imprinting magnetism in otherwise non-magnetic graphene has aroused significant attention in the scientific community and prompted research on other 2D layered materials, of which layered transition metal dichalcogenides (TMDCs) are vital members.[484] While graphene is single atom thick, TMDC consists of transition metals in between two layers of chalcogen atoms. TMDCs are described by the formula MX_2, where M is the transition metal (*e.g.*, Mo, W, Ti, Nb, Re, V, Zr, Ta, Hf, *etc.*) and X denotes the chalcogen atom (*e.g.*, S, Se, or Te). The layers in any TMDC

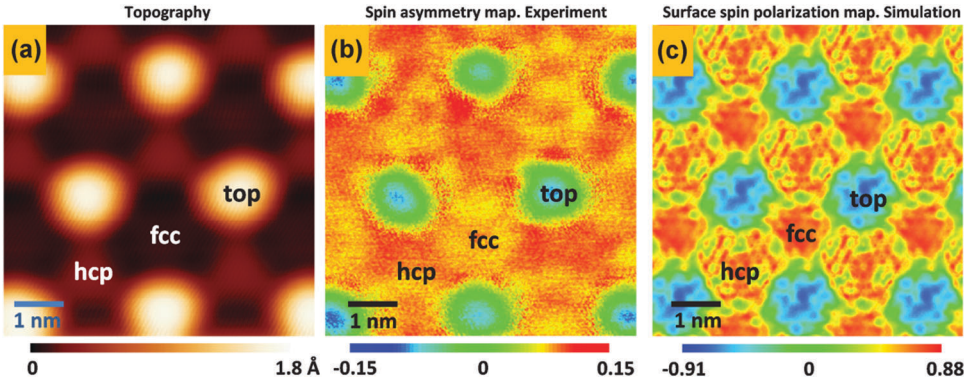

Fig. 111 (a) Topography of the Co-intercalated graphene/Ir(111) region. (b) Spin-asymmetry map of the region shown in panel (a). (c) Simulated surface spin polarization map. Panels (b and c) define a magnetic Moiré pattern of the graphene–Co/Ir(111) intercalation region. Reprinted with permission from ref. 482. Copyright 2013 American Physical Society.

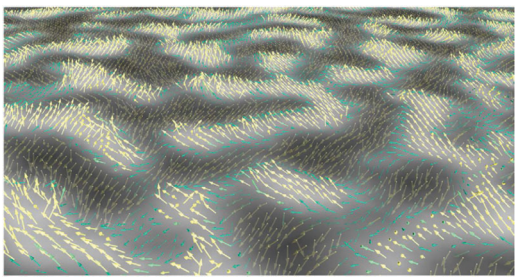

Fig. 112 Three-dimensional representation of the magnetization vector (arrows) in the case of 16 monolayers of graphene/Ir(111) intercalated Co. Dark and light domains represent the out-of-plane component of the magnetization vector. The magnetization vector is represented by colored arrows (yellow when magnetization is out-of-plane, green when it is in-plane) and smoothly rotates in all space directions in the form of waves across the field of view, like a wheat field in the wind. Reprinted with permission from ref. 483. Copyright 2016 Macmillan Publishers Limited.

are held tight by van der Waals interactions. Three crystallographic arrangements are recognized for such layered materials: (i) semiconducting 2H (trigonal prism) form, (ii) metallic 1T (octahedral) form, and (iii) semiconducting 3R (trigonal prism) form.[484–486]

Various single- and few-layered TMDCs have been synthesized and characterized so far.[487] They are frequently prepared by exfoliation, chemical vapor deposition, or molecular beam epitaxy techniques. There have been several reports on the magnetism of TMDCs published so far in the literature.[488–493] The pristine bulk form of molybdenum disulfide (MoS_2) shows only diamagnetism. Moreover, ESR studies on inorganic fullerene-like MoS_2 nanoparticles[494] confirmed the presence of a large density of dangling bonds carrying unpaired electrons that signifies a more defective nature than that of its bulk form. Like highly oriented pyrolitic graphite, MoS_2 exhibited room-temperature FIM order upon exposure to a 2 MeV proton beam with a Curie temperature of 895 K (see Fig. 113).[495] Proton irradiation can induce defects such as atomic vacancies, displacements, and saturation of a vacancy by the implanted protons which are all regarded as a possible source of the high-temperature magnetism. Recently, intriguing physical properties were theoretically proposed for the 1T′ phase of MoS_2.[496] In particular, it was found that the 1T′ phase of MoS_2, semi-metallic in nature, can host lattice imperfections more readily than its 2H phase; they preferentially form at the S atom closer to the Mo atomic plane. Local magnetic moments are then induced by the Mo adatoms and Mo antisites. In contrast, S vacancies, S adatoms, and Mo vacancies do not cause emergence of any spin polarization.[496]

The room-temperature ferromagnetism in MoS_2 has been mainly attributed to edge states, vacancies, vacancy clusters, and reconstruction of the lattices. Edge-oriented MoS_2 nanosheet-like films were shown to exhibit room-temperature ferromagnetism due to the presence of a high density of prismatic edges containing unsaturated Mo and S atoms.[497] Similarly, magnetization measurements on MoS_2 nanosheets of different sizes prepared by exfoliation of bulk MoS_2 in dimethylformamide solution revealed room-temperature ferromagnetism (see Fig. 114).[498] The X-ray photoelectron spectroscopy, TEM, and ESR results suggested that the origin of such FM order is related to the presence of edge spins on the edges of the nanosheets. Field-cooled (FC) and zero-field-cooled (ZFC) magnetization (see Fig. 114d) diverged from about 300 K. Such divergence of ZFC and FC magnetization curves is expected in magnetically frustrated systems (*e.g.*, spin glasses) where FM and AFM domains are randomly distributed. The nanosheets are non-magnetic beyond a certain thickness.[499] First-principles calculations on MoS_2 clusters showed a magnetic ordering arising due to the unsaturated metal center with partially filled d orbitals.[500] Besides, the FM response was detected in MoS_2 partly due to the presence of zigzag edges in the magnetic ground state.[501] Similar to GNRs, magnetic edge states were theoretically identified in MoS_2.[502] It was claimed that the magnetic ordering can evolve only due to the presence of sulfur-terminated edges resulting from splitting of metallic edge states at E_F. Moreover, first-principles calculations[503] predicted spin-polarized states in zigzag MoS_2 nanoribbons and spin-unpolarized ground states in armchair MoS_2. FM and metallic nature of zigzag-edged MoS_2 nanoribbons is independent of their width and

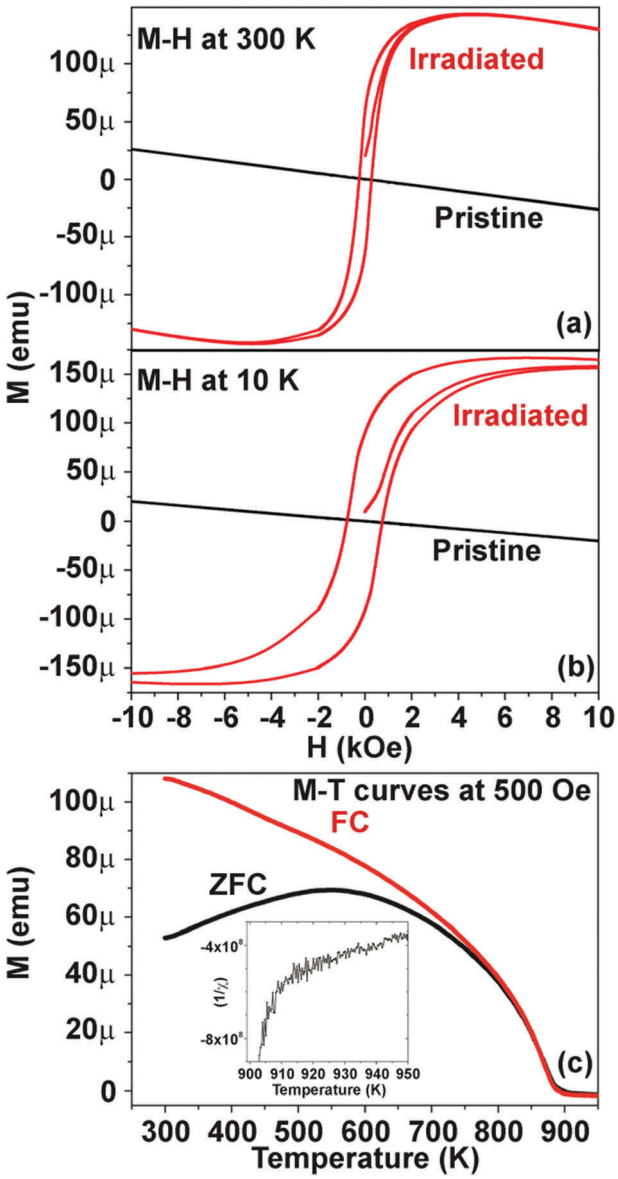

Fig. 113 Magnetization *vs.* magnetic field (*M vs. H*) curves (a) at 300 K and (b) at 10 K for an untreated and irradiated MoS_2. (c) Zero-field-cooled (ZFC) and field-cooled (FC) magnetization *vs.* temperature measurements in an applied field of 500 Oe for an irradiated MoS_2 at 5×10^{18} ions cm^{-2}. The inset shows the inverse of the estimated magnetic susceptibility *vs.* temperature plot near the Curie temperature (900–950 K). The estimated value of the Curie temperature is 895 K. Reprinted with permission from ref. 495. Copyright 2012 American Institute of Physics.

thickness, while the armchair nanoribbons are non-magnetic with a semiconducting behavior.

The possibility of imprinting FM behavior, sustainable at room temperature, by adsorption of light elements (*i.e.*, H, F, and Li) and exposed to strain was theoretically explored for MoS_2 monolayers.[504] Besides shifting E_F of MoS_2 in the conduction or valence band (depending on the charge polarity of the adsorbed atom), no induction of magnetic moments was found for adsorption at the S site. However, when the strain was applied increasing the density of states at E_F, magnetic moments emerged in MoS_2 with H, F, and Li adsorbed. Moreover, it was suggested that the FM state is more energetically stable than the AFM regime. Importantly, half-metallic ferromagnetism was found to emerge for the MoS_2 monolayers with H and F atoms adsorbed on their surfaces.[504]

Analogous to MoS_2, tungsten disulfide (WS_2) is non-magnetic in the bulk form. More recently, structural and magnetic properties of MoS_2 and WS_2 exfoliated using various alkali metal intercalating compounds such as butyllithium and sodium naphthalenide were thoroughly analyzed.[505] It has been shown that effective exfoliation, leading to the formation of a single layer of TMDCs by using sodium naphthalenide, and a corresponding phase transition from semiconducting 2H to metallic 1T polymorph along with the formation of defects on the edges of TMDC sheets resulted in the development of a room-temperature FM phase (see Fig. 115).[505] This effect was observed neither in bulk TMDCs nor in the butyllithium exfoliated samples. The latter exhibited a considerably lower degree of exfoliation and, accordingly, a lower concentration of defects on the edges of individual sheets as compared with sodium naphthalenide exfoliated materials, which further highlighted the role of structural disorder on the sheet edges in the conductive metallic phase of TMDCs for the room-temperature ferromagnetism.

Mao *et al.*[506] measured the saturation magnetization of WS_2 reaching a value of about 0.004 emu g^{-1} at 10 K. The corresponding magnetization *vs.* magnetic field plots of bulk and nanosheets at various temperatures are shown in Fig. 116.[506] The Curie temperature of WS_2 nanosheets estimated from the ZFC/FC plots, shown in Fig. 116c, is found to be $\sim$330 K.[506] Like graphene, the zigzag edges contribute to the ferromagnetism of WS_2 layers. In addition, the impurities can also trigger FM behavior in WS_2. DFT calculations show that doping of V, Nb, and Ta in WS_2 is preferred when WS_2 is rich in S instead of W. The doping causes a coupling between the dopant's unpaired d orbital and the nearest neighbors of W 5d and S 3p states, thereby inducing ferromagnetism. This signifies that the magnetic properties of such materials could be tuned using metal dopants.[507] First-principles theoretical computations for monolayered WS_2 nanoribbons suggest that zigzag edges are responsible for FM metallic behavior.[507] The magnetic moments reside at the W and S edge atoms. The magnetic ordering can be varied by changing the width of zigzag WS_2 nanoribbons.[507] In contrast, armchair WS_2 nanoribbons show a semiconducting behavior similar to their MoS_2 counterparts.

Recently, vanadium disulfide (VS_2) attracted significant attention due to the $3d^1$ electronic configuration of quadrivalent vanadium and strong electron coupling manifested, among others, by collective electronic behaviors including charge density wave order. More importantly, existence of intrinsic magnetic ordering was theoretically proposed to occur in VS_2 when the magnetic coupling can be readily tuned by a strain. The room-temperature FM ordering in VS_2 can be stabilized by a few-layered architecture;[508] if properly engineered, the van der Waals interactions were identified to play a crucial role providing regulation of spin properties and band gap in VS_2. Specifically, enlarging the van der Waals interactions was found to encourage a metal-

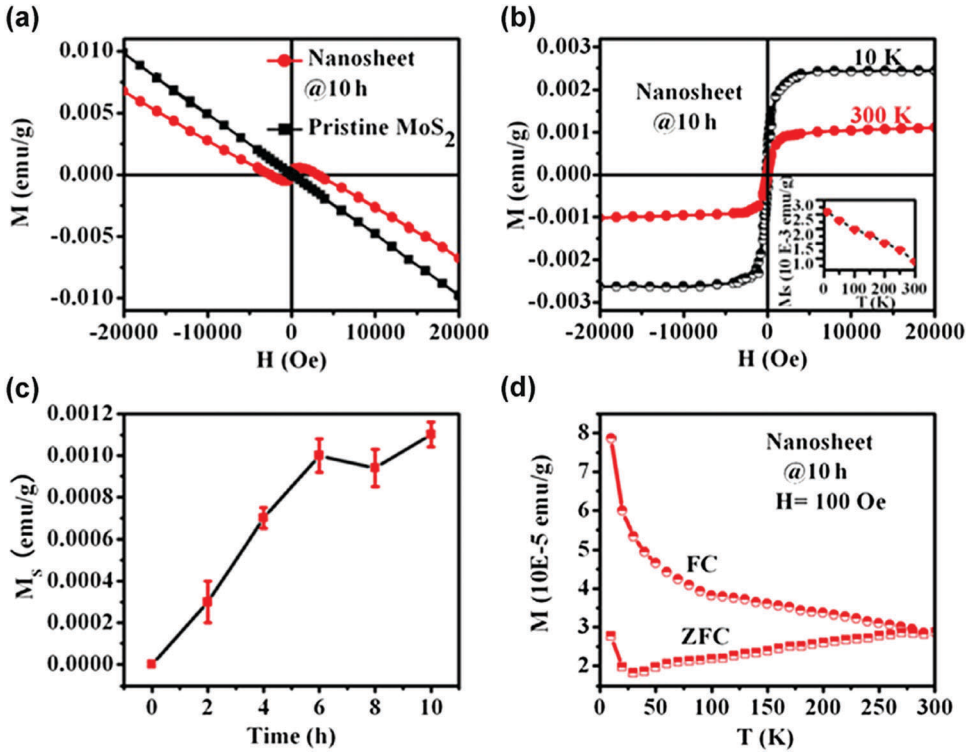

Fig. 114 (a) Room-temperature magnetization *vs.* magnetic field (*M vs. H*) curves for MoS_2 pristine powders and the exfoliated nanosheets (sonicated in dimethylformamide for 10 h). The exfoliated MoS_2 nanosheets show the FM signal in the lower field region, in contrast to MoS_2 powders which show only the diamagnetic signal. (b) *M vs. H* curves for MoS_2 nanosheets measured at 10 and 300 K. After deducting the diamagnetic signal, the saturation magnetizations (M_S) are 0.0025 and 0.0011 emu g^{-1} at 10 and 300 K, respectively, which are comparable to other dopant-free diluted magnetic semiconductors. (c) M_S of MoS_2 nanosheets increases as the ultrasonic time increases, and then becomes invariable when the ultrasonic time exceeds 6 h. (d) ZFC and field-cooled FC magnetization curves for the exfoliated MoS_2 nanosheets sonicated in DMF for 10 h. FC and ZFC magnetization curves diverge from about 300 K. Reprinted with permission from ref. 498. Copyright 2013 Springer.

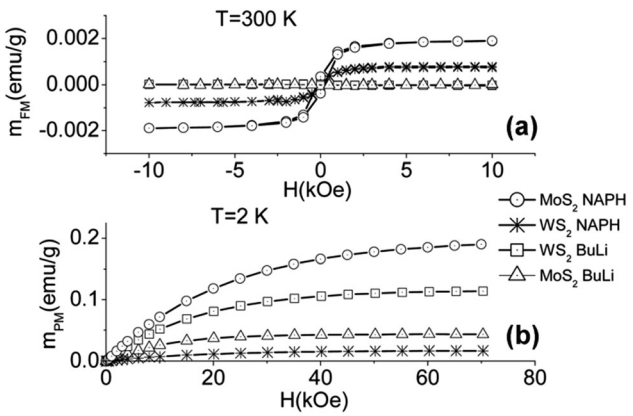

Fig. 115 Magnetization curves for MoS_2 and WS_2 at (a) T = 300 K and (b) at T = 2 K (measured data are depicted by symbols, lines correspond to theoretical calculations with S = 1) exfoliated by using butyllithium (BuLi) and sodium naphthalenide (NAPH). Reprinted with permission from ref. 505. Copyright 2016 The Royal Society of Chemistry.

to-semiconductor transition while compression of van der Waals interactions was responsible for strengthening the metallic behavior of VS_2 resulting from an increased overlap of chalcogens between the neighboring layers. Thus, both charge and spin degrees of freedom can be precisely tuned within the VS_2 lattice, which is viewed as highly promising for future generation of spintronic devices.[508]

Although ReS_2 is an inorganic analogue of graphene belonging to the TMDC family, it exhibits a unique distorted orthogonal structure with an in-plane structural anisotropy.[509] Re atoms in ReS_2 are dimerized due to the Peierls distortion to form the zigzag chains. Thus, the layers in ReS_2 are decoupled electronically and vibrationally, thereby reducing the layer-dependent physical and chemical properties. ReS_2 behaves as a diamagnetic semiconductor with a direct gap. If sulfur vacancies are present, they stabilize non-magnetic semiconducting ground states. In contrast, rhenium vacancies promote generation of spin-polarized ground states with localized magnetic moments ranging from 1 to 3 μ_B; however, the formation of a Re vacancy needs much larger energy and is, thus, less likely to occur.[509] Moreover, the theoretical calculations suggest the formation of mid-gap states due to fluorination of the Re chains.[510] AFM coupling between Re chains and FM coupling within Re chains are observed for the metallic mid-gap states, while the semiconducting mid-gap states show no magnetic couplings. Recently, ReS_2 was also found to possess FM behavior at its wrinkled regions.[511] In addition, adsorption of nitrogen and phosphorus atoms on the ReS_2 sheets was found to generate spin-polarized defect states, leading to a half-semiconducting behavior.[512]

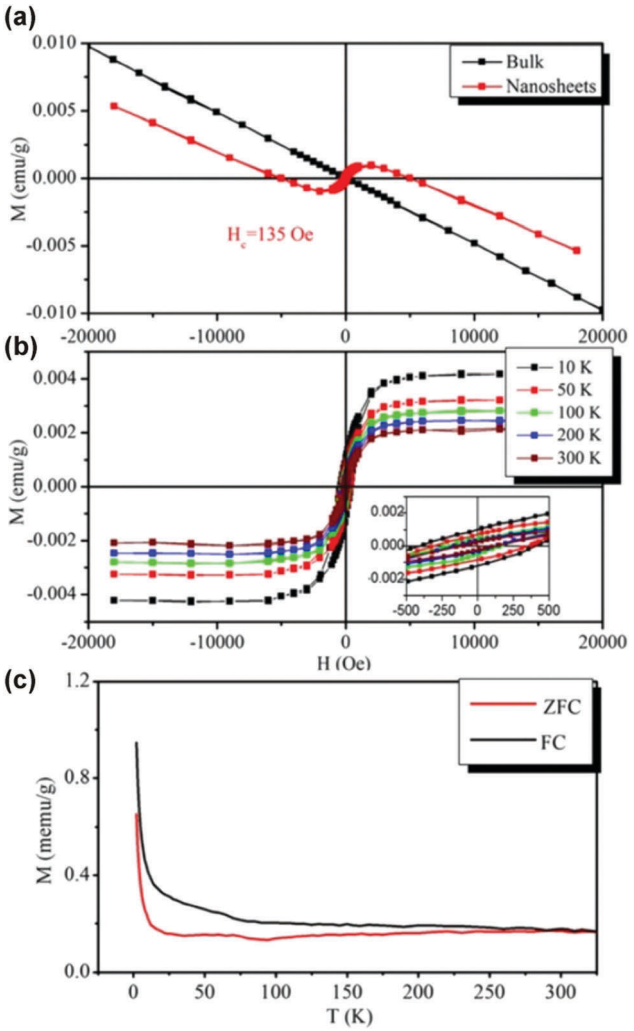

Fig. 116 (a) Magnetization *vs.* magnetic field (*M vs. H*) curves for bulk and nanosheets of WS_2, (b) *M vs. H* plot of WS_2 nanosheets at different temperatures with background correction, and (c) ZFC/FC magnetization curves of WS_2 nanosheets. Reprinted with permission from ref. 506. Copyright 2013 Springer.

Significant attention was also devoted to $MoSe_2$-, WSe_2-, and $ReSe_2$-type TMDCs with potential evolution of magnetically-ordered regimes. In particular, room-temperature FM behavior was observed for WSe_2 nanosheets; employing the MFM technique, the magnetic regions were identified to be located at the edges.[513] The existence of edge magnetic moments was also confirmed by the theoretical calculations, originating from unsaturated Se and W atoms at the edges. More specifically, FM ground states were found to exist only in cases when the edges are terminated fully or by 50% terminated by Se atoms. Upon increasing the thickness of the WSe_2 nanosheets, FM response was observed to decrease rapidly, disappearing at a critical number of layers (*i.e.*, 6 atomic layers).[513] Alternatively, application-promising magnetic features can be tuned by doping as proved for the $MoSe_2$ nanosheets.[514] The recent theoretical study on doped $MoSe_2$ systems showed that if N and F atoms are substituted (at a concentration of 3.12 at%) at the Se-sites (*i.e.*, under Mo-rich conditions) to the $MoSe_2$ crystal structure, an FM ground state is expected. More interestingly, a half-metallic ferromagnetism appeared for the Cl-, Br-, and I-doped $MoSe_2$ nanosheets. The origin of magnetism in such atom-substituted systems was then explained in terms of the p–d hybridization between the p orbitals of doped atoms and the d orbitals of the neighboring three Mo atoms.[514] Similarly, a room-temperature ferromagnetism was recently reported for the Re-doped $MoSe_2$ systems stemming from ordering of the next nearest-neighboring Re pairs.[515] In the $ReSe_2$-based systems, the magnetic ground state can evolve due to a cationic defect (*i.e.*, Re vacancy), resulting in the reconstruction and orbital hybridization between neighboring Se atoms; the magnetic response can be significantly regulated by the external strain, modifying the distribution of the spin polarization among neighboring Se atoms.[516]

Monolayered metal dihalides, *i.e.*, MX_2 where X = Cl, Br, I, are regarded as a new class of 2D materials with crystal structures closely resembling those of TMDCs; in metal dihalides, a layer of transition metal atoms is sandwiched between two layers of halogen atoms. In the family of metal halides, $GaBiCl_2$, ZrBr, and HfCl monolayered nanosheets were found to behave as room-temperature quantum spin Hall insulators with large and nontrivial band gaps.[517,518] FM ordering was, for example, observed for monolayered $FeCl_2$[519] and CrI_3,[520] the former with a half-metallic feature and the latter with a remarkable out-of-plane spin orientation. Very recently, an FM ground state was reported for 2D $FeCl_2$, $FeBr_2$, FeI_2, $NiCl_2$, $NiBr_2$, NiI_2, $CoCl_2$, and $BoBr_2$ whereas an AFM ground state was identified for VCl_2, VBr_2, VI_2, $CrCl_2$, $CrBr_2$, CrI_2, $MnCl_2$, $MnBr_2$, and MnI_2 nanosheets; the existence of different magnetic states in metal halides was explained in terms of the competition between AFM direct nearest-neighbor d–d exchange interactions and FM exchange interactions mediated by the halogen p-states.[521] In addition, it was proposed that the values of the Curie temperature calculated for transition metal halides are comparable to those of TMDCs due to a tight ionic bonding in halides, significantly encouraging the superexchange interactions between the magnetic metal ions *via* the halogen atoms.[521] Furthermore, a half-metallic feature was predicted for a family of iron dihalides, *i.e.*, $FeCl_2$, $FeBr_2$, and FeI_2 (see Fig. 117a).[522] They show a large magnetic moment of 4 μ_B, originating from high-spin d^6 Fe^{2+} octahedral coordination, and an easy magnetization plane characterized by no energy requirement for rotation of the magnetic moment within the plane of the 2D layer. In addition, large half-metallic spin gaps were identified for iron dihalides, *i.e.*, 6.4, 5.5, and 4.0 for $FeCl_2$, $FeBr_2$, and FeI_2, respectively, resulting from a quantum confinement effect. Such 2D materials can then be used in a potential spintronic device illustrated schematically in Fig. 117b;[522] the hypothetical magnetic tunnel junction is composed of a BN tunneling layer sandwiched between two half-metallic contacts, one from $FeCl_2$ and the other from $FeBr_2$. Here, the magnetoresistance is maximized by the 100% spin polarization of 2D $FeCl_2$, $FeBr_2$, and FeI_2. Moreover, such 2D half-metals can be used in Datta–Das spintronic transistors or spin transistors with a high

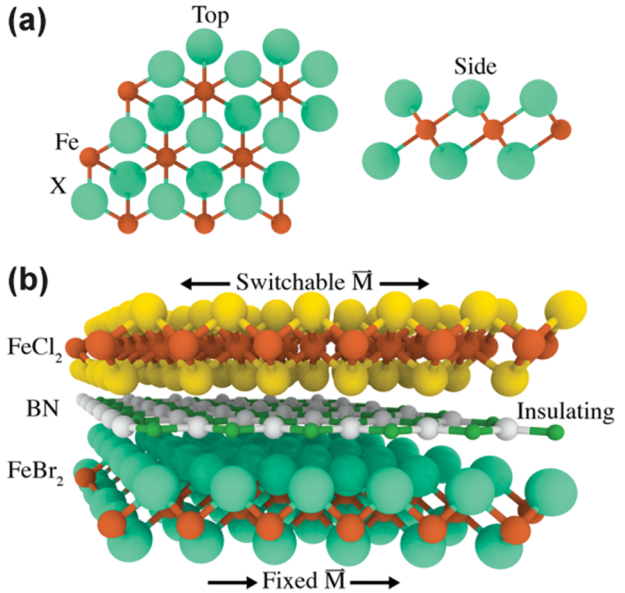

Fig. 117 (a) Top and side views of the crystal structure of 2D iron dihalides ($FeCl_2$, $FeBr_2$, and FeI_2). (b) Scheme of a hypothetical magnetic junction based on 2D iron dihalides. The magnetization of the top layer can be reoriented by an external magnetic field while the magnetization of the bottom layer is pinned by a suitable substrate. The junction operates in "ON" and "OFF" states corresponding to parallel and antiparallel orientation of the layers, respectively. Reprinted with permission from ref. 522. Copyright 2017 American Chemical Society.

transmissivity (promoted by spin–orbit coupling from an appropriate insulating layer).[522]

Transition metal dinitrides are regarded as another class of atomic-scale materials. MoN_2 is a typical example of 2D transition metal dinitrides; due to inability of Mo to saturate all three 2p orbitals of N, a spontaneous magnetic moment is believed to emerge at N sites.[523] 2D MoN_2 was proposed to behave as a ferromagnet with a theoretically calculated Curie temperature of 420 K. The advantage of MoN_2 over other 2D materials relies on the nature of magnetism originating from electron-deficient N orbitals when no doping or structure modification is needed to imprint magnetic features. Moreover, MoN_2 can be turned to a half-metal once exposed to a tensile stress. In contrast, YN_2 and 1T-TaN_2 are intrinsically half-metallic with an FM ground state;[523,524] in 1T-TaN_2, the magnetic moments and half-metallic behavior are mainly ascribed to the p orbitals of N instead of d orbitals of Ta atoms, which is believed to be beneficial to overcome a problem with a short spin relaxation time caused by a large spin coupling of transition metal atoms.[524] Other recently studied 2D half-metallic materials with a robust FM ground state and high Curie temperature include, for example, Fe_2Si,[525] Co_9Se_8,[526] and g-C_4N_3;[527] moreover, Fe_2Si shows a large magnetic anisotropic energy.[525]

The half-metallic behavior was also theoretically suggested to occur in free-standing 2D purely organic dimethylmethylene-bridged triphenylamine (DTPA) porous sheets.[528] The structure of a DTPA molecule closely resembles that of triangular zigzag-edged GNF, when the central carbon atom is substituted with a nitrogen atom; isolated DTPA molecule is magnetic and

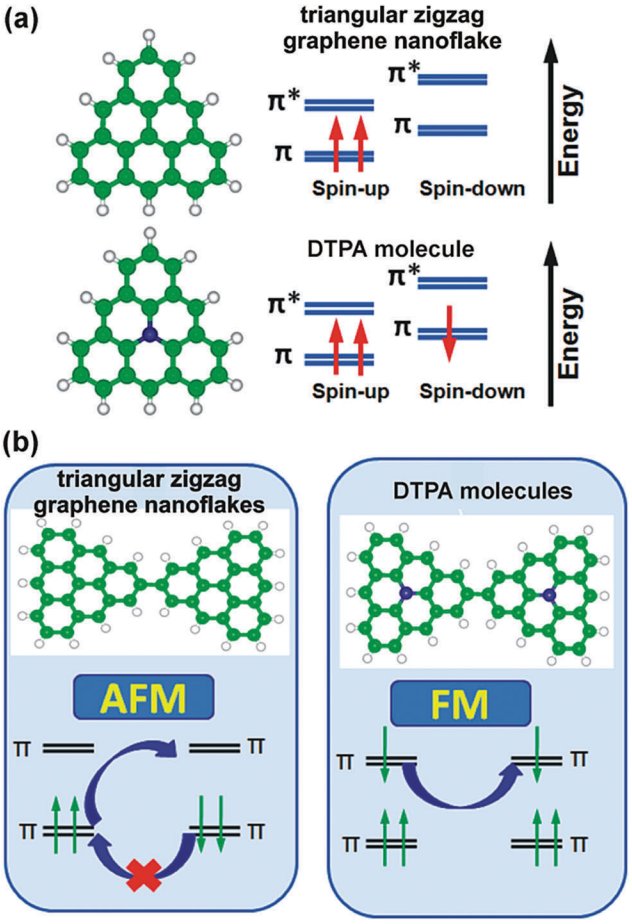

Fig. 118 (a) Structures and schematic diagrams of spin-resolved orbital energy levels for a triangular zigzag-edged GNF and a DTPA molecule. (b) Schematic diagrams showing exchange mechanisms for 2D sheets composed of triangular GNFs and DTPA molecules. AFM/FM ground state is favored by virtual hopping. In panels (a and b), the blue, green, and white balls represent nitrogen, carbon, and hydrogen atoms. Reprinted with permission from ref. 528. Copyright 2012 American Chemical Society.

carries a magnetic moment of 1 μ_B (see Fig. 118a). If 2D DTPA molecules form a network, an FM ground state is favored contrary to an AFM ground state for a 2D sheet composed of GNF molecules (see Fig. 118b). Moreover, the band gap in the semiconducting channel was estimated to be $\sim$1 eV and half-metallicity was found to be robust if the 2D DTPA porous sheet was exposed to a strain with values well beyond those evoked by a substrate.[528]

MXenes belong to another emerging family of 2D materials; they include 2D-transition metal carbides, nitrides, and carbonitrides and are described by the general formula $M_{n+1}X_nT_x$, where M denotes a transition metal, X represents C and/or N, T stands for O, OH and/or F, and n = 1, 2, or 3. Currently, the class features more than 100 members, both theoretically predicted and experimentally synthesized. Thus, it is highly expected to achieve desired magnetic properties for MXenes upon suitable combinations of the transition metal involved and surface termination groups used. Among MXenes, Cr_2N and Cr_2C monolayers were found to be very appealing as they

intrinsically show the FM ground state and half-metallic behavior.[529] However, their magnetic features can be dramatically altered by surface terminating groups (*i.e.*, F, OH, H, and Cl), eventually losing their ferromagnetism and half-metallicity and, instead, becoming AFM semiconductors.[530] Nearly half-metallic ferromagnetism was proposed for Ti_2C and Ti_2N monolayers;[531] while Ti_2C is supposed to undergo a phase transition from a nearly half-metallic state to a half-metallic, spin-gapless semiconducting, and metallic regime upon a gradual increase in the biaxial strain, Ti_2N retains its nearly half-metallic properties irrespective of the biaxial strain applied. On the other hand, V_2C and V_2N, showing AFM and non-magnetic ground states, respectively, can be equipped with large magnetic moments once exposed to the biaxial tensile and compressive strains.[531] Recently, theoretical calculations were used to comprehensively address the issue of magnetism in nitride MXenes, particularly focusing on identification of those representatives with intrinsic FM ground states that are stable and robust enough with regard to the surface terminations and thermal fluctuations at room temperature.[532] Due to an additional electron from nitrogen, the FM phase is energetically favored in nitride MXenes in line with the Stoner criterion. In addition, the two oxidation states of the transition metal atom can coexist in nitride MXenes promoting evolution of the double exchange mechanism. More specifically, Mn_2NF_2, Mn_2NO_2, $MnN(OH)_2$, Ti_2NO_2, and Cr_2NO_2 were found to show a robust FM ground state with a magnetic moment per formula unit reaching up to 9 μ_B.[532] For these systems, the interlayer and intralayer couplings are of FM nature and the Curie temperatures lie in the interval from 566 to 1877 K. Moreover, a half-metallic behavior was predicted for Mn_2N MXenes with a wide band gap for the minority spins for all three surface terminations (*i.e.*, F, O, and OH). In contrast, an AFM ground state was calculated for Ti_2NF_2, $Ti_2N(OH)_2$, V_2NF_2, V_2NO_2, $V_2N(OH)_2$, Cr_2NF_2, and $Cr_2N(OH)_2$ monolayers; for these systems, the interlayer interaction is of FM character while AFM interactions are expected within one layer.[532] The stabilization of either FM or AFM ground state in nitride MXenes can be understood in terms of relative strengths of the superexchange and double exchange interactions. From the theoretical analysis, it can then be inferred that oxygen termination should be considered in syntheses of nitride MXenes as it encourages a robust FM ground state.[532] High magnetic moments (from 3 to 4 μ_B per unit cell) and high Curie temperatures (from 495 to 1133 K) were also predicted for $Hf_2MnC_2O_2$, $Hf_2VC_2O_2$, and $Ti_2MnC_2T_x$ (with T = O, OH, and F) monolayers.[533] Moreover, if exposed to the tensile in-plane strains, these double-transition metal MXene structures are expected to show semi-metal-to-semiconductor and FM-to-AFM phase transitions.[533]

Among graphene-related materials, hexagonal boron nitride (h-BN) has also received significant attention, as the h-BN polymorph, which is remarkably similar to graphene with the alternating B and N atoms forming two-dimensional layers of strong sp^2 bonds within a honeycomb arrangement, can be well suited for integration with graphene as their lattice constant mismatch is less than 2%.[534,535] Furthermore, h-BN shows enhanced chemical and thermal stability resulting from a bond ionicity that can localize the electron states. There is, however, an important difference, *i.e.*, due to the chemically inequivalent sublattices, h-BN is an insulator with a band gap of 6.0 eV.[536] Similar to graphene, h-BN can also form nanotubes, nanoribbons and other similar structures.

Theoretical calculations predicted that several factors may give rise to the magnetic state in h-BN systems, including defects in the atomic network,[537–539] substrate-induced magnetism,[540,541] and bare-edge localized states.[542] Many growth techniques yielded few-layered h-BN.[543] Recently, magnetization measurements performed on few-layered h-BN nanosheets, exfoliated from bulk by using a mechanical cleavage approach, revealed room-temperature FM order with a Curie temperature above 400 K (see Fig. 119),[543] in contrast to the pristine diamagnetic h-BN system. Further, DFT calculations and spherical-aberration

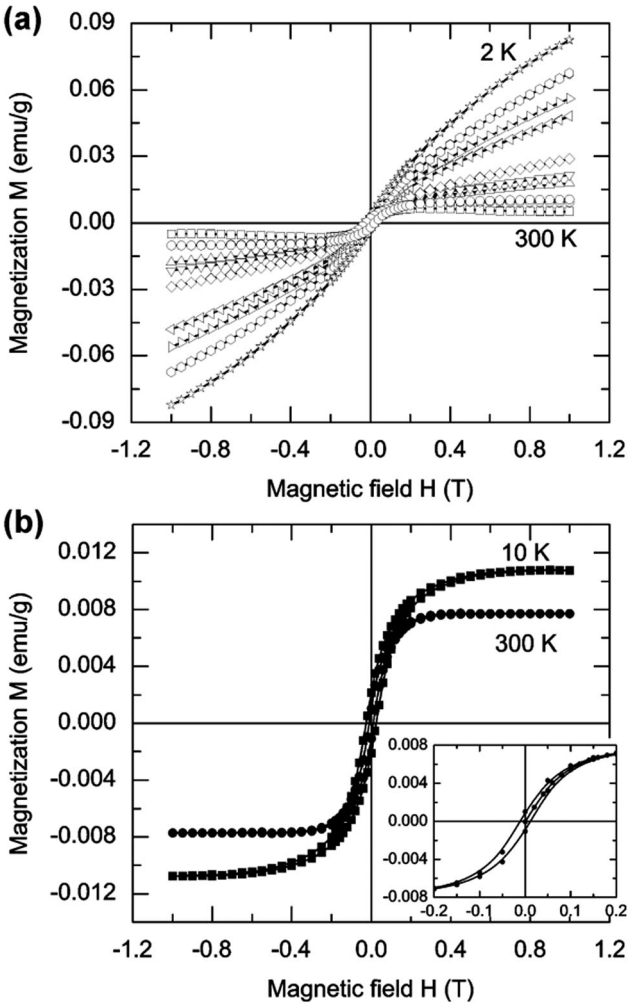

Fig. 119 (a) Magnetization *vs.* magnetic field (*M vs. H*) curves of few-layered h-BN nanosheets for various temperatures in the range of 2–300 K from top to bottom. (b) Magnetization (*M*) after subtracting the paramagnetic and diamagnetic signals as a function of magnetic field (*H*) at a temperature of 10 and 300 K. The inset shows a smaller field region of the hysteresis loop at T = 300 K, which exhibits a typical FM character. Reprinted with permission from ref. 543. Copyright 2014 AIP Publishing LLC.

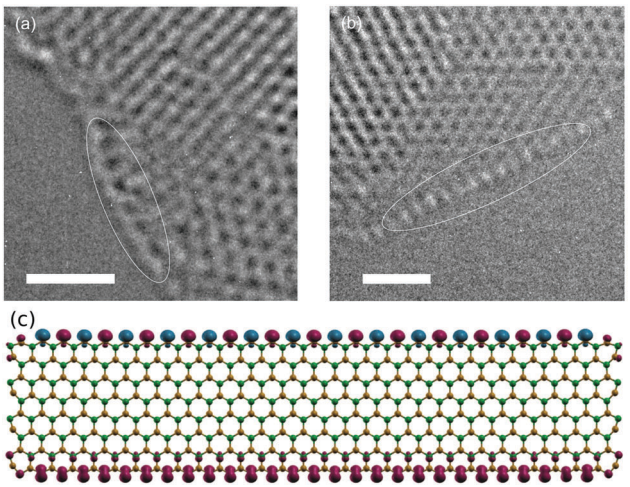

Fig. 120 SACS-TEM images of h-BN showing (a) distorted pentagonal rings and (b) zigzag edges. The scale bars are set to 1 nm. (c) Theoretical h-BN nanoribbon and the corresponding spin-density distributions (red and blue isosurfaces denote spin-up and spin-down, respectively), where distorted pentagonal rings at the armchair edges and magnetic moment localized mainly at the zigzag edges are visible. Boron and nitrogen atoms are represented by yellow and green spheres, respectively. Reprinted with permission from ref. 543. Copyright 2014 AIP Publishing LLC.

corrected transmission electron microscopy (SACS-TEM) revealed a hexagonal–pentagonal ring transition at the armchair edges. The distorted armchair edges carried relatively small magnetic moments. The main FM contribution stemmed, however, from the FM ordering at the N-zigzag edges, whereas B-zigzag edges exhibited AFM coupling (see Fig. 120).[543]

It was theoretically proposed that the magnetic properties of h-BN are independent of the N-vacancy defects.[538] The nearest nitrogen atoms get the spin polarization by the B-vacancy defects, thereby creating a magnetic moment of 0.87 μ_B within the muffin-tin radius. Only a weak spin polarization of about 0.1 μ_B evolves due to the B-adatom defects, while in the case of the N-adatom defects, a larger magnetic moment of about 0.38 μ_B is predicted to emerge. Furthermore, another set of first-principles calculations were employed to understand the effect of non-magnetic impurities on the magnetism of BN sheets.[538] To do so, a rectangular supercell with cell dimensions of 20.05 and 17.37 Å was constructed (see Fig. 121a).[538] Be, B, C, N, O, Al, and Si atoms were selected to replace B or N atoms to change the density of states and spatial distribution of defect states. Fig. 121b then shows the calculated magnetic moments as a function of the nearest-neighbor distance (d_D).[538] The partially filled defect bands produced finite magnetic moments. Moreover, C and Ge atoms were found to preferentially dope the B-sites than the N-sites; for the 3-fold doping configurations, the spins were localized dominantly on the Ge-p/d orbitals and C-p orbitals.[544] In contrast, the 4-fold C_{BN} and Ge_{BN} doping configurations did not cause evolution of any magnetism due to sp^2d and sp^3 type of hybridization. Nevertheless, a spin filtering phenomenon was observed under various bias voltages for h-BN systems doped with carbon at the B- and N-sites and germanium at the B-sites.[544] Spontaneous magnetization can also be induced by adsorption of single H atoms on the external surface of BN nanotubes. However, adsorption of two H atoms on two neighboring N atoms or on two neighboring B and N atoms results in no magnetic ordering. The magnetic moment can be induced if the two adsorbed H atoms are attached to the two B atoms, which are separated. The hydrogenated BN nanotubes exhibited zero magnetic moment if an odd number (1 or 3) of H atoms were adsorbed on a vacancy defect, while an even number of H-atom adsorptions induced a finite magnetic moment.[538] This clearly illustrates the general criteria for the existence of magnetism due to unpaired electrons. Such a magnetic behavior is very promising

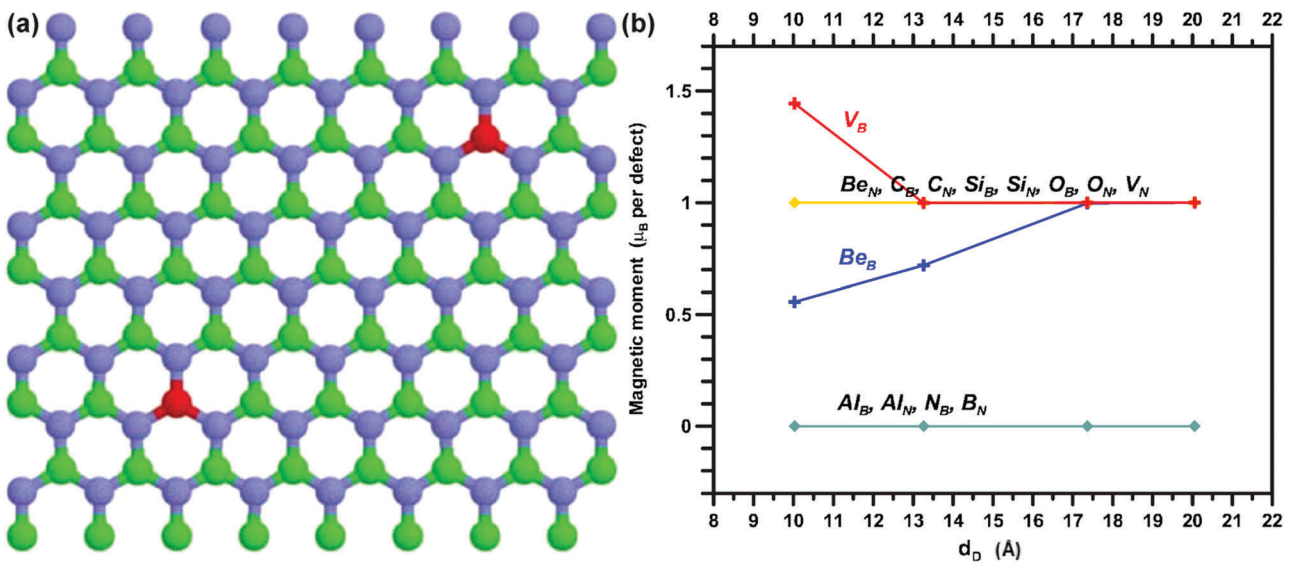

Fig. 121 (a) Rectangular supercell structure containing 64 primitive cells of BN sheets (dimensions: 20.05 and 17.37 Å). (b) Magnetic moment of the supercell as a function of the nearest-neighbor distance (d_D). Reprinted with permission from ref. 538. Copyright 2007 American Physical Society.

for realizing devices only when it could be tuned by application of an external force.[538] The ground state magnetic moment of the defects can be tailored by modifying the geometry by a stress.[545] In this respect, it was shown that a triangular shape of defects may create strong spin localization in the magnetic state. The magnetic moment of these defect states and the N–N distance are strongly related to each other.

Similar to the case of graphene, the magnetic properties of h-BN predominantly vary upon functionalization. A suitable surface functionalization may result in h-BN becoming FM, AFM or magnetically degenerate.[546] As h-BN is heteroatomic in nature, doping can generate anisotropic structures with interesting electronic and magnetic features. Hydrogenation and fluorination in h-BN are endothermic and exothermic processes, respectively. The band gap of h-BN sheet can vary from 4.7 to 0.6 eV depending upon the degree of hydrogenation while graphene undergoes a metal-to-insulator transition when it is fully hydrogenated. Theoretical calculations[547] showed that a spontaneous magnetization is induced upon chemisorption of F atoms on the B atoms in an h-BN nanotube. The evolved magnetic ordering can disappear if both B and N atoms are equally fluorinated. Similarly, fluorination was predicted to promote room-temperature ferromagnetism with a half-metallic feature for h-BN single layers; the partially filled bands were proposed to develop due to the large number of holes.[548] Experimentally, after exfoliation, h-BN nanosheets can be readily fluorinated with ammonium fluoride (NH_4F); such fluorinated h-BN single layers were observed to show FM behavior up to the deduced Curie temperature of $\sim$580 K.[549] From the theoretical calculations, it also turned out that the magnetic moments evolved from the spin polarization of F and three N atoms sitting nearest to the sp^3-hybridized B atom underlying the F atom.[549]

Finally, very recent computational discovery of new 2D materials with a high Néel temperature[550] and Curie temperature[551,552] must be mentioned. The former includes Cr_2CFCl, Cr_2CClBr, Cr_2CHCl, Cr_2CHF, and Cr_2CFOH for which a Néel temperature reaching 400 K has been predicted (see Fig. 122).[550] The latter includes Mn_2CF_2 with a Curie temperature of 520 K (see Fig. 123a–c)[551] and $NiCl_3$ with a Curie temperature of $\sim$400 K (see Fig. 123d).[552]

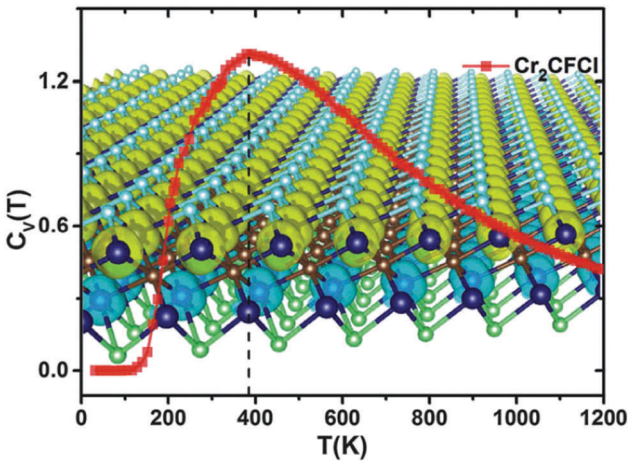

Fig. 122 Specific heat (C_V) *vs.* temperature plot simulated for Cr_2CFCl. The background figure displays spin-polarized charge densities, where spin-up (-down) densities are shown in yellow (cyan). Reprinted with permission from ref. 550. Copyright 2016 The Royal Society of Chemistry.

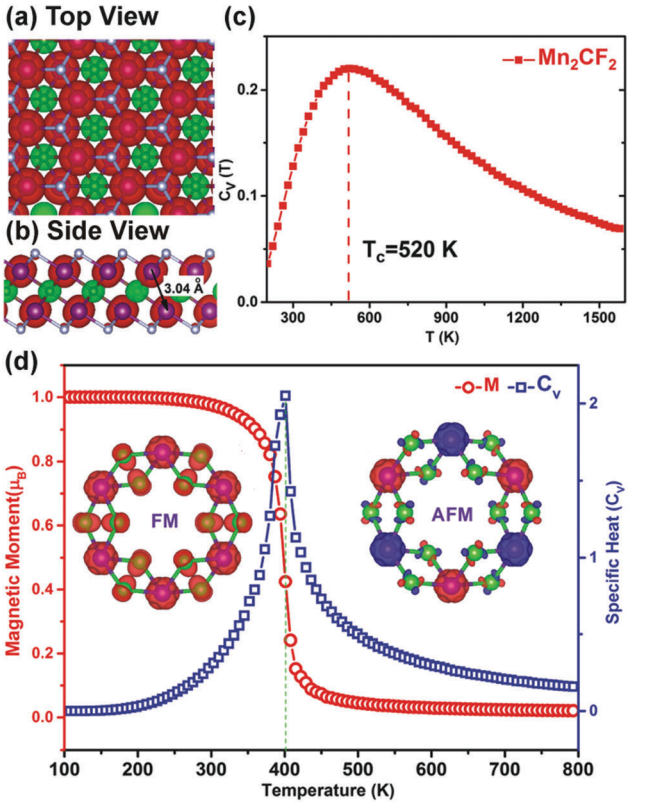

Fig. 123 (a and b) Theoretical spin-polarized charge densities of Mn_2CF_2, where spin-up (-down) densities are shown in red (green). (c) Specific heat (C_V) *vs.* temperature plot simulated for Mn_2CF_2 with the Curie temperature (T_C) indicated. Reprinted with permission from ref. 551. Copyright 2016 The Royal Society of Chemistry. (d) Average magnetic moment (red) and C_V (blue) *vs.* temperature plot calculated for a monolayer of $NiCl_3$. Isosurfaces of spin-polarized charge densities are depicted in the insets. Reprinted with permission from ref. 552. Copyright 2017 The Royal Society of Chemistry.

9. Magnetic impurities in graphene-based systems and methods of deconvolution of individual contributions to the magnetic response

The magnetism of carbon-based materials containing only s- and p-electrons is very intriguing and a much debated topic in the literature. Here, it should be stressed that the observed magnitude of magnetization is comparable to that of the background. Thus, it is very important that the measurement process is accurate and free of errors. Several errors can often happen during data collection in the measurement. Briefly, we present a few important issues that are constantly faced by experimentalists

during the data collection process and should be taken into consideration for accurate measurements/interpretations.

Magnetic impurities like Fe, Co, Ni, and Mn (*i.e.*, 3d-block elements) are the main hindrances that ignite doubts when dealing with magnetism of low-magnetic-moment materials. Even traces of materials with such high magnetization can contribute equally and can lead to wrong conclusions. For example, 1 ng of Fe impurity in the matrix can produce a magnetic moment of ~0.22 μemu.[553] Thus, one should very accurately measure the impurity concentration to avoid misleading results. The measured magnetization of a material is the sum of all the contributions that arise from the sample itself, sample holder, and any other cavity that are used to mount the samples. Usually, the sample holders (Teflon wraps, straws, cavities, *etc.*) exhibit a diamagnetic response, which should be subtracted from the final measured value.[554] Because the magnetization of such low-magnetic-moment materials is comparable to that of the background, a careful treatment of such data is essential to understand the origin of magnetism. Sometimes, it can be surprising to see that a negative moment becomes positive after the background subtraction. For a better representation of magnetic susceptibility *vs.* temperature data, one can simply plot the difference of ZFC and FC magnetization curves against temperature. This will clearly remove the background and any common errors of the measurement.[553,555] Another typical source of error comes from the Teflon tapes used to wrap powder samples for recording the magnetic data. Although Teflon tapes are diamagnetic in nature, they can induce an FM signal when tempered. Any tempering in the form of mechanical stretching, cutting or heating can change the true magnetic nature by creating dangling bonds.[554] In turn, these dangling bonds can interact with the neighboring carbon atoms to produce a defect-mediated magnetic order that is comparable to that of the primary material under consideration. Although the sensitivity of the superconducting quantum interference device (SQUID)-type magnetometer is very high, the errors due to instrumental artifacts can never be ignored. The common instrumental artifacts come from sensors and the sequence used for measuring the data. Synchronization between the data collection process and temperature or field ramp is necessary to avoid any unusual spikes/transitions. Fig. 124a shows the effect of different heating rates on the ZFC magnetization plots. A noticeable hump can be seen when the heating rate is changed. Fig. 124b shows the change in the profile of the plot when magnetization data are collected with transitions in heating rates. Subsequently, this effect is then clearly manifested in the magnetization *vs.* temperature plots, which could lead to misguided results. However, if the transition and data collection rates are in sync, one can easily avoid such instrumental errors.

Inductively coupled plasma mass spectrometry (ICP-MS) is very efficient in detecting metals and several non-metals at very low concentrations (parts per quadrillion, ppq). The ICP-MS technique is very popular due to its high precision, fast speed, and sensitivity. X-ray magnetic circular dichroism (XMCD) and X-ray absorption spectroscopy (XAS) are useful in determining

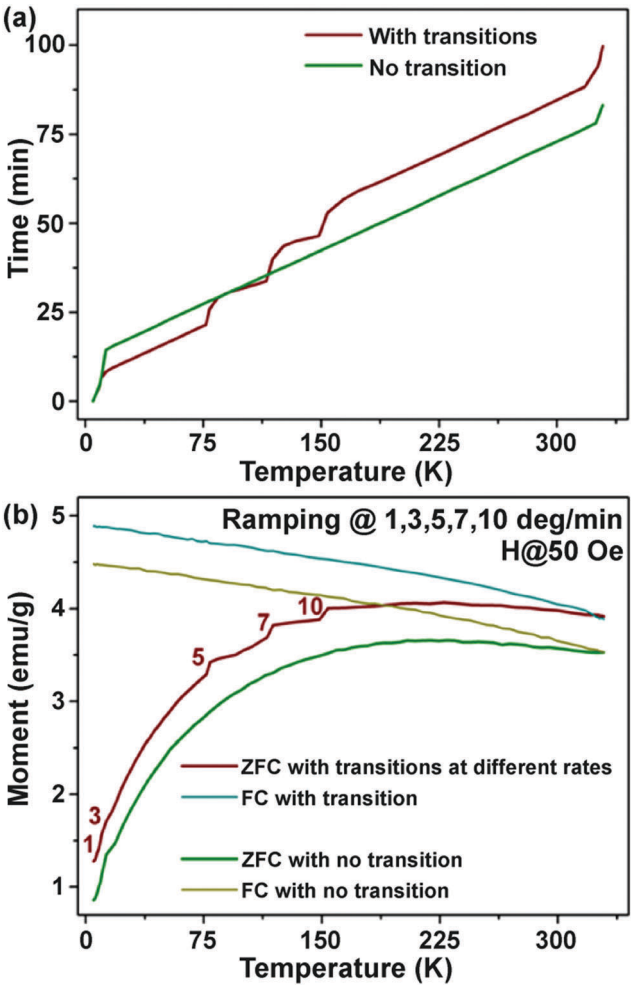

Fig. 124 (a) Effect of heating rate on ZFC magnetization data. (b) Effect of transitions in heating rate on the magnetic moment of the material.

the presence of d-shell elements and their contribution as impurities in graphene-based systems. However, the requirement of synchrotron radiation and a cryomagnetic environment to operate XMCD makes the technique disadvantageous for routine studies of d-shell impurities. The ESR technique is widely used to measure the presence of unpaired electrons and their interactions with the surroundings. The presence of FM centers would have a different nature of ESR patterns and *g*-value in comparison to those characteristic of conduction/paramagnetic centers. X-ray powder diffraction (XRD) is very useful and sensitive in sensing a small wt% of magnetic impurities.

There have been many reports on simultaneous occurrence of ferromagnetism, antiferromagnetism, paramagnetism, and diamagnetism in graphene and its derivatives. In the absence of any magnetic impurities, the important factors that would decide the magnetic state of a material include the density of states, defect states, temperature, external fields, and possible interactions within the system. The delocalized π-electrons due to sp^2 hybridization in graphene can trigger many interactions between the guest and the host lattice. Moreover, magnetic ordered states can be maintained by exchange interactions.

In general, the magnetic susceptibility (χ) of a system is basically a mixture of all the forms of magnetic contributions, *i.e.*,

$$\chi = \chi_{BG} + \chi_{dia} + \chi_{para} + \chi_{FM/AFM}, \quad (10)$$

where χ_{BG} corresponds to the contribution of the background, χ_{dia} is the diamagnetic response, χ_{para} stands for the paramagnetic term, and $\chi_{FM/AFM}$ denotes the FM/AFM contribution (for details, see Section 2). To understand the true nature of such a mixed state, it is essential to separate various contributions to χ of the system. Swain *et al.*[553,556] proposed a low field-high field technique to deconvolute the mixed magnetic state. The basic principle of the suggested procedure lies in the physics of interaction between the states and the external field. The paramagnetic (diamagnetic) susceptibility is directly (inversely) proportional to the external field. The FM/AFM states do not show a linear dependence to the field and rather exhibit hysteresis. The diamagnetic background can be easily separated by measuring the susceptibility in the absence of the material. After getting rid of the background contribution, any further paramagnetic (plus diamagnetic) contribution can be calculated from the slope of the linear portion of the magnetization *vs.* field curve at high fields. As FM materials saturate at high magnetic fields, the presence of any saturation in magnetization can be seen once both background and paramagnetic contributions are deducted as shown in Fig. 125.[556] In addition, the FM/AFM states can be noticed from low-field ZFC/FC magnetization measurements by virtue of their transition temperatures.

The low-magnetic-moment materials usually show a very high magnetization value at very low temperatures. The abrupt increase in magnetization is mainly due to a strong internal molecular field that boosts the collective magnetic order at low temperatures (below 10 K). The internal molecular field at such temperatures is at least 1000 times stronger than the applied magnetic field.[557] Thus, the magnetic centers experience a very strong effective field, thereby giving rise to a very high magnetic moment.

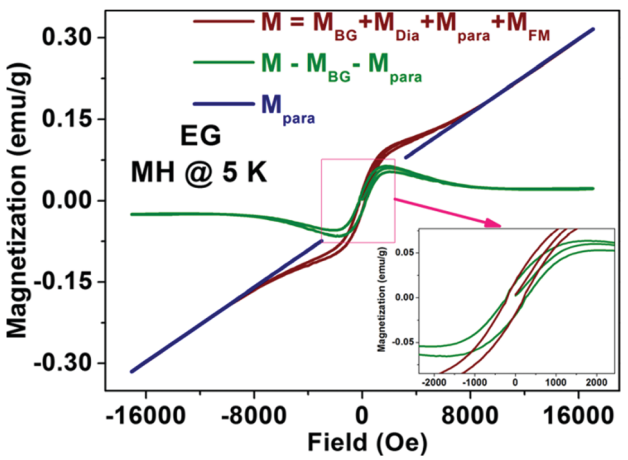

Fig. 125 FM response deduced after subtraction of both diamagnetic and paramagnetic contributions. Reprinted with permission from ref. 556. Copyright 2014 AIP Publishing LLC.

10. Conclusions, applications of "magnetic" graphene in spintronics and biomedicine and future challenges

The goal of the review was to systematically classify and thoroughly describe the approaches used to imprint magnetic behavior into intrinsically non-magnetic graphene. To do so, several strategies must be adopted, all relying on the introduction of defects into graphene. In general, the defects, to some extent, disturb the ideal structure of graphene, modifying its electronic features, leading, among others, to an evolution of magnetic moments that can interact with each other if a suitable communication medium is provided and interaction pathways are secured. The diverse theoretical studies identified various ground magnetic states evolved depending on the nature of the defects and how they can be altered upon doping, functionalization, edge engineering, spatial confinement, and external stimuli. A significant number of experimental works confirmed the predictions from calculations synthesizing graphene-based systems with magnetic ordering effectively resisting the thermal fluctuations and preserving even up to room temperature. The examples of room-temperature ferromagnets/antiferromagnets include, in particular, functionalized graphenes where the communication among the defect-induced localized magnetic moments is suggested to result from a complex interplay between interaction mechanisms of various natures. Sustainable magnetism can also emerge in graphene analogues and other classes of 2D materials such as transition metal dichalcogenides, metal dihalides, metal dinitrides, MXenes, h-BN or 2D organic porous sheets, implying that the concept of equipping magnetic features to 2D materials by defects seems to be of universal character for originally non-magnetic systems. However, false interpretations on observed magnetic behavior may happen in cases, when magnetic impurities (especially, 3d-block elements) are present either from the synthesis itself or from sample handling as they often overshadow the magnetic signal from the carbon-based materials.

Several challenges still remain untouched. Most of them are connected with experimental difficulties to synthesize graphene-based systems with introduction of defects in a controllable manner. Moreover, the issue of homogeneity of distribution of defects within each sheet is still experimentally unsolved and very hard to tackle as it needs a sophisticated optimization of the synthetic protocols. Frequently, only a certain portion of defect-modified graphene sheets in the sample show a desired magnetic behavior in agreement with the theoretical predictions. The defects may induce a large number of configurations when some of them are magnetically-active whereas others are non-magnetic. The energy differences between magnetic and non-magnetic configurations can be, in some cases, very tiny favoring stabilization of non-magnetic states during the synthetic conditions used. Moreover, the defects have different tendencies for localization in particular sites in graphene (*i.e.*, in the interior, close to the edges, at the edges), resulting in potential commutation at preferred regions.

For adatoms, migration energy barriers should be carefully considered, preventing their movement on the graphene surface and grouping at positions hindering evolution of whatever magnetic ordering. Another challenge involves experimental engineering of size and edges in spatially confined graphene representatives. Currently, there are only a few ways to cut graphene into pieces with a proper edge structure and geometry, most of them exploiting conditions of ultra-high vacuum and microscopy-based techniques. Due to the high reactivity of edges, post-process treatments are necessary to preserve the edge structure, which can be chemically highly demanding. Thus, for example, for GNRs, it is very hard to experimentally reproduce the theoretical results in terms of altering the magnetic states by width, edge termination or doping. Another option to imprint magnetic ordering into graphene, which has not been synthetically explored, involves combination of defects of various natures. For example, confined carrier-doped graphene sheets with an appropriate edge structure and surface functionalization would show magnetic features that can be sustainable up to room temperature. Here, it should be stressed that for every strategy exploited, a threshold value exists when the number of defects breaks the graphene structure or completely modifies its electronic features, precluding emergence of magnetic states. Moreover, the sustainability of the magnetic ordering against thermal fluctuations is closely related to the strength of the interactions among the defect-induced magnetic moments. Thus, competition/interplay among various types of interactions (*i.e.*, π-electron-mediated interactions, exchange interactions, *etc.*) should be thoroughly engineered all positively contributing to the stabilization of magnetic ordering up to high temperatures. Alternatively, the magnetism in graphene (or graphene derivatives) can be induced by the generation of radical-like magnetic moments; here, a vast space for theoretical modeling and experimenting is, in particular, viewed in evaluating the thermodynamic stability of radicals and their motifs, identification of magnetically-active motifs, potential arrangement (*i.e.*, hierarchical organization) of radical motifs in "magnetic superstructures" encouraging a long-range magnetic ordering, and development of sophisticated synthetic protocols providing engineering of the suitable structure(s) of motifs and their homogeneous distribution within each single sheet of graphene in the specimen. Tuning the magnetically-active motifs and interaction pathways may then further lead to a stabilization of the magnetic ordering with Curie and/or Néel temperature above the room temperature, opening doors to new applications of graphene. Equally important, strengthening the magnetic anisotropy in graphene is an experimentally challenging task requiring control over intrinsic and extrinsic sources of spin–orbit coupling or introducing other types of coupling such an exchange bias. In this respect, graphene analogues and other 2D materials can be regarded as equal competitors offering much higher Curie/Néel temperatures and stronger magnetic anisotropies, showing intrinsically without a need to introduce defects; however, overwhelming majority of these rivals have been only predicted theoretically and, nowadays, it is very hard to anticipate the difficulties and problems associated with their synthesis in order to reproduce completely the theoretical behaviors. Last but not least, from the practical viewpoint, a fundamental challenge is viewed in connecting "magnetic" graphenes and other 2D materials to other functional components in devices in a way not degrading or destroying the spin transport and magnetic response.

Once graphene or its 2D analogues become magnetic, it can be applied in branches requiring a sustainable magnetic response of a material. Recently, "magnetic" graphene has been suggested as a promising candidate in spintronic applications. In general, spintronics exploits the spin degree of freedom of electrons, thus developing the new technological concepts for information storage and logic devices; in other words, its main goals are to understand mechanisms behind the control of spin configurations and spin currents and to design/discover materials with suitable spin generation and transport features. Spin-based information technology offers several advantages over classical electronics such as high speed of data processing, high circuit integration density, low-power operation, and reconfigurable option. In order to both meet the criteria for ideal spintronic materials on one hand and to find an optimal design and fabrication procedure of a spintronic device on the other hand, several challenges have been identified so far such as generation of fully-polarized carriers and injection into spin devices, long-distance spin propagation (and, hence, long spin lifetime), and manipulation and detection of spin orientation of the carriers. Regarding the materials appealing for spintronics, a behavior intrinsic to half metals, spin-gapless semiconductors and/or bipolar magnetic semiconductors is highly desirable. As proved by a number of theoretical and experimental studies, graphene and/or its 2D analogues can behave as a half metal, spin-gapless semiconductor or bipolar magnetic semiconductor depending on the structure modification/functionalization or exposure to external stimuli or combination of both approaches. In particular, in half metals, one spin channel is metallic while the other spin channel is insulating or semiconducting (see Fig. 126a).[60] However, for preservation of half-metallicity at room temperature, a high Curie temperature is not a sufficient prerequisite; in addition, a wide half-metallic gap is required to avoid occurrence of thermally-agitated spin–flip transitions. In graphene, a half-metallic property is often observed upon an appropriate chemical modification; however, its stabilization needs exclusion of non-local exchange interactions stemming from impurities and improper (irregular) incorporation of foreign elements or sheet and edge functionalization. Equally important, the occurrence of half-metallicity in graphene without applying an external electric field or strain is highly unlikely. For a spin-gapless semiconductor, the valence band maximum and conduction band minimum touch each other exactly at E_F and at least one of the valence band maximum and conduction band minimum is fully spin-polarized (see Fig. 126b).[60] In spin-gapless semiconductors, excitation of an electron from the valence band to the conduction band does not require any threshold energy; more importantly, the excited carriers may then show a full spin polarization. In graphene, for example, the emergence of spin-gapless semiconducting behavior strongly

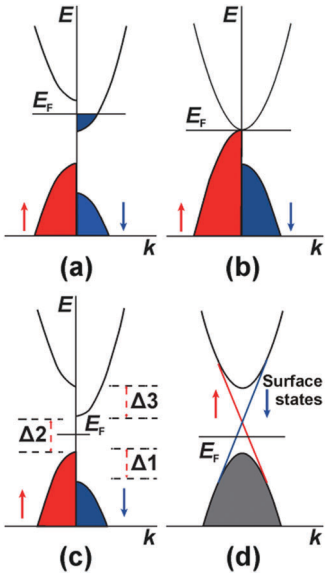

Fig. 126 Schematic band structure of (a) half metal, (b) spin-gapless semiconductor, (c) bipolar magnetic semiconductor, and (d) topological insulator, where k is the wave vector, E represents the energy, and E_F denotes the Fermi level. In panel (c), Δ1, Δ2, and Δ3 correspond to the spin–flip gap in the valence band, band gap, and spin–flip gap in the conduction band, respectively. Reprinted with permission from ref. 60. Copyright 2016 Oxford University Press on behalf of China Science Publishing & Media Ltd.

depends on the dopant and vacancy sites and distances between them, which could be hardly controlled during the synthesis. Bipolar magnetic semiconductors, for which the valence band maximum and conduction band minimum are completely spin-polarized in the opposite spin direction (see Fig. 126c),[60] offer fully spin-polarized currents with reversible spin polarization which can be readily controlled by applying a gate voltage. However, such a feature was theoretically predicted for GNRs with a special morphology and edge geometries that can be hardly achieved by currently mastered experimental top-down or bottom-up procedures. Currently, equipping graphene with properties resembling those of topological insulators is regarded as a challenging task. To imprint such a behavior when the metallic surface states are symmetry-protected and the electrons with spin-up and spin-down move in the opposite direction on the 2D surface (see Fig. 126d),[60] an appropriate functionalization strategy of graphene should be identified theoretically and verified experimentally.

Due to a long spin lifetime and spin diffusion length defined by a weak spin–orbit coupling, graphene has been suggested to effectively work as a spin conserver which can provide transmission of the spin-encoded information across a device with high fidelity. The theory predicts that the spin relaxation time in graphene can reach $\sim$1 μs; however, the values observed for synthesized graphenes lie in the interval from tens of picoseconds to units of nanoseconds. Such a difference between the experimental and theoretical values of the spin relaxation times is often explained in terms of the presence of impurities, defects, and static ripples. Thus, introduction of defects to raise magnetism in graphene should not significantly alter the spin relaxation time towards lower values as it could then ruin an effective spin transport through the device.

Besides, materials involving only sp elements have been predicted to show high magnitudes of spin-wave stiffness and, hence, higher magnetic transition (Curie/Néel) temperatures. However, to realize a robust magnetic ordering in graphene-based systems, the existence and significant strength of magnetic anisotropy are highly needed besides high values of Curie/Néel temperature. For such systems, the spin–orbit coupling is responsible for magnetic anisotropy. Adopting a simple model, it can be inferred that for temperatures sufficiently higher than the so-called crossover temperature, T_X ($\approx$ 10 K), the spin correlation length, ξ, is inversely proportional to the temperature, *i.e.*, $\xi \propto T^{-1}$, as a weak magnetic anisotropy is not expected to play any role above T_X.[45] Below T_X, ξ is supposed to increase exponentially upon lowering the temperature. Thus, $\xi \approx 1$ nm at 300 K.[45] In order to increase T_X and, hence, ξ at room temperature, it is necessary to modify appropriately the magnetic anisotropy. To do so, several approaches have been suggested so far, most of them relying on the introduction of foreign atoms with an intrinsically large anisotropy into the graphene lattice, surface functionalization with suitable adatoms and/or functional groups or deposition on a substrate. Besides, the magnetic anisotropy of graphene can be alternatively controlled by the Rashba effect and associated Rashba coupling originating from the π–σ hybridization. Increasing the magnetic anisotropy in graphene is believed to encourage its new role as a spin generator when combined with transport currents. Moreover, the ''magnetic'' graphene could effectively work as a component in magnetoresistive junctions used in the sensors of magnetic fields; a very high magnetoresistive ratio has already been reported for an architecture composed of GNRs placed between the two FM contacts.

Apart from electronics and spintronics, a vast number of experimental studies have proved graphene's prominent application potential in biomedicine. However, as graphene is hydrophobic, its surface must be functionalized with appropriate functional groups in order to make it hydrophilic. Moreover, surface functionalization significantly improves its colloidal stability, another feature highly required for biomedical applications. Regarding the toxicity issues, GQDs have been identified as low toxic graphene-based systems.[5] They currently work as photoluminescence agents for biomedical imaging; if equipped with the paramagnetic centers, they could offer an option of dual imaging, *i.e.*, in fluorescence and magnetic domain. Moreover, it is speculated that due to a slightly different nature of spins in sp-based systems (*i.e.*, existence of pseudospin) compared to that of the traditional d-block-element- or f-block-element-containing magnetic materials, the spin–lattice and spin–spin relaxation may provide interesting contrast properties in T_1- or T_2-weighted magnetic resonance images. Moreover, once spatially confined, the magnetic moment of graphene is believed to show magnetic phenomena activated by external stimuli including temperature, light, and external magnetic field; such magnetic features would be promising in designing graphene-based imaging agents.

Besides, as graphene possesses a large surface area, if magnetic, graphene or its derivatives can be further functionalized with biomolecules and other compounds, thus serving as a platform for active drug targeting. Experimentally, size, morphology, functionalization, long-term toxicity, repeatability, and yield aspects are currently considered as highly challenging with a potentially long journey to achieve biomedically-appealing "magnetic" graphenes in the near future.

Abbreviations

AC-HRTEM	Aberration corrected high resolution transmission electron microscopy
AFM	Antiferromagnetic
CVD	Chemical vapor deposition
DFT	Density functional theory
DTPA	Dimethylmethylene-bridged triphenylamine
E_F	Fermi level
ESR	Electron spin resonance
FAG	Fluoranthene group
FC	Field-cooled
FIM	Ferrimagnetic
FLG	Few-layered graphite
FM	Ferromagnetic
GGA	Generalized gradient approximation
GIC	Graphite intercalation compound
GMR	Giant magnetoresistance
GNRs	Graphene nanoribbons
GNFs	Graphene nanoflakes
GQDs	Graphene quantum dots
HAADF-STEM	High angle annular dark field scanning transmission electron microscopy
HOMO	Highest occupied molecular orbital
HOPG	Highly oriented pyrolytic graphite
ICP-MS	Inductively coupled plasma mass spectrometry
LUMO	Lowest unoccupied molecular orbital
MD	Molecular dynamics
MFM	Magnetic force microscopy
OVER	6-Oxoverdazyl
PDA	Polydiacetylene
RKKY	Ruderman–Kittel–Kasuya–Yosida
SACS-TEM	Spherical-aberration corrected transmission electron microscopy
SPLEEM	Spin-polarized low-energy electron microscopy
SP-STM	Spin-polarized scanning tunneling microscopy
SQUID	Superconducting quantum interference device
STM	Scanning tunneling microscopy
STS	Scanning tunneling spectroscopy
SW	Stone–Wales
TDAE	Tetrakis-dimethylaminoethylene
TEM	Transmission electron microscopy
TMDC	Transition metal dichalcogenide
TMM	Trimethylenemethane
TMR	Tunnel magnetoresistance
TSW	Thrower–Stone–Wales
VASP	Vienna ab initio simulation package
XAS	X-ray absorption spectroscopy
XMCD	X-ray magnetic circular dichroism
XRD	X-ray powder diffraction
ZFC	Zero-field-cooled

Conflicts of interest

There are no conflicts to declare.

Acknowledgements

The authors gratefully acknowledge the support from the Ministry of Education, Youth and Sports of the Czech Republic under Project No. LO1305 and the support by the Operational Programme Research, Development and Education – European Regional Development Fund, Project No. CZ.02.1.01/0.0/0.0/16_019/0000754 of the Ministry of Education, Youth and Sports of the Czech Republic.

References

1 M. Tamura, Y. Nakazawa, D. Shiomi, K. Nozawa, Y. Hosokoshi, M. Ishikawa, M. Takahashi and M. Kinoshita, *Chem. Phys. Lett.*, 1991, **186**, 401–404.
2 M. Takahashi, P. Turek, Y. Nakazawa, M. Tamura, K. Nozawa, D. Shiomi, M. Ishikawa and M. Kinoshita, *Phys. Rev. Lett.*, 1991, **67**, 746–748.
3 H. W. Kroto, J. R. Heath, S. C. O'Brien, R. F. Curl and R. E. Smalley, *Nature*, 1985, **318**, 162–163.
4 S. Iijima, *Nature*, 1991, **354**, 56–58.
5 V. Georgakilas, J. A. Perman, J. Tucek and R. Zboril, *Chem. Rev.*, 2015, **115**, 4744–4822.
6 R. B. Heimann, S. E. Evsvukov and Y. Koga, *Carbon*, 1997, **35**, 1654–1658.
7 T. L. Makarova, *Superconductors*, 2004, **38**, 615–638.
8 A. Oshiyama, S. Okada and S. Saito, *Physica B*, 2002, **323**, 21–29.
9 S. Okada and A. Oshiyama, *J. Phys. Soc. Jpn.*, 2003, **72**, 1510–1515.
10 L. W. Chang and J. T. Lue, *J. Nanosci. Nanotechnol.*, 2009, **9**, 1956–1963.
11 S. Okada, K. Nakada, K. Kuwabara, K. Daigoku and T. Kawai, *Phys. Rev. B: Condens. Matter Mater. Phys.*, 2006, **74**, 121412.
12 J. Klinovaja and D. Loss, *Phys. Rev. B: Condens. Matter Mater. Phys.*, 2013, **87**, 045422.
13 S. Bandow, F. Kokai, K. Takahashi, M. Yudasaka and S. Iijima, *Appl. Phys. A: Mater. Sci. Process.*, 2001, **73**, 281–285.
14 S. Bandow, T. Yamaguchi and S. Iijima, *Chem. Phys. Lett.*, 2005, **401**, 380–384.
15 R. C. Haddon, *Science*, 1993, **261**, 1545–1550.
16 R. Zanasi and P. Fowler, *Chem. Phys. Lett.*, 1995, **238**, 270–280.

17 R. C. Haddon and A. Pasquarello, *Phys. Rev. B: Condens. Matter Mater. Phys.*, 1994, **50**, 16459–16463.
18 M. Saunders, A. Jimenez-Vazquez, R. J. Cross, W. E. Billups, C. Gesenberg, A. Gonzalez, W. Luo, R. C. Haddon, F. Diederich and A. Herrmann, *J. Am. Chem. Soc.*, 1995, **117**, 9305–9308.
19 P.-M. Allemand, K. C. Khemani, A. Koch, F. Wudl, K. Holczer, S. Donovan, G. Gruner and J. D. Thompson, *Science*, 1991, **253**, 301–303.
20 M. Ata, M. Machida, H. Watanabe and J. Seto, *Jpn. J. Appl. Phys.*, 1994, **33**, 1865–1871.
21 Y. M. Shul'ga, A. S. Lobach, I. N. Ivleva, Y. G. Morozov, V. N. Spector and A. A. Ovchinnikov, *Mol. Cryst. Liq. Cryst. Sci. Technol., Sect. C*, 1998, **10**, 201–206.
22 A. S. Lobach, Y. M. Shul'ga, O. S. Roshchupkina, A. I. Rebrov, A. A. Perov, Y. G. Morozov, V. N. Spector and A. A. Ovchinnikov, *Fullerene Sci. Technol.*, 1998, **6**, 375–391.
23 Y. Iwasa, T. Arima, R. M. Fleming, T. Siegrist, O. Zhou, R. C. Haddon, L. J. Rothberg, K. B. Lyons, H. L. Carter, Jr., A. F. Hebard, R. Tycko, G. Dabbagh, J. J. Krajevski, G. A. Thomas and T. Yagi, *Science*, 1994, **264**, 1570–1572.
24 M. Nuñez-Regueiro, L. Marques, J.-L. Hodeau, O. Berthoux and M. Perroux, *Phys. Rev. Lett.*, 1995, **74**, 278–281.
25 R. A. Wood, M. H. Lewis, M. R. Lees, S. M. Bennington, M. G. Cain and N. Kitamura, *J. Phys.: Condens. Matter*, 2002, **14**, L385–L391.
26 A. Mrzel, A. Omerzu, P. Umek, D. Mihailovic, Z. Jaglicic and Z. Trontelj, *Chem. Phys. Lett.*, 1998, **298**, 329–334.
27 K. Prassides, S. Margadonna, D. Arcon, A. Lappas, H. Shimoda and Y. Iwasa, *J. Am. Chem. Soc.*, 1999, **121**, 11227–11228.
28 L. Rondin, J. P. Tetienne, T. Hingant, J. F. Roch, P. Maletinsky and V. Jacques, *Rep. Prog. Phys.*, 2014, **77**, 056503.
29 A. A. Ovchinnikov and I. L. Shamovsky, *THEOCHEM*, 1991, **251**, 133–140.
30 A. A. Ovchinnikov, I. L. Shamovsky and K. V. Bozhenko, *THEOCHEM*, 1991, **251**, 141–151.
31 A. V. Rode, E. G. Gamaly, A. G. Christy, J. G. Fitz Gerald, S. T. Hyde, R. G. Elliman, B. Luther-Davies, A. I. Veinger, J. Androulakis and J. Giapintzakis, *Phys. Rev. B: Condens. Matter Mater. Phys.*, 2004, **70**, 054407.
32 D. Arčon, Z. Jagličič, A. Zorko, A. V. Rode, A. G. Christy, N. R. Madsen, E. G. Gamaly and B. Luther-Davies, *Phys. Rev. B: Condens. Matter Mater. Phys.*, 2006, **74**, 014438.
33 G. D. Yu, Z. Liu, W. Z. Gao and Y. S. Zheng, *J. Phys.: Condens. Matter*, 2013, **25**, 285502.
34 Y. P. Zheng, Y. H. Chen, L. H. Lin, Y. Y. Sun, H. B. Liu, Y. L. Li, Y. W. Du and N. J. Tang, *Appl. Phys. Lett.*, 2017, **111**, 033101.
35 M. J. Zhang, X. X. Wang, H. J. Sun, N. Wang, Q. Lv, W. W. Cui, Y. Z. Long and C. S. Huang, *Sci. Rep.*, 2017, **7**, 11535.
36 K. S. Novoselov, A. K. Geim, S. V. Morozov, D. Jiang, Y. Zhang, S. V. Dubonos, I. V. Grigorieva and A. A. Firsov, *Science*, 2004, **306**, 666–669.
37 A. H. Castro Neto, F. Guinea, N. M. R. Peres, K. S. Novoselov and A. K. Geim, *Rev. Mod. Phys.*, 2009, **81**, 109–162.
38 M. J. Allen, V. C. Tung and R. B. Kaner, *Chem. Rev.*, 2010, **110**, 132–145.
39 V. Georgakilas, M. Otyepka, A. B. Bourlinos, V. Chandra, N. Kim, K. C. Kemp, P. Hobza, R. Zboril and K. S. Kim, *Chem. Rev.*, 2012, **112**, 6156–6214.
40 V. Georgakilas, J. N. Tiwari, K. C. Kemp, J. A. Perman, A. B. Bourlinos, K. S. Kim and R. Zboril, *Chem. Rev.*, 2016, **116**, 5464–5519.
41 P. Avouris, Z. H. Chen and V. Perebeinos, *Nat. Nanotechnol.*, 2007, **2**, 606–615.
42 W. Han, R. K. Kawakami, M. Gmitra and J. Fabian, *Nat. Nanotechnol.*, 2014, **9**, 794–807.
43 J. M. Yoo, J. H. Kang and B. H. Hong, *Chem. Soc. Rev.*, 2015, **44**, 4835–4852.
44 G. Z. Kyzas, E. A. Deliyanni and K. A. Matis, *J. Chem. Technol. Biotechnol.*, 2014, **89**, 196–205.
45 O. V. Yazyev, *Rep. Prog. Phys.*, 2010, **73**, 056501.
46 J. Červenka, M. I. Katsnelson and C. F. J. Flipse, *Nat. Phys.*, 2009, **5**, 840–844.
47 O. V. Yazyev and L. Helm, *Phys. Rev. B: Condens. Matter Mater. Phys.*, 2007, **75**, 125408.
48 A. Carpio, L. L. Bonilla, F. de Juan and M. A. H. Vozmediano, *New J. Phys.*, 2008, **10**, 053021.
49 L. Ciric, D. M. Djokic, J. Jacimovic, A. Sienkiewicz, A. Magrez, L. Forro, Z. Sljivancanin, M. Lotya and J. N. Coleman, *Phys. Rev. B: Condens. Matter Mater. Phys.*, 2012, **85**, 205437.
50 J. Tucek, P. Blonski, Z. Sofer, P. Simek, M. Petr, M. Pumera, M. Otyepka and R. Zboril, *Adv. Mater.*, 2016, **28**, 5045–5053.
51 P. Blonski, J. Tucek, Z. Sofer, V. Mazanek, M. Petr, M. Pumera, M. Otyepka and R. Zboril, *J. Am. Chem. Soc.*, 2017, **139**, 3171–3180.
52 J. Zhou, Q. Wang, Q. Sun, X. S. Chen, Y. Kawazoe and P. Jena, *Nano Lett.*, 2009, **9**, 3867–3870.
53 R. R. Nair, M. Sepioni, I. L. Tsai, O. Lehtinen, J. Keinonen, A. V. Krasheninnikov, T. Thomson, A. K. Geim and I. V. Grigorieva, *Nat. Phys.*, 2012, **8**, 199–202.
54 J. Tucek, K. Hola, A. B. Bourlinos, P. Blonski, A. Bakandritsos, J. Ugolotti, M. Dubecky, F. Karlicky, V. Ranc, K. Cepe, M. Otyepka and R. Zboril, *Nat. Commun.*, 2017, **8**, 14525.
55 D. W. Boukhvalov and M. I. Katsnelson, *ACS Nano*, 2011, **5**, 2440–2446.
56 Y. Kobayashi, K. Fukui, T. Enoki, K. Kusakabe and Y. Kaburagi, *Phys. Rev. B: Condens. Matter Mater. Phys.*, 2005, **71**, 193406.
57 G. Z. Magda, X. Z. Jin, I. Hagymasi, P. Vancso, Z. Osvath, P. Nemes-Incze, C. Y. Hwang, L. P. Biro and L. Tapaszto, *Nature*, 2014, **514**, 608–611.
58 E. J. Kan, Z. Y. Li and J. L. Yang, *NANO*, 2008, **3**, 433–442.
59 W. Q. Liu and Y. B. Xu, *Curr. Opin. Solid State Mater. Sci.*, 2016, **20**, 388–395.
60 X. X. Li and J. L. Yang, *Natl. Sci. Rev.*, 2016, **3**, 365–381.
61 S. Das Sarma, S. Adam, E. H. Hwang and E. Rossi, *Rev. Mod. Phys.*, 2011, **83**, 407–470.
62 K. S. Novoselov, A. K. Geim, S. V. Morozov, D. Jiang, M. I. Katsnelson, I. V. Grigorieva, S. V. Dubonos and A. A. Firsov, *Nature*, 2005, **438**, 197–200.
63 Y. B. Zhang, T. W. Tan, H. L. Stormer and P. Kim, *Nature*, 2005, **438**, 201–204.

64 R. Shimano, G. Yumoto, J. Y. Yoo, R. Matsunaga, S. Tanabe, H. Hibino, T. Morimoto and H. Aoki, *Nat. Commun.*, 2013, **4**, 1841.
65 I. V. Fialkovsky, V. N. Marachevsky and D. V. Vassilevich, *Phys. Rev. B: Condens. Matter Mater. Phys.*, 2011, **84**, 035446.
66 D. Basko, *Science*, 2011, **334**, 610–611.
67 H. B. Heersche, P. Jarillo-Herrero, J. B. Oostinga, L. M. K. Vandersypen and A. F. Morpurgo, *Nature*, 2007, **446**, 56–59.
68 K. Xu, K. Wang, W. Zhao, W. Z. Bao, E. F. Liu, Y. F. Ren, M. Wang, Y. J. Fu, J. W. Zeng, Z. G. Li, W. Zhou, F. Q. Song, X. R. Wang, Y. Shi, X. G. Wan, M. S. Fuhrer, B. G. Wang, Z. H. Qiao, F. Miao and D. Y. Xing, *Nat. Commun.*, 2015, **6**, 8119.
69 S. Park, G. Wang, B. Cho, Y. Kim, S. Song, Y. Ji, M. H. Yoon and T. Lee, *Nat. Nanotechnol.*, 2012, **7**, 438–442.
70 L. Tapaszto, G. Dobrik, P. Lambin and L. P. Biro, *Nat. Nanotechnol.*, 2008, **3**, 397–401.
71 T. H. Han, Y. Lee, M. R. Choi, S. H. Woo, S. H. Bae, B. H. Hong, J. H. Ahn and T. W. Lee, *Nat. Photonics*, 2012, **6**, 105–110.
72 S. J. Han, A. V. Garcia, S. Oida, K. A. Jenkins and W. Haensch, *Nat. Commun.*, 2014, **5**, 3086.
73 O. Y. Loh and H. D. Espinosa, *Nat. Nanotechnol.*, 2012, **7**, 283–295.
74 Y. W. Zhu, S. Murali, M. D. Stoller, K. J. Ganesh, W. W. Cai, P. J. Ferreira, A. Pirkle, R. M. Wallace, K. A. Cychosz, M. Thommes, D. Su, E. A. Stach and R. S. Ruoff, *Science*, 2011, **332**, 1537–1541.
75 M. Q. Zhao, Q. Zhang, J. Q. Huang, G. L. Tian, J. Q. Nie, H. J. Peng and F. Wei, *Nat. Commun.*, 2014, **5**, 3410.
76 L. T. Qu, Y. Liu, J. B. Baek and L. M. Dai, *ACS Nano*, 2010, **4**, 1321–1326.
77 Z. F. Liu, Q. Liu, Y. Huang, Y. F. Ma, S. G. Yin, X. Y. Zhang, W. Sun and Y. S. Chen, *Adv. Mater.*, 2008, **20**, 3924–3930.
78 F. N. Xia, T. Mueller, Y. M. Lin, A. Valdes-Garcia and P. Avouris, *Nat. Nanotechnol.*, 2008, **4**, 839–843.
79 Q. L. Bao, H. Zhang, B. Wang, Z. H. Ni, C. H. Y. X. Lim, Y. Wang, D. Y. Tang and K. P. Loh, *Nat. Photonics*, 2011, **5**, 411–415.
80 C. Zhu, T. Y. J. Han, E. B. Duoss, A. M. Golobic, J. D. Kuntz, C. M. Spadaccini and M. A. Worsley, *Nat. Commun.*, 2015, **6**, 6962.
81 J. J. Liang, Y. Wang, Y. Huang, Y. F. Ma, Z. F. Liu, J. M. Cai, C. D. Zhang, H. J. Gao and Y. S. Chen, *Carbon*, 2009, **47**, 922–925.
82 S. K. Min, W. Y. Kim, Y. Cho and K. S. Kim, *Nat. Nanotechnol.*, 2011, **6**, 162–165.
83 X. M. Sun, Z. Liu, K. Welsher, J. T. Robinson, A. Goodwin, S. Zaric and H. J. Dai, *Nano Res.*, 2008, **1**, 203–212.
84 Y. Han, Z. Xu and C. Gao, *Adv. Funct. Mater.*, 2013, **23**, 3693–3700.
85 J. Abraham, K. S. Vasu, C. D. Williams, K. Gopinadhan, Y. Su, C. T. Cherian, J. Dix, E. Prestat, S. J. Haigh, I. P. Grigorieva, P. Carbone, A. K. Geim and R. R. Nair, *Nat. Nanotechnol.*, 2017, **12**, 546–550.
86 M. K. Shin, B. Lee, S. H. Kim, J. A. Lee, G. M. Spinks, S. Gambhir, G. G. Wallace, M. E. Kozlov, R. H. Baughman and S. J. Kim, *Nat. Commun.*, 2012, **3**, 650.
87 C. L. Kane and E. J. Mele, *Phys. Rev. Lett.*, 2005, **95**, 226801.
88 O. V. Yazyev, *Nano Lett.*, 2008, **8**, 1011–1015.
89 O. V. Yazyev, *Phys. Rev. Lett.*, 2008, **101**, 037203.
90 H. Feldner, Z. Y. Meng, A. Honecker, D. Cabra, S. Wessel and F. F. Assaad, *Phys. Rev. B: Condens. Matter Mater. Phys.*, 2010, **81**, 115416.
91 J. Fernandez-Rossier and J. J. Palacios, *Phys. Rev. Lett.*, 2007, **99**, 177204.
92 D. D. Gunlycke, D. A. Areshkin, J. Li, J. W. Mintmire and C. T. White, *Nano Lett.*, 2007, **7**, 3608–3611.
93 L. Pisani, J. A. Chan, B. Montanari and N. M. Harrison, *Phys. Rev. B: Condens. Matter Mater. Phys.*, 2007, **75**, 064418.
94 O. V. Yazyev, I. Tavernelli, L. Helm and U. Röthlisberger, *Phys. Rev. B: Condens. Matter Mater. Phys.*, 2005, **71**, 115110.
95 H. Thomann, L. K. Dalton, M. Grabowski and T. C. Clarke, *Phys. Rev. B: Condens. Matter Mater. Phys.*, 1985, **31**, 3141–3143.
96 S. Kuroda and H. Shirakawa, *Phys. Rev. B: Condens. Matter Mater. Phys.*, 1987, **35**, 9380–9382.
97 S. Sorella and E. Tosatti, *Europhys. Lett.*, 1992, **19**, 699.
98 S. Fajtlowicz, P. E. John and H. Sachs, *Croat. Chem. Acta*, 2005, **78**, 195–201.
99 J. J. Palacios, J. Fernandez-Rossier and L. Brey, *Phys. Rev. B: Condens. Matter Mater. Phys.*, 2008, **77**, 195428.
100 E. H. Lieb, *Phys. Rev. Lett.*, 1989, **62**, 1201–1204.
101 Y. Kopelevich, P. Esquinazi, J. H. S. Torres and S. Moehlecke, *J. Low Temp. Phys.*, 2000, **119**, 691–702.
102 P. Esquinazi, A. Setzer, R. Höhne, C. Semmelhack, Y. Kopelevich, D. Spemann, T. Butz, B. Kohlstrunk and M. Lösche, *Phys. Rev. B: Condens. Matter Mater. Phys.*, 2002, **66**, 024429.
103 P. Esquinazi, D. Spemann, R. Höhne, A. Setzer, K.-H. Han and T. Butz, *Phys. Rev. Lett.*, 2003, **91**, 227201.
104 Z. Li and F. Chen, *Appl. Phys. Rev.*, 2017, **4**, 011103.
105 R. Singh, *J. Magn. Magn. Mater.*, 2013, **346**, 58–73.
106 F. Banhart, J. Kotakoski and A. V. Krasheninnikov, *ACS Nano*, 2011, **5**, 26–41.
107 O. V. Yazyev and Y. P. Chen, *Nat. Nanotechnol.*, 2014, **9**, 755–767.
108 S. Nigar, Z. Zhou, H. Wang and M. Imtiaz, *RSC Adv.*, 2017, **7**, 51546–51580.
109 S. T. Skowron, I. V. Lebedeva, A. M. Popov and E. Bichoutskaia, *Chem. Soc. Rev.*, 2015, **44**, 3143–3176.
110 H. Terrones, R. Lv, M. Terrones and M. S. Dresselhaus, *Rep. Prog. Phys.*, 2012, **75**, 062501.
111 R. H. Telling and M. I. Heggie, *Philos. Mag.*, 2007, **87**, 4797–4846.
112 P. A. Thrower and R. M. Mayer, *Phys. Status Solidi A*, 1978, **47**, 11–37.
113 A. J. Stone and D. J. Wales, *Chem. Phys. Lett.*, 1986, **128**, 501–503.
114 A. A. El-Barbary, R. H. Telling, C. P. Ewels, M. I. Heggie and P. R. Briddon, *Phys. Rev. B: Condens. Matter Mater. Phys.*, 2003, **68**, 144107.
115 Y. Ma, P. O. Lehtinen, A. S. Foster and R. M. Nieminen, *New J. Phys.*, 2004, **6**, 68.
116 P. O. Lehtinen, A. S. Foster, Y. Ma, A. V. Krasheninnikov and R. M. Nieminen, *Phys. Rev. Lett.*, 2004, **93**, 187202.

117 S. F. Asbaghian Namin and R. Pilafkan, *Phys. E*, 2017, **93**, 257–264.
118 A. V. Krasheninnikov, P. O. Lehtinen, A. S. Foster and R. M. Nieminen, *Chem. Phys. Lett.*, 2006, **418**, 132–136.
119 C. Ronchi, M. Datteo, D. Perilli, L. Ferrighi, G. Fazio, D. Selli and C. Di Valentin, *J. Phys. Chem. C*, 2017, **121**, 8653–8661.
120 R. Singh and P. Kroll, *J. Phys.: Condens. Matter*, 2009, **21**, 196002.
121 X. Q. Dai, J. H. Zhao, M. H. Xie, Y. N. Tang, Y. H. Li and B. Zhao, *Eur. Phys. J. B*, 2011, **80**, 343–349.
122 A. W. Robertson, B. Montanari, K. He, C. S. Allen, Y. A. Wu, N. M. Harrison, A. I. Kirkland and J. H. Warner, *ACS Nano*, 2013, **7**, 4495–4502.
123 A. Hashimoto, K. Suenaga, A. Gloter, K. Urita and S. Iijima, *Nature*, 2004, **430**, 870–873.
124 M. H. Gass, U. Bangert, A. L. Bleloch, P. Wang, R. R. Nair and A. K. Geim, *Nat. Nanotechnol.*, 2008, **3**, 676–681.
125 M. M. Ugeda, I. Brihuega, F. Guinea and J. M. Gómez-Rodríguez, *Phys. Rev. Lett.*, 2010, **104**, 096804.
126 J. C. Meyer, F. Eder, S. Kurasch, V. Skakalova, J. Kotakoski, H. J. Park, S. Roth, A. Chuvilin, S. Eyhusen, G. Benner, A. V. Krasheninnikov and U. Kaiser, *Phys. Rev. Lett.*, 2012, **108**, 196102.
127 H. I. Rasool, C. Ophus and A. Zettl, *Adv. Mater.*, 2015, **27**, 5771–5777.
128 G.-D. Lee, C. Z. Wang, E. Yoon, N.-M. Hwang, D.-Y. Kim and K. M. Ho, *Phys. Rev. Lett.*, 2005, **95**, 205501.
129 T. Trevethan, C. D. Latham, M. I. Heggie, P. R. Briddon and M. J. Rayson, *Nanoscale*, 2014, **6**, 2978–2986.
130 P. A. Denis and F. Iribarne, *J. Phys. Chem. C*, 2013, **117**, 19048–19055.
131 A. R. Botello-Méndez, X. Declerck, M. Terrones, H. Terrones and J.-C. Charlier, *Nanoscale*, 2011, **3**, 2868–2872.
132 M. M. Ugeda, I. Brihuega, F. Hiebel, P. Mallet, J.-Y. Veuillen, J. M. Gómez-Rodríguez and F. Ynduráin, *Phys. Rev. B: Condens. Matter Mater. Phys.*, 2012, **85**, 121402.
133 Ç. Ö. Girit, J. C. Meyer, R. Erni, M. D. Rossell, C. Kisielowski, L. Yang, C.-H. Park, M. F. Crommie, M. L. Cohen, S. G. Louie and A. Zettl, *Science*, 2009, **323**, 1705–1708.
134 Y. Kim, J. Ihm, E. Yoon and G.-D. Lee, *Phys. Rev. B: Condens. Matter Mater. Phys.*, 2011, **84**, 075445.
135 A. Zobelli, V. Ivanovskaya, P. Wagner, I. Suarez-Martinez, A. Yaya and C. P. Ewels, *Phys. Status Solidi B*, 2012, **249**, 276–282.
136 G. López-Polín, C. Gómez-Navarro, V. Parente, F. Guinea, M. I. Katsnelson, F. Pérez-Murano and J. Gómez-Herrero, *Nat. Phys.*, 2015, **11**, 26–31.
137 G. López-Polín, M. Jaafar, F. Guinea, R. Roldán, C. Gómez-Navarro and J. Gómez-Herrero, *Carbon*, 2017, **124**, 42–48.
138 Y. Zhang, M. P. K. Sahoo and J. Wang, *Nanotechnology*, 2016, **27**, 435206.
139 I. Y. Sagalianov, T. M. Radchenko, Y. I. Prylutskyy, V. A. Tatarenko and P. Szroeder, *Eur. Phys. J. B*, 2017, **90**, 112.
140 L. Li, S. Reich and J. Robertson, *Phys. Rev. B: Condens. Matter Mater. Phys.*, 2005, **72**, 184109.
141 P. O. Lehtinen, A. S. Foster, A. Ayuela, A. Krasheninnikov, K. Nordlund and R. M. Nieminen, *Phys. Rev. Lett.*, 2003, **91**, 017202.
142 E. J. Duplock, M. Scheffler and P. J. D. Lindan, *Phys. Rev. Lett.*, 2004, **92**, 225502.
143 H. González-Herrero, J. M. Gómez-Rodríguez, P. Mallet, M. Moaied, J. J. Palacios, C. Salgado, M. M. Ugeda, J.-Y. Veuillen, F. Yndurain and I. Brihuega, *Science*, 2016, **352**, 437–441.
144 D. W. Boukhvalov, M. I. Katsnelson and A. I. Lichtenstein, *Phys. Rev. B: Condens. Matter Mater. Phys.*, 2008, **77**, 035427.
145 F. Karlický, B. Lepetit and D. Lemoine, *J. Chem. Phys.*, 2014, **140**, 124702.
146 D. Cortés-Arriagada, S. Gutiérrez-Oliva, B. Herrera, K. Soto and A. Toro-Labbé, *J. Chem. Phys.*, 2014, **141**, 134701.
147 B. Lepetit and B. Jackson, *Phys. Rev. Lett.*, 2011, **107**, 236102.
148 J. Zhang, Y. Yan, W. Zong, A. Li, Z. Qiao and T. Sun, *J. Phys.: Condens. Matter*, 2017, **29**, 195001.
149 K. M. McCreary, A. G. Swartz, W. Han, J. Fabian and R. K. Kawakami, *Phys. Rev. Lett.*, 2012, **109**, 186604.
150 A. I. Podlivaev and L. A. Openov, *Phys. Solid State*, 2015, **57**, 820–824.
151 J. González, F. Guinea and M. A. H. Vozmediano, *Phys. Rev. B: Condens. Matter Mater. Phys.*, 2001, **63**, 134421.
152 M. Marcaccio and F. Paolucci, Making and Exploiting Fullerenes, Graphene, and Carbon Nanotubes, in *Topics in Current Chemistry*, Springer-Verlag, Berlin Heidelberg, 2014, pp. 1–270.
153 J. Ma, D. Alfè, A. Michaelides and E. Wang, *Phys. Rev. B: Condens. Matter Mater. Phys.*, 2009, **80**, 033407.
154 K. Ulman and S. Narasimhan, *Phys. Rev. B: Condens. Matter Mater. Phys.*, 2014, **89**, 245429.
155 A. I. Podlivaev and L. A. Openov, *Phys. Lett. A*, 2015, **379**, 1757–1761.
156 N. S. Shirodkar and U. V. Waghmare, *Phys. Rev. B: Condens. Matter Mater. Phys.*, 2012, **86**, 165401.
157 J. Kotakoski, J. C. Meyer, S. Kurasch, D. Santos-Cottin, U. Kaiser and A. V. Krasheninnikov, *Phys. Rev. B: Condens. Matter Mater. Phys.*, 2011, **83**, 245420.
158 S. T. Skowron, V. O. Koroteev, M. Baldoni, S. Lopatin, A. Zurutuza, A. Chuvilin and E. Besley, *Carbon*, 2016, **105**, 176–182.
159 N. Jing, Q. Xue, C. Ling, M. Shan, T. Zhang, X. Zhou and Z. Jiao, *RSC Adv.*, 2012, **2**, 9124–9129.
160 B. Mortazavi and S. Ahzi, *Carbon*, 2013, **63**, 460–470.
161 A. Verma and A. Parashar, *Phys. Chem. Chem. Phys.*, 2017, **19**, 16023–16037.
162 A. Lherbier, S. M.-M. Dubois, X. Declerck, Y.-M. Niquet, S. Roche and J.-C. Charlier, *Phys. Rev. B: Condens. Matter Mater. Phys.*, 2012, **86**, 075402.
163 X. Peng and R. Ahuja, *Nano Lett.*, 2008, **8**, 4464–4468.
164 L. Vicarelli, S. J. Heerema, C. Dekker and H. W. Zandbergen, *ACS Nano*, 2015, **9**, 3428–3435.
165 O. V. Yazyev and S. G. Louie, *Phys. Rev. B: Condens. Matter Mater. Phys.*, 2010, **81**, 195420.

166 B. W. Jeong, J. Ihm and G.-D. Lee, *Phys. Rev. B: Condens. Matter Mater. Phys.*, 2008, **78**, 165403.
167 J. Lahiri, Y. Lin, P. Bozkurt, I. I. Oleynik and M. Batzill, *Nat. Nanotechnol.*, 2010, **5**, 326–329.
168 S. Malola, H. Häkkinen and P. Koskinen, *Phys. Rev. B: Condens. Matter Mater. Phys.*, 2010, **81**, 165447.
169 P. Y. Huang, C. S. Ruiz-Vargas, A. M. van der Zande, W. S. Whitney, M. P. Levendorf, J. W. Kevek, S. Garg, J. S. Alden, C. J. Hustedt, Y. Zhu, J. Park, P. L. McEuen and D. A. Muller, *Nature*, 2011, **469**, 389–393.
170 J.-R. Yin, W.-H. Wu, W. Xie, Y.-H. Ding and P. Zhang, *Phys. E*, 2015, **68**, 102–106.
171 T. R. Albrecht, H. A. Mizes, J. Nogami, S.-I. Park and C. F. Quate, *Appl. Phys. Lett.*, 1988, **52**, 362–364.
172 P. Simonis, C. Goffaux, P. A. Thiry, L. P. Biro, P. Lambin and V. Meunier, *Surf. Sci.*, 2002, **511**, 319–322.
173 Y. Liu and B. I. Yakobson, *Nano Lett.*, 2010, **10**, 2178–2183.
174 D. Berger and C. Ratsch, *Phys. Rev. B: Condens. Matter Mater. Phys.*, 2016, **93**, 235441.
175 Y. Li, R.-Q. Zhang, Z. Lin and M. A. Van Hove, *Appl. Phys. Lett.*, 2012, **101**, 253105.
176 W. T. Pong, J. Bendall and C. Durkan, *Surf. Sci.*, 2007, **601**, 498–509.
177 Q. Yu, L. A. Jauregui, W. Wu, R. Colby, J. Tian, Z. Su, H. Cao, Z. Liu, D. Pandey, D. Wei, T. F. Chung, P. Peng, N. P. Guisinger, E. A. Stach, J. Bao, S.-S. Pei and Y. P. Chen, *Nat. Mater.*, 2011, **10**, 443–449.
178 B. Yang, H. Xu, J. Lu and K. P. Loh, *J. Am. Chem. Soc.*, 2014, **136**, 12041–12046.
179 S. Kurasch, J. Kotakoski, O. Lehtinen, V. Skákalová, J. Smet, C. E. Krill III, A. V. Krasheninnikov and U. Kaiser, *Nano Lett.*, 2012, **12**, 3168–3173.
180 Y. Wei, J. Wu, H. Yin, X. Shi, R. Yang and M. Dresselhaus, *Nat. Mater.*, 2012, **11**, 759–763.
181 R. Grantab, V. B. Shenoy and R. S. Ruoff, *Science*, 2010, **330**, 946–948.
182 J. Červenka and C. F. J. Flipse, *Phys. Rev. B: Condens. Matter Mater. Phys.*, 2009, **79**, 195429.
183 V. N. Narozhnyi, K.-H. Müller, D. Eckert, A. Teresiak, L. Dunsch, V. A. Davydov, L. S. Kashevarova and A. V. Rakhmanina, *Phys. B*, 2003, **329–333**, 1217–1218.
184 T. L. Makarova and F. Palacio, in *Carbon Based Magnetism: An Overview of the Magnetism of Metal Free Carbon-based Compounds and Materials*, Elsevier, Amsterdam, 2006.
185 H. Ohldag, T. Tyliszczak, R. Höhne, D. Spemann, P. Esquinazi, M. Ungureanu and T. Butz, *Phys. Rev. Lett.*, 2007, **98**, 187204.
186 T. L. Makarova, B. Sundqvist, R. Höhne, P. Esquinazi, Y. Kopelevich, P. Scharff, V. A. Davydov, L. S. Kashevarova and A. V. Rakhmanina, *Nature*, 2001, **413**, 716–718.
187 T. L. Makarova, B. Sundqvist, R. Höhne, P. Esquinazi, Y. Kopelevich, P. Scharff, V. A. Davydov, L. S. Kashevarova and A. V. Rakhmanina, *Nature*, 2006, **440**, 707.
188 M. A. H. Vozmediano, M. P. López-Sancho, T. Stauber and F. Guinea, *Phys. Rev. B: Condens. Matter Mater. Phys.*, 2005, **72**, 155121.
189 V. M. Pereira, F. Guinea, J. M. B. Lopes dos Santos, N. M. R. Peres and A. H. Castro Neto, *Phys. Rev. Lett.*, 2006, **96**, 036801.
190 J. J. Palacios and F. Ynduráin, *Phys. Rev. B: Condens. Matter Mater. Phys.*, 2012, **85**, 245443.
191 B. Wang and S. T. Pantelides, *Phys. Rev. B: Condens. Matter Mater. Phys.*, 2012, **86**, 165438.
192 V. Antonov, D. Borisova and A. Proykova, *Int. J. Quantum Chem.*, 2013, **113**, 792–796.
193 L. Rodrigo, P. Pou and R. Pérez, *Carbon*, 2016, **103**, 200–208.
194 H. Padmanabhan and B. R. K. Nanda, *Phys. Rev. B: Condens. Matter Mater. Phys.*, 2016, **93**, 165403.
195 W. S. Paz, W. L. Scopel and J. C. C. Freitas, *Solid State Commun.*, 2013, **175-176**, 71–75.
196 Y. Zhang, S.-Y. Li, H. Huang, W.-T. Li, J.-B. Qiao, W.-X. Wang, L.-J. Yin, K.-K. Bai, W. Duan and L. He, *Phys. Rev. Lett.*, 2016, **117**, 166801.
197 F. Gao and S. Gao, *Sci. Rep.*, 2017, **7**, 1792.
198 E. J. G. Santos, S. Riikonen, D. Sánchez-Portal and A. Ayuela, *J. Phys. Chem. C*, 2012, **116**, 7602–7606.
199 R. Faccio and A. W. Mombrú, *J. Phys.: Condens. Matter*, 2012, **24**, 375304.
200 S. Lei, B. Li, E. Kan, J. Huang, Q. Li and J. Yang, *J. Appl. Phys.*, 2013, **113**, 213709.
201 W. L. Scopel, W. S. Paz and J. C. C. Freitas, *Solid State Commun.*, 2016, **240**, 5–9.
202 J. Barzola-Quiquia, P. Esquinazi, M. Rothermel, D. Spemann, T. Butz and N. García, *Phys. Rev. B: Condens. Matter Mater. Phys.*, 2007, **76**, 161403.
203 Q. Zhou, Y. Yong, W. Ju, X. Su and X. Li, *Phys. E*, 2017, **91**, 65–71.
204 M. Riccò, D. Pontiroli, M. Mazzani, M. Choucair, J. A. Stride and O. V. Yazyev, *Nano Lett.*, 2011, **11**, 4919–4922.
205 M. P. López-Sancho, F. de Juan and M. A. H. Vozmediano, *Phys. Rev. B: Condens. Matter Mater. Phys.*, 2009, **79**, 075413.
206 P. Lu, Z. Zhang and W. Guo, *Phys. Lett. A*, 2009, **373**, 3354–3358.
207 J.-C. Ren, Z. Ding, R.-Q. Zhang and M. A. Van Hove, *Phys. Rev. B: Condens. Matter Mater. Phys.*, 2015, **91**, 045425.
208 S. Dutta and K. Wakabayashi, *Sci. Rep.*, 2015, **5**, 11744.
209 L. Kou, C. Tang, W. Guo and C. Chen, *ACS Nano*, 2011, **5**, 1012–1017.
210 T. Enoki and K. Takai, Unconventional Magnetic Properties of Nanographite, in *Carbon-Based Magnetism*, ed. T. L. Makarova and F. Palacio, Elsevier B.V., 2006, pp. 397–416.
211 T. Enoki, Y. Kobayashi and K.-I. Fukui, *Int. Rev. Phys. Chem.*, 2007, **26**, 609–645.
212 T. Enoki, Magnetism of Nanographene, in *Graphene: Synthesis, Properties, and Phenomena*, ed. C. N. R. Rao and A. K. Sood, Wiley-VCH Verlag GmbH & Co. KGaA, Weinheim, Germany, 2013, pp. 131–157.
213 S. E. Stein and R. L. Brown, *J. Am. Chem. Soc.*, 1987, **109**, 3721–3729.
214 K. Tanaka, S. Yamashita, H. Yamabe and T. Yamabe, *Synth. Met.*, 1987, **17**, 143–148.

215 M. Fujita, K. Wakabayashi, K. Nakada and K. Kusakabe, *J. Phys. Soc. Jpn.*, 1996, **65**, 1920–1923.
216 Y. Niimi, T. Matsui, H. Kambara, K. Tagami, M. Tsukada and H. Fukuyama, *Appl. Surf. Sci.*, 2005, **241**, 43–48.
217 Y. Kobayashi, K.-I. Fukui, T. Enoki and K. Kusakabe, *Phys. Rev. B: Condens. Matter Mater. Phys.*, 2006, **73**, 125415.
218 E. Clar, *The Aromatic Sextet*, Wiley, London, 1972.
219 K. Wakabayashi, M. Sigrist and M. Fujita, *J. Phys. Soc. Jpn.*, 1998, **67**, 2089–2093.
220 M. Bendikov, H. M. Duong, K. Starkey, K. N. Houk, E. A. Carter and F. Wudl, *J. Am. Chem. Soc.*, 2004, **126**, 7416–7417.
221 O. Hod, V. Barone and G. E. Scuseria, *Phys. Rev. B: Condens. Matter Mater. Phys.*, 2008, **77**, 035411.
222 D. E. Jiang and S. Dai, *J. Phys. Chem. A*, 2008, **112**, 332–335.
223 J. C. Freitas, W. L. Scopel, W. S. Paz, L. V. Bernardes, F. E. Cunha-Filho, C. Speglich, F. M. Araujo-Moreira, D. Pelc, T. Cvitanic and M. Pozek, *Sci. Rep.*, 2015, **5**, 14761.
224 Y. Shibayama, H. Sato, T. Enoki and M. Endo, *Phys. Rev. Lett.*, 2000, **84**, 1744–1747.
225 K. Nakada, M. Fujita, G. Dresselhaus and M. S. Dresselhaus, *Phys. Rev. B: Condens. Matter Mater. Phys.*, 1996, **54**, 17954–17961.
226 K. Wakabayashi, M. Fujita, H. Ajiki and M. Sigrist, *Phys. Rev. B: Condens. Matter Mater. Phys.*, 1999, **59**, 8271–8282.
227 M. Terrones, A. R. Botello-Mendez, J. Campos-Delgado, F. Lopez-Urias, Y. I. Vega-Cantu, F. J. Rodriguez-Macias, A. L. Elias, E. Munoz-Sandoval, A. G. Cano-Marquez, J. C. Charlier and H. Terrones, *Nano Today*, 2010, **5**, 351–372.
228 Y. Segawa, H. Ito and K. Itami, *Nat. Rev. Mater.*, 2016, **1**, 1.
229 M. Yagmurcukardes, F. M. Peeters, R. T. Senger and H. Sahin, *Appl. Phys. Rev.*, 2016, **3**, 041302.
230 X. W. Zhang, O. V. Yazyev, J. J. Feng, L. M. Xie, C. G. Tao, Y. C. Chen, L. Y. Jiao, Z. Pedramrazi, A. Zettl, S. G. Louie, H. J. Dai and M. F. Crommie, *ACS Nano*, 2013, **7**, 198–202.
231 P. Ruffieux, S. Y. Wang, B. Yang, C. Sanchez-Sanchez, J. Liu, T. Dienel, L. Talirz, P. Shinde, C. A. Pignedoli, D. Passerone, T. Dumslaff, X. L. Feng, K. Mullen and R. Fasel, *Nature*, 2016, **531**, 489–492.
232 H. J. Xiang, E. J. Kan, S. H. Wei, M. H. Whangbo and J. L. Yang, *Nano Lett.*, 2009, **9**, 4025–4030.
233 Y. Son, M. Cohen and S. Louie, *Phys. Rev. Lett.*, 2006, **97**, 216803.
234 L. Sun, Q. Li, H. Ren, H. Su, Q. Shi and J. Yang, *J. Chem. Phys.*, 2008, **129**, 074704.
235 B. Sahu, H. K. Min and S. K. Banerjee, *Phys. Rev. B: Condens. Matter Mater. Phys.*, 2010, **82**, 115426.
236 F. Wu, E. Kan, H. Xiang, S. Wei, M. Whangbo and J. Yang, *Appl. Phys. Lett.*, 2009, **94**, 223105.
237 S. Y. Li, L. L. Shi, L. Wen and T. X. Ma, *J. Phys.: Condens. Matter*, 2016, **28**, 086001.
238 B. Sahu, H. Min, A. H. MacDonald and S. K. Banerjee, *Phys. Rev. B: Condens. Matter Mater. Phys.*, 2008, **78**, 045404.
239 V. L. J. Joly, M. Kiguchi, S. J. Hao, K. Takai, T. Enoki, R. Sumii, K. Amemiya, H. Muramatsu, T. Hayashi, Y. A. Kim, M. Endo, J. Campos-Delgado, F. Lopez-Urias, A. Botello-Mendez, H. Terrones, M. Terrones and M. S. Dresselhaus, *Phys. Rev. B: Condens. Matter Mater. Phys.*, 2010, **81**, 245428.
240 H. U. Ozdemir, A. Altintas and A. D. Guclu, *Phys. Rev. B: Condens. Matter Mater. Phys.*, 2016, **93**, 014415.
241 S. L. Chang, B. R. Wu, J. H. Wong and M. F. Lin, *Carbon*, 2014, **77**, 1031–1039.
242 S. L. Chang, B. R. Wu, P. H. Yang and M. F. Lin, *RSC Adv.*, 2016, **6**, 64852–64860.
243 K. K. Paulla and A. A. Farajian, *J. Phys.: Condens. Matter*, 2013, **25**, 115303.
244 G. Kim and S. H. Jhi, *Appl. Phys. Lett.*, 2010, **97**, 263114.
245 J. Kunstmann, C. Ozdogan, A. Quandt and H. Fehske, *Phys. Rev. B: Condens. Matter Mater. Phys.*, 2011, **83**, 045414.
246 M. Golor, S. Wessel and M. J. Schmidt, *Phys. Rev. Lett.*, 2014, **112**, 046601.
247 M. Raczkowski and F. F. Assaad, *Phys. Rev. B: Condens. Matter Mater. Phys.*, 2017, **96**, 115155.
248 B. Huang, F. Liu, J. Wu, B. L. Gu and W. H. Duan, *Phys. Rev. B: Condens. Matter Mater. Phys.*, 2008, **77**, 153411.
249 C. Koop and S. Wessel, *Phys. Rev. B: Condens. Matter Mater. Phys.*, 2017, **96**, 165114.
250 S. S. Rao, S. N. Jammalamadaka, A. Stesmans, V. V. Moshchalkov, J. van Tol, D. V. Kosynkin, A. Higginbotharn-Duque and J. M. Tour, *Nano Lett.*, 2012, **12**, 1210–1217.
251 D. J. Klein, *Chem. Phys. Lett.*, 1994, **217**, 261–265.
252 D. J. Klein and L. Bytautas, *J. Phys. Chem. A*, 1999, **103**, 5196–5210.
253 K. He, A. W. Robertson, S. Lee, E. Yoon, G. D. Lee and J. H. Warner, *ACS Nano*, 2014, **8**, 12272–12279.
254 P. Wagner, V. V. Ivanovskaya, M. Melle-Franco, B. Humbert, J. J. Adjizian, P. R. Briddon and C. P. Ewels, *Phys. Rev. B: Condens. Matter Mater. Phys.*, 2013, **88**, 094106.
255 K. Wakabayashi, S. Okada, R. Tomita, S. Fujimoto and Y. Natsume, *J. Phys. Soc. Jpn.*, 2010, **79**, 034706.
256 L. P. Chen, L. J. Wang and D. Beljonne, *Carbon*, 2014, **77**, 868–879.
257 J. Z. Liu, B. W. Li, Y. Z. Tan, A. Giannakopoulos, C. Sanchez-Sanchez, D. Beljonne, P. Ruffieux, R. Fasel, X. L. Feng and K. Mullen, *J. Am. Chem. Soc.*, 2015, **137**, 6097–6103.
258 P. Koskinen, S. Malola and H. Hakkinen, *Phys. Rev. Lett.*, 2008, **101**, 115502.
259 T. Wassmann, A. P. Seitsonen, A. M. Saitta, M. Lazzeri and F. Mauri, *Phys. Rev. Lett.*, 2008, **101**, 096402.
260 F. J. Owens, *J. Chem. Phys.*, 2008, **128**, 194701.
261 E. Cruz-Silva, Z. M. Barnett, B. G. Sumpter and V. Meunier, *Phys. Rev. B: Condens. Matter Mater. Phys.*, 2011, **83**, 155445.
262 J. Lan, X. H. Zheng, L. L. Song, R. N. Wang and Z. Zeng, *Solid State Commun.*, 2012, **152**, 1635–1640.
263 Y. F. Li, Z. Zhou, P. W. Shen and Z. F. Chen, *ACS Nano*, 2009, **3**, 1952–1958.
264 S. Q. Zhao, Y. Lu, W. G. Lu, W. J. Liang and E. G. Wang, *Chin. Phys. B*, 2014, **23**, 067305.
265 S. S. Kim, H. S. Kim, H. S. Kim and Y. H. Kim, *Carbon*, 2015, **81**, 339–346.

266 E. J. Kan, X. J. Wu, Z. Y. Li, X. C. Zeng, J. L. Yang and J. G. Hou, *J. Chem. Phys.*, 2008, **129**, 084712.
267 M. Topsakal, E. Aktürk, H. Sevinçli and S. Ciraci, *Phys. Rev. B: Condens. Matter Mater. Phys.*, 2008, **78**, 235435.
268 D. Midtvedt and A. Croy, *J. Phys.: Condens. Matter*, 2016, **28**, 045302.
269 K. Sawada, F. Ishii and M. Saito, *J. Phys. Soc. Jpn.*, 2011, **80**, 044712.
270 T. X. Ma, S. H. Liu, P. Gao, Z. B. Huang and H. Q. Lin, *J. Appl. Phys.*, 2012, **112**, 073922.
271 Q. Q. Dai, Y. F. Zhu and Q. Jiang, *Phys. Chem. Chem. Phys.*, 2014, **16**, 10607–10613.
272 A. J. Simbeck, D. Y. Gu, N. Kharche, P. V. Satyam, P. Avouris and S. K. Nayak, *Phys. Rev. B: Condens. Matter Mater. Phys.*, 2013, **88**, 035413.
273 B. Sahu, H. Min and S. K. Banerjee, *Phys. Rev. B: Condens. Matter Mater. Phys.*, 2011, **84**, 075481.
274 N. Gorjizadeh, A. A. Farajian, K. Esfarjani and Y. Kawazoe, *Phys. Rev. B: Condens. Matter Mater. Phys.*, 2008, **78**, 155427.
275 N. K. Jaiswal and P. Srivastava, *IEEE Trans. Nanotechnol.*, 2013, **12**, 685–691.
276 P. Srivastava, S. Dhar and N. K. Jaiswal, *Phys. Lett. A*, 2015, **379**, 835–842.
277 Z. Zhu, D. Wang, Z. H. Zhang and M. Qiu, *Carbon*, 2016, **106**, 252–259.
278 Z. F. Liu, Q. P. Wu, A. X. Chen, X. B. Xiao, N. H. Liu and G. X. Miao, *Sci. Rep.*, 2017, **7**, 8854.
279 M. H. Wu, X. C. Zeng and P. Jena, *J. Phys. Chem. Lett.*, 2013, **4**, 2482–2488.
280 K. Sawada, F. Ishii, M. Saito, S. Okada and T. Kawai, *Nano Lett.*, 2009, **9**, 269–272.
281 K. Sawada, F. Ishii and M. Saito, *Phys. Rev. B: Condens. Matter Mater. Phys.*, 2010, **82**, 245426.
282 B. Xu, J. Yin, Y. D. Xia, X. G. Wan, K. Jiang and Z. G. Liu, *Appl. Phys. Lett.*, 2010, **96**, 163102.
283 K. Sawada, F. Ishii, M. Saito, S. Okada and T. Kawai, *Nano Lett.*, 2009, **9**, 269–272.
284 S. Dutta and S. K. Pati, *J. Phys. Chem. B*, 2008, **112**, 1333–1335.
285 E. J. Kan, Z. Y. Li, J. L. Yang and J. G. Hou, *J. Am. Chem. Soc.*, 2008, **130**, 4224–4225.
286 S. Dutta, A. K. Manna and S. K. Pati, *Phys. Rev. Lett.*, 2009, **102**, 096601.
287 S. Dutta and K. Wakabayashi, *Sci. Rep.*, 2012, **2**, 519.
288 W. Z. Wu, Z. H. Zhang, P. Lu and W. L. Guo, *Phys. Rev. B: Condens. Matter Mater. Phys.*, 2010, **82**, 085425.
289 P. Cui, Q. Zhang, H. B. Zhu, X. X. Li, W. Y. Wang, Q. X. Li, C. G. Zeng and Z. Y. Zhang, *Phys. Rev. Lett.*, 2016, **116**, 026802.
290 K. Tarawneh and N. Al-Aqtash, *J. Nano Res.*, 2014, **27**, 65–73.
291 M. Kan, J. Zhou, Q. Sun, Q. Wang, Y. Kawazoe and P. Jena, *Phys. Rev. B: Condens. Matter Mater. Phys.*, 2012, **85**, 155450.
292 Q. Q. Dai, Y. F. Zhu and Q. Jiang, *J. Phys. Chem. C*, 2013, **117**, 4791–4799.
293 G. P. Tang, Z. H. Zhang, X. Q. Deng, Z. Q. Fan and H. L. Zhu, *Phys. Chem. Chem. Phys.*, 2015, **17**, 638–643.
294 B. Mandal, S. Sarkar, A. Pramanik and P. Sarkar, *RSC Adv.*, 2014, **4**, 49946–49952.
295 C. Chakravarty, B. Mandal and P. Sarkar, *Phys. Lett. A*, 2017, **381**, 307–313.
296 P. Lu, Z. H. Zhang and W. L. Guo, *Phys. Lett. A*, 2009, **373**, 3354–3358.
297 J. N. B. Rodrigues, P. A. D. Goncalves, N. F. G. Rodrigues, R. M. Ribeiro, J. M. B. Lopes dos Santos and N. M. R. Peres, *Phys. Rev. B: Condens. Matter Mater. Phys.*, 2011, **84**, 155435.
298 W. X. Zhang, C. He, T. Li and S. B. Gong, *RSC Adv.*, 2015, **5**, 33407–33413.
299 X. H. Hu, L. T. Sun and A. V. Krasheninnikov, *Appl. Phys. Lett.*, 2012, **100**, 263115.
300 X. D. Tan, X. P. Liao and L. T. Sun, *Physica E*, 2017, **85**, 302–307.
301 S. Y. Yue, Q. B. Yan, Z. G. Zhu, H. J. Cui, Q. R. Zheng and G. Su, *Carbon*, 2014, **71**, 150–158.
302 D. Soriano, F. Muñoz-Rojas, J. Fernández-Rossier and J. J. Palacios, *Phys. Rev. B: Condens. Matter Mater. Phys.*, 2010, **81**, 165409.
303 B. Xu, J. Yin, Y. D. Xia, X. G. Wan, K. Jiang and Z. G. Liu, *Appl. Phys. Lett.*, 2010, **96**, 163102.
304 Z. Y. Guan, C. Si, S. L. Hu and W. H. Duan, *Phys. Chem. Chem. Phys.*, 2016, **18**, 12350–12356.
305 J. Kang, F. M. Wu and J. B. Li, *Appl. Phys. Lett.*, 2011, **98**, 083109.
306 H. Z. Zhang, S. Meng, H. F. Yang, L. Li, H. X. Fu, W. Ma, C. Y. Niu, J. T. Sun and C. Z. Gu, *J. Appl. Phys.*, 2015, **117**, 113902.
307 W. C. Yi, W. Liu, L. Zhao, R. Islam, M. S. Miao and J. Y. Liu, *RSC Adv.*, 2017, **7**, 27932–27937.
308 O. Hod, V. Barone, J. E. Peralta and G. E. Scuseria, *Nano Lett.*, 2007, **7**, 2292–2299.
309 J. Guan, W. Chen, Y. F. Li, G. T. Yu, Z. M. Shi, X. R. Huang, C. C. Sun and Z. F. Chen, *Adv. Funct. Mater.*, 2013, **23**, 1507–1518.
310 R. Ortiz, J. L. Lado, M. Melle-Franco and J. Fernández-Rossier, *Phys. Rev. B: Condens. Matter Mater. Phys.*, 2016, **94**, 094414.
311 J. Bhattacharjee, *J. Chem. Phys.*, 2012, **137**, 094705.
312 D. Cho, K. C. Ko, H. Park and J. Y. Lee, *J. Phys. Chem. C*, 2015, **119**, 10109–10115.
313 Y. F. Li, Z. Zhou, C. R. Cabrera and Z. F. Chen, *Sci. Rep.*, 2013, **3**, 2030.
314 Y. Wang and Y. F. Li, *Theor. Chem. Acc.*, 2014, **133**, 1548.
315 V. A. Rigo, T. B. Martins, A. J. R. da Silva, A. Fazzio and R. H. Miwa, *Phys. Rev. B: Condens. Matter Mater. Phys.*, 2009, **79**, 075435.
316 G. D. Yu, X. L. Lu, Y. S. Zheng and W. J. Tian, *J. Appl. Phys.*, 2012, **111**, 033707.
317 X. H. Hu, W. Zhang, L. T. Sun and A. V. Krasheninnikov, *Phys. Rev. B: Condens. Matter Mater. Phys.*, 2012, **86**, 195418.

318 M. M. Zhong, C. Huang and G. Z. Wang, *J. Mater. Sci.*, 2017, **52**, 12307–12313.
319 P. P. Shinde, O. Groning, S. Y. Wang, P. Ruffieux, C. A. Pignedoli, R. Fasel and D. Passerone, *Carbon*, 2017, **124**, 123–132.
320 Y. Li, W. Zhang, M. Morgenstern and R. Mazzarello, *Phys. Rev. Lett.*, 2013, **110**, 216804.
321 S. B. Tang and X. R. Cao, *Phys. Chem. Chem. Phys.*, 2014, **16**, 23214–23223.
322 G. D. Belletti, S. D. Dalosto and S. Tinte, *J. Phys.: Condens. Matter*, 2016, **28**, 435002.
323 Y. W. Son, M. L. Cohen and S. G. Louie, *Nature*, 2006, **444**, 347–349.
324 M. R. Rezapour, J. Yun, G. Lee and K. S. Kim, *J. Phys. Chem. Lett.*, 2016, **7**, 5049–5055.
325 F. J. Culchac, R. B. Capaz, A. T. Costa and A. Latgé, *J. Phys.: Condens. Matter*, 2014, **26**, 216002.
326 Z. Y. Li, H. Y. Qian, J. Wu, B. L. Gu and W. H. Duan, *Phys. Rev. Lett.*, 2008, **100**, 206802.
327 G. Yang, B. Y. Li, W. Zhang, M. Ye and T. X. Ma, *J. Phys.: Condens. Matter*, 2017, **29**, 365601.
328 L. L. Sun, P. Wei, J. H. Wei, S. Sanvito and S. M. Hou, *J. Phys.: Condens. Matter*, 2011, **23**, 425301.
329 M. Golor, T. C. Lang and S. Wessel, *Phys. Rev. B: Condens. Matter Mater. Phys.*, 2013, **87**, 155441.
330 A. R. Carvalho, J. H. Warnes and C. H. Lewenkopf, *Phys. Rev. B: Condens. Matter Mater. Phys.*, 2014, **89**, 245444.
331 X. Li, X. Wang, L. Zhang, S. Lee and H. Dai, *Science*, 2008, **319**, 1229–1232.
332 J. Cai, P. Ruffieux, R. Jaafar, M. Bieri, T. Braun, S. Blankenburg, M. Muoth, A. P. Seitsonen, M. Saleh, X. Feng, K. Mullen and R. Fasel, *Nature*, 2010, **466**, 470–473.
333 Y. P. Chen, Y. E. Xie and X. H. Yan, *J. Appl. Phys.*, 2008, **103**, 063711.
334 L. Zhu, J. Wang, T. Zhang, L. Ma, C. W. Lim, F. Ding and X. C. Zeng, *Nano Lett.*, 2010, **10**, 494–498.
335 Z. F. Wang, Q. Li, Q. W. Shi, X. Wang, J. G. Hou, H. Zheng and J. Chen, *Appl. Phys. Lett.*, 2008, **92**, 133119.
336 X. Wu and X. C. Zeng, *Nano Res.*, 2008, **1**, 40–45.
337 T. Jayasekera and J. W. Mintmire, *Nanotechnology*, 2007, **18**, 424033.
338 Y. F. Li, Z. Zhou, P. W. Shen and Z. F. Chen, *J. Phys. Chem. C*, 2012, **116**, 208–213.
339 D. Wang, Z. Zhang, Z. Zhu and B. Liang, *Sci. Rep.*, 2014, **4**, 7587.
340 Z. F. Wang, S. Jin and F. Liu, *Phys. Rev. Lett.*, 2013, **111**, 096803.
341 Y. Ding and Y. L. Wang, *Phys. Chem. Chem. Phys.*, 2012, **14**, 2040–2049.
342 L. A. Ma, H. Hu, L. Y. Zhu and J. L. Wang, *J. Phys. Chem. C*, 2011, **115**, 6195–6199.
343 W. L. Wang, S. Meng and E. Kaxiras, *Nano Lett.*, 2008, **8**, 241–245.
344 M. Ezawa, *Phys. Rev. B: Condens. Matter Mater. Phys.*, 2007, **76**, 245115.
345 O. V. Yazyev, W. L. Wang, S. Meng and E. Kaxiras, *Nano Lett.*, 2008, **8**, 766.
346 W. L. Wang, O. V. Yazyev, S. Meng and E. Kaxiras, *Phys. Rev. Lett.*, 2009, **102**, 157201.
347 A. M. Silva, M. S. Pires and V. N. Freire, *J. Phys. Chem. C*, 2010, **114**, 17472–17485.
348 S. Ganguly, M. Kabir and T. Saha-Dasgupta, *Phys. Rev. B: Condens. Matter Mater. Phys.*, 2017, **95**, 174419.
349 H. Sahin and R. T. Senger, *Phys. Rev. B: Condens. Matter Mater. Phys.*, 2008, **78**, 205423.
350 W. Sheng, Z. Y. Ning, Z. Q. Yang and H. Guo, *Nanotechnology*, 2010, **21**, 385201.
351 M. Kabir and T. Saha-Dasgupta, *Phys. Rev. B: Condens. Matter Mater. Phys.*, 2014, **90**, 035403.
352 A. Valli, A. Amaricci, A. Toschi, T. Saha-Dasgupta, K. Held and M. Capone, *Phys. Rev. B: Condens. Matter Mater. Phys.*, 2016, **94**, 245146.
353 K. Szałowski, *Phys. Rev. B: Condens. Matter Mater. Phys.*, 2011, **84**, 205409.
354 S. K. Saha, M. Baskey and D. Majumdar, *Adv. Mater.*, 2010, **22**, 5531–5536.
355 X. Guo, C. D. Wang and Y. G. Zhou, *Phys. Lett. A*, 2013, **377**, 993–996.
356 Y. G. Zhou, Z. G. Wang, P. Yang, X. Sun, X. T. Zu and F. Gao, *J. Phys. Chem. C*, 2012, **116**, 5531–5537.
357 J. Kang, F. M. Wu and J. B. Li, *J. Appl. Phys.*, 2012, **112**, 104328.
358 K. Szałowski, *J. Appl. Phys.*, 2013, **114**, 243908.
359 A. P. Zhou, W. D. Sheng and S. J. Xu, *Appl. Phys. Lett.*, 2013, **103**, 133103.
360 Y. Ge, J. L. Ji, Z. Z. Shen, Q. Zhang, A. Q. Jian, Q. Q. Duan, C. Wang, J. Jiang, W. D. Zhang and S. B. Sang, *Carbon*, 2018, **127**, 432–436.
361 J. Zhou, Q. Wang, Q. Sun and P. Jena, *Phys. Rev. B: Condens. Matter Mater. Phys.*, 2011, **84**, 081402.
362 X. W. Li and Q. Wang, *Phys. Chem. Chem. Phys.*, 2012, **14**, 2065–2069.
363 X. W. Li, Q. Wang, X. S. Chen, Y. Kawazoe and P. Jena, *New J. Phys.*, 2012, **14**, 033043.
364 K. Gopinadhan, Y. J. Shin, I. Yudhistira, J. Niu and H. Yang, *Phys. Rev. B: Condens. Matter Mater. Phys.*, 2013, **88**, 195429.
365 P. Lu, Z. H. Zhang, C. H. Woo and W. L. Guo, *J. Phys. Chem. C*, 2012, **116**, 626–631.
366 J. Shen, Y. Zhu, X. Yang and C. Li, *Chem. Commun.*, 2012, **48**, 3686–3699.
367 J. Viana-Gomes, V. M. Pereira and N. M. R. Peres, *Phys. Rev. B: Condens. Matter Mater. Phys.*, 2009, **80**, 245436.
368 T. Espinosa-Ortega, I. A. Lukyanchuk and Y. G. Rubo, *Phys. Rev. B: Condens. Matter Mater. Phys.*, 2013, **87**, 205434.
369 M. Koshino and T. Ando, *Phys. Rev. B: Condens. Matter Mater. Phys.*, 2010, **81**, 195431.
370 B. Jaworowski, P. Potasz and A. Wójs, *Superlattices Microstruct.*, 2013, **64**, 44–51.
371 O. Voznyy, A. D. Guclu, P. Potasz and P. Hawrylak, *Phys. Rev. B: Condens. Matter Mater. Phys.*, 2011, **83**, 165417.

372 S. Bhowmick and V. B. Shenoy, *J. Chem. Phys.*, 2008, **128**, 244717.
373 S. Cheng, J. M. Yu, T. X. Ma and N. M. R. Peres, *Phys. Rev. B: Condens. Matter Mater. Phys.*, 2015, **91**, 075410.
374 J. L. Lado and J. Fernández-Rossier, *Phys. Rev. Lett.*, 2014, **113**, 027203.
375 I. Weymann, J. Barnas and S. Krompiewski, *Phys. Rev. B: Condens. Matter Mater. Phys.*, 2015, **92**, 045427.
376 A. D. Guclu, P. Potasz and P. Hawrylak, *Phys. Rev. B: Condens. Matter Mater. Phys.*, 2011, **84**, 035425.
377 A. K. Swain, D. Li and D. Bahadur, *Carbon*, 2013, **57**, 346–356.
378 H. S. S. R. Matte, K. S. Subrahmanyam and C. N. R. Rao, *J. Phys. Chem. C*, 2009, **113**, 9982–9985.
379 R. McIntosh, M. A. Mamo, B. Jamieson, S. Roy and S. Bhattacharyya, *Europhys. Lett.*, 2012, **97**, 38001.
380 O. E. Andersson, B. L. V. Prasad, H. Sato, T. Enoki, Y. Hishiyama, Y. Kaburagi, M. Yoshikawa and S. Bandow, *Phys. Rev. B: Condens. Matter Mater. Phys.*, 1998, **58**, 16387–16395.
381 R. Hohne and P. Esquinazi, *Adv. Mater.*, 2003, **14**, 753–756.
382 Y. Y. Sun, Y. P. Zheng, J. Chen, W. L. Zhang, N. J. Tang and Y. W. Du, *Appl. Phys. Lett.*, 2016, **108**, 033105.
383 J. Liu, H. Bi, P. C. Morais, X. Zhang, F. P. Zhang and L. Hu, *Sci. Rep.*, 2017, **7**, 2165.
384 A. S. Arico, P. Bruce, B. Scrosati, J. M. Tarascon and W. van Schalkwijk, *Nat. Mater.*, 2005, **4**, 366–377.
385 X. Wang, X. Li, L. Zhang, Y. Yoon, P. K. Weber, H. Wang, J. Guo and H. Dai, *Science*, 2009, **324**, 768–771.
386 H. Pinto, R. Jones, J. P. Goss and P. R. Briddon, *Phys. Status Solidi A*, 2010, **207**, 2131–2136.
387 S. Y. Zhou, D. A. Siegel, A. V. Fedorov and A. Lanzara, *Phys. Rev. Lett.*, 2008, **101**, 086402.
388 K. S. Mali, J. Greenwood, J. Adisoejoso, R. Phillipson and S. De Feyter, *Nanoscale*, 2015, **7**, 1566–1585.
389 J. Jin, X. Fu, Q. Liu, Y. Liu, Z. Wei, K. Niu and J. Zhang, *ACS Nano*, 2013, **7**, 4764–4773.
390 P. Lazar, R. Zboril, M. Pumera and M. Otyepka, *Phys. Chem. Chem. Phys.*, 2014, **16**, 14231–14235.
391 D. M. Edwards and M. I. Katsnelson, *J. Phys.: Condens. Matter*, 2006, **18**, 7209–7225.
392 Y. Ito, C. Christodoulou, M. V. Nardi, N. Koch, M. Klaui, H. Sachdev and K. Mullen, *J. Am. Chem. Soc.*, 2015, **137**, 7678–7685.
393 Q. H. Miao, L. D. Wang, Z. Y. Liu, B. Wei, F. B. Xu and W. D. Fei, *Sci. Rep.*, 2016, **6**, 21832.
394 J. Y. Li, X. H. Li, P. H. Zhao, D. Y. Lei, W. L. Li, J. T. Bai, Z. Y. Ren and X. L. Xu, *Carbon*, 2015, **84**, 460–468.
395 J. Zhu, H. Park, R. Podila, A. Wadehra, P. Ayala, L. Oliveira, J. He, A. A. Zakhidov, A. Howard, J. Wilkins and A. M. Rao, *J. Magn. Magn. Mater.*, 2016, **401**, 70–76.
396 P. Willke, J. A. Amani, A. Sinterhauf, S. Thakur, T. Kotzott, T. Druga, S. Weikert, K. Maiti, H. Hofsass and M. Wenderoth, *Nano Lett.*, 2015, **15**, 5110–5115.
397 F. Cervantes-Sodi, G. Csanyi, S. Piscanec and A. C. Ferrari, *Phys. Rev. B: Condens. Matter Mater. Phys.*, 2008, **77**, 165427.
398 E. J. G. Santos, D. Sanchez-Portal and A. Ayuela, *Phys. Rev. B: Condens. Matter Mater. Phys.*, 2010, **81**, 125433.
399 E. J. G. Santos, A. Ayuela, S. B. Fagan, J. Mendes Filho, D. L. Azevedo, A. G. Souza Filho and D. Sanchez-Portal, *Phys. Rev. B: Condens. Matter Mater. Phys.*, 2008, **78**, 195420.
400 E. J. G. Santos, A. Ayuela and D. Sanchez-Portal, *J. Phys. Chem. C*, 2012, **116**, 1174–1178.
401 J. Tucek, K. C. Kemp, K. S. Kim and R. Zboril, *ACS Nano*, 2014, **8**, 7571–7612.
402 W. Zhang, W. C. Lu, H. X. Zhang, K. M. Ho and C. Z. Wang, *J. Phys.: Condens. Matter*, 2016, **28**, 115001.
403 R. R. Nair, I. L. Tsai, M. Sepioni, O. Lehtinen, J. Keinonen, A. V. Krasheninnikov, A. H. C. Neto, M. I. Katsnelson, A. K. Geim and I. V. Grigorieva, *Nat. Commun.*, 2013, **4**, 2010.
404 E. J. G. Santos, A. Ayuela and D. Sánchez-Portal, *New J. Phys.*, 2012, **14**, 043022.
405 D. W. Boukhvalov and M. I. Katsnelson, *Nano Lett.*, 2008, **8**, 4373–4379.
406 D. W. Boukhvalov and M. I. Katsnelson, *Phys. Rev. B: Condens. Matter Mater. Phys.*, 2008, **78**, 085413.
407 F. P. OuYang, B. Huang, Z. Y. Li, J. Xiao, H. Y. Wang and H. Xu, *J. Phys. Chem. C*, 2008, **112**, 12003–12007.
408 D. C. Elias, R. R. Nair, T. M. Mohiuddin, S. V. Morozov, P. Blake, M. P. Halsall, A. C. Ferrari, D. W. Boukhvalov, M. I. Katsnelson, A. K. Geim and K. S. Novoselov, *Science*, 2009, **323**, 610–613.
409 P. Laaksonen, M. Kainlauri, T. Laaksonen, A. Shchepetov, H. Jiang, J. Ahopelto and M. B. Linder, *Angew. Chem., Int. Ed.*, 2010, **49**, 4946–4949.
410 V. E. Antonov, I. O. Bashkin, A. V. Bazhenov, B. M. Bulychev, V. K. Fedotov, T. N. Fursova, A. I. Kolesnikov, V. I. Kulakov, R. V. Lukashev, D. V. Matveev, M. K. Sakharov and Y. M. Shulga, *Carbon*, 2016, **100**, 465–473.
411 A. Y. S. Eng, H. L. Poh, F. Sanek, M. Marysko, S. Matejkova, Z. Sofer and M. Pumera, *ACS Nano*, 2013, **7**, 5930–5939.
412 J. Berashevich and T. Chakraborty, *Nanotechnology*, 2010, **21**, 355201.
413 H. Sahin, C. Ataca and S. Ciraci, *Appl. Phys. Lett.*, 2009, **95**, 222510.
414 H. Sahin, C. Ataca and S. Ciraci, *Phys. Rev. B: Condens. Matter Mater. Phys.*, 2010, **81**, 205417.
415 Y. Li, Z. Zhou, P. Shen and Z. Chen, *J. Phys. Chem. C*, 2009, **113**, 15043–15045.
416 C.-K. Yang, *Carbon*, 2010, **48**, 3901–3905.
417 H. Da, Y. P. Feng and G. Liang, *J. Phys. Chem. C*, 2011, **115**, 22701–22706.
418 N. Kharche and S. K. Nayak, *Nano Lett.*, 2011, **11**, 5274–5278.
419 L. Feng and W. X. Zhang, *AIP Adv.*, 2012, **2**, 042138.
420 D. W. Boukhvalov, *Physica E*, 2010, **43**, 199–201.
421 F. Buonocore, A. M. Conte and N. Lisi, *Physica E*, 2016, **78**, 65–72.
422 L. X. Liu, S. D. Liu, Z. Y. Zhang and W. G. Zhu, *J. Phys. Chem. C*, 2017, **121**, 24824–24830.
423 M. Wang and C. M. Li, *Phys. Chem. Chem. Phys.*, 2013, **15**, 3786–3792.

424 A. M. Panich, A. I. Shames and T. Nakajima, *J. Phys. Chem. Solids*, 2001, **62**, 959–964.
425 R. Zboril, F. Karlicky, A. B. Bourlinos, T. A. Steriotis, A. K. Stubos, V. Georgakilas, K. Safarova, D. Jancik, C. Trapalis and M. Otyepka, *Small*, 2010, **6**, 2885–2891.
426 R. R. Nair, W. C. Ren, R. Jalil, I. Riaz, V. G. Kravets, L. Britnell, P. Blake, F. Schedin, A. S. Mayorov, S. J. Yuan, M. I. Katsnelson, H. M. Cheng, W. Strupinski, L. G. Bulusheva, A. V. Okotrub, I. V. Grigorieva, A. N. Grigorenko, K. S. Novoselov and A. K. Geim, *Small*, 2010, **6**, 2877–2884.
427 D. D. Chronopoulos, A. Bakandritsos, M. Pykal, R. Zboril and M. Otyepka, *Appl. Mater. Today*, 2017, **9**, 60–70.
428 H. Y. Liu, Z. F. Hou, C. H. Hu, Y. Yang and Z. Z. Zhu, *J. Phys. Chem. C*, 2012, **116**, 18193–18201.
429 T. L. Makarova, A. L. Shelankov, A. A. Zyrianova, A. I. Veinger, T. V. Tisnek, E. Lahderanta, A. I. Shames, A. V. Okotrub, L. G. Bulusheva, G. N. Chekhova, D. V. Pinakov, I. P. Asanov and Z. Sljivancanin, *Sci. Rep.*, 2015, **5**, 13382.
430 R. J. Kashtiban, M. A. Dyson, R. R. Nair, R. Zan, S. L. Wong, Q. Ramasse, A. K. Geim, U. Bangert and J. Sloan, *Nat. Commun.*, 2014, **5**, 4902.
431 V. V. Mazurenko, A. N. Rudenko, S. A. Nikolaev, D. S. Medvedeva, A. I. Lichtenstein and M. I. Katsnelson, *Phys. Rev. B: Condens. Matter Mater. Phys.*, 2016, **94**, 214411.
432 T. L. Makarova, A. L. Shelankov, A. I. Shames, A. A. Zyrianova, A. A. Komlev, G. N. Chekhova, D. V. Pinakov, L. G. Bulusheva, A. V. Okotrub and E. Lahderanta, *Sci. Rep.*, 2017, **7**, 16544.
433 W. F. Li, M. W. Zhao, Y. Y. Xia, R. Q. Zhang and Y. G. Mu, *J. Mater. Chem.*, 2009, **19**, 9274–9282.
434 H. Lin, G. Fratesi and G. P. Brivio, *Phys. Chem. Chem. Phys.*, 2015, **17**, 2210–2215.
435 A. Ravikumar, A. Baby, H. Lin, G. P. Brivio and G. Fratesi, *Sci. Rep.*, 2016, **6**, 24603.
436 A. J. M. Giesbers, K. Uhlirova, M. Konecny, E. C. Peters, M. Burghard, J. Aarts and C. F. Flipse, *Phys. Rev. Lett.*, 2013, **111**, 166101.
437 T. Tang, N. J. Tang, Y. P. Zheng, X. G. Wan, Y. Liu, F. C. Liu, Q. H. Xu and Y. W. Du, *Sci. Rep.*, 2015, **5**, 8448.
438 X. Huang, X. Y. Qi, F. Boey and H. Zhang, *Chem. Soc. Rev.*, 2012, **41**, 666–686.
439 J. Chen, W. L. Zhang, Y. Y. Sun, Y. P. Zheng, N. J. Tang and Y. W. Du, *Sci. Rep.*, 2016, **6**, 26862.
440 K. Bagani, M. K. Ray, B. Satpati, N. R. Ray, M. Sardar and S. Banerjee, *J. Phys. Chem. C*, 2014, **118**, 13254–13259.
441 D. W. Boukhvalov, *Phys. Chem. Chem. Phys.*, 2010, **12**, 15367–15371.
442 D. Lee, J. Seo, X. Zhu, J. M. Cole and H. B. Su, *Appl. Phys. Lett.*, 2015, **106**, 172402.
443 M. Wang and C. M. Li, *New J. Phys.*, 2010, **12**, 129801.
444 T. Tang, F. Liu, Y. Liu, X. Li, Q. H. Xu, Q. Feng and N. J. Tang, *Appl. Phys. Lett.*, 2014, **104**, 123104.
445 M. Wang, W. Huang, M. B. Chan-Park and C. M. Li, *Nanotechnology*, 2011, **22**, 105702.
446 N. Liaros, J. Tucek, K. Dimos, A. Bakandritsos, K. S. Andrikopoulos, D. Gournis, R. Zboril and S. Couris, *Nanoscale*, 2016, **8**, 2908–2917.
447 Y. Liu, N. J. Tang, X. G. Wan, Q. Feng, M. Li, Q. H. Xu, F. Liu and Y. W. Du, *Sci. Rep.*, 2013, **3**, 2566.
448 S. K. Sarkar, K. K. Raul, S. S. Pradhan, S. Basu and A. Nayak, *Physica E*, 2014, **64**, 78–82.
449 P. Z. Sun, K. L. Wang, J. Q. Wei, M. L. Zhong, D. H. Wu and H. W. Zhu, *Nano Res.*, 2014, **7**, 1507–1518.
450 G. Khurana, N. Kumar, R. K. Kotnala, T. Nautiyal and R. S. Katiyar, *Nanoscale*, 2013, **5**, 3346–3351.
451 L. Majchrzycki, M. A. Augustyniak-Jablokow, R. Strzelczyk and M. Mackowiak, *Acta Phys. Pol., A*, 2015, **127**, 540–542.
452 S. Qin, X. T. Guo, Y. Q. Cao, Z. H. Ni and Q. Y. Xu, *Carbon*, 2014, **78**, 559–565.
453 S. B. Kumar and J. Guo, *Nanoscale*, 2012, **4**, 982–985.
454 J. Bai, R. Cheng, F. Xiu, L. Liao, M. Wang, A. Shailos, K. L. Wang, Y. Huang and X. Duan, *Nat. Nanotechnol.*, 2010, **5**, 655–659.
455 W. Shu-Wei, H. E. Lin, L. Huang-De, K. Y. Chen, T. Kun-Hua, C. W. Chen, C. Ju-Ying, L. Cheng-Hua, C. T. Liang and Y. F. Chen, *Nanotechnology*, 2011, **22**, 335701.
456 E. McCann, K. Kechedzhi, V. I. Fal'ko, H. Suzuura, T. Ando and B. L. Altshuler, *Phys. Rev. Lett.*, 2006, **97**, 146805.
457 N. M. R. Peres, A. H. Castro Neto and F. Guinea, *Phys. Rev. B: Condens. Matter Mater. Phys.*, 2006, **73**, 195411.
458 N. M. R. Peres, A. H. Castro Neto and F. Guinea, *Phys. Rev. B: Condens. Matter Mater. Phys.*, 2006, **73**, 241403.
459 Y. C. Huang, C. P. Chang and M. F. Lin, *Nanotechnology*, 2007, **18**, 495401.
460 J. Liu, A. R. Wright, C. Zhang and Z. Ma, *Appl. Phys. Lett.*, 2008, **93**, 041106.
461 C. Ritter, S. S. Makler and A. Latgé, *Phys. Rev. B: Condens. Matter Mater. Phys.*, 2008, **77**, 195443.
462 T. S. Li, Y. C. Huang, S. C. Chang, C. P. Chang and M. F. Lin, *Philos. Mag.*, 2009, **89**, 697–709.
463 A. Diamantopoulou, S. Glenis, G. Zolnierkiwicz, N. Guskos and V. Likodimos, *J. Appl. Phys.*, 2017, **121**, 043906.
464 S. Qin and Q. G. Xu, *J. Alloys Compd.*, 2017, **692**, 332–338.
465 Y. Liu, Q. Feng, N. J. Tang, X. G. Wan, F. C. Liu, L. Y. Lv and Y. W. Du, *Carbon*, 2013, **60**, 549–551.
466 A. Bakandritsos, M. Pykal, P. Blonski, P. Jakubec, D. D. Chronopoulos, K. Polakova, V. Georgakilas, K. Cepe, O. Tomanec, V. Ranc, A. B. Bourlinos, R. Zboril and M. Otyepka, *ACS Nano*, 2017, **11**, 2982–2991.
467 A. Y. S. Eng, Z. Sofer, D. Sedmidubský and M. Pumera, *ACS Nano*, 2017, **11**, 1789–1797.
468 C. Schafhaeutl, *J. Prakt. Chem.*, 1840, **21**, 129–157.
469 M. S. Dresselhaus and G. Dresselhaus, *Adv. Phys.*, 1981, **30**, 139–326.
470 M. S. Dresselhaus, *Phys. Scr.*, 2012, **T146**, 014002.
471 N. Kim, K. S. Kim, N. Jung, L. Brus and P. Kim, *Nano Lett.*, 2011, **11**, 860–865.
472 I. Khrapach, F. Withers, T. H. Bointon, D. K. Polyushkin, W. L. Barnes, S. Russo and M. F. Craciun, *Adv. Mater.*, 2012, **24**, 2844–2849.
473 Y. Lia and Q. Yue, *Physica B*, 2013, **425**, 72–77.

474 T. H. Bointon, I. Khrapach, R. Yakimova, A. V. Shytov, M. F. Craciun and S. Russo, *Nano Lett.*, 2014, **14**, 1751–1755.
475 S. Ichinokura, K. Sugawara, A. Takayama, T. Takahashi and S. Hasegawa, *ACS Nano*, 2016, **10**, 2761–2765.
476 J. Kim, P. Lee, M. Ryu, H. Park and J. Chung, *RSC Adv.*, 2016, **6**, 114219–114223.
477 N. A. Kaskhedikar and J. Maier, *Adv. Mater.*, 2009, **21**, 2664–2680.
478 J. Wan, S. D. Lacey, J. Dai, W. Bao, M. S. Fuhrer and L. Hu, *Chem. Soc. Rev.*, 2016, **45**, 6742–6765.
479 M. Suzuki and I. S. Suzuki, *Phys. Rev. B: Condens. Matter Mater. Phys.*, 1998, **58**, 371–384.
480 Y. Li and Q. Yue, *Physica B*, 2013, **425**, 72–77.
481 T. H. Bointon, I. Khrapach, R. Yakimova, A. V. Shytov, M. F. Craciun and S. Russo, *Nano Lett.*, 2014, **14**, 1751–1755.
482 R. Decker, J. Brede, N. Atodiresei, V. Caciuc, S. Blügel and R. Wiesendanger, *Phys. Rev. B: Condens. Matter Mater. Phys.*, 2013, **87**, 041403(R).
483 A. D. Vu, J. Coraux, G. Chen, A. T. N'Diaye, A. K. Schmid and N. Rougemaille, *Sci. Rep.*, 2016, **6**, 24783.
484 S. Manzeli, D. Ovchinnikov, D. Pasquier, O. V. Yazyev and A. Kis, *Nat. Rev. Mater.*, 2017, **2**, 17033.
485 B. Schonfeld, J. J. Huang and S. C. Moss, *Acta Crystallogr., Sect. B: Struct. Sci.*, 1983, **39**, 404–407.
486 F. Wypych and R. Schollhorn, *J. Chem. Soc., Chem. Commun.*, 1992, 1386–1388.
487 M. K. Jana and C. N. R. Rao, *Philos. Trans. R. Soc., A*, 2016, **374**, 20150318.
488 H. Pan and Y.-W. Zhang, *J. Phys. Chem. C*, 2012, **116**, 11752–11757.
489 C. N. Rao, H. S. Matte and U. Maitra, *Angew. Chem., Int. Ed.*, 2013, **52**, 13162–13185.
490 Y. Zhou, Q. Su, Z. Wang, H. Deng and X. Zu, *Phys. Chem. Chem. Phys.*, 2013, **15**, 18464–18470.
491 M. Sagynbaeva, P. Panigrahi, L. Yunguo, M. Ramzan and R. Ahuja, *Nanotechnology*, 2014, **25**, 165703.
492 Z. Yang, D. Gao, J. Zhang, Q. Xu, S. Shi, K. Tao and D. Xue, *Nanoscale*, 2015, **7**, 650–658.
493 Z. H. Zhang, X. F. Liu, J. Yu, Y. Hang, Y. Li, Y. F. Guo, Y. Xu, X. Sun, J. X. Zhou and W. L. Guo, *WIREs Comput. Mol. Sci.*, 2016, **6**, 324–350.
494 A. M. Panich, A. I. Shames, R. Rosentsveig and R. Tenne, *J. Phys.: Condens. Matter*, 2009, **21**, 395301.
495 S. Mathew, K. Gopinadhan, T. K. Chan, X. J. Yu, D. Zhan, L. Cao, A. Rusydi, M. B. H. Breese, S. Dhar, Z. X. Shen, T. Venkatesan and J. T. L. Thong, *Appl. Phys. Lett.*, 2012, **101**, 102103.
496 M. Pizzochero and O. V. Yazyev, *Phys. Rev. B: Condens. Matter Mater. Phys.*, 2017, **96**, 245402.
497 J. Zhang, J. M. Soon, K. P. Loh, J. H. Yin, J. Ding, M. B. Sullivian and P. Wu, *Nano Lett.*, 2007, **7**, 2370–2376.
498 D. Q. Gao, M. S. Si, J. Y. Li, J. Zhang, Z. P. Zhang, Z. L. Yang and D. S. Xue, *Nanoscale Res. Lett.*, 2013, **8**, 129.
499 H. Li, X. Y. Qi, J. Wu, Z. Y. Zeng, J. Wei and H. Zhang, *ACS Nano*, 2013, **7**, 2842–2849.
500 P. Murugan, V. Kumar, Y. Kawazoe and N. Ota, *Phys. Rev. A: At., Mol., Opt. Phys.*, 2005, **71**, 063203.
501 S. Tongay, S. S. Varnoosfaderani, B. R. Appleton, J. Wu and A. F. Hebard, *Appl. Phys. Lett.*, 2012, **101**, 123105.
502 A. Vojvodic, B. Hinnemann and J. K. Nørskov, *Phys. Rev. B: Condens. Matter Mater. Phys.*, 2009, **80**, 125416.
503 Y. Li, Z. Zhou, S. Zhang and Z. Chen, *J. Am. Chem. Soc.*, 2008, **130**, 16739–16744.
504 A. U. Rahman, G. Rahman and V. M. Garcia-Suarez, *J. Magn. Magn. Mater.*, 2017, **443**, 343–351.
505 J. Luxa, O. Jankovsky, D. Sedmidubsky, R. Medlin, M. Marysko, M. Pumera and Z. Sofer, *Nanoscale*, 2016, **8**, 1960–1967.
506 X. Mao, Y. Xu, Q. Xue, W. Wang and D. Gao, *Nanoscale Res. Lett.*, 2013, **8**, 430.
507 H. P. Li, S. Liu, S. L. Huang, D. Q. Yin, C. S. Li and Z. C. Wang, *Ceram. Int.*, 2016, **42**, 2364–2369.
508 Y. Q. Guo, H. T. Deng, X. Sun, X. L. Li, J. Y. Zhao, J. C. Wu, W. S. Chu, S. J. Zhang, H. B. Pan, X. S. Zheng, X. J. Wu, C. Q. Jin, C. Z. Wu and Y. Xie, *Adv. Mater.*, 2017, **29**, 1700715.
509 R. Rahman, K. Davey and S. Z. Qiao, *Adv. Funct. Mater.*, 2017, **27**, 1606129.
510 G. C. Loh and R. Pandey, *Phys. Chem. Chem. Phys.*, 2015, **17**, 18843–18853.
511 S. X. Yang, C. Wang, H. Sahin, H. Chen, Y. Li, S. S. Li, A. Suslu, F. M. Peeters, Q. Liu, J. B. Li and S. Tongay, *Nano Lett.*, 2015, **15**, 1660–1666.
512 X. O. Zhang and Q. F. Li, *J. Appl. Phys.*, 2015, **118**, 064306.
513 L. Tao, F. C. Meng, S. D. Zhao, Y. L. Song, J. X. Yu, X. J. Wang, Z. G. Liu, Y. Wang, B. S. Li, Y. Wang and Y. Sui, *Nanoscale*, 2017, **9**, 4898–4906.
514 X. Zhao, X. N. Zhang, T. X. Wang, S. Y. Wei and L. Yang, *RSC Adv.*, 2017, **7**, 26673–26679.
515 V. Kochat, A. Apte, J. A. Hachtel, H. Kumazoe, A. Krishnamoorthy, S. Susarla, J. C. Idrobo, F. Shimojo, P. Vashishta, R. Kalia, A. Nakano, C. S. Tiwary and P. M. Ajayan, *Adv. Mater.*, 2017, **29**, 1703754.
516 M. Meng, C. G. Shi, T. Li, S. E. Shi, T. H. Li and L. Z. Liu, *Appl. Surf. Sci.*, 2017, **425**, 696–701.
517 L. Li, O. Leenaerts, X. Kong, X. Chen, M. W. Zhao and F. M. Peeters, *Nano Res.*, 2017, **10**, 2168–2180.
518 L. Zhou, L. Kou, Y. Sun, C. Felser, F. M. Hu, G. C. Shan, S. C. Smith, B. H. Yan and T. Frauenheim, *Nano Lett.*, 2015, **15**, 7867–7872.
519 E. Torun, H. Sahin, C. Bacaksiz, R. T. Senger and F. M. Peeters, *Phys. Rev. B: Condens. Matter Mater. Phys.*, 2015, **92**, 104407.
520 B. Huang, G. Clark, E. Navarro-Moratalla, D. R. Klein, R. Cheng, K. L. Seyler, D. Zhong, E. Schmidgall, M. A. McGuire, W. Yao, D. Xiao, P. Jarillo-Herrero and X. D. Xu, *Nature*, 2017, **546**, 270–273.
521 V. V. Kulish and W. Huang, *J. Phys. Chem. C*, 2017, **5**, 8734–8741.
522 M. Ashton, D. Gluhovic, S. B. Sinnott, J. Guo, D. A. Stewart and R. G. Hennig, *Nano Lett.*, 2017, **17**, 5251–5257.
523 F. Wu, C. X. Huang, H. P. Wu, C. Lee, K. M. Deng, E. J. Kan and P. Jena, *Nano Lett.*, 2015, **15**, 8277–8281.

524 J. Y. Liu, Z. F. Liu, T. L. Song and X. Cui, *J. Phys. Chem. C*, 2017, **5**, 727–732.
525 Y. J. Sun, Z. W. Zhuo, X. J. Wu and J. L. Yang, *Nano Lett.*, 2017, **17**, 2771–2777.
526 X. D. Zhang, J. J. Zhang, J. Y. Zhao, B. C. Pan, M. G. Kong, J. Chen and Y. Xie, *J. Am. Chem. Soc.*, 2012, **134**, 11908–11911.
527 A. J. Du, S. Sanvito and S. C. Smith, *Phys. Rev. Lett.*, 2012, **108**, 197207.
528 E. J. Kan, W. Hu, C. Y. Xiao, R. F. Lu, K. M. Deng, J. L. Yang and H. B. Su, *J. Am. Chem. Soc.*, 2012, **134**, 5718–5721.
529 M. Khazaei, M. Arai, T. Sasaki, C. Y. Chung, N. S. Venkataramanan, M. Estili, Y. Sakka and Y. Kawazoe, *Adv. Funct. Mater.*, 2013, **23**, 2185–2192.
530 C. Si, J. Zhou and Z. Sun, *ACS Appl. Mater. Interfaces*, 2015, **7**, 17510–17515.
531 G. Y. Gao, G. Q. Ding, J. Li, K. L. Yao, M. H. Wu and M. C. Qian, *Nanoscale*, 2017, **8**, 8986–8994.
532 H. Kumar, N. C. Frey, L. Dong, B. Anasori, Y. Gogotsi and V. B. Shenoy, *ACS Nano*, 2017, **11**, 7648–7655.
533 L. Dong, H. Kumar, B. Anasori, Y. Gogotsi and V. B. Shenoy, *J. Phys. Chem. Lett.*, 2017, **8**, 422–428.
534 B. Sachs, T. O. Wehling, M. I. Katsnelson and A. I. Lichtenstein, *Phys. Rev. B: Condens. Matter Mater. Phys.*, 2011, **84**, 195414.
535 L. Ci, L. Song, C. H. Jin, D. Jariwala, D. X. Wu, Y. J. Li, A. Srivastava, Z. F. Wang, K. Storr, L. Balicas, F. Liu and P. M. Ajayan, *Nat. Mater.*, 2010, **9**, 430–435.
536 K. Watanabe, T. Taniguchi and H. Kanda, *Nat. Mater.*, 2004, **3**, 404–409.
537 M. S. Si and D. S. Xue, *Phys. Rev. B: Condens. Matter Mater. Phys.*, 2007, **75**, 193409.
538 R.-F. Liu and C. Cheng, *Phys. Rev. B: Condens. Matter Mater. Phys.*, 2007, **76**, 014405.
539 P. Dev, Y. Xue and P. Zhang, *Phys. Rev. Lett.*, 2008, **100**, 117204.
540 M. N. Huda and L. Kleinman, *Phys. Rev. B: Condens. Matter Mater. Phys.*, 2006, **74**, 075418.
541 N. Joshi and P. Ghosh, *Phys. Rev. B: Condens. Matter Mater. Phys.*, 2013, **87**, 235440.
542 V. Barone and J. E. Peralta, *Nano Lett.*, 2008, **8**, 2210–2214.
543 M. S. Si, D. Q. Gao, D. Z. Yang, Y. Peng, Z. Y. S. Zhang, D. S. Xue, Y. S. Liu, X. H. Deng and G. P. Zhang, *J. Chem. Phys.*, 2014, **140**, 204701.
544 S. K. Gupta, H. Y. He, I. Lukacevic and R. Pandey, *Phys. Chem. Chem. Phys.*, 2017, **19**, 30370–30380.
545 E. Machado-Charry, P. Boulanger, L. Genovese, N. Mousseau and P. Pochet, *Appl. Phys. Lett.*, 2012, **101**, 132405.
546 J. Zhou, Q. Wang, Q. Sun and P. Jena, *Phys. Rev. B: Condens. Matter Mater. Phys.*, 2010, **81**, 085442.
547 F. Li, Z. G. Zhu, X. D. Yao, G. Q. Lu, M. W. Zhao, Y. Y. Xia and Y. Chen, *Appl. Phys. Lett.*, 2008, **92**, 102515.
548 E. J. Kan, H. J. Xiang, F. Wu, C. Tian, C. Lee, J. L. Yang and M. H. Whangbo, *Appl. Phys. Lett.*, 2010, **97**, 122503.
549 M. Du, X. L. Li, A. Z. Wang, Y. Z. Wu, X. P. Hao and M. W. Zhao, *Angew. Chem., Int. Ed.*, 2014, **53**, 3645–3649.
550 J. J. He, P. B. Lyu, L. Z. Sun, A. M. Garcia and P. Nachtigall, *J. Mater. Chem. C*, 2016, **4**, 6500.
551 J. He, P. Lyu and P. Nachtigall, *J. Mater. Chem. C*, 2016, **4**, 11143–11149.
552 J. J. He, X. Li, P. B. Lyu and P. Nachtigall, *Nanoscale*, 2017, **9**, 2246–2252.
553 A. K. Swain and D. Bahadur, *RSC Adv.*, 2013, **3**, 19243–19246.
554 Y. W. Ma, Y. H. Lu, J. B. Yi, Y. P. Feng, T. S. Herng, X. Liu, D. Q. Gao, D. S. Xue, J. M. Xue, J. Y. Ouyang and J. Ding, *Nat. Commun.*, 2012, **3**, 727.
555 T. Scheike, W. Bohlmann, P. Esquinazi, J. Barzola-Quiquia, A. Ballestar and A. Setzer, *Adv. Mater.*, 2012, **24**, 5826–5831.
556 A. K. Swain and D. Bahadur, *Appl. Phys. Lett.*, 2014, **104**, 242413.
557 L. Chen, L. Guo, Z. Li, H. Zhang, J. Lin, J. Huang, S. Jin and X. Chen, *Sci. Rep.*, 2013, **3**, 2599.

